AN INVESTIGATION INTO HIGH TEMPERATURE SUPERCONDUCTING FLUX PUMP TECHNOLOGY WITH THE CIRCULAR TYPE MAGNETIC FLUX PUMP DEVICES AND YBaCuO FILMS

WEI WANG (王为)

MAGDALENE COLLEGE

UNIVERSITY OF CAMBRIDGE

A THESIS SUBMITTED FOR THE DEGREE OF

DOCTOR OF PHILOSOPHY

APRIL 2014

DECLARATION

The work presented in this thesis was carried out at the Department of Engineering, University of Cambridge, between Oct 2010 and Mar 2014 under the supervision of Dr. Tim Coombs.

The author declares that, except for where specific reference is made to the work of other authors or specially indicated in the text, the contents of this report are his own work, and include nothing done in collaboration. This report has not been previously submitted in part, or in whole, to any other universities for a degree, diploma or other qualification. This dissertation is within the limit of 65,000 words length.

ACKNOWLEDGEMENTS

It is my pleasure to express my tremendous gratitude towards my PhD supervisor, Dr. Tim Coombs, and his wife Mrs. Coombs. During the three and half years over which I have pursued my PhD, Dr. Coombs has given me a lot of valuable advices, along with the freedom to carry out independent research. Without his support, I wouldn't have been able to choose this interesting topic or to complete this thesis. I would like to give my thanks to Mrs. Coombs for her maternal care during my stay in Cambridge over the past three and a half years.

I would like to thank my colleagues in the superconductivity group in the electric engineering division. Happy memories have been shared with them during my stay in Cambridge. In no particular order, I would like to thank Dr. Zhiyong Hong, Dr. Weijia Yuan, Dr. Yu Yan, Dr. Wei Xian, Dr. Min Zhang, Dr. Michal Chudi, Dr. Koichi Matsuda, Dr. Harold Ruiz, Dr. Oliver Hadeler, Dr. Chia-hao Hsu, Dr. Yiran Chen, Fred Spaven, Felix Elefant, Zhaoyang Zhong, Yujia Zhai, Zhen Huang, Mehdi Baghdadi, Lin Fu, Heng Zhang and Xiuchang Zhang. Your friendship and support have been a most valuable asset during the course of my PhD studies. I would also like to offer my gratitude to Mr. Fred Spaven and Mr. John Grundy. Without your experimental support, I would not have been able to set up my experiments successfully.

I would like to thank Dr. Robert Semerad and Ceraco Ceramic Coating GmbH, Germany for providing the YBCO samples for my experiments. I would also like to thank Prof. Yukikazu Iwasa, Dr. Seungyong Hahn, and Dr. John Voccio from the Francis Bitter Magnet Lab, MIT for providing me with their ten square shape YBCO samples. Without your support, I wouldn't have been able to finish my PhD thesis. I would like to thank Dr. David Hasko from the Cambridge Engineering Department for the helping of depositing gold layer on the YBCO thin film. I would also like to acknowledge my previous supervisors Prof. Jiasu Wang, Prof. Suyu Wang and former colleagues from SWJTU, China for valuable discussions about my work. My gratitude also goes to Dr. Xiaorong Wang from the Lawrence Berkeley National Lab, and Dr. Honghai Song from the FRIB, MSU. I would also like to acknowledge Prof. Archie Campbell from Cambridge University for his interest in my work.

Last but not least, I would also like to thank my families and my dear friends for their love and support. My special gratitude gives to Ms. Jie Zhang, for her love and care, which have accompanied me and supported me to pursue a higher dream.

PUBLICATIONS DURING PHD

[1] **Wei Wang**, Min Zhang, Zhen Huang, Yujia Zhai, Zhaoyang Zhong, Fred Spaven, Mehdi Baghdadi, Tim Coombs, "Study of the Penetration of a 2 Inches Diameter YBCO Thin Film with the Travelling Magnetic Wave", *IEEE Trans. Appl. Supercond.*, vol. 24, no.3, pp: 4600304, Jun 2014

[2] **Wei Wang**, Fred Spaven, Mehdi Bagdadi, Tim Coombs, "Direct measurement of the vortex migration caused by travelling magnetic wave", *Appl. Phys. Lett.* **104**, 032602 (2014)

[3] **Wei Wang**, Tim Coombs, "The magnetisation and ac magnetisation losses caused by travelling magnetic wave on a single layer YBCO thin film", Submitted to *Superconductor Science and Technology*, 2014

[4] **Wei Wang**, Tim Coombs, "Vortex migration caused by travelling magnetic wave in a 2 inches diameter $YBa_2Cu_3O_{7-\delta}$ thin film", *Journal of Applied Physics*, **113**, 213906(2013)

[5] **Wei Wang**, Tim Coombs, "The Investigation of Sweeping Speed on the Magnetization of a 2 Inches Diameter $YBa_2Cu_3O_{7-\delta}$ Thin Film with the Circular-Type Magnetic Flux Pump ", *IEEE Trans. Appl. Supercond.*, vol. 23, no.3, pp: 8201104, Jun 2013

[6] **Wei Wang**, Min Zhang, Chaihao Hsu, Tim Coombs, "Design Consideration of a Circular Type Magnetic Flux Pump Device", *IEEE Trans. Appl. Supercond.*, vol. 22, no.3, pp: 5201304, Jun 2012

[7] Min Zhang, **Wei Wang**, YR Chen, Tim Coombs, "Design Methodology of HTS Bulk Machine for Direct-driven Wind Generation", *IEEE Trans. Appl. Supercond.*, vol.22, no.3, pp: 5201804, Jun 2012

[8] M. Zhang, **W. Wang**, Z. Huang, M.Baghdadi, W. Yuan, J. Kvitkovic, S.Pamidi, T.A.Coombs, "AC loss measurements for 2G HTS racetrack coils with heat-shrink tube insulation", *IEEE Trans. Appl. Supercond.*, vol.24, no.3, pp: 4700704, Jun 2014

[9] M. Zhang, M. Chudy, **W. Wang**, Y. Chen, Z. Huang, Z. Zhong, W. Yuan, J. Kvitkovic, S. Pamidi, T. A. Coombs, "AC Loss Estimation of HTS Armature Windings for Electric Machines", *IEEE Trans. Appl.Supercond.*, vol.23, no. 3, pp:5900604, Jun 2013

[10] Z. Huang, M. Zhang, **W. Wang**, T.A.Coombs, "Trial Test of the World's First Bulk-type Fully HTS Synchronous Motor", *IEEE Trans. Appl. Supercond.*, vol.24, no.3, pp: 4602605, Jun 2014

[11] C.H. Hsu, Y. Zhai, M. Zhang, **W. Wang**, T.A. Coombs, "Thermal Material with Low Curie Temperature in a Thermally Actuated Superconducting Flux Pump System", *IEEE Trans. Appl. Supercond.*, vol.23, no. 3, pp:7800304, Jun 2013

[12] Y. Chen, M. Zhang, M. Chudy, **W. Wang**, Z. Zhong, Z. Huang, T. A. Coombs, "Theoretical and Experimental Magnetization Loss Comparison Between IBAD Coils and RABiTS Coils", *IEEE Trans. Appl. Supercond.*, vol.23, no.3, pp: 8201504, Jun 2013

[13] Z. Zhong, M. Zhang, **W. Wang**, M. Chudy, Y. Chen, C.H. Hsu, Z. Huang, T.A. Coombs, "3D Modeling of High Temperature Superconducting Staggered Array Undulator", *IEEE Trans. Appl. Supercond.*, vol.23, no.3, pp: 4101004, Jun 2013

[14] Y. Zhai, C.H. Hsu, F. Spaven, M. Zhang, **W. Wang** and T.A. Coombs, "Soft Ferrite Used as Thermal-Magnetic Conversion Intermedium in the Flux Pumping Technology", *IEEE Trans. Appl. Supercond.*, vol.23, no.3, pp: 7800104, Jun 2013

[15] Z. Huang, W. Xian, M. Zhang, M. Chudy, Y. Chen, Z. Zhong, M. Baghdadi, **W. Wang**, F. Spaven, K. Matsuda, T.A. Coombs, "Control and Operation of a High Temperature Superconducting Synchronous Motor", *IEEE Trans. Appl. Supercond.*, vol.23, no.3, pp: 5200204, Jun 2013

ABSTRACT

The rapid development of second generation (2G) high temperature superconducting (HTS) wires in the last decade has made it possible to wind high quality 2G HTS coils. These 2G HTS coils show promise for future applications such as magnetic resonance imaging (MRI) magnets, electrical machines, magnetic levitation trains, energy storage, etc. 2G HTS coils can be operated using either dc current or ac current. Several important issues have yet to be resolved, such as how to properly magnetise an HTS coil under dc conditions, or how to minimise losses under ac conditions. These problems should be carefully studied before the 2G HTS coils can be widely applied in scientific and industrial applications.

This thesis focuses on emerging HTS flux pump technology for HTS coils operating in a dc environment. HTS flux pump technology applies a travelling magnetic wave to fully magnetise an HTS coil, which is both efficient and economical, and has in recent years been proven feasible. However, the underlying physics of this technology are so far poorly understood. In order to study the influence of a travelling magnetic wave on HTS films such as $YBa_2Cu_3O_{7-\delta}$, two types of circular-type magnetic flux pump (CTMFP) devices were proposed and built. These novel devices generate an annular-shape travelling magnetic wave. The first type was the original CTMFP magnet, which produces the longest wavelength of travelling wave. The second type was the updated CTMFP magnet, which can produce a shorter wavelength of travelling wave (1/2 of the original CTMFP magnet in the six phase connection and 1/4 in the three phase connection). A 2 inch diameter round shape YBCO thin film (200 nm thick of the YBCO layer) and a 46 mm × 46 mm square shape YBCO tape (1.0 μm thick of the YBCO layer, with a hole of Φ26 mm in the centre) were tested.

When using a round shape YBCO thin film and the original CTMFP magnet, it was found that the travelling wave tends to decrease the existing critical magnetic gradient inside the YBCO film. The experiment was repeated under different conditions, such as zero-field cooling (ZFC), field cooling (FC), delta-shape trapped field, etc. A simulation based on the H-formulation using FEM software revealed that, after application of the travelling wave, the current density distribution inside the round shape YBCO sample was disturbed, becoming much lower than its critical current density J_C. This discovery is interesting because the Bean model suggests that the current density inside a type-II superconductor should be equal to either $+J_C$ or $-J_C$ (the critical state model). It was found that a round shape YBCO sample follows the Bean model prediction for the homogeneous oscillating field

(homogeneous in space), which suggests that the travelling wave is more efficient for transporting the magnetic flux inside YBCO film, compared to a homogeneous oscillating field.

An updated CTMFP magnet was designed and built to investigate the influence of the degree of field inhomogeneity on the change of an existing critical magnetic gradient. The results were compared between the six phase connection (1/2 wavelength of the original CTMFP magnet) and the three phase connection (1/4 wavelength of the original CTMFP magnet). It was found that with a travelling wave of consistent amplitude, by shortening the wavelength, the change of magnetic gradient is made stronger. The result supports the assumption that the field inhomogeneity in space may have an important influence on the magnetisation of a YBCO sample. Additionally, in the case of a three phase connection (1/4 wavelength), by reversing the direction of the travelling wave, a different magnetisation profile was obtained, which suggests that the experiment may have detected a macroscopic "magnetic coupling" phenomenon. However, this result needs further study before it can be confirmed.

The square shape YBCO sample was tested by applying a travelling wave in a dc background field under FC conditions. The square shape YBCO sample has a centre hole (Φ26 mm), which is closest to the condition of an HTS coil (single layer instead of multi-layer). However, in the experiment there was no clear change of magnetic flux inside the superconducting loop after application of the travelling wave. This might be attributed to the fact that, the field inhomogeneity is not strong enough to cause flux migration in the experiments, and the YBCO layer is relatively thicker which increases the difficulties. Moreover, the width of the superconducting region is relatively small (10 mm), in order to help magnetic flux migrate into the superconducting loop, the field inhomogeneity must be strong enough in the superconducting region, which increases the technical difficulties. However, this might be able to be accomplished by increase the amplitude of the travelling waves. Some experiments will be carried out in the future.

The experimental findings in this thesis can not only aid in understanding the mechanism of HTS flux pump technology for an HTS coil, but also can help in understanding ac loss from a coil exposed to a travelling wave. As was suggested by the experimental results, the magnetisation of the YBCO film due to the travelling wave is very different from the magnetisation induced by a homogeneous oscillating field. Under operational conditions, such as inside an HTS motor, the HTS coils experience a travelling wave rather than a homogeneous oscillating field. This thesis discusses the difference in resultant ac loss from a travelling wave and a homogeneous oscillating field of the same amplitude. It was found that, for the round shape YBCO sample, the ac loss from a travelling wave is about 1/3 of the loss from a homogeneous oscillating field. The regions in which the ac loss occurred are also different between a travelling wave and a homogeneous oscillating field. These results suggest that the travelling wave cannot be equated to a homogeneous oscillating field when calculating ac loss.

In conclusion, this thesis studies two novel experimental devices, built to study the magnetisation of YBCO films under the influence of a travelling wave. Several novel electromagnetic behaviours were observed in the YBCO films under the influence of a travelling wave, which may help improve understanding of HTS flux pump technology for an HTS coil, and the ac loss induced by a travelling wave.

CONTENTS

FIGURE LIST

TABLE LIST

CHAPTER 1

OUTLINE

The high temperature superconducting (HTS) flux pump technology for HTS coils is an interesting and promising technology which can be used to fully magnetise an HTS magnet in an efficient and economical way. Although there is experimental evidence which supports the feasibility of this technology, the underlying physics is not yet fully understood. This thesis studies the underlying physics behind HTS flux pump technology through the development of two novel devices, which can generate annular-shape travelling magnetic waves. These devices are circular-type magnetic flux pump (CTMFP) devices. In this chapter, an outline is provided for the study of $YBa_2Cu_3O_{7-\delta}$ film using these devices.

Chapter 2 provides an introduction to superconductivity and its basic theories. This chapter begins by introducing type-I and type-II superconducting materials and their related theories, such as the London equation and the Ginzburg Landau (GL) theory. From these theories, it will be shown that the superconductivity phenomenon is a thermodynamic phenomenon which can be explained by minimising the internal free energy. Using the GL theory, the quantisation of magnetic flux lines in the mixed state of type-II superconducting materials will be introduced, followed by the introduction of basic vortex dynamics (fluxons, interactive forces, pinning forces, etc.). In the latter part of this chapter, macroscopic electromagnetic theories for type-II superconducting materials will be derived based on basic vortex dynamics. Concepts such as flux creep and flux flow, and macroscopic electromagnetic models such as the critical state model and the *E-J* power relation will be introduced. Other electromagnetic behaviour such as intrinsic pinning and cross field effect will also be introduced.

Chapter 3 provides an introduction to flux pump technologies for superconducting coils. This chapter begins by discussing the necessity of using flux pump technology to magnetise a HTS magnet. Type-I superconducting flux pump technology for low temperature superconducting (LTS) magnets will be introduced. This is followed by an introduction to the "dc transformer" which suggests a microscopic magnetic coupling phenomenon in type-II superconducting films due to field inhomogeneity. The latter part of the chapter provides an introduction to a possible HTS flux pump technology for HTS magnets, which indicates the possibility of applying a travelling magnetic wave

to fully magnetise an HTS magnet. In order to investigate the effect of the travelling wave on an HTS film and show how an HTS magnet is fully magnetised by a travelling wave, a novel research method is proposed toward the end of this chapter, which introduces the main topic of study for this thesis.

Chapter 4 introduces the experimental systems and the simulation method used. The concept of the circular-type magnetic flux pump (CTMFP) device is introduced, followed by a discussion on the design, build, and assembly of the original CTMFP magnet and the updated CTMFP magnet. The magnets' properties and a circuit analysis will also be introduced. The power system for the magnet (dc power source and three phase inverter) and the measurement system (Hall sensor and calibration method, data acquisition equipment, Labview program) are detailed. The two types of YBCO sample used (2 inch diameter round shape sample and 46 mm × 46 mm square shape sample) and the machining of their holders is described. The final part of this chapter describes the integration of the experimental system and the simulation method based on the H-formulation.

The study aims at using a travelling magnetic wave to magnetise a single layer YBCO sample. To the author's opinion, to successfully "pump" magnetic flux into a type-II superconducting loop, the travelling wave should be able to migrate the flux inside the type-II superconducting film effectively. Moreover, in order to achieve a net magnetisation inside the type-II superconducting loop, a macroscopic "magnetic coupling" phenomenon should be present. In other words, the magnetisation is dependent on the travelling direction of the wave. The topic of the study will be focusing on identifying the flux migration and magnetic coupling due to the travelling wave.

Chapter 5 presents the experimental and simulation results for the original CTMFP magnet and the round shape YBCO thin film. The travelling wave of the original CTMFP magnet has the longest wavelength, or the smallest field inhomogeneity. In the experiment with the round shape YBCO thin film, it was found that the travelling wave is more effective in transporting magnetic flux comparing with the homogeneous oscillating field. An interesting phenomenon was identified such as the travelling wave tends to attenuate the existing critical magnetic gradient. This phenomenon is verified in various condictions, such as zero field cooling (ZFC), field cooling (FC), delta shape trapped field, zero dc background field, etc. Simulations based on the H-formulation were performed to show that the magnetisation based on the travelling wave does not follow the constant current density assumption, or the Bean model. Moreover, it was found that the magnetisation is dependent on the sweeping speed, but is independent on the travelling direction. In other words, the macroscopic magnetic coupling phenomenon is not observed by this device. Other experiments were performed to show that, the travelling wave is more effectively in fully penetrating the YBCO thin film compare with the homogeneous oscillating field. In the final part of the chapter, a topic is proposed to study the ac loss caused by the travelling wave. A comparison will be drawn between ac loss caused by the

travelling wave and the homogeneous oscillating field. The final part is helpful in better understanding of the ac magnetisation loss inside superconducting electric machines, etc.

To identify how the field inhomogeneity influences the magnetisation and to observe a possible "magnetic coupling", an updated CTMFP with shorter wavelength was developed. In Chapter 6, the experimental results for the updated CTMFP magnet and the round shape YBCO thin film are presented. The chapter is divided into two parts. The first part presents the experimental results obtained using a six phase connection (1/2 of the wavelength comparing with the original CTMFP magnet). The second part presents the experimental results obtained using a three phase connection (1/4 of the wavelength comparing with the original CTMFP magnet). The experiment is performed under ZFC and FC conditions. It was identified that, as the wavelength decreases, move flux is migrated into the YBCO sample, which proves that the field inhomogeneity is the key factor in transporting the flux. Moreover, in the three phase connection, it was found that the magnetisation is dependent on the travelling direction, in other words, a possible macroscopic magnetic coupling phenomenon was observed in the experiment. However, as this part of experiment is still in process, further confirmation should be made in the future.

Chapter 7 presents the experimental attempt to magnetise the single layer YBCO loop. The sample is the square shape YBCO sample with a whole in the middle. According to the author's assumption, if magnetic coupling is present in the square shape YBCO tape, the single layer YBCO loop can be gradually magnetised if the dc background field is slightly offset to give unbalanced positive and negative flux transport into the sample centre. The experiment is performed using the original CTMFP magnet, the updated CTMFP magnet with a six phase connection and the updated CTMFP magnet with a three phase connection. Up to this point, there were no observable changes of magnetic flux found in the sample centre. Further studies were recommended as to continue increase the amplitude of the travelling wave.

Chapter 8 discusses a general conclusion to the studies, and proposes future work on this topic.

CHAPTER 2

INTRODUCTION TO SUPERCONDUCTIVITY

Superconductivity describes the phenomenon in which certain materials lose their electric resistivity below a critical temperature T_C. The critical temperature is normally very low (close to absolute zero) for most superconducting materials. Mercury ($T_C \approx 4.2$ K, Table 2.1) was the first superconducting material discovered by the Dutch scientist H.K. Onnes in 1911. This discovery was made possible only due to the successful liquefaction of helium gas, which reaches its boiling point at 4.2 K. The earliest discovered superconducting materials were mostly metals and simple alloys. These metallic superconducting materials work only at very low temperatures (below 30 K) which normally require liquid helium as a cryogen. It wasn't until 1986 that K. Müller and J. Bednorz [2] discovered "cuprate" superconducting materials, which operate at a critical temperature above 30 K. A year later in 1987, C.W. Chu et al. discovered the cuprate superconducting material YBaCuO, which has a T_C higher than the boiling point of liquid nitrogen (77 K) [3]. Thereafter, superconducting materials have been classified into two categories:

- Low Temperature Superconducting (LTS) materials: the critical temperature T_C is lower than around 30 K
- High Temperature Superconducting (HTS) materials: the critical temperature T_C is higher than around 30 K

Superconducting materials are also classified into two categories based on their physical properties in a magnetic field, and are labelled as Type-I or Type-II. Type-I superconducting materials possess a single critical field B_C, while Type-II superconducting materials possess a lower critical field B_{C1} and an upper critical field B_{C2}:

- Type-I superconducting materials: $B < B_C$, superconducting state (Meissner state[1]); $B \geq B_C$, normal state.

- Type-II superconducting materials: $B < B_{C1}$, superconducting state (Meissner state); $B_{C1} \leq B < B_{C2}$, superconducting state (mixed state[2]); $B \geq B_{C2}$, normal state

Presently, the only practically useful superconducting materials are Type-II materials such as Nb_3Sn, NbTi, YBaCuO, BiSrCaCuO, MgB_2 [4], etc. In this chapter, the theoretical interpretation focuses on Type-I and Type-II superconducting materials in relation to the Meissner state and the mixed state. The Meissner state describes the phenomenon of perfect diamagnetism in Type-I and Type-II superconducting materials. The mixed state describes the phenomenon in which flux lines penetrate into superconducting materials in the form of quantised magnetic fluxons (Type-II superconducting materials only). A detailed discussion of these phenomena is presented later in this chapter.

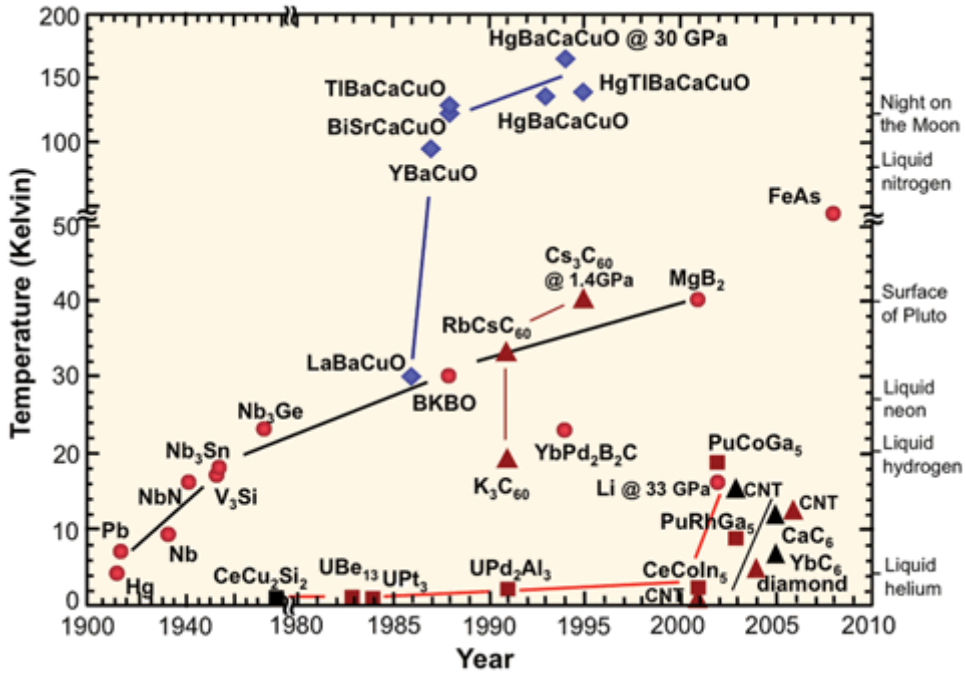

FIG.2.1. The discovery of superconducting materials and their critical temperature [5].

Superconducting materials are widely used in various areas such as medical diagnosis, research facilities, transportation, electric system, energy storage, magnetic measurement, etc. The best known applications of superconductivity are in medical diagnosis in the form of magnetic resonance imaging

[1] Will be discussed in detail in Section 2.1.
[2] Will be discussed in detail in Section 2.2.

(MRI), research equipments such as nuclear magnetic resonance (NMR) and functional magnetic resonance imaging (fMRI), as well as in large research facilities such as the large hadron collider (LHC) and the International Thermonuclear Experimental Reactor (ITER). Almost all these applications adopt LTS materials such as Nb_3Sn or NbTi for the magnet windings. HTS materials are not yet sufficiently developed for widely commercial use. However, there is great potential for HTS materials to be effective for various fields. Applications of HTS materials such as YBaCuO can be classified into two major categories: bulk application and film application. Bulk applications, include an HTS flywheel [6-8], HTS maglev [9], bulk electric machine [10, 11], particle separation [12], vibration isolation [13], etc. Film applications include HTS coils [14, 15], superconducting fault current limiters (FCL) [16, 17], superconducting cables [18], etc. There are two kinds of HTS wire which have been commercialised at present: BSSCO wire and YBCO wire. BSSCO tape is known as the first generation (1G) HTS wire [19] and YBCO is the second generation (2G) HTS wire [20, 21].

This chapter describes the basic physics of superconductivity, in order to establish basic knowledge for later chapters. The Meissner effect and London equations are used for type-I superconductors, and the Ginzburg-Landau theory is a powerful tool for the analysis of type-II superconductors. Basic vortex dynamics are introduced to provide understanding of various electromagnetic phenomena in the mixed state. Specific magnetic phenomena such as intrinsic pinning, the cross-field effect, and the flux shaking effect will also be introduced.

2.1 Type-I superconducting materials

Type-I superconducting materials have a clearly defined phase diagram, as shown in Fig. 2.2. The Meissner state (or the superconducting state) lies below the *H/T* curve, and the normal state or non-superconducting state lies above the curve. This phase diagram is characteristic of type-I superconducting materials. Examples of type-I superconducting materials include metals and alloys such as Hg, Al, Sn, In, etc. In the superconducting state, type-I superconducting materials show two distinct properties: perfect conductivity (zero resistivity), and perfect diamagnetism (or the Meissner effect). The Meissner effect distinguishes type-I superconducting materials from an imaginary ideal perfect conductor. The Meissner effect and its related London equations will be discussed in Section 2.1.1. The intermediate state is discussed in Section 2.1.2, and will be addressed again in Chapter 3.

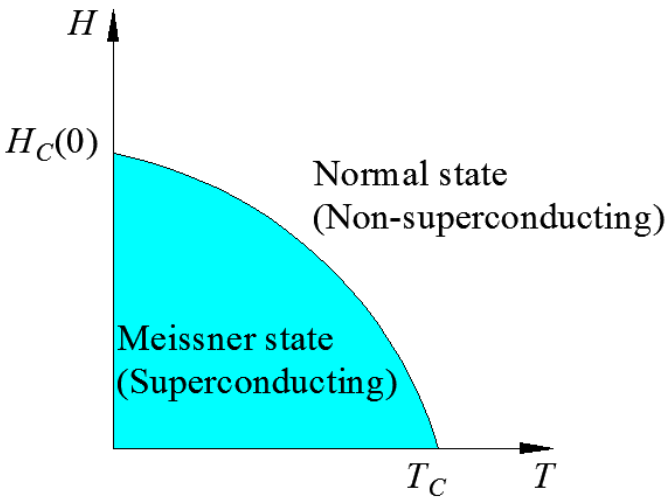

FIG. 2.2. The phase diagram of a type-I superconducting material. The shaded area is the Meissner state (superconducting), while above the *H*-*T* curve is the normal state (non-superconducting).

2.1.1 The Meissner effect and London equations

The Meissner effect describes the phenomenon in which a type-I superconductor (or a type-II superconductor at a magnetic field below H_{C1}) expels magnetic flux from itself, no matter the order of cooling and applying the field. Details of this phenomenon can be found in any textbook on superconductivity. The Meissner effect is the crucial detail by which a superconductor is differentiated from a theoretical ideal conductor ($\sigma = \infty$). While the ideal conductor obeys Lenz's law, a type-I superconductor does not. Comparisons between a type-I superconductor and a perfect conductor are shown in Fig. 2.3. Fig.2.3(a) demonstrates the effect of field cooling (FC), in which the magnetic field is applied prior to cooling the sample. For a type-I superconducting material, after the sample is cooled down to below its critical temperature T_C, the magnetic field is expelled from the inner area (Meissner effect). However, for a perfect conductor, the magnetic field remains stable within the conductor after it has been cooled down (Lenz's law). Fig.2.3(b) shows the effect of zero field cooling (ZFC), in which the sample is cooled before applying the magnetic field. Both a type-I superconducting material and a perfect conductor, will expel a magnetic field from the inner area under these conditions. Although the result appears similar, the expulsion of magnetic flux in a type-I superconducting material is caused by the Meissner effect, whereas the expulsion of magnetic flux in a perfect conductor is due to Lenz's law.

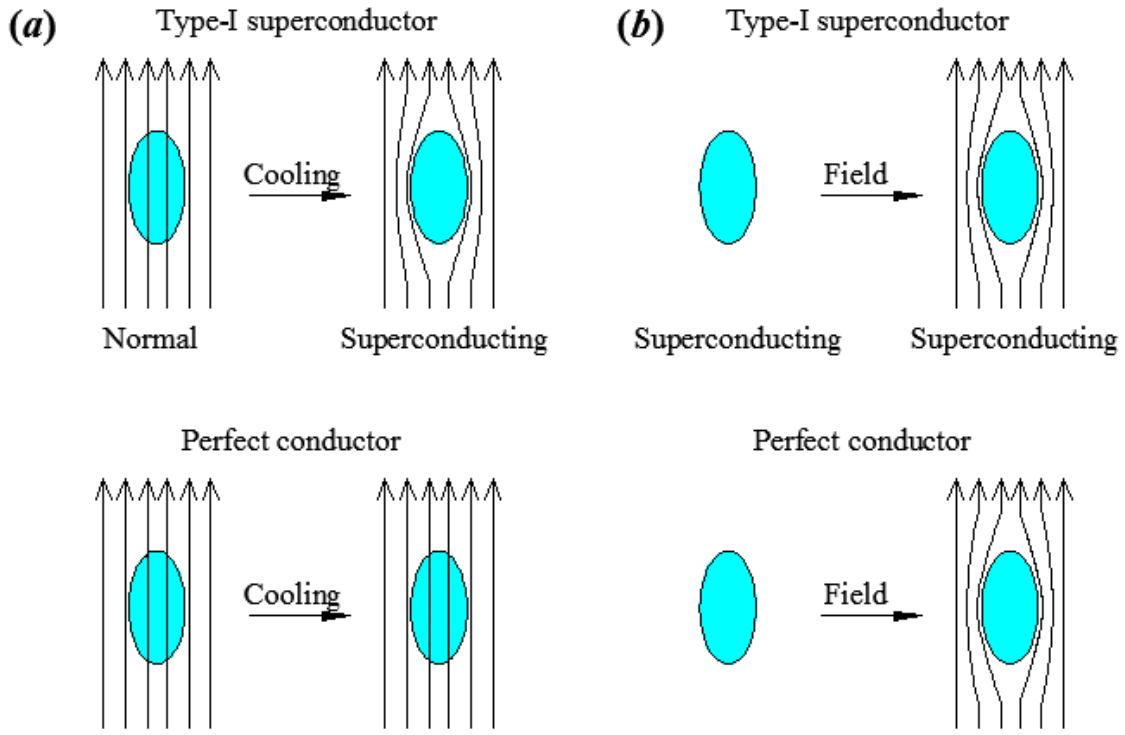

FIG. 2.3. A comparison between the Meissner effect in a type-I superconductor and a perfect conductor. (a) Field cooling (the magnetic field is applied prior to cooling the sample); (b) zero field cooling (the sample is cooled before applying the magnetic field).

The Meissner effect was discovered by Meissner and Ochesenfeld [22], 22 years after the discovery of superconductivity by Onnes. Thereafter, the state of superconductivity is considered to be a thermodynamic phenomenon, since its state is defined by thermodynamic variables such as temperature T and applied magnetic field H. In general, type-I superconducting materials possess the following two properties:

- Property of perfect conductor $\rho=0$
- Property of perfect diamagnetism $\chi = \dfrac{dM}{dH} = -1$

The perfect diamagnetism or Meissner effect is due to a shielding current which develops on the surface of the superconductor when in the presence of an applied magnetic field H. The shielding current is the result of the change in thermodynamic phase in the (H, T) – plane, as shown in Fig. 2.2. Since the current density of the screen current cannot be infinitely large, the magnetic field must penetrate into the superconductor to a finite depth, which is termed the penetration depth λ of the superconductor. The derivation of the penetration depth λ is derived from basic electrodynamics, and

leads to the phenomenological London equations which explain the Meissner effect. The London equation is introduced in the following paragraphs.

In the beginning, assume q is the charge of the carriers (super-electrons, or Cooper-pairs) in the superconductor, m_q is the mass of the carrier, and n_s is the carrier density. Assume the charge carrier experiences no friction in the superconductor (perfect conductivity). In the presence of an electric field $\boldsymbol{E}$, the acceleration of a superconducting charge carrier can be expressed as:

$$m_q \dot{\boldsymbol{v}} = -q\boldsymbol{E} \tag{2.1}$$

where $\boldsymbol{v}$ is the carrier velocity, and $\dot{\boldsymbol{v}}$ is the time derivation (acceleration). The current density can be expressed as $\boldsymbol{J} = -n_s q\boldsymbol{v}$, and Equation (2.1) can be re-written as:

$$\boldsymbol{E} = -\frac{m_q \dot{\boldsymbol{v}}}{q} = \frac{m_q \dot{\boldsymbol{J}}}{n_s q^2} \tag{2.2}$$

The electrodynamic screening length λ was predicted by Haas Lorentz [23] in 1925 to be:

$$\lambda = \left(m_q \big/ \mu_0 n_s q^2 \right)^{1/2} \tag{2.3}$$

Therefore, Equation (2.2) can be re-written as:

$$\boldsymbol{E} = \frac{\mu_0 m_q \dot{\boldsymbol{J}}}{\mu_0 n_s q^2} = \mu_0 \lambda^2 \dot{\boldsymbol{J}} \tag{2.4}$$

Taking the curl on both sides of Equation (2.4):

$$\nabla \times \boldsymbol{E} - \mu_0 \lambda^2 \nabla \times \dot{\boldsymbol{J}} = 0 \tag{2.5}$$

From Faraday's law of induction $\nabla \times \boldsymbol{E} = -\dot{\boldsymbol{B}}$, Equation (2.5) can be re-written as:

$$\mu_0 \lambda^2 \nabla \times \dot{\boldsymbol{J}} + \dot{\boldsymbol{B}} = 0 \tag{2.6}$$

If the time integration is performed on Equation (2.6) and set the integration constant to zero, the result is that:

$$\boldsymbol{B} = -\mu_0 \lambda_L^2 \nabla \times \boldsymbol{J} \tag{2.7}$$

Equation (2.7) was first proposed by Heinz and Fritz London [24], and is the **second London equation**. In this equation, λ is re-written as λ_L to represent the London penetration depth in a

superconductor. λ_L is fundamentally different from the skin effect in metals, since the frictionless motion of charge carriers has been assumed for the superconductor as in Equation (2.1).

The second London equation successfully explains the Meissner effect in superconductors. From Ampere's law of circulation $\nabla \times \boldsymbol{B} = \mu_0 \boldsymbol{J}$, substitute current density $\boldsymbol{J}$ in Equation (2.7) gives:

$$\lambda_L^2 \nabla \times \nabla \times \boldsymbol{B} + \boldsymbol{B} = 0 \tag{2.8}$$

Using the derivative property $\nabla \times \nabla \times \boldsymbol{B} = \nabla(\nabla \cdot \boldsymbol{B}) - \nabla^2 \boldsymbol{B}$ and the conservation of magnetic flux $\nabla \cdot \boldsymbol{B} = 0$, Equation (2.8) can be re-written as:

$$\nabla^2 \boldsymbol{B} = \frac{1}{\lambda_L^2} \boldsymbol{B} \tag{2.9}$$

The one-dimension solution for Equation (2.9) is:

$$B(x) = B_a e^{-x/\lambda_L} \tag{2.10}$$

when $B_a = \mu_0 H_a$, which is the magnetic flux density of the applied magnetic field. The London penetration depth λ_L represents the depth at which the magnetic flux density is reduced to the value B_a / e . Values of λ_L for metallic type-I superconductors such as Al, Sn and Pb lie in the range 40-50 nm.

From Equation (2.3), it is clear that the London penetration depth is dependent only on the density of the charge carriers n_s . According to the phenomenological two-fluid model by Gorter and Casimir [25], a superconductor contains two types of charge carriers: normal electrons and superconducting electrons. The carrier densities of normal electrons n_n and superconducting electrons n_s are functions of temperature. Below the transition temperature, T_C , as the temperature drops, the proportion of superconducting electrons increases. Assuming that λ_0 is the London penetration depth at 0 K, λ is the London penetration depth at temperature *T*. The two-fluid model shows that $\left(\frac{\lambda}{\lambda_0}\right)^2 = \frac{1}{1-(T/T_C)^4}$.

The London equation can also be derived from the free energy, as shown by Fossheim and Sudbo [25]. At a temperature $T<T_C$, the superconducting region contains three types of energy: condensation energy density F_s, kinetic energy F_k of charge carriers and magnetic energy density F_m. The total energy *F* is the integration of the three energies in the superconducting region:

$$F = \int_V F_s(\boldsymbol{r})\mathrm{d}^3\boldsymbol{r} + \int_V F_k(\boldsymbol{r})\mathrm{d}^3\boldsymbol{r} + \int_V F_m(\boldsymbol{r})\mathrm{d}^3\boldsymbol{r} \tag{2.11}$$

The condensation energy density F_s is assumed to be not affected by the magnetic field, and is remains constant as the background energy.

The kinetic energy is expressed as:

$$\begin{aligned} F_k &= \int_V F_k(\boldsymbol{r})\mathrm{d}^3\boldsymbol{r} = \int_V \frac{1}{2} m\boldsymbol{v}_s^2(\boldsymbol{r}) n_s \mathrm{d}^3\boldsymbol{r} \\ &= \frac{\mu_0}{2}\int_V \lambda_L^2 \boldsymbol{J}^2(\boldsymbol{r})\mathrm{d}^3\boldsymbol{r} \end{aligned} \tag{2.12}$$

The magnetic energy is express as:

$$F_m = \int_V F_m(\boldsymbol{r})\mathrm{d}^3\boldsymbol{r} = \int_V \frac{1}{2\mu_0}\boldsymbol{b}^2(\boldsymbol{r})\mathrm{d}^3\boldsymbol{r} \tag{2.13}$$

Then equation (2.11) can be re-written as:

$$F = F_s + \frac{1}{2\mu_0}\int_V \left[\lambda_L^2\left(\nabla\times\boldsymbol{b}(\boldsymbol{r})\right)^2 + \boldsymbol{b}^2(\boldsymbol{r})\right]\mathrm{d}^3\boldsymbol{r} \tag{2.14}$$

By varying $b(\boldsymbol{r})$ by a small amount $\delta b(\boldsymbol{r})$, and subtracting Equation (2.14), the change of the free energy in the superconductor can be expressed as:

$$\delta F = \frac{1}{2\mu_0}\int_V \left[2\boldsymbol{b}\delta\boldsymbol{b} + 2\lambda_L^2\left(\nabla\times\boldsymbol{b}\right)\left(\nabla\times\delta\boldsymbol{b}\right)\right]\mathrm{d}^3\boldsymbol{r} \tag{2.15}$$

If $\delta F = 0$ is the minimised free energy in the superconductor, then:

$$\boldsymbol{b}\delta\boldsymbol{b} + \lambda_L^2\left(\nabla\times\boldsymbol{b}\right)\left(\nabla\times\delta\boldsymbol{b}\right) = 0 \tag{2.16}$$

Using the vector calculus $\nabla\cdot\left(\boldsymbol{A}\times\boldsymbol{B}\right) = \boldsymbol{B}\cdot\nabla\times\boldsymbol{A} - \boldsymbol{A}\cdot\nabla\times\boldsymbol{B}$ [26]:

$$\boldsymbol{b}(\boldsymbol{r}) + \lambda_L^2\nabla\times\nabla\times\boldsymbol{b}(\boldsymbol{r}) = 0 \tag{2.17}$$

Here the second London equation is retained.

This solution based on minimising the free energy in superconductor is very important as it indicates that **the presence of the Meissner effect is to minimise the internal energy inside the superconductor**. In general, minimising the free energy is a very powerful tool to explain the superconductivity, as will discuss later in the Ginzburg-Landau theory.

2.1.2 Intermediate state

In the discussion of the Meissner effect in Section 2.1.1, the geometry effect was ignored for simplicity. In a practical experiment, different geometries of the sample may result in different demagnetisation factors, which in turn affect the flux distribution inside the superconductor. For instance, when an infinitely long superconducting rod is placed inside a magnetic field (parallel to its axis, weaker than the critical field H_C), the demagnetisation factor is equal to zero (N=0), which means that the surface field is equal to the applied field. However, for other geometries (sphere, short cylinder, film, etc.), the field produced by the screening current will partially increase the field at the surface, exceeding its critical field H_C and normalising the type-I superconductor in these regions. The co-existence of superconducting and non-superconducting regions in a type-I superconductor is known as the intermediate state.

The magnetic field required for an intermediate state is [27]:

$$(1-N)B_C < B_{app} < B_C \tag{2.18}$$

For a disk shaped film of radius a and thickness $t \ll a$, the demagnetisation factor is $N \approx 1-\pi t/2a \approx 1.0$ [27]. Based on Equation (2.18), the intermediate state exists in the superconducting film within any field region in which the magnetic field is weaker than the critical field ($B_{app} < B_C$, normal to the surface). The perpendicular applied magnetic field produces domains of normal state inside the superconducting film, as shown in Fig. 2.4. In the normal state domains, the flux density is equal to $\mu_0 H_C$, but in the superconducting region, the flux density is equal to zero (the Meissner effect). In order to simplify the mathematics, the width of the domain wall (penetration depth λ) was neglected. By defining the width of the normal region to be D_n and the width of the superconducting region to be D_s, it is clear that:

$$\mu_0 H_C D_n = \mu_0 H_{app} D \tag{2.19}$$

$$D = D_n + D_s \tag{2.20}$$

This means that the fraction of normal state is equal to:

$$f_n = \frac{D_n}{D} = \frac{H_{app}}{H_C} \tag{2.21.1}$$

For a film of length L, the number of domains N_d is equal to:

$$N_d = \frac{L}{D} \tag{2.21.2}$$

The intermediate state is a very interesting topic which is further explored in the later discussions of a type-I superconducting flux pump.

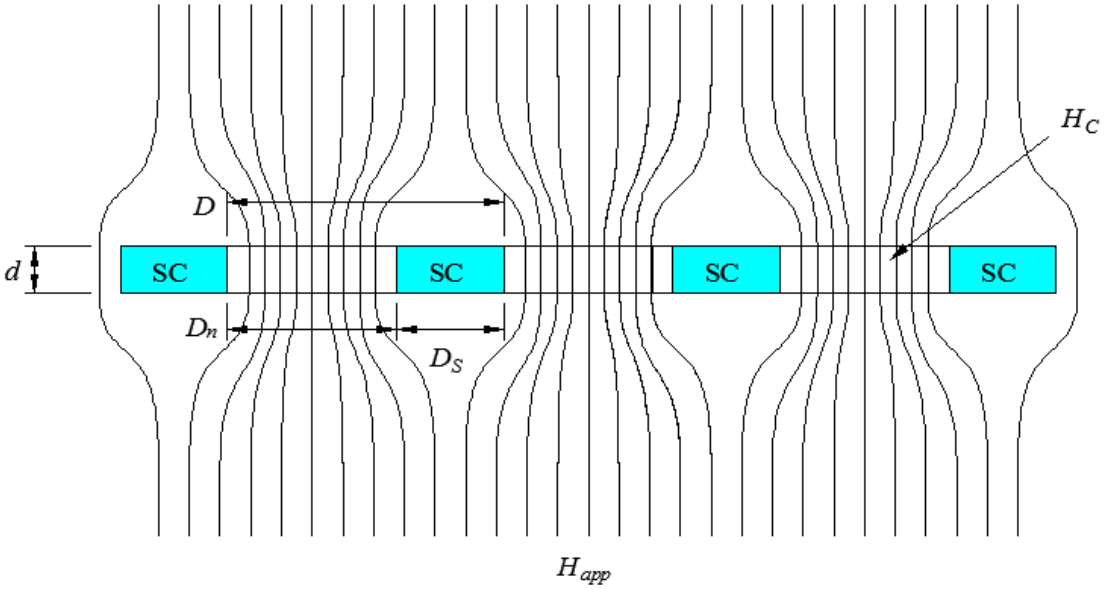

FIG. 2.4. The intermediate state in a type-I superconducting film [27].

This section discusses type-I superconducting materials and their properties, such as perfect conductivity and the Meissner effect. Although type-I superconducting materials have perfect conductivity, their critical field H_C is very low, impossible for use in practical applications. Table 2.1 shows typical type-I superconducting materials and their critical temperatures T_C and critical fields H_C. It is clear that type-I superconducting materials cannot be used for high field applications, and cannot carry large currents (the field produced from the transport current easily exceeds the critical field H_C). Moreover, a transport current can only flow at the surface of type-I superconducting materials within the penetration depth λ, which leaves the central region effectively unused. For these reasons, type-I superconducting materials have no practical value for large scale applications.

TABLE. 2.1

Examples of Type-I superconducting materials

Formula	T_C (K)	$\mu_0 H_C$ (T)	Formula	T_C (K)	$\mu_0 H_C$ (T)
Al	1.20	0.01	α-La	4.9	
Cd	0.52	0.0028	β-Hg	6.3	
Ga	1.083	0.0058	Mo	0.92	0.0096
Hf	0.165		Os	0.65	0.007
α-Hg	4.15	0.04	Pa	1.4	
β-Hg	3.95	0.04	Pb	7.19	0.08
Ga	1.1	0.005	Re	2.4	0.03
In	3.4	0.03	Ru	0.49	0.005
Ir	0.14	0.0016	Sn	3.72	0.03
Ta	4.48	0.09	Zn	0.855	0.005
Zr	0.55	0.014	FeB_4	2.9	
ZrB_{12}	6.0				

*Data are taken from Ref. [28].

2.2 Type-II superconducting materials

Unlike type-I superconducting materials, type-II superconducting materials have two critical fields: the lower critical field H_{C1} and the upper critical field H_{C2}. Between H_{C1} and H_{C2} lies a phase known as the "mixed state". A phase diagram of type-II superconducting materials is shown in Fig. 2.5. The mixed state lies between the phase curves H_{C1}-T and H_{C2}-T, in which the magnetic flux enters the superconductor in the form of quantised magnetic flux or fluxons. The flux quantisation in type-II superconducting materials was theoretically predicted by Abrikosov based on the Ginzburg-Landau (GL) theory. Using the GL theory, type-I and type-II superconducting materials can be clearly defined from the ratio of their coherence length ξ and their penetration depth λ. Almost all superconducting materials used for large scale applications are type-II superconducting materials working in the mixed state. In the mixed state, all electromagnetic behaviours and related thermodynamics are caused by the dynamics of fluxons (vortex dynamics). For this reason, GL theory is vital for an in-depth understanding of the mixed state in type-II superconducting materials.

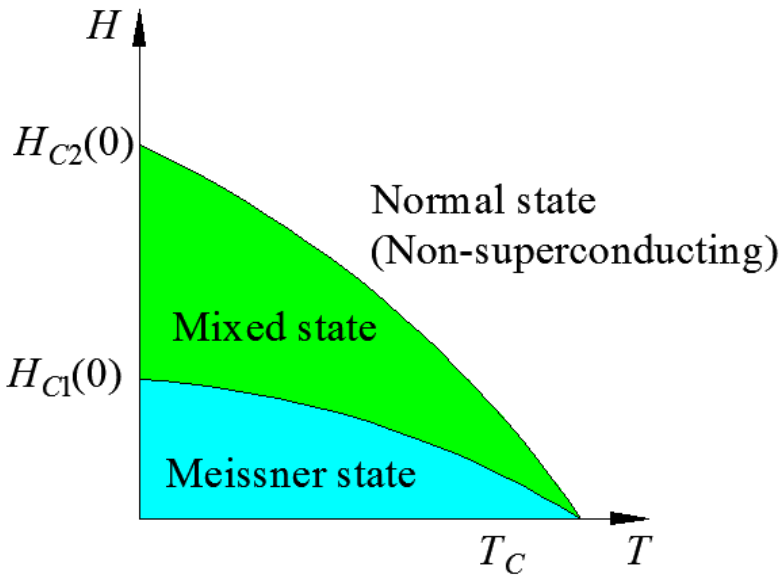

FIG. 2.5. The phase diagram of a type-II superconducting material. There are two critical fields: the upper critical field H_{C1} and the lower critical field H_{C2}. Below the H_{C1}-T curve is the Meissner state (perfect diamagnetism); the phase between the H_{C1}-T and H_{C2}-T curves is the mixed state, where the magnetic flux enters the type-II superconducting materials in the form of fluxons, As will be introduced in later paragraphs; the phase outside the H_{C2}-T curve is the normal state.

In this section, GL theory is introduced, along with its predictions of flux quantisation. The distinction between type-I and type-II superconducting materials is addressed based on GL theory. Additionally, vortex structures and their interactive forces are discussed, along with the pinning force in type-II superconducting materials. This section lays a foundation for an introduction to macroscopic electromagnetic theories for type-II superconducting materials.

2.2.1 Ginzburg-Landau (GL) theory

The Ginzburg-Landau (GL) theory was developed from the Landau theory proposed by L.D.Landau [29] in 1937, for interpretation of all second-order phase transitions. The GL theory was formulated by V.L.Ginzburg and L.D.Landau [30] in 1950 as a phenomenological theory to explain the superconductivity phase transition. The GL theory not only explains long coherence length superconductors, such as low temperature superconductors, but also works well for short coherence length superconductors such as high temperature superconductors.

GL theory minimises the free energy inside the superconducting materials, and the first step is to define the GL free energy inside the superconductor. In GL theory, a superconducting wave function ψ is defined as an order parameter that is equal to zero above the critical temperature T_C, and increases with decreasing temperature below T_C [25]:

$$\psi = \sqrt{n_s} e^{i\varphi} = |\psi| e^{i\varphi} \tag{2.22}$$

where n_s is either the density of Cooper pairs or the density of the superconducting electrons. From quantum mechanics, the momentum operator in a magnetic field is written as:

$$\boldsymbol{G} = \left(-i\hbar\nabla - 2e\boldsymbol{A}\right) \tag{2.23}$$

where -2*e* is the charge of a Cooper pair.

The Ginzburg-Landau free energy density for a superconductor is written as:

$$F_S\left(\boldsymbol{r},T\right) = F_n\left(\boldsymbol{r},T\right) + \alpha|\psi|^2 + \frac{\beta}{2}|\psi|^4 + \frac{1}{2m}\left|\left(-i\hbar\nabla - 2e\boldsymbol{A}\right)\psi\right|^2 + \frac{1}{2\mu_0}B^2 \tag{2.24}$$

where $\alpha = a\left(T - T_C\right)$ and $\beta > 0$, which assumes that the free energy is analytic near the critical temperature T_C.

The total Ginzburg-Landau free energy in the superconductor is the integration of the free energy density inside the superconductor:

$$F_S\left(T\right) = \int_V F_S\left(\boldsymbol{r},T\right) dV \tag{2.25}$$

In order to minimise the free energy, a small variation was made to Equation (2.24). If ψ changes to $\psi + \delta\psi$, and ψ^* changes to $\psi^* + \delta\psi^*$:

$$\begin{aligned}\delta F_S\left(\boldsymbol{r},T\right) = {} & \alpha\left[\left(\psi+\delta\psi\right)\left(\psi^*+\delta\psi^*\right) - \psi\psi^*\right] \\ & + \frac{\beta}{2}\left[\left(\psi+\delta\psi\right)^2\left(\psi^*+\delta\psi^*\right)^2 - \psi^2\psi^{*2}\right] \\ & + \frac{1}{2m}\left[\boldsymbol{G}\left(\psi+\delta\psi\right)\boldsymbol{G}^*\left(\psi^*+\delta\psi^*\right) - \boldsymbol{G}\psi\boldsymbol{G}^*\psi^*\right]\end{aligned} \tag{2.26}$$

After simplification of Equation (2.26) and a partial integration:

$$\delta F_S\left(T\right) = \int_V \left\{\left[\alpha\psi + \beta|\psi|^2\psi + \frac{1}{2m}\left(-i\hbar\nabla - 2e\boldsymbol{A}\right)^2\psi\right]\delta\psi^* + c.c.\right\} dV \tag{2.27}$$

In order Equation (2.27) may be equal to zero, the content in front of $\delta\psi^*$ must equal zero, which gives the **first Ginzburg-Landau equation**:

$$\alpha\psi + \beta|\psi|^2\psi + \frac{1}{2m}\left(-i\hbar\nabla - 2e\boldsymbol{A}\right)^2\psi = 0 \tag{2.28}$$

The second Ginzburg-Landau equation is derived by varying the vector potential $\boldsymbol{A}$ in the free energy $F_S(\boldsymbol{r},T,\boldsymbol{A})$:

$$\begin{aligned}\delta F_S(\boldsymbol{r},T,\boldsymbol{A}) &= F_S(\boldsymbol{r},T,\boldsymbol{A}+\delta\boldsymbol{A}) - F_S(\boldsymbol{r},T,\boldsymbol{A})\,a \\ &= -\frac{e}{m}\left[i\hbar\psi^*\nabla\psi - i\hbar\psi\nabla\psi^* + 4e|\psi|^2\boldsymbol{A}\right]\delta\boldsymbol{A} \\ &\quad + \frac{1}{\mu_0}(\nabla\times\delta\boldsymbol{A})(\nabla\times\boldsymbol{A})\end{aligned} \tag{2.29}$$

By integrating Equation (2.29) in the superconducting region:

$$\delta F_S(T) = \int_V dV\left[\frac{ie\hbar}{m}\left(\psi\nabla\psi^* - \psi^*\nabla\psi\right) - \frac{4e^2}{m}|\psi|^2\boldsymbol{A} + \frac{1}{\mu_0}\nabla^2\boldsymbol{A}\right]\delta\boldsymbol{A} \tag{2.30}$$

In order that Equation (2.30) may be equal to zero, the content in front of $\delta\boldsymbol{A}$ must be equal to zero:

$$\frac{ie\hbar}{m}\left(\psi\nabla\psi^* - \psi^*\nabla\psi\right) - \frac{4e^2}{m}|\psi|^2\boldsymbol{A} + \frac{1}{\mu_0}\nabla^2\boldsymbol{A} = 0 \tag{2.31}$$

From Ampere's Law and vector calculus:

$$\boldsymbol{J} = \nabla\times\boldsymbol{H} = \frac{1}{\mu_0}\nabla\times\nabla\times\boldsymbol{A} = \frac{1}{\mu_0}\left[\nabla(\nabla\cdot\boldsymbol{A}) - \nabla^2\boldsymbol{A}\right] \tag{2.32}$$

In the gauge $\nabla\cdot\boldsymbol{A} = 0$ which leads to:

$$\boldsymbol{J} = -\frac{1}{\mu_0}\nabla^2\boldsymbol{A} \tag{2.33}$$

Substitute Equation (2.33) into Equation (2.31):

$$\boldsymbol{J} = \frac{ie\hbar}{m}\left(\psi\nabla\psi^* - \psi^*\nabla\psi\right) - \frac{4e^2}{m}|\psi|^2\boldsymbol{A} \tag{2.34}$$

which is the **second Ginzburg-Landau equation.**

The Ginzburg-Landau theory gives two differential equations: (2.28) and (2.34). From these two equations, superconductivity properties such as coherence length ξ, penetration depth λ and quantum of magnetic flux can be calculated.

2.2.2 Flux quantisation

One of the most striking phenomena predicted from the Ginzburg-Landau equations is the flux line quantisation. Giving that the gradients of the order parameter and its conjugate are expressed as:

$$\nabla\psi = i\psi\nabla\varphi + e^{i\varphi}\nabla|\psi| \tag{2.35}$$

$$\nabla\psi^* = -i\psi^*\nabla\varphi + e^{-i\varphi}\nabla|\psi| \tag{2.36}$$

By substituting Equations (2.35) and (2.36) into the second Ginzburg-Landau equation (2.34) get:

$$\boldsymbol{J} = \frac{2\hbar e}{m}|\psi|^2\nabla\varphi - \frac{4e^2}{m}|\psi|^2\boldsymbol{A} \tag{2.37}$$

Integrating Equation (2.37) in a closed circle gives:

$$\frac{m}{4e^2}\oint\frac{\boldsymbol{J}}{|\psi|^2}\cdot d\boldsymbol{l} = \frac{\hbar}{2e}\oint\nabla\varphi\cdot d\boldsymbol{l} - \oint\boldsymbol{A}\cdot d\boldsymbol{l} \tag{2.38}$$

The integration over a closed circle of the first term on the right hand side of Equation (2.38) must be equal to $2\pi n$, or:

$$\oint\nabla\varphi\cdot d\boldsymbol{l} = 2\pi n \tag{2.39}$$

The integration of the vector potential in a closed circle is equal to the encircled magnetic flux as derived from the Stokes' theorem:

$$\oint\boldsymbol{A}\cdot d\boldsymbol{l} = \Phi \tag{2.40}$$

Therefore, Equation (2.38) can be re-written as:

$$\frac{m}{4e^2}\oint \frac{\boldsymbol{J}}{|\psi|^2}\cdot d\boldsymbol{l} + \Phi = n\Phi_0 \tag{2.41}$$

while $\Phi_0 = h/2e = 2.0679\times10^{-15}\ T\cdot m^2$ is defined as the quantised magnetic flux or fluxon. Equation (2.41) implies that the sum of the enclosed magnetic flux Φ and the integration involved with the current density is equal to the integer number of a single fluxon. This conclusion applies to both type-I superconductors in the intermediate state, and type-II superconductors in the mixed state. This is discussed further in following paragraphs.

2.2.3 Characteristic lengths

There are two characteristic lengths which can be derived from the GL equations. One is the GL coherence length ξ and the other is the penetration depth λ. From the ratio of these two lengths, the difference between type-I and type-II superconducting materials can be clearly defined using the GL theory.

Coherence length ξ is fundamentally important in superconductivity, because it presents the distance over which the order parameter ψ resumes its full value in case the wave function is perturbed by a magnetic field, or by normal regions inside the superconductor. ξ is the wall thickness within which the density of the Cooper pairs is too low to be considered in the normal state. The coherence length ξ is derived from the first GL equation. In the case of a zero magnetic field, from Equation (2.28):

$$\alpha(T)\psi + \beta|\psi|^2\psi + \frac{1}{2m}\left(-i\hbar\nabla\right)^2\psi = 0 \tag{2.42}$$

In 1D condition, Equation (2.42) can be written as:

$$-\frac{\hbar^2}{2m\alpha(T)}\frac{d^2\psi}{dx^2} + \psi + \frac{\beta}{\alpha(T)}|\psi|^2\psi = 0 \tag{2.43}$$

The coherence length is defined by:

$$\xi = \left(\frac{\hbar^2}{2m\alpha(T)} \right)^{\frac{1}{2}} \tag{2.44}$$

The penetration depth λ is derived from the second GL equation. In this case, the density of the Cooper pairs is not perturbed and the gradient of order parameter ψ is neglected. From Equation (2.34):

$$\boldsymbol{J} = -\frac{4e^2 |\psi|^2}{m} \boldsymbol{A} \tag{2.45}$$

Comparing with the London Equation $\boldsymbol{J} = -\left(1/\mu_0 \lambda^2\right) \boldsymbol{A}$, can get that:

$$\lambda^2 = \frac{m}{(2e)^2 \mu_0 |\psi|^2} \tag{2.46}$$

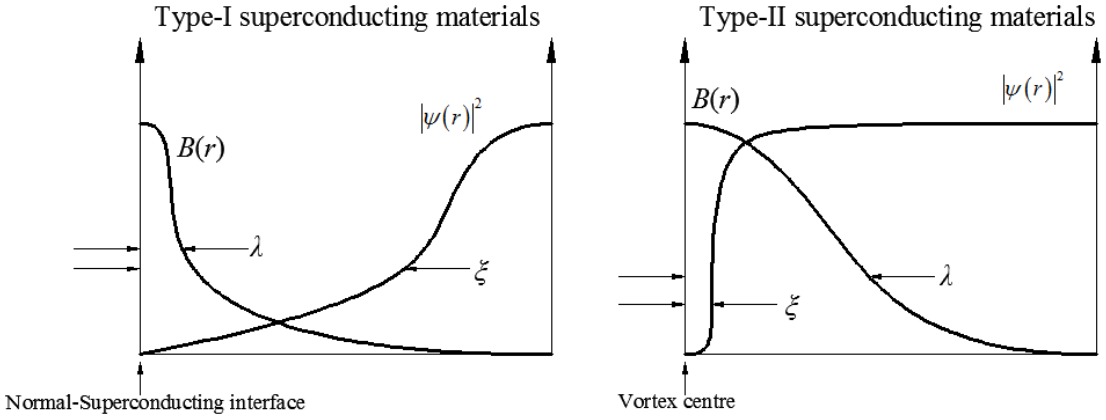

FIG.2.6. The coherence length and penetration depth in two types of superconducting materials.

A clear definition of type-I and type-II superconducting materials is derived from the prospect of the surface energy on the normal-superconducting interface. As shown in Fig. 2.6, the ratio of the penetration depth and the coherence length is the key to distinguish the two types of superconductor. This ratio is called the Ginzburg-Landau parameter, κ:

$$\kappa = \frac{\lambda}{\xi} \tag{2.47}$$

Change to the GL parameter κ changes the surface energy on the normal-superconducting interface. The interface area is created by the magnetic energy that penetrates within the penetration depth. The energy provided by the magnetic field breaks off the Cooper pairs within the coherence length ξ. As a rough estimate, supposing that A is the area of the interface, the magnetic energy which penetrates the superconductor is:

$$E_1 = \lambda A \frac{1}{2\mu_0} B_C^2 \tag{2.48}$$

while the energy requires to break down the Cooper-pairs within the coherence length is:

$$E_2 = \xi A \frac{1}{2\mu_0} B_C^2 \tag{2.49}$$

The abstraction of the two items gives the energy that is absorbed by the interface:

$$\Delta E = E_2 - E_1 = A \frac{1}{2\mu_0} B_C^2 \left(\xi - \lambda\right) \tag{2.50}$$

If $\Delta E < 0$, the interface transfers energy to the superconductor. Therefore, the more interfaces which are created, the greater the energy gained by the superconductor. This phenomenon maximises the interface area A which ends up with the nucleation of the vortices inside the superconductor. Each vortex contains a single magnetic fluxon Φ_0. This is the type-II superconductor.

As demonstrated in Fig.2.5, type-II superconductors have two critical fields: the upper critical field B_{C2} and the lower critical field B_{C1}. B_{C2} stands for the magnetic field high enough to overlap the normal regions of neighbouring vortices. A clear definition of type-I and type-II superconducting materials can be derived from the relationship between B_{C2} and B_{C1}, which is obtained using the GL theory:

$$B_{C2} = \kappa\sqrt{2} B_{C1} \tag{2.51}$$

Superconducting materials are defined according to whether B_{C2} is larger than B_{C1}:

$\kappa < 1/\sqrt{2}$: type-I superconducting materials since $B_{C2} < B_{C1}$, therefore B_{C2} doesn't exist;

$\kappa > 1/\sqrt{2}$: type-II superconducting materials since $B_{C2} > B_{C1}$ and B_{C2} does exist.

Table 2.2 shows some examples of type-II superconducting materials.

TABLE 2.2
Examples of type-II superconducting materials

Formula	T_C (K)	$\mu_0 H_{C1}$ (mT)	$\mu_0 H_{C2}$ (T)	λ (nm)	ξ (nm)	κ
NbTi	9.6		14	130	3.8	27
Nb_3Sn	18	45.6	33	65	3	22
$Bi_2Sr_2CaCu_2O_{8+x}$ (Bi2212)	89		36 (at 65 K)	250	1.8	139
YBCO	91		180 (0 K) 35 (77.3 K)	156(ab)	1.65(ab)	95

*Data are taken from Ref. [31]; "ab" refers to the ab-plane.

2.2.4 Basic vortex dynamics

As mentioned in the previous section, type-II superconducting materials have a negative surface energy, which triggers the formation of quantised vortices within the materials. Each vortex contains a single magnetic fluxon $\Phi_0 = h/2e = 2.0679\times10^{-15}\ T\cdot m^2$ as introduced in Section 2.2.2. Fig. 2.7 shows the structure of a single vortex, which contains a core region within the coherence length ξ. The core region can be considered to be a normal region, since the density of the Cooper pairs is very low as shown to the left in Fig. 2.6. Surrounding the core region is the circulating current (superconducting current) which shields the magnetic field. The peak value of the magnetic field lies at the centre of the vortex.

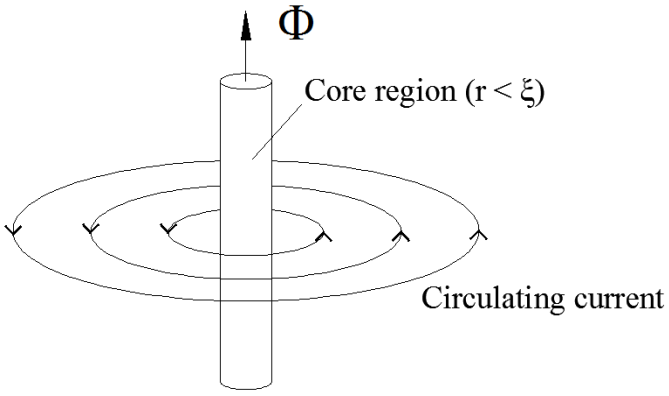

FIG.2.7. The structure of a single vortex [32].

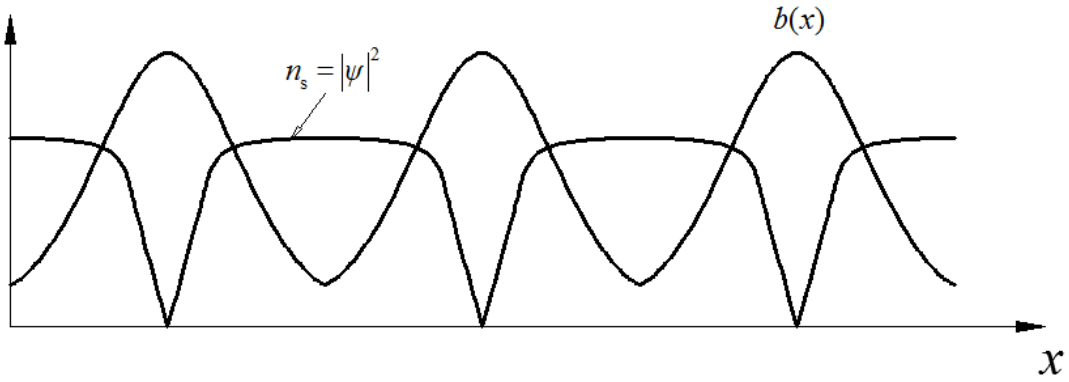

FIG. 2.8. Cut through the centres of neighbouring vortices, showing the distribution of magnetic flux density $b(x)$ and the density of Cooper pairs n_s [25].

Fig. 2.8 shows the distribution of magnetic flux density and the density of the Cooper pairs across the centres of neighbouring vortices. This assumes that the applied field is far smaller than the upper critical field $B_{C1} < B \ll B_{C2}$.

A vortex in the mixed state is a quasi-particle, and the core region together with the circulation current shown in Fig. 2.7 are considered to be a whole body. When the circulating current in Fig.2.7 experiences a Lorentz force, the force is transmitted to the whole vortex [33].

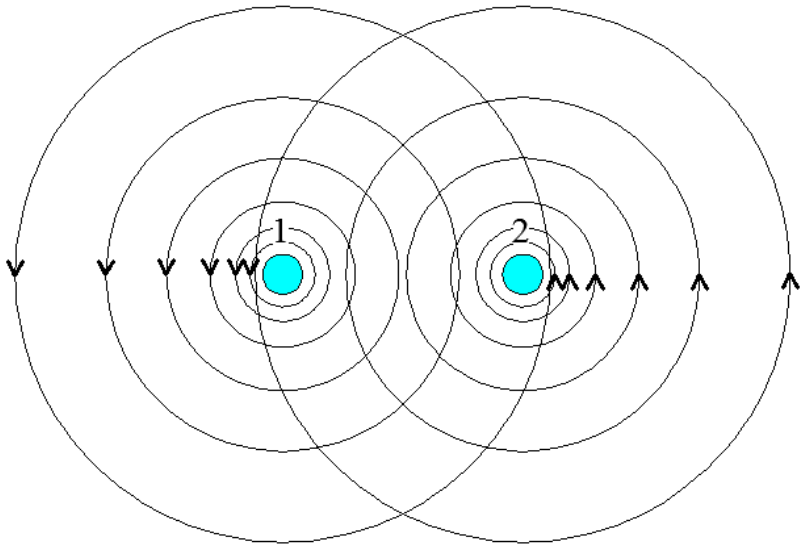

FIG.2.9. The current distribution of two neighbouring vortices [25].

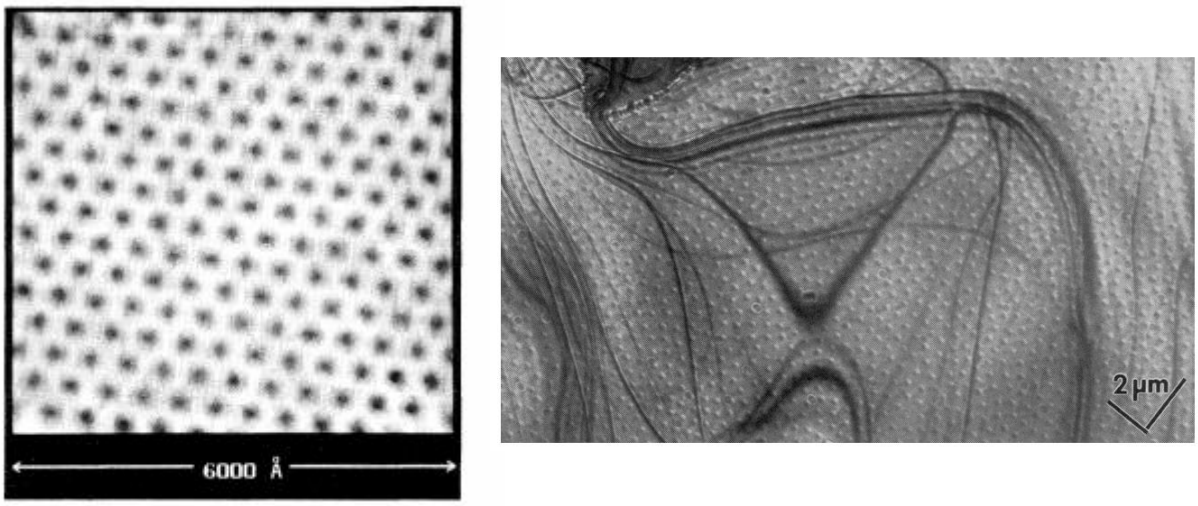

FIG. 2.10. The figure on the left shows Abrikosov FLL experimentally observed using a 1 T magnetic field in $NbSe_2$ at 1.8 K using a scanning tunnelling microscope [34]. The figure on the right shows the Abrikosov FLL of a Nb thin film in a magnetic field of 10 mT at 4.5 K observed using Lorentz microscropy [35].

Fig. 2.9 shows two neighbouring vortices with the same polarisation (a parallel magnetic field). The problem can be simplified by assuming the circulating current J_2 from vortex 2 to be uniform in the area of vortex 1, in which case vortex 2 experiences a repulsive force from vortex 1 which is equal to:

$$\boldsymbol{f}_2 = \boldsymbol{J}_2 \times \vec{\phi}_0 \tag{2.52}$$

Accordingly, vortex 1 experiences a repulsive force from vortex 2.

In the mixed state, the nature of the repulsive forces between neighbouring vortices is equal to the magnetic stress. The repulsive forces between neighbouring vortices produce a stable vortex pattern which is known as the Abrikosov flux line lattice (FLL) [36]. The vortices are arranged into a hexagon pattern which minimises the potential energies between vortices. There are many methods for experimentally observing the FLL, such as small-angle neutron-scattering experiments [37, 38], Bitter decoration [39-41], a scanning tunnelling microscope [42-44], Lorentz microscopy [35, 45], etc.

The FLL shown to the left of Fig. 2.10 shows a perfect hexagonal pattern, which only appears in pure superconducting materials. In a pure superconductor, the vortices are uniformly distributed and a magnetic gradient cannot form. The magnetic gradient inside type-II superconducting materials is equal to a macroscopic current, according to Ampere's law. Therefore, pure type-II superconducting materials cannot sustain either magnetisation current or transportation current. In general, pure type-II superconducting materials have little use in practical engineering.

However, if type-II superconducting materials contain impurities, crystalline defects, etc., the vortices can be "trapped" to form a magnetic gradient. This phenomenon is known as "flux pinning" and the impurities or crystalline defects are known as the "pinning centres". Fig. 2.11 shows the Lorentz force $\boldsymbol{f}_l$ and pinning force $\boldsymbol{f}_p$ on a vortex system. The magnetic flux density $\boldsymbol{B}$ can be either applied field or self-field, and the current density $\boldsymbol{J}$ can be either a transport current or a magnetisation current. The Lorentz force for a single vortex is $\boldsymbol{f}_l = \boldsymbol{J} \times \vec{\phi}_0$. Therefore, if the pinning force is larger than the Lorentz force $f_p \geq f_l$, the vortex is pinned by the pinning force. If the pinning force is smaller than the Lorentz force $f_p < f_l$, the vortex is unpinned from the pinning centre and starts to move in the direction of the Lorentz force. Therefore, without flux pinning, type-II superconducting materials cannot support a macroscopic current density. "Flux pinning" is therefore crucial in the practical applications.

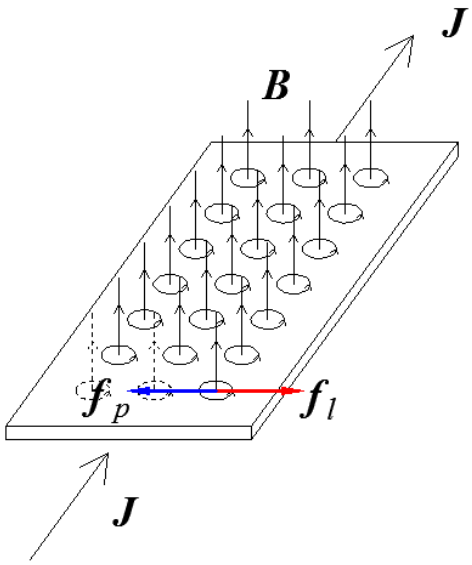

FIG.2.11. The Lorentz force and pinning force on the vortex system in a type-II superconductor.

Since the vortex system is self-organising with the help of mutual repulsive forces, the whole vortex system can be "pinned" by a few pinning centres. If the magnetic field is averaged throughout space, the macroscopic magnetic flux density $\boldsymbol{B}$ is considered, the average Lorentz force $\boldsymbol{F}_l$ on the FLL can be expressed as:

$$\boldsymbol{F}_l = \boldsymbol{J} \times \boldsymbol{B} \tag{2.53}$$

Since the pinning force on the FLL is $\boldsymbol{F}_p$, then the maximum current density (critical current density J_C) for the materials equals to:

$$J_C = \frac{F_P}{B} \tag{2.54}$$

Therefore, for a type-II superconducting material in a fixed temperature and magnetic field, the stronger the pinning force, the larger the critical current density J_C.

A vortex interacts with forces between the lattices of the material. The movement of the vortices causes vibration of the lattice, which leads to thermal dissipation in type–II superconducting materials. This is quite different from the common metals, in which the scattering of free electrons is the major cause of thermal dissipation. In the mixed state, if $f_l > f_p$, the FLL is driven by the Lorentz force. This kind of movement is known as "flux flow". The motion of the vortices interacts with the lattice to give rise to thermal dissipation. However, if $f_p \geq f_l$ while $T > 0$ K, there is still the possibility for single vortices to "jump out" of the pinning potential due to thermal activation. This

phenomenon is called “flux creep”. Flux creep and flux flow are the two basic magnetic behaviours of type-II superconducting materials, and will be discussed in detail in the next section. The macroscopic electromagnetic theories for type-II superconducting materials are built on an understanding of these two phenomena. In the next section, macroscopic electromagnetic theories are introduced for type-II superconducting materials.

2.3 Macroscopic electromagnetic theories for type-II superconducting materials

As discussed in the previous section, a magnetic field enters a type-II superconductor in the form of quantised vortices, each containing a magnetic fluxon. All macroscopic electromagnetic behaviour in the mixed state are caused by the dynamics of these vortices. The superconducting state is a macroscopic quantum state fundamentally different from normal metals such as copper. Therefore, in order to understand the macroscopic electromagnetic behaviour of the mixed state, some basic vortex dynamics are necessary.

As mentioned in the previous section, vortices enter the superconductor in the form of the Abrikosov flux line lattice (FFL). This is the case in an ideal type-II superconducting materials, in which there is no perturbance (pinning centres) in the background energy. However, if the material contains crystalline defects, impurities, etc., the background energy is perturbed and these defects and impurities act like potential traps which “pin” the vortices into position. The “pinning force” is transmitted through vortex-vortex interactive forces, and results in the collective pinning of the whole FFL. Flux pinning is fundamentally important to practical applications of type-II superconducting materials. Without flux pinning, the FFL cannot form a magnetic gradient and the macroscopic superconducting current could not exist.

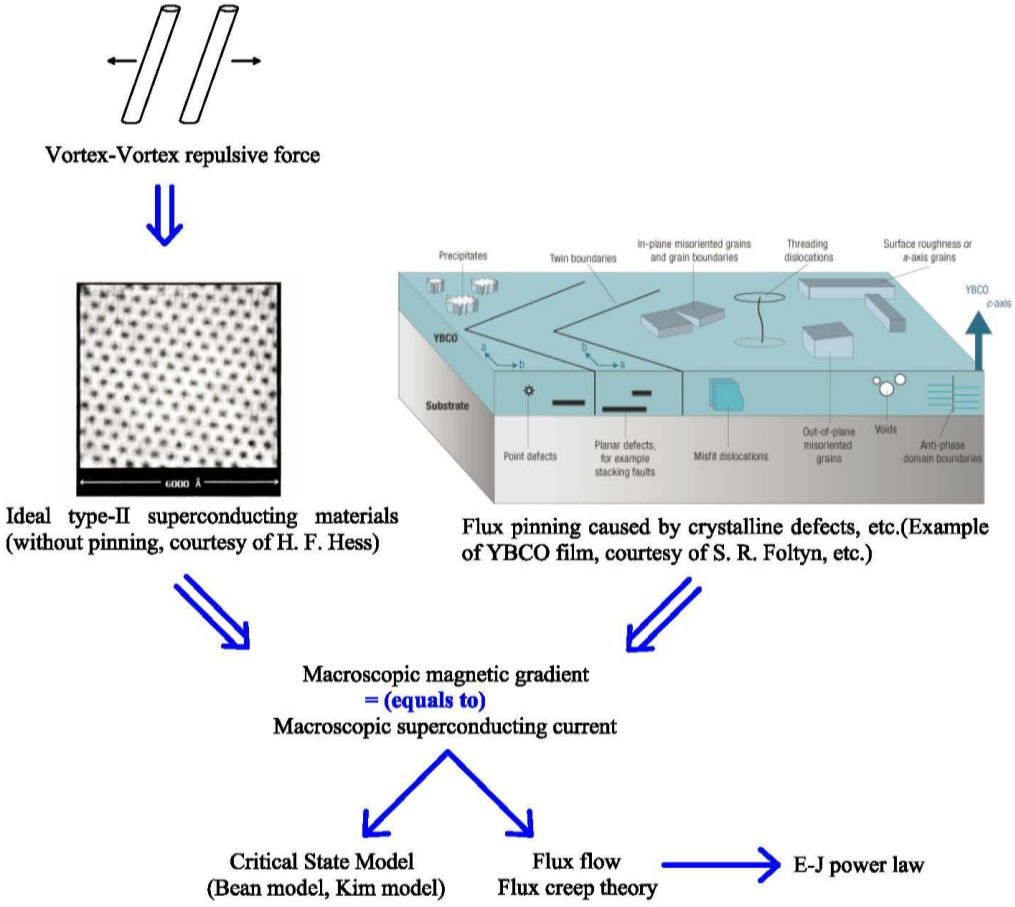

FIG.2.12. The relationship between microscopic vortex dynamics and macroscopic electromagnetic theories for type-II superconducting materials in the mixed state. Courtesy of H.F.Hess [34] and S.R.Foltyn [46].

Fig. 2.12 shows the relationship between microscopic vortex dynamics and the macroscopic electromagnetic theories for type-II superconducting materials in the mixed state. The FLL and the pinning force give rise to macroscopic electromagnetic phenomena in type-II superconducting materials. The electromagnetic phenomenon is most commonly explained using two models: the critical state model and the flux flow and creep model. The flux flow and creep model is more easily described using the E-J power law. This section contains a brief discussion regarding basic vortex dynamics in type-II superconducting materials, followed by consideration of macroscopic electromagnetic models such as the critical state model and the E-J power law. These are widely used in numerical modelling of type-II superconducting materials.

2.3.1 Critical state model

The critical state model assumes that the magnetic gradient inside a type-II superconductor is always in the critical state, i.e. the value of the magnetic gradient is equal to the critical current density J_C. The critical state model does not consider the flux creep. The critical state model is the most useful tool for explaining the magnetisations of hard superconductors.

There are two types of critical state model. One is the Bean model, which assumes a constant critical current density J_C in the materials. The other is the Kim model, which considers the field-dependence of the critical current density $J_C(B)$. The Bean model can be used to intuitively estimate the magnetisation of a regular shape (long slab or long rod) hard superconductor. The Kim model produces a more precise prediction of the magnetisation.

(1) Bean model

The Bean model [47] assumes that the current density inside a hard superconductor has only three possible values: 0, $\pm J_C$, while $J = 0$ is the area which experiences no flux flow, and $J = \pm J_C$ is the area which experiences the flux flow. The Bean model is widely used to estimate magnetisation based on zero-field cooling and field cooling. These two methods are the most widely used to magnetise a hard superconductor. Fig. 2.13 shows the process of the two methods, based on the Bean model. Ideal geometries are the infinitely long rod and the infinitely wide slab, which have no demagnetisation effect. Fig. 2.13(a) shows the ZFC condition in which the hard superconductor is cooled before applying the field. As shown in Fig. 2.13(a), as the magnetic field is applied to the hard superconductor, the flux starts to penetrate the surface. The macroscopic current density is induced in the area in which the flux penetrates. The value of the critical current density is equal to $\pm J_C$. If the maximum trapping field of the hard superconductor is H_p at the centre, then the applied field must be greater than $2H_p$ in order to fully magnetise the sample. However, under FC conditions, the applied field only needs to be equal to H_p in order to fully magnetise a hard superconductor, as shown in Fig. 2.13(b). To date, the maximum field a bulk superconductor can trap is 17 T, as reported by Murakami et al [48]. Fig. 2.14 shows the YBCO bulk and trapped field profile for a 17 T trapped field, which demonstrates that the magnetisation profile follows the Bean model. Fig.2.14 also shows that when the temperature drops, the pinning force increases, resulting in a steeper magnetic gradient. Therefore, for real applications, in order to obtain a higher critical current and stable trapping field, the superconductor must normally be kept at a low temperature.

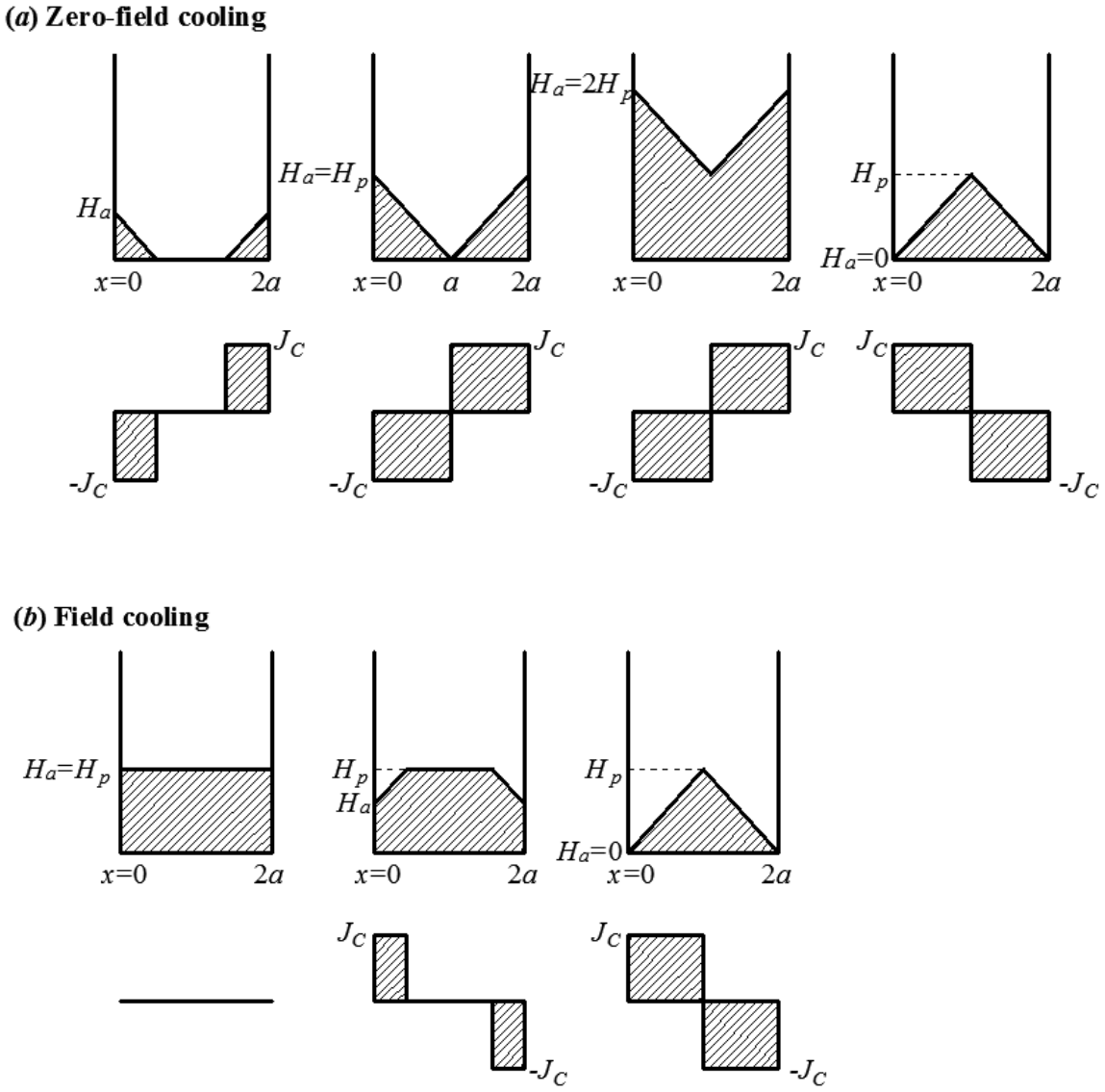

FIG. 2.13. Demonstration of zero-field cooling and field cooling methods to fully magnetise a hard superconductor.

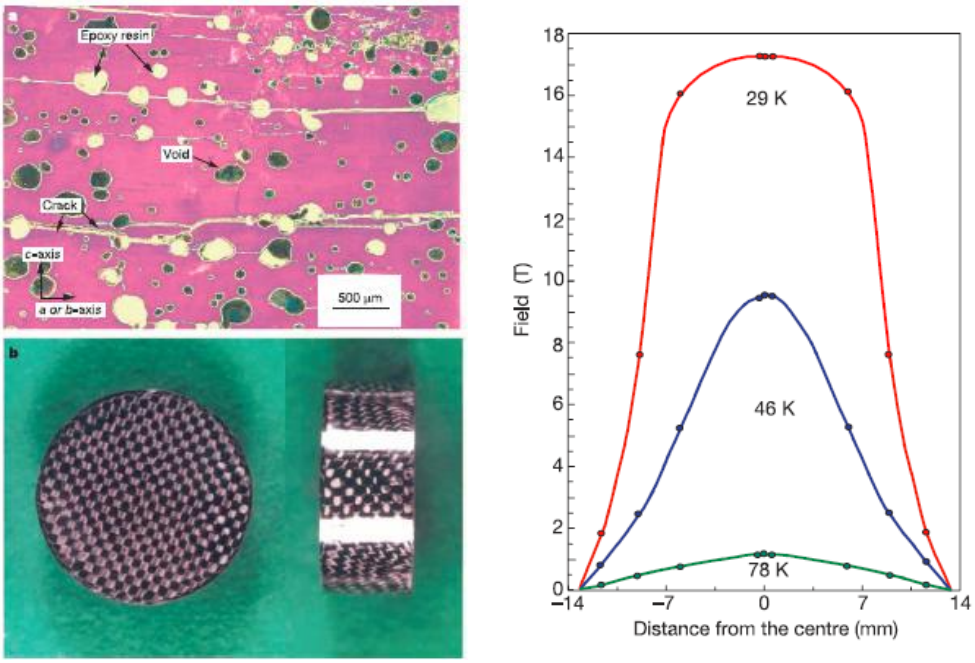

FIG. 2.14. YBCO bulk that can trap 17 K at 29 K. Courtesy of Murakami, et al [48].

In practical experiments, the flux flow normally produces a great deal of heat in the superconductor which locally increases the internal temperature and decreases the critical current density. In order to avoid this problem, the variation of the applied field should take place at a reasonably slow rate. This is especially important in pulse magnetisation [49] which is not addressed in this thesis.

As well as estimating the manetisation of an infinitely long rod or infinitely wide slab, the Bean model can also be used to estimate the magnetisation and ac losses inside type-II superconducting wires [50]. The Bean model is a powerful tool which can be used to explain general magnetisation behaviours inside type-II hard superconductors.

.

(b) Kim model

The Kim model [51] is an improved critical state model which considers the field-dependence of the critical current density. The field-dependence of the critical current density can be clearly seen in their vortex dynamics Equation (2.53). Since the pinning force at a specific temperature is fixed within a particular hard superconductor, as the magnetic field increases, the Lorentz force also increases, which leads to a smaller critical current density. There are many forms of the $J_C(B)$ relationship [52], and the most commonly used equation is [51, 53, 54]:

$$J_C\left(B_i\right) = \frac{J_{C0}(T)}{1 + B/B_0} \tag{2.55}$$

where $J_{C0}(T)$ and B_0 are positive constants. This specific relationship between J_C and B is the "Kim model".

2.3.2 Flux creep, flux flow and the *E*-*J* power law

The effect of flux creep is ignored in the critical state model. In the critical state model, the FLL is considered to be very stable, and not disturbed by thermal activation. However, this is not true when T >0 K, especially for HTS materials which operate at 77 K, where relaxation of the magnetisation due to flux creep is pronounced [55].

As previously mentioned in Section 2.2.4, when $J \leq J_C$, the FLL is pinned by the pinning force, however, thermal activation helps the vortices to "hop" out of the pinning potentials, a process known as the "flux creep". For $J > J_C$, the Lorentz force is greater than the pinning force, which forces the FLL to move, called "flux flow". In both cases, movement of the vortices gives rise to an electric field according to the Lorentz transformation [56]:

$$\boldsymbol{E} = \boldsymbol{v} \times \boldsymbol{B} \tag{2.56}$$

where $\boldsymbol{v}$ is the speed of the FLL.

The electric fields measured in both type-I and type-II superconducting materials are all generated by flux motions as described in Equation (2.56). The parallel component of the electric field compared to the transport current gives rise to heat loss, and the perpendicular component gives rise to the Hall effect [57-60]. This is fundamentally different from normal conductors, from which heat losses are caused by the scattering of free electrons, and the Hall effect is caused by accumulation of charges at the edge of the conductor.

According to Anderson's flux creep model [61], when $J \leq J_C$, flux lines jump out of the pinning centre at a certain rate, described using the Arrhenius equation [62]:

$$R = \nu_0 e^{-U/kT} \tag{2.57}$$

where R is the attempt rate, v_0 is the microscopic attempt frequency of order 10^{-8} - 10^{-10} s^{-1}, U is the effective pinning potential, k is the Boltzmann constant, ad T is the absolute temperature.

A theoretical explanation for this is shown in Fig. 2.15. When a uniform transport current (or magnetisation current, $J \le J_C$) flows across the vortex, the pinning barrier becomes tilted as shown in Fig. 2.15. The probability for the vortex to hop to one side is greater than the probability to hop to the other.

The effective potential on both sides could be expressed as [63]:

$$U_+ = U_0\left(1 - J/J_C\right) \tag{2.58}$$

$$U_- = U_0\left(1 + J/J_C\right) \tag{2.59}$$

After substituting Equation (2.58) and (2.59) into Equation (2.57), the attempt velocity becomes:

$$\begin{aligned} v &= v_0 l\left\{\exp\left(-\frac{U_+}{kT}\right) - \exp\left(-\frac{U_-}{kT}\right)\right\} \\ &= v_0 l \sinh\left(\frac{U_0}{kT}\frac{J}{J_C}\right)\exp\left(-\frac{U_0}{kT}\right) \end{aligned} \tag{2.60}$$

where l is the effective jump distance. Thereby, the E-J relationship during the flux-creep is:

$$E = Bv = \rho_C J_C \sinh\left(\frac{U_0}{kT}\frac{J}{J_C}\right)\exp\left(-\frac{U_0}{kT}\right), \qquad J \le J_C \tag{2.61}$$

where $\rho_C = Bv_0 l/J_C$, which is the flux creep resistance.

For $J > J_C$, the potential barrier is lower than the pinning position, and the vortices flow to one side as shown in Fig. 2.15. The electric field induced by the flux flow can be expressed as [64]:

$$E = E_C + \rho_f J_C\left(\frac{J}{J_C} - 1\right), \qquad J > J_C \tag{2.62}$$

where E_C is the electric field due to flux creep at $J=J_C$, and ρ_f is the flux flow resistance.

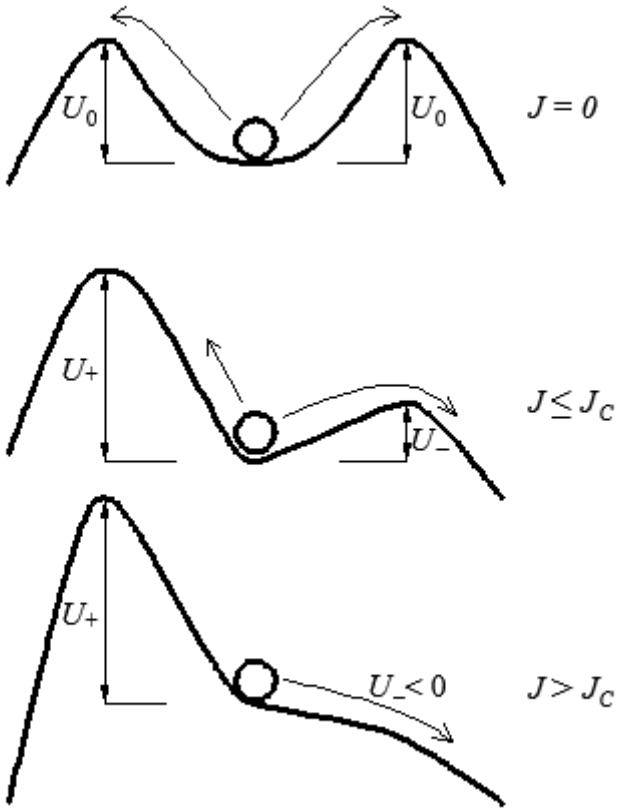

FIG. 2.15. The energy landscape of a pinned vortex in a uniform external current [25].

The combination of Equation (2.61) and (2.62) provides an *E-J* relationship for type-II superconducting materials. However, this relationship is not commonly used in for practical simulations. A more practical *E-J* relationship for HTS materials is the *E-J* power law. The *E-J* power law is derived from the direct four-point probe method [65] of the voltage-current relationship in the transport measurement. The *E-J* power law is expressed as[66]:

$$E = E_C \left(\frac{J}{J_C} \right)^n \tag{2.63}$$

$n = U/kT$ shows the stiffness of the *E-J* relationship, when E_C=10^{-4} V/m is the criteria used to determine the critical current density J_C in the four-point measurement. The application of Equation (2.63) in modeling HTS materials is discussed in Chapter 4. By varying the *n*-value in the *E-J* power law, the properties of a material can be altered from common metal (*n*=1) to the critical state model (*n*= ∞).

2.3.3 Intrinsic pinning and anisotropy

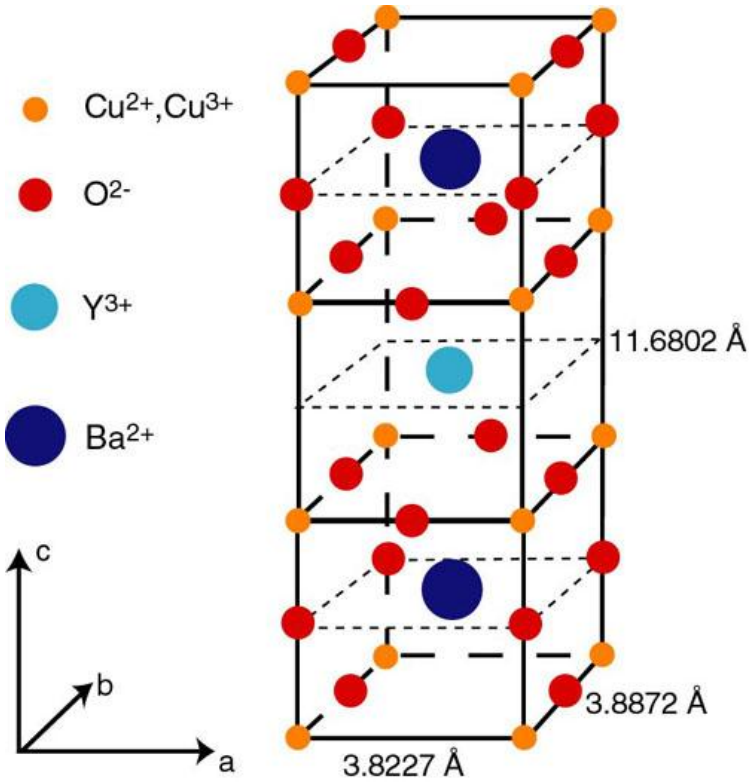

FIG.2.16. Structure of a single unit cell of YBCO.

For some materials, such as $YBa_2Cu_3O_{7-\delta}$, the supercurrent flows more easily within the CuO_2 plane (*ab* plane) than between the layers (*c* direction). The typical unit cell structure of YBCO is shown in Fig. 2.16. In an absence of pinning centres, the motion of vortices in the *ab* plane is not prohibited. However, motion of vortices between the CuO_2 layers is hindered due to the *intrinsic pinning* [27]. Intrinsic pinning produces anisotropy in superconducting materials. The direct effect of the anisotropy is that the critical current J_C develops an angular-dependent relation with the applied magnetic field [67]. For instance, the peak value of J_C normally applies when $H \parallel ab$.

2.3.4 Cross field effect and flux shaking

The cross field effect and flux shaking effects show that a transverse magnetic field may decrease the existing magnetisation of a bulk superconductor or a superconducting film. The cross field effect often refers to bulk superconducting materials, while flux shaking refers to a superconducting film.

Fig. 2.17 shows the modeled cross field effect using a YBCO single domain bulk [68]. The figure shows that the reason for the cross field effect is that, by applying a transverse magnetic field, a magnetisation current has been induced in the top and bottom areas of the bulk superconductor, acting to cancel the transverse field. This decreases the effective area for the magnetisation in the vertical direction.

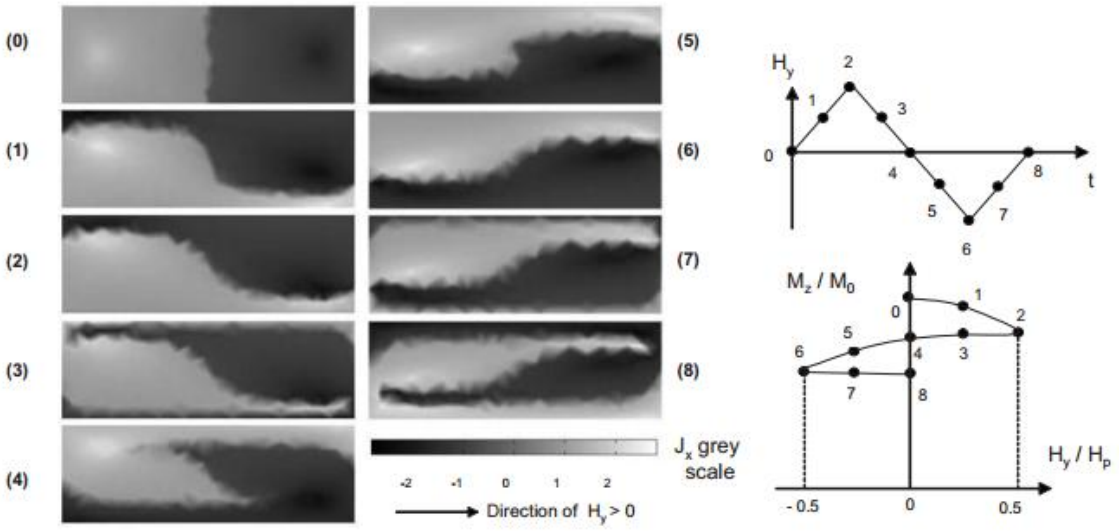

FIG. 2.17. Left: modelled data of the current density distribution $J_x(y,z)$ within the cross section of a YBCO sample during one cycle of the transverse magnetic field of amplitude $0.5H_p$. A field-dependent $J_C(B)$ is assumed. The scale of current density J_x is expressed in 103 A/cm2. The arrow indicates the direction of the positive transverse field. Right: schematic diagram showing the times at which the current density distributions were determined. Courtesy of Vanderbemden, et al [68].

Flux shaking refers to the superconducting films. By applying a small transverse ac field to a magnetised superconducting film, the circulating critical current in the strip will become decayed. This is due to the "walking" motion of vortices in the two-dimensional critical state of the strip in-plane with the ac field [69]. Applying the ac field in the vertical direction may also cause the "cross field effect" or "flux shaking" effect, which is due to the bending of flux lines in the presence of the

superconducting material (bulk or film). However, these effects are very small compared to the direct application of an ac transverse field.

2.4 Conclusion

This chapter introduced basic superconductivity theories and macroscopic electromagnetic theories for type-I and type-II superconducting materials. The Meissner effect was introduced for type-I superconducting materials and the London equations were presented in explanation. In order to understand the mixed state in type-II superconducting materials, the Ginzburg-Landau equations were introduced, from which flux quantisation, characteristic lengths, basic vortex dynamics and pinning forces were derived. Type-I and type-II superconducting materials were clearly defined using the GL parameter.

Macroscopic electromagnetic theories for type-II superconducting materials were derived in the chapter. Critical state models such as Bean model and Kim model were introduced, along with the concepts of flux creep, flux flow and the *E-J* power relation. Intrinsic pinning and cross field effect were introduced.

This chapter provides basic knowledge about superconductivity. The next chapter introduces flux pump technologies for superconducting magnets.

CHAPTER 3

INTRODUCTION TO FLUX PUMP TECHNOLOGIES

This chapter introduces flux pump technologies for superconducting magnets. The introduction focuses on technologies which use a travelling magnetic wave to gradually magnetise a superconducting coil. Section 3.1 contains a discussion on why flux pump technologies are indispensable for HTS magnets. Section 3.2 introduces the mature flux pump technology with a type-I superconducting film, and discusses the underlying physics and three different methods. Section 3.3 provides a discussion on the "dc transformer". This introduction shows that magnetic field inhomogeneity causes vortex motion in type-II superconducting films. Section 3.4 introduces a possible flux pump technology for an HTS coil. Although flux pump technology appears to successfully magnetise an HTS magnet, the underlying physics is not yet fully understood. Section 3.5 outlines a research proposal to study flux pump technology and the electromagnetic behaviour of HTS film in a travelling wave.

3.1 Why a flux pump for superconducting coils?

Superconducting magnet technology is widely used for various applications such as magnetic resonance imaging (MRI), nuclear resonance imaging (NMR), accelerator technologies such as the large hadron collider (LHC), fusion technologies such as TOKAMAK, superconducting windings inside superconducting electric machines, magnetic levitation trains, superconducting magnetic energy storage system, etc. The transport current inside a superconducting coil can be either dc or transient. Superconductors can carry a very large persistent current without decay, which is ideal for use in dc magnets such as MRI and NMR magnets. The MRI machine is the only superconductivity product that has been widely commercialised. The global MRI market is currently valued in the

region of US$5.5 billion (2010) and is estimated to rise to US$7.5 billion (2015). Leading MRI producers include GE (Signa brand), Siemens (Magnetom), Philips (Achieva, Intera, Panorama), Hitachi (Aaltaire, Airis) and Toshiba (Vantage, Opart, Ultra). Products range from low field systems (<0.5T) through middle field (0.5-1T) high field (usually 1.5T) to very high field (usually 3T) [16].

Commercial MRI machines use low temperature superconducting (LTS) materials such as NbTi and Nb_3Sn for the magnet windings. NbTi is cheaper than Nb_3Sn, however, in high field application, Nb_3Sn is better than NbTi. Even so, the properties of NbTi are sufficient for most common applications [18]. A NbTi magnet operates at 4.2 K with current densities up to 3000 A/mm^2. In the present market, 1.5 T MRI machines are very common, whereas 3.0 T MRI machines have only been recently released to the market in the USA, Japan and EU. 7.0 T MRI machines are only available for research purposes. All these MRI machines mentioned use NbTi wire for the magnet windings [70]. However, for high field applications such as NMR (>20 T), or fusion projects (>13 T), Nb_3Sn wire is essential [20].

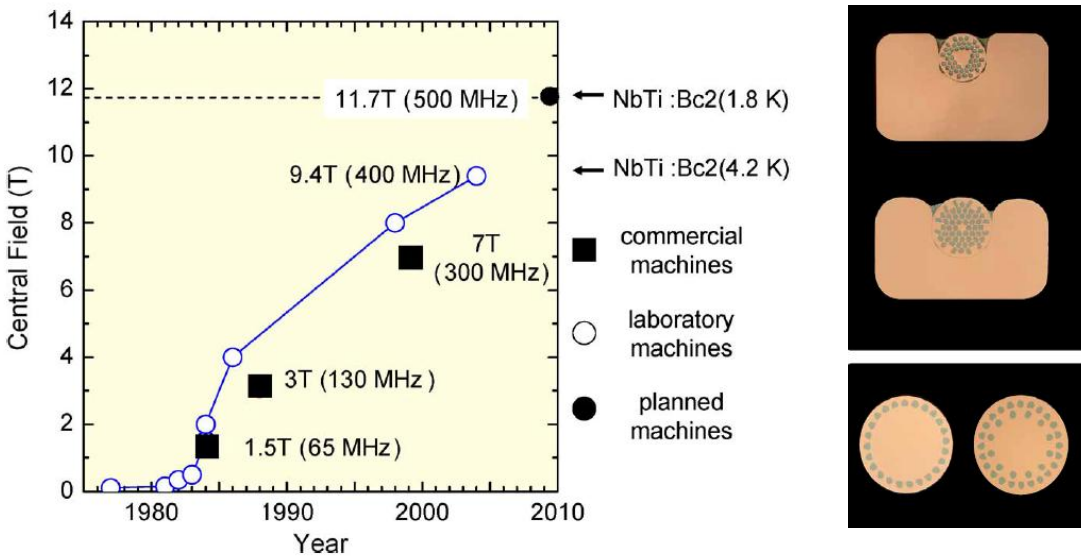

FIG.3.1. The diagram on the left shows the development of field strength of whole body MRI scanners [70]. The figure on the right shows the NbTi wire used for MRI applications [20].

Superconducting magnets operating in dc current conditions such as MRI or NMR machines require a persistent current switch (PCS) which short-circuits the magnet after it has been fully energised. A well-made PCS has very low resistivity (in the range of 10^{-15} Ω) and large current

capacity, which provides stability for the magnetic field. The PCS is connected in parallel with the power source. After the PCS is switched on, the current flows through the PCS instead of through the power source, which maintains a persistent current inside the superconducting magnet [71]. Nowadays, there are many methods for fabricating the LTS joints for either NbTi wire or Nb_3Sn wire [72-75]. A PCS can be switched on and off by thermally cooling and heating the LTS joints [76-78].

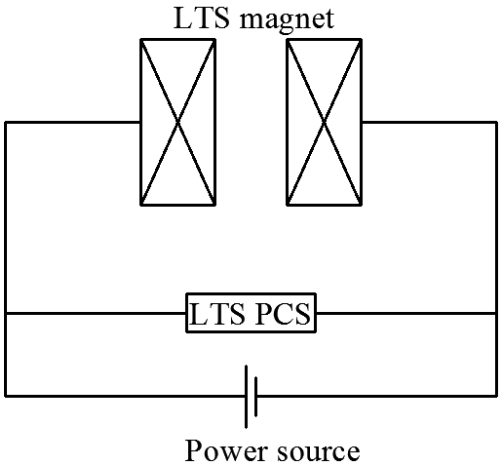

FIG. 3.2. The circuit of the LTS magnet connected to a power source and a LTS PCS. The LTS magnet is charged by the power source at the first step, then the LTS PCS is cooled down to a superconducting state in order to short-circuit the power source and maintain a persistent current in the LTS magnet.

In recent years, the rapid development of HTS wires has made magnet windings possible [79, 80]. There are several advantages to using HTS magnets over LTS magnets, such as the higher operating temperature (77 K), which lowers the cost of necessary cryogenic liquids (e.g. liquid nitrogen). The temperature span over which the magnet remains superconducting is also much wider than that of an LTS magnet [81]. As shown in the left figure of Fig.3.3, the upper critical fields of an HTS material such as YBCO and BSCCO are much higher than an LTS (NbTi and Nb_3Sn), which indicates that HTS materials can operate at a much stronger field than can LTS materials (in practical engineering, the irreversible field [82] is considered rather than the upper critical field). In the current market, the BSCCO wire is known as first generation (1G) HTS wire, and YBCO wire is known as second generation (2G) HTS wire. YBCO performs better in a magnetic field, which is ideal for use in magnet windings, even though YBCO wire is more difficult to fabricate [31, 83, 84]. The figure at the bottom right of Fig. 3.3 shows the structure of a commercial YBCO wire as fabricated by Superpower [31]. Apart from the YBCO layer, there are buffer layers and copper stabiliser layers to improve the mechanical strength and thermal properties of the YBCO wire. The thickness of the YBCO layer is only 1% of the total thickness of the wire.

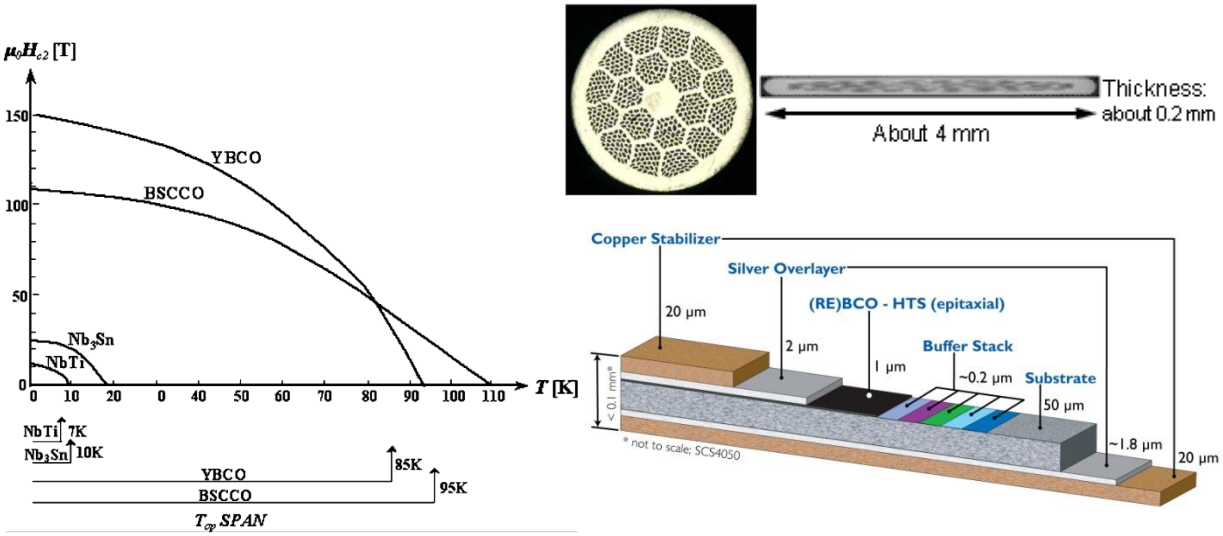

FIG. 3.3. The figure on the left shows the $\mu_0 H_{C2}$ vs. T curves for LTS (NbTi and Nb_3Sn) and HTS materials (YBCO and BSCCO) [81]; the figure on the top right shows the cross section view of a BSCCO wire or first generation (1G) HTS wire [84, 85]; the figure on the bottom right shows the structure of the YBCO wire or the second generation (2G) HTS wire [31].

Although the 2G HTS wire is preferable for magnet windings, there are several technical challenges which need to be tackled. Since 2G HTS wire has a very complicated layered structure, as shown in Fig. 3.3, it is very difficult to construct a superconducting joint with a very low resistance. When two 2G HTS wires are joined together, the superconducting layers of the two wires cannot be in direct contact. Instead, the current must flow through the copper layers and the soldering point, which are not superconducting. Therefore, loss at the joint is inevitable, which will lead to the decay of the circulating current in 2G HTS magnet. Additionally, when YBCO operates at 77 K, giant flux creep [86] cannot be avoided, which leads to a logarithmic decay of the trapped field and a low *n*-value for the superconductor. This problem can be tackled by operating the HTS magnet at a lower temperature such as at 20 K, however this will correspondingly increase the cryogenic cost.

In conclusion, the circulating current inside a HTS magnet will inevitably decay due to two major reasons: joint resistance and the giant flux creep. In order to operate an HTS magnet in a persistent current, a flux injection device or flux pump device is necessary to compensate for the decayed current in the HTS magnet.

The following section introduces a mature flux pumping technology for type-I superconducting films. Although this type of flux pump technology is not used in practical engineering, it provides clues on how a superconducting magnet can be magnetised using novel methods.

3.2 Flux pump technology with type-I superconducting film

The flux pump technology for an LTS coil with a type-I superconducting film is a mature technology which was developed several decades ago. Although there are many forms of type-I superconducting flux pump, they all share the same basic physics. This type of flux pump technology can be easily understood and easily controlled, however, this technology is not widely applied for practical engineering purposes. The main reason for this is probably that an LTS magnet doesn't necessarily need a flux pump device, since a well-designed LTS PCS already suitable, and the *n*-values of the LTS materials are high enough to prevent current decay in the magnet. Another reason is that a type-I superconducting film can only bear a very limited current density. However, understanding the mechanism of a type-I superconducting flux pump is crucial in order to understand the design of a type-II superconducting flux pump.

The basic physics of the type-I superconducting flux pump are relatively simple. As discussed in Section 2.1, type-I superconductors have two basic properties: perfect conductivity and perfect diamagnetism (the Meissner effect). As discussed in Section 2.1.2, when a magnetic field is applied perpendicular to a type-I superconducting film, the superconducting and non-superconducting regions co-exist inside the superconducting film in an "intermediate state". The creation of a non-superconducting region is due to the Meissner effect of the superconducting regions, which expels the flux line into neighbouring regions and locally increases the magnetic field in the these regions above the critical field H_C. After the H_C is breached, these areas become non-superconducting and thereby lose their perfect conductivity. Compared to the superconducting region, the non-superconducting region is equivalent to an electrically insulated area such as an electric switch.

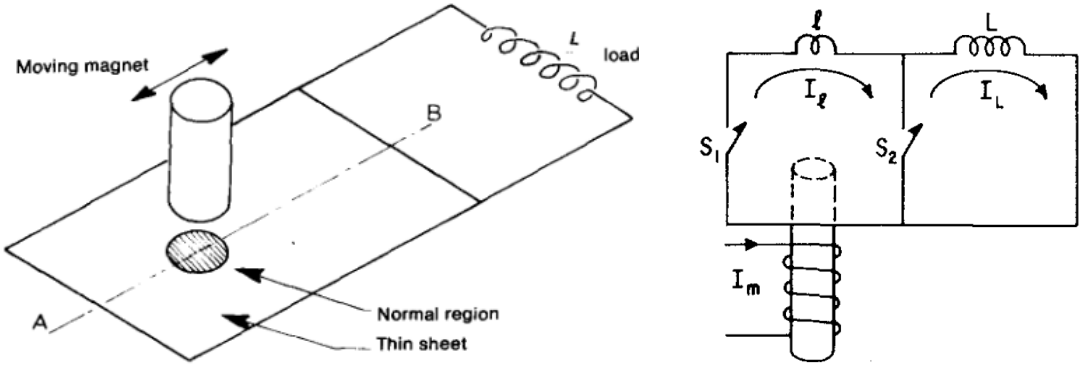

FIG. 3.4. Superconducting flux pump with type-I superconducting film. The figure on the left shows the basic structure. The magnet is responsible for the creation of the non-superconducting region (normal region) and the transport of magnetic flux into the superconducting loop [87]. The figure on the right shows the equivalent circuit [88].

Fig. 3.4 shows an example of a flux pump for use with a type-I superconducting film. The load is a common LTS magnet (using a type-II superconducting material such as NbTi and Nb_3Sn) which is connected to a wide type-I superconducting film with the help of superconducting joints. As shown on the left of Fig. 3.4, when a strong magnet is placed above the type-I superconducting film, the area below the magnet becomes non-superconducting. As the magnet moves, this normal region moves accordingly. The right hand figure in Fig. 3.4 shows the equivalent circuit. When the normal region is created at the sides, it behaves like an open electric switch, like S_1 and S_2 as shown in Fig. 3.4.

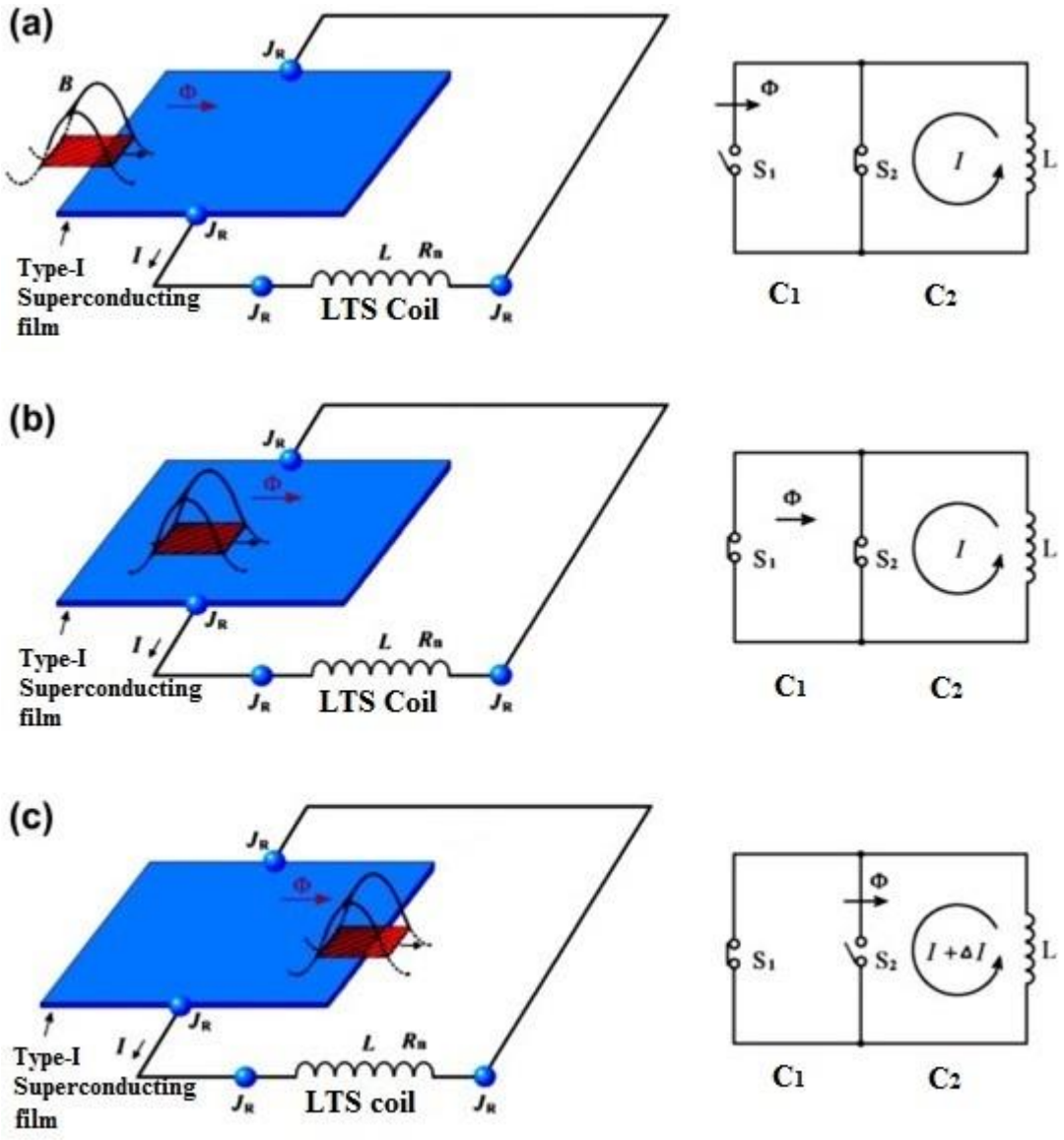

FIG. 3.5. The process which shows how magnetic flux has been transport into the superconducting loop by the flux pump with type-I superconducting film [89].

The detailed process of how the magnetic flux is transported into the superconducting loop is shown in Fig. 3.5. The magnetic flux travel in the type-I superconducting film in four steps:

Step 1. As shown in Fig.3.5(a), when the magnet arrives at the outer edge of the film, a normal region is created at the edge, which is equivalent to the opening up of switch S_1. The existing current *I* flows through the switch S_2 (the superconducting region). Since the loop C_1 is open when the flux travels through the loop, there is no induced current in C_1. Since there is no change of magnetic flux in loop C2, there is no induced current in C_2 either.

Step 2. As shown in Fig.3.5(b), when the normal region travels to the centre of the film, both switches S_1 and S_2 are closed. From Step 1 to Step 2, there is no change of magnetic flux in the loop C_1, therefore there is still no induced current in C_1. Meanwhile, there is no change of magnetic flux in C_2, therefore no induced current in C_2 either.

Step 3. As shown in Fig.3.5(c), when the normal region travels to the inner edge of the film, the switch S_2 is open. From Step 2 to Step 3, there is no change of magnetic flux within the combined loop C_1+C_2. Therefore, there is no induced current within the superconducting loop. However, the magnetic flux inside the superconducting loop has increased by $\Delta\Phi$. This magnetic flux is provided by the moving magnet.

Step 4. The final and most important step is to swipe the magnet out of the superconducting loop, which changes the magnetic flux by $-\Delta\Phi$. In order to keep the magnetic flux stable inside the superconducting loop, a current ΔI must be induced according to Faraday's law. This induced current ΔI counteracts the change in magnetic flux, and is added to the existing current I as shown in Fig. 3.5(c). The flux increases by $\Delta\Phi$ inside the superconducting loop, compared to the magnetic flux at the beginning of the cycle.

The above discussion shows that the type-I superconducting film must be wide enough for the successful operation of the flux pump for the following two reasons. First, the film must be wider than the width of the normal region, otherwise there is no superconducting region while the flux travels in the film. Second, when the normal region is created in the film, the superconducting region decreases correspondingly. The type-I superconducting film must be wide enough to ensure the successful bypass of the existing transport current in the superconducting loop.

The above mentioned method applies to type-I superconducting films. However, for a type-II superconducting film, in order to create a normal region, the applied magnetic field must exceed the upper critical field $\mu_0 H_{C2}$. For HTS materials, the upper critical field $\mu_0 H_{C2}$ is very high, as shown in Fig. 3.3, and therefore it is unlikely to be created using the magnetic field. However, for some LTS materials, since the upper critical field H_{C2} is relatively low, it is possible to create a normal region using the magnetic field. For instance, Chung [90] used the LTS material Nb foil for experiments. Nb is a type-II superconducting material for which the lower critical field $\mu_0 H_{C1}$ is equal to 0.14 T, and the upper critical field $\mu_0 H_{C2}$ is equal to 0.31 T. The upper critical field $\mu_0 H_{C2}$ = 0.31 T can be easily achieved using a magnet, and thereby the flux pump method can be used with this type-II superconducting material with the same mechanism as for a type-I superconducting material.

There are two methods for creating a travelling magnetic wave for the flux pump device. One uses a rotating magnet, while the other uses a linear three phase winding. The rotating magnet method is shown on the left of Fig. 3.6 [91, 92]. Either a permanent magnet or an electric magnet can be rotated. The magnet generates magnetic flux, which creates the normal region in the type-I superconducting film, while travelling of the normal region is induced by mechanically rotating the magnet. The linear three phase winding method is shown on the right of Fig. 3.6 [90, 92-95]. The linear three phase winding is normally used in a linear motor to generate linearly travelling magnetic poles [96]. The peak value of the magnetic wave must be greater than the critical field H_C in order to create a normal region in the superconducting film. Moreover, the magnetic wave generated by the linear three phase windings must be offset by a carefully chosen dc background field, otherwise both the positive and negative flux will be transported into the superconducting loop [95].

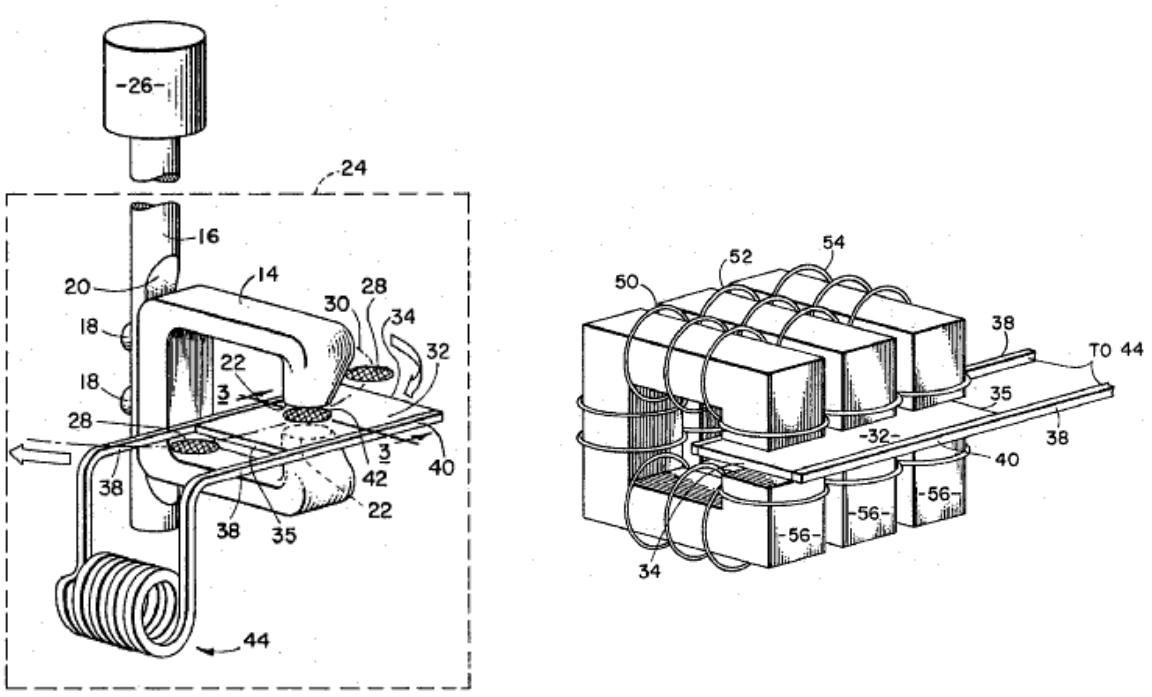

FIG. 3.6. The two methods to generate a travelling magnetic wave for the flux pump device with type-I superconducting material [92].

An alternative method for creating and transporting a normal region is to locally heat the sample using radiation light [97, 98]. As shown in Fig. 3.7, this method requires a radiation source to locally heat a region of the type-I superconducting film above its critical temperature T_C. A magnet is placed below the normal region and moved accordingly with the movement of the normal region. This

method is more complicated than the previously mentioned method, and may not be practical for use in a real experiment.

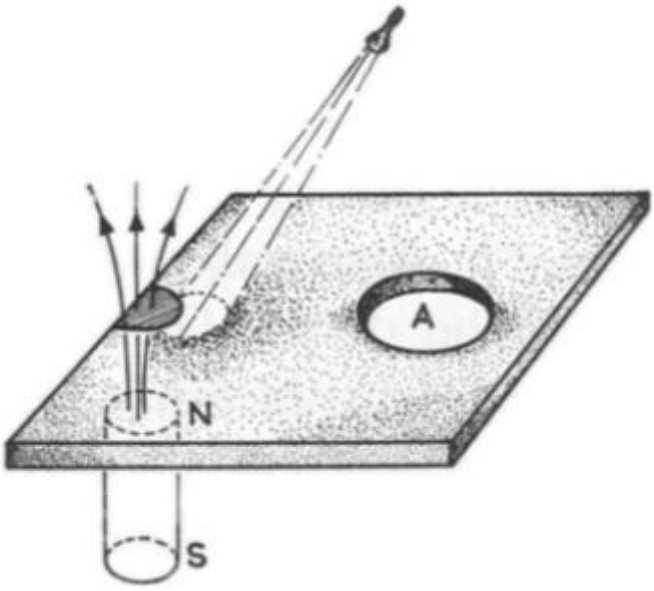

FIG. 3.7. The normal region created by radiation [98].

The advantages and disadvantages of each of the three methods (rotating magnet, linear three phase winding and radiation) are listed in Table. 3.1. Of these methods, the linear three phase winding is the most practical, except that heat might be generated by the phase windings, which may add an extra heat load to the cryogenic system. However, the heat can be calculated into the cryogenic temperature, and it may be small enough to be easily taken compensated for by the cooling system.

This section has introduced three methods of flux pump technology for use with type-I superconducting films: a rotating magnet, linear three phase windings, and radiation. In the following sections, the possibility of using flux pump technology with type-II superconducting films will be addressed. It will show that the physics of type-II flux pump technology can be very different from those in a type-I flux pump. The “dc transformer”, developed several decades ago, will be introduced.

TABLE. 3.1.

The pros and cons of the three flux pump methods with type-I superconducting film

	Rotating magnet	Linear three phase windings	Radiation
Free from mechanical moving components	×	√	×
Free from vibrations and noise	×	√	√
Ease of control	Very simple	Yes	Complicated
Speed of the normal region	Fast	Fast	Slow
Zero heat generation by the device	√	×	×

3.3 "DC transformer" for superconducting films

This section introduces the "dc transformer" for superconducting films. The "dc transformer" is not directly related to flux pump technology, however, its underlying physics provide useful information on how the vortices can be transported using field inhomogeneity. These experiments provide details on how a travelling wave can differ from a conventional homogeneous oscillating field when applied to a type-II superconducting film. A travelling wave is a magnetic wave that has been generated using a rotating magnet or three phase windings, as discussed in the previous section. The travelling wave has a crest region and trough region, i.e., the magnetic field is inhomogeneous in the space. This is in contrast to the definition of a homogeneous oscillating field, such as the magnetic wave in the middle of a one-phase solenoid. Ideally, the magnetic field for the homogeneous oscillating field is homogeneous throughout the space.

The "dc transformer" experiment was first performed by the Nobel Prize Laureate I. Giaever to demonstrate the magnetic coupling of vortices between two adjacent but insulated type-II superconducting layers [99]. The sample was prepared as shown at the top of Fig. 3.8. The first layer of type-II superconducting material is an Sn film which is deposited onto a glass microscope slide. A thin insulating layer of SiO_2 is deposited over the primary, and a second layer of Sn is deposited on the top of the SiO_2 layer. The sample is then exposed to a dc background field perpendicular to the sample surface, and a dc current is applied to the primary film. Since both the current and the background field are dc, there should be no change in magnetic flux, which shouldn't lead to an induced voltage according to Faraday's law. However, a voltage is measured at the secondary film

even though it is insulated from the primary film and no current flows between them. The bottom of Fig. 3.8 shows a comparison of the primary and secondary voltages V_p and V_s as a function of current I_p.

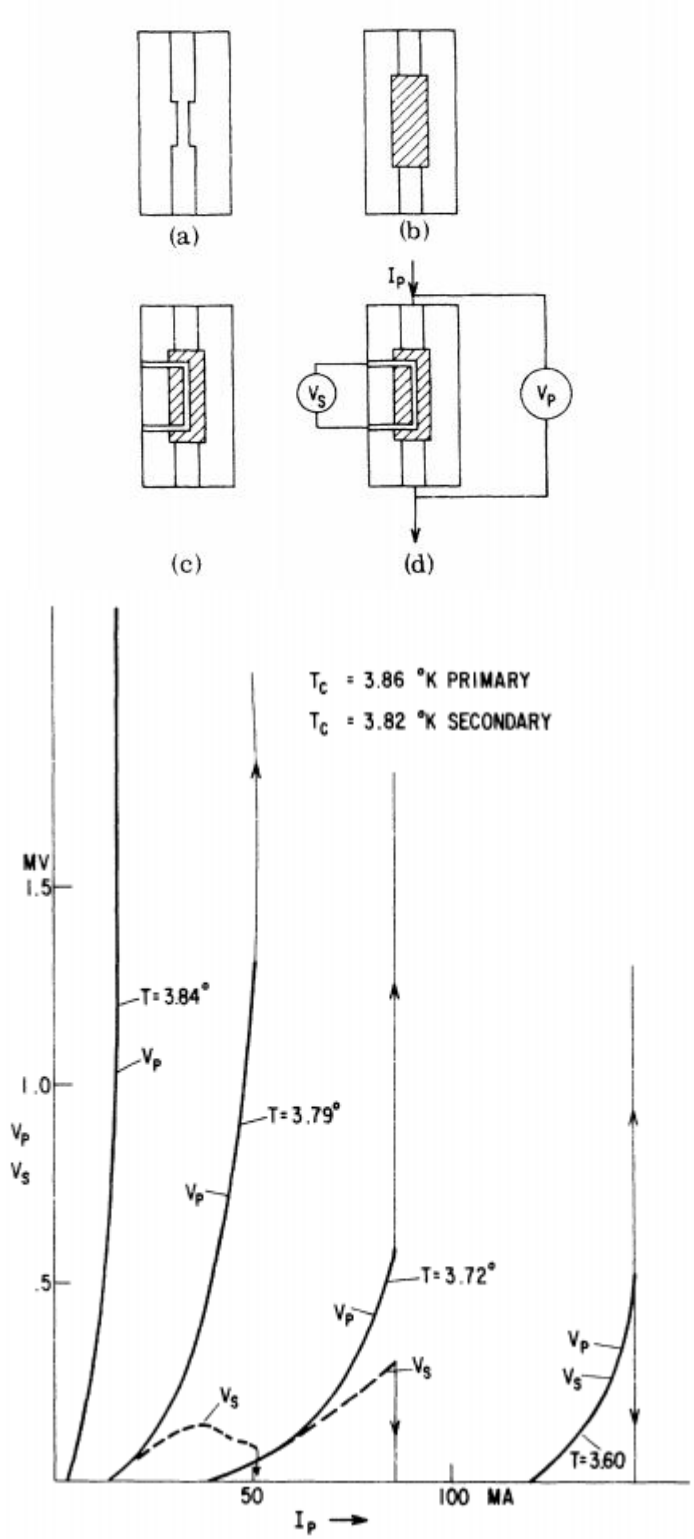

FIG. 3.8. The figures on the top show the preparation of the "dc transformer": An Sn film is deposited onto a microscope glass slide as the primary Sn film. A thin insulating layer of SiO_2 is deposited over

the primary Sn film, then a second layer of Sn film is deposited over the first two layers. Current flows through the primary Sn film and voltage is measured at the secondary Sn film [99]. The figure on the bottom shows the measured primary and secondary voltages V_p and V_s as a function of current I_p in the primary at different temperatures [99].

The measured voltage from the secondary film can be explained by the migration of vortices in the secondary type-II superconducting film. As discussed in Chapter 2, the magnetic field enters the type-II superconductor in the form of vortices, each containing a quantised magnetic fluxon in the "mixed state". The GL theory states that, within the coherence length ξ of each vortex, the absolute value of the order parameter is very low, produces a tiny normal region. The magnetic structure of each vortex is such that the magnetic field is at a peak in the centre of the vortex, and decays with distance. Giaever's explanation of the "dc transformer" is based on the fact that, when two layers of type-II superconducting film are placed in a perpendicular magnetic field, the magnetic flux penetrates through the two layers (primary and secondary). For a single fluxon, the vortices of the primary and secondary film must be aligned in order to minimise the potential energy, provided that the insulation layer is sufficiently thin. This leads to a coupling of the vortices between the two layers. If a dc current is applied, this induces flux flow in the primary type-II superconducting layer, the coupled vortices in the secondary type-II superconducting layer flow accordingly. Using Equation (2.56), it is evident that a flux flow in the mixed state gives rise to an electric field, according to the Lorentz transformation. However, this can also be explained using Faraday's law, as preferred by Giaever. Giaever's explanation of the induced electric field resembles that of a type-I flux pump technology. Giaever's explanation for the measured voltage in a secondary type-II superconducting film is [99]:

"…The simplest way of interpreting the voltage which may be seen on the voltmeter when the superconductor is in the resistive state is to consider 'flux rings' to be created on one side of the film and annihilated on the other side…"

This argument offers a clue on how a flux pump technology might be created for a type-II superconducting film, that is, to transport vortices across a type-II superconducting film into the superconducting loop. Vortices can act as numerous tiny normal regions each containing a quantised fluxon. If the vortices are transported across a type-II superconducting film into the superconducting

loop, then the four steps of the type-I flux pump can be fulfilled, which will create an induced current ΔI according to Faraday's law.

The "dc transformer" shows that field inhomogeneity can help vortices to move across the superconducting film. Field inhomogeneity is induced by the magnetic field of the vortices in the primary film. The coupling forces between the primary vortex and secondary vortex have been studied extensively [100-107]. The coupling force can be calculated from the magnetic energy distribution. As shown in Fig. 3.9, there are several parameters which affect the coupling force of the vortices, such as the thickness of the primary and secondary films, the thickness of the insulation layer, and the pinning force of the primary and secondary films. In general, the pinning force in the secondary film ought to be smaller than the pinning force in the primary film. Since the field inhomogeneity is provided by the vortices, the thickness of the insulation layer should be sufficiently thin, otherwise the field inhomogeneity will not be strong enough to cause vortices to move in the secondary film. The thickness of the insulating layer should be within the range of the coherence length of the vortices.

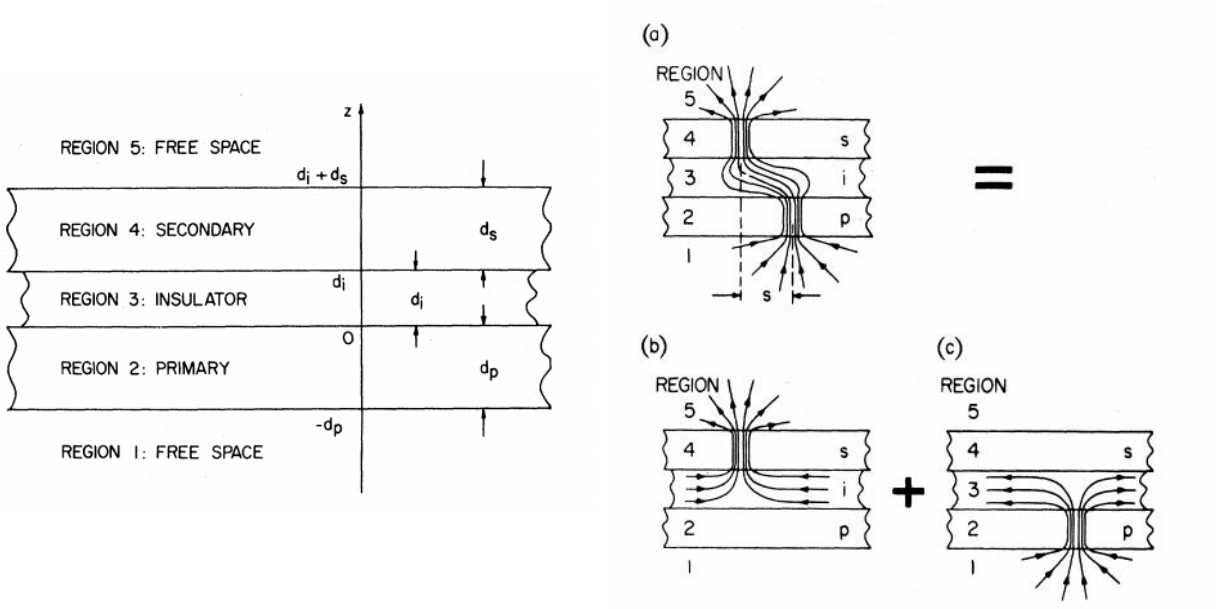

FIG. 3.9. The figure on the left shows the geometry of coupled superconducting primary and secondary films; the figure on the right shows sketches of the magnetic field line for a fluxoid pair [100].

The right hand figure of Fig. 3.9 shows the coupling of the two vortices in the primary and secondary type-II superconducting thin films. The coupling is due to the fact that, when there is a displacement between the two vortices (as "*s*" in Fig. 3.9), the potential energy for the two vortices increases. In order to minimise the potential energy, the coupled vortices in the secondary move accordingly with the primary vortex.

This coupling phenomenon can also occur in type-I superconducting films, as demonstrated by Solomon [108]. His "dc transformer" had the same structure as that of Fig. 3.9, except that type-I superconducting materials were used for the primary and secondary films. This work suggests that the normal regions in the intermediate state of a type-I superconducting film can also be coupled, except that each normal region contains a large quantity of magnetic fluxons while a vortex in the type-II superconducting film contains only one fluxon. The coupled movement of the normal regions in the intermediate state is also induced by the field inhomogeneity from the moving normal regions in the primary film.

From this, the following two conclusions can be drawn, which lead to a possible design for a type-II superconducting flux pump:

1. If a single vortex is transported across a type-II superconducting film into a superconducting loop, a small current ΔI will be induced, which resembles the mechanism for a type-I superconducting flux pump;
2. The vortices in the type-II superconducting film can be transported by a travelling inhomogeneous magnetic field, as demonstrated by the "dc transformer". However, the "wavelength" of the dc transformer is the inter-vortex distance, which is at the microscopic scale and cannot be achieved using practical engineering. At the macroscopic scale, the travelling inhomogeneous magnetic field can be achieved by a moving magnet or by three phase windings. If the moving magnet or three phase windings can transport vortices in type-II superconducting films, then a flux pump technology for use with type-II superconducting film becomes available.

The next sections introduce two possible type-II flux pump technologies for use with HTS films. A discussion follows regarding the travelling magnetic wave, along with the introduction of a novel device, which forms the main subject of this thesis.

3.4 HTS flux pump technology for a bulk superconductor

The idea of using a travelling magnetic wave to magnetise a HTS bulk was first proposed by Coombs [109-115] at Cambridge University. The original concept involved sweeping a magnetic field beneath a YBCO bulk, so that the magnetic flux could gradually accumulate in the bulk superconductor. The travelling wave was generated by creating a travelling heat wave inside a ferromagnetic material such as Gadolinium, which has a Curie point of 294 K [112] and a relative permeability of approximately 10.0. By heating the sample above its Curie point, the ferromagnetic material becomes "switched off". By cooling the sample down again below its Curie point, the ferromagnetic material becomes "switched on". Therefore, as the travelling heat wave travels across the ferromagnetic materials in a dc background field, a quasi-travelling magnetic wave is generated. Fig. 3.10 shows the key components of the "thermally actuated flux pump" device (figure on the left) and the magnetic circuit (figure on the right).

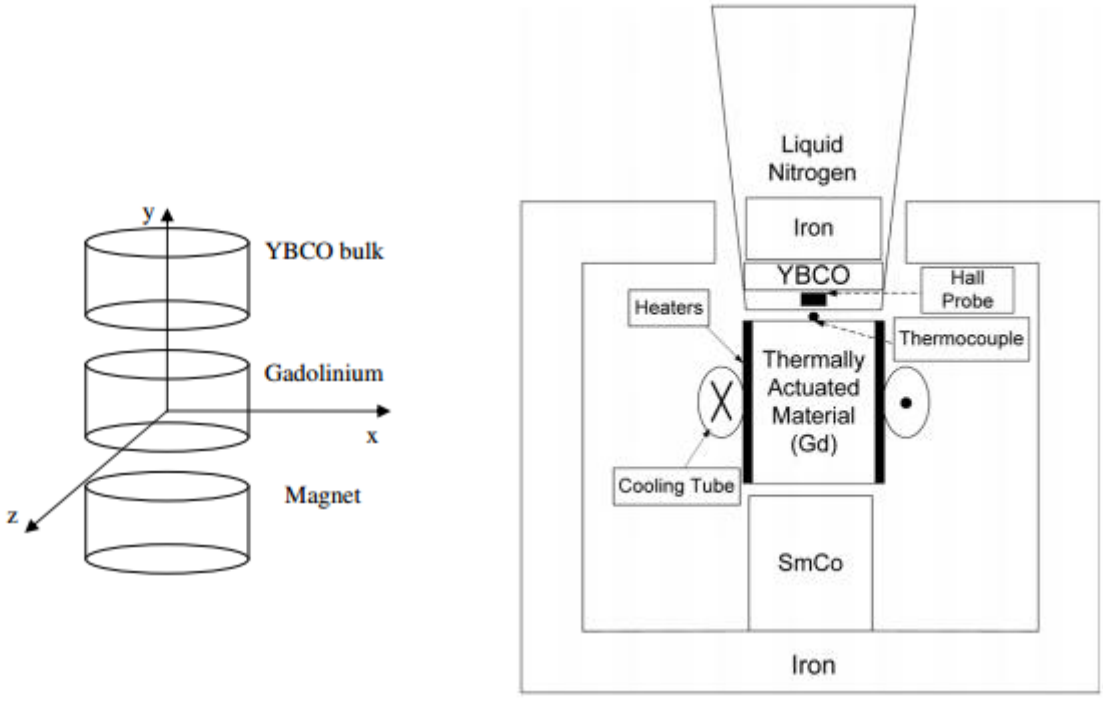

FIG. 3.10. The key components of the "thermally actuated flux pump" device (figure on the left) and the magnetic circuit (figure on the right).

The idea of using a travelling magnetic wave as proposed by Coombs can also be applied to HTS films. The next section discusses a possible HTS flux technology for use with HTS coils. This technology uses the travelling magnetic wave to fully magnetise an HTS magnet.

3.5 Possible HTS flux pump technology for HTS coils

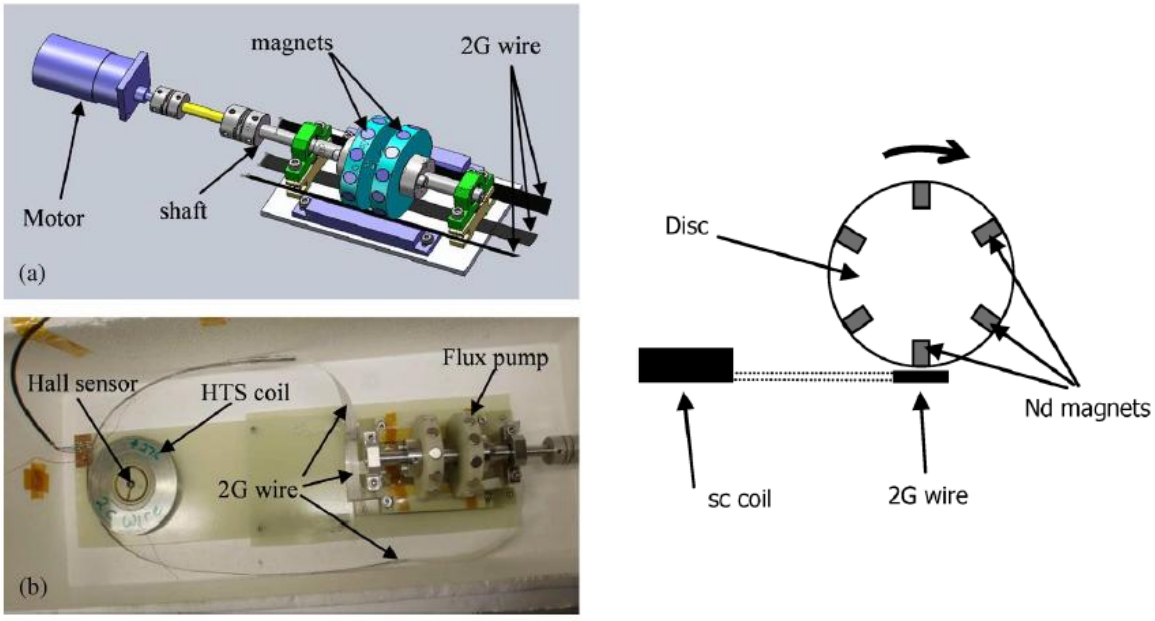

FIG. 3.11. The flux pump device with YBCO film demonstrated by Hoffman[116]. The HTS coil is soldered with the YBCO film with the joint resistance in the order 40 – 200 nΩ.

This section introduces two possible type-II superconducting flux pump technologies for use with HTS films. The careful choice of the word "possible" is due to the fact that, even though these flux pump designs seem quite successful, their underlying physics is not yet fully understood. Both experiments used HTS films for the flux pump. A travelling magnetic wave is applied across the HTS film, and the accumulation of magnetic flux is measured in the HTS coil connected (by soldering) to the HTS film. The travelling magnetic wave is either generated by a rotating permanent magnet as demonstrated by Hoffman [116] or by three phase windings as demonstrated by Bai [89]. Fig. 3.3 shows that that HTS materials such as YBCO has a very high upper critical field $\mu_0 H_{C2}$ at 77 K. The field generated by the permanent magnet or three phase windings is normally weaker than 1.0 T,

which is far below this upper critical field. As such, a normal region cannot be created using either method. A type-I superconducting flux pump would not be able to operate in these conditions.

Hoffman's experiment is shown in Fig. 3.11. The main idea of this flux pump is the rotation of a magnetic disk above a YBCO film. The disk is embedded with permanent magnets (NdFeB). The YBCO film is connected by soldering to a HTS coil. Both the HTS coil and the YBCO film are made from 2G YBCO tape produced by American Superconductor (AMSC) Corp. The coil has an inductance of 2.7 mH and a critical current of 55 A. The YBCO film used for the flux pump purpose has a width of 12 mm, and is soldered to the HTS coil leads using InBi solder. The joint resistance is in the order of 40 – 200 nΩ [116]. His experiment shows that the circulating current inside the HTS coil can be easily ramped up to a value close to its critical current, with the help of a rotating magnet. A net dc current is induced inside the superconducting loop after rotation of the magnet above the 12 mm wide YBCO film. This phenomenon is notable for the following two reasons. First, it was known that for normal conductors such as copper, the induced current inside the copper coil caused by the rotating magnet must be ac according to Faraday's law. This is most common in electric machines such as the electric generator. However, in Hoffman's experiment, a dc current is induced instead. Second, the magnetic field provided by the NdFeB N38 described in the experiment is far below the upper critical field $\mu_0 H_{C2}$ of the YBCO material, which makes it impossible to create a normal region on the YBCO film. However, the flux pump phenomenon has been achieved using the rotating magnet, which resembles a type-I superconducting flux pump.

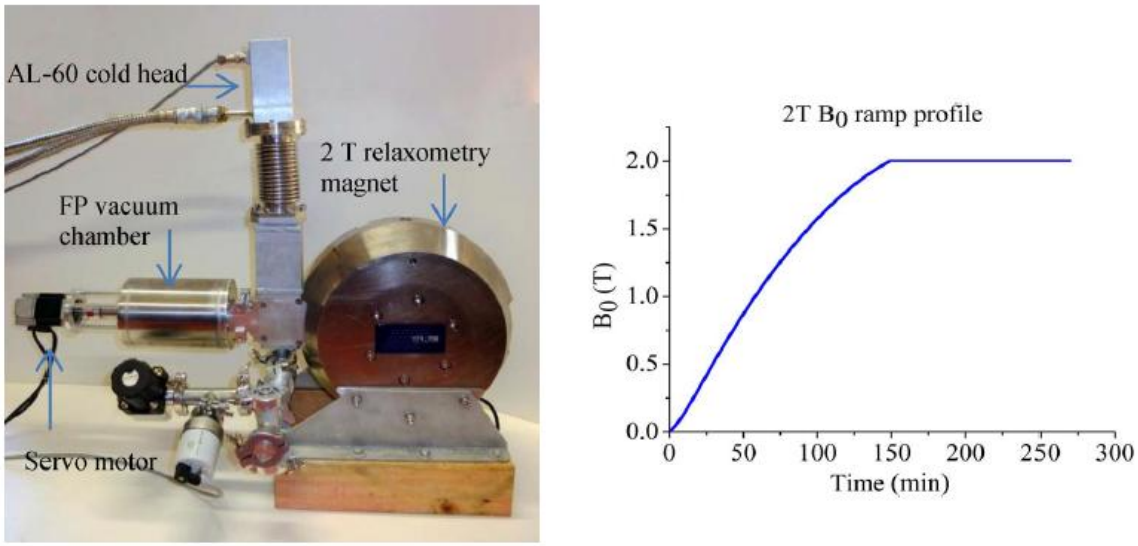

FIG. 3.12. The NMR relaxometry magnet which is powered up using Hoffman's method. The magnetic field in the centre can ramp up to 2 T [117].

Hoffman showed that the accumulation of dc current inside the HTS coil is dependent on the rotating speed of the disk. The higher the speed of rotation, the faster the dc current ramped up to the critical current. The direction of the dc current is also related to the direction of rotation of the disk, which is to be expected since the induced voltage should reverse the direction as the rotating magnet changes direction. This issue is further addressed in later chapters, in the context of magnetic coupling.

The Gallaghan Innovation Research LTD in New Zealand has recently developed a 2 T NMR relaxometry magnet which is powered up using Hoffman's method. The rotating magnet can fully magnetise an HTS magnet to its maximum field of 2T (at 110 A) in 2.5 hours [117]. The dipole magnet is made from BSCCO wire, and has an inductance of 0.4 H. The rotating magnet and the NMR magnet are integrated inside a cryogenic chamber which can operate at 32 K. The heat generated by the flux pump is below 2 W which is 4.5 times lower than the conventional current leads. Fig. 3.12 shows the NMR relaxometry magnet integrated with the flux pump device with the ramped field in the middle of the magnet. Hoffman's work not only proves that flux can be transported into an HTS loop by a rotating magnet, but also proves that it is capable of being suitable for practical use.

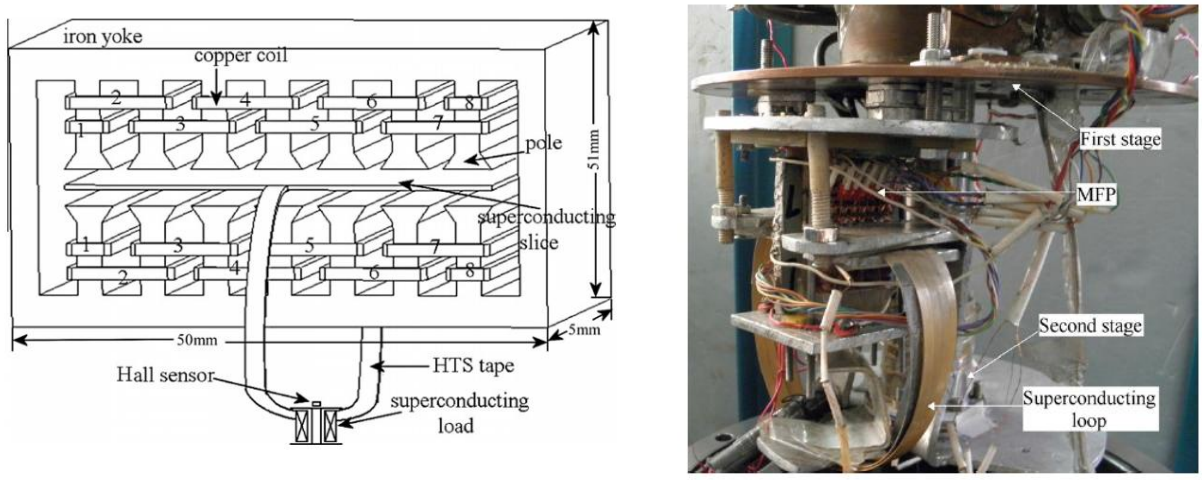

FIG. 3.13. The HTS flux pump with linear three phase windings [118].

There are also other methods for providing a travelling magnetic wave. Another method is to use linear three phase windings, as discussed in Section 3.2. Bai applied this method to magnetise an HTS coil [89, 118]. A dc current accumulated in the HTS loop can reach approximately 200 A for Bi2223 coil and 80 A for MgB_2 coil at 20 K.

Hoffman and Bai show that a travelling wave is able to transport magnetic flux into an HTS loop through an HTS film. However, this is not achieved by creating normal regions as is the case for a flux pump used with a type-I superconducting film, since the upper critical field of the HTS is too high to be achieved using a normal magnet. Although the dc current accumulated inside the HTS loop is quite remarkable (close to critical current I_C), the underlying physics is not clearly understood. Therefore, a further study is necessary to understand the underlying physics for these HTS flux pump technologies. A novel experiment to study the physics of an HTS flux pump is proposed by the author in the next section.

3.6 Novel research on the magnetisation based on a travelling magnetic wave

Section 3.5 showed that a travelling magnetic wave can successfully magnetise an HTS coil to its critical current I_C. However, it is still not clear why or how magnetic flux is transported into the superconducting loop by the travelling wave. Although the magnetisation of type-II superconductors has been studied for decades, knowledge is still limited on how a travelling wave can magnetise a type-II superconductor. This is due to the fact that a travelling wave is constantly equated to a homogeneous oscillating field without any proper argument. For instance, ac magnetisation losses are very common with travelling waves such as inside a superconducting electric machine. However, almost all the literature concerning about ac magnetisation loss calculations use homogeneous oscillating field rather than travelling waves [50].

In light of the above discussion, it was necessary to conduct research into how a travelling magnetic wave can magnetise a type-II superconducting film. The experiment was carefully designed so that the results can be easily compared to the effects of a homogeneous oscillating field. The Bean model [47] is a powerful tool that can be used to predict the magnetisation based on a homogeneous oscillating field. The Bean model assumes that the induced current density inside a type-II superconductor is equal to the critical current density J_C. Ideal geometries for the Bean model are an infinitely long cylinder or an infinitely wide slab, which have a zero demagnetisation factor (N=0). Although the samples used for experiment were HTS films with a high demagnetisation factor (N≈1.0), numerous books and articles [50] have shown that the magnetisation of type-II

superconducting films more or less follows the constant current density assumption of the Bean model.

The ideal geometry for the investigation is a round shaped axisymmetric HTS film, so that the magnetisation of this geometry with a homogeneous oscillating field can be easily predicted using the Bean model. Therefore, in order to investigate magnetisation based on a travelling wave, device was need which can produce an axisymmetric travelling wave. The magnetisation based on the travelling wave could be easily compared with the homogeneous oscillating field. Therefore, it was decided that the key components of the experiment should include:

1. A round shaped YBCO film with a large diameter;
2. A device which can produce both homogeneous oscillating fields and travelling waves. The travelling wave should be axisymmetric (annular shape). Both the homogeneous oscillating field and travelling wave could be easily controlled during the experiment.

Based on the above discussions, a circular-type magnetic flux pump (CTMFP) will be proposed, as will be discussed in the following chapter.

CHAPTER 4

EXPERIMENTAL SYSTEMS AND MODELLING METHOD

In the previous chapter, an experiment was proposed to study the magnetisation of a type-II superconducting film using a travelling magnetic wave. It was decided that the YBCO sample should be round shaped, and the travelling wave should be annular shaped. The device must be capable of producing both an annular shaped travelling wave and a conventional homogeneous oscillating field. This chapter proposes a novel device for use in the experiment, named the "circular-type magnetic flux pump (CTMFP)". Two types of CTMFP were built for study. Calculations were also performed with the help of the commercial finite element method (FEM) software, COMSOL Multiphysics. This chapter introduces the experimental systems and the FEM method used, to provide a general idea of the studies the author has performed during his PhD.

4.1 The concept of a circular-type magnetic flux pump (CTMFP)

As mentioned in Chapter 3, the basic principle of flux pump technology is the application of a travelling magnetic wave to a superconducting film which is jointed to a superconducting magnet. This method applies to both type-I and type-II superconducting films, although the mechanisms involved can be very different.

In order to study the magnetisation of a round-shape YBCO film under the influence of a travelling magnetic wave, the circular-type magnetic flux pump (CTMFP) was proposed. The CTMFP combines the idea of a linear-type magnetic flux pump (LTMFP) [93-95, 119] and the thermally actuated flux

pump [109, 113, 114, 120-123] described in Section 3.4. The LTMFP uses three phase windings to produce a linear travelling magnetic wave. The thermally actuated flux pump generates an annular shape travelling magnetic wave by heating a gadolinium cylinder in a dc background magnetic field. The linear travelling magnetic wave generated by the LTMFP can be easily controlled using a three phase inverter, by adjusting the output voltage and frequency. The CTMFP uses three phase windings to generate an annular-shape travelling magnetic wave. The advantage of using phase windings is increased control over the annular-shape travelling wave.

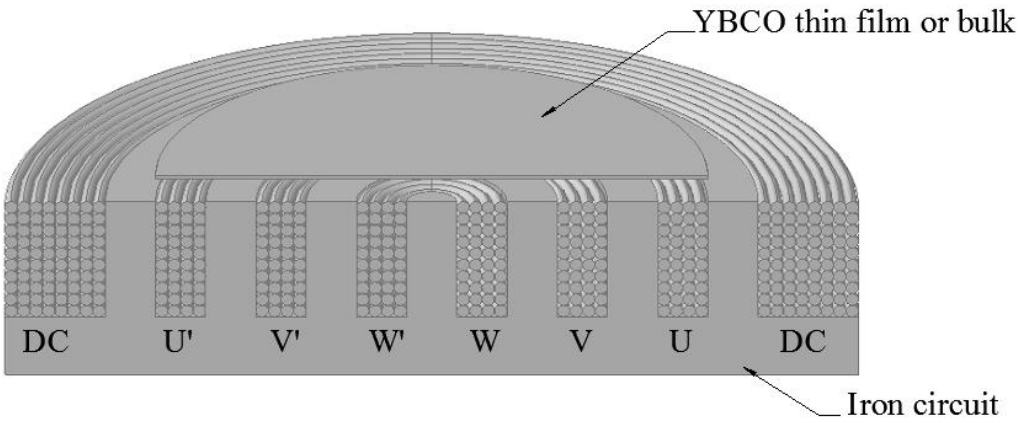

FIG. 4.1. The original design for the CTMFP [124]. The YBCO thin film is placed above the iron circuit. The iron circuit has three phase windings with positive phase sequence U, V, and W, as illustrated in the diagram. A coil carrying a dc current is wound around the iron circuit to provide a dc background field.

The original design of the CTMFP device is shown in Fig.4.1. The CTMFP magnet comprises three phase windings and dc coils, all of which are concentric. An iron yoke is sandwiched in between the windings to concentrate the magnetic flux, as is normally used in electric machines. A round shaped YBCO thin film or bulk is placed above the CTMFP. In this thesis, only YBCO thin film or tapes was used.

The three phase windings are designed to connect with a commercial three phase inverter which is used for the motor drive. The phase arrangement is shown in Fig. 4.1, such that the travelling wave moves inwardly from the outside into the centre. However, to reverse the travelling direction of the magnetic wave, the inverter can be switched into “reverse mode” as preset of the machine. The dc coil is connected to a dc power supply, to provide the dc background field. In general, the advantages of this design are:

1. The amplitude of the travelling wave can be controlled by altering the output voltage V_{ac} of the inverter;
2. The speed of the travelling wave can be controlled by altering the output frequency f of the inverter;
3. The direction of the travelling wave (inward or outward) can be controlled by altering the preset rotate-direction of the inverter;
4. The dc background field can be controlled by the altering output dc voltage V_{dc} of the dc power source.

The CTMFP is expected to produce an annular-shape travelling magnetic wave similar to that shown in Fig. 4.2. The magnetic field B_x is perpendicular to the surface of the YBCO sample (a-b plane). One defect of the design in Fig. 4.1 is that the YBCO sample could experience a magnetic field which is not normal to its surface, i.e. there is a component of the magnetic field which lies parallel to its surface. As discussed in Section 2.3.4, this parallel component may cause a "cross field effect" [68] for bulk superconductor, or a "flux shaking effect" [125, 126] for thin film. This may lead to the decay of the magnetisation of the superconducting sample. In order to mitigate this problem, it was proposed to use the combination of two identical CTMFP magnets, which will be discussed in the next section.

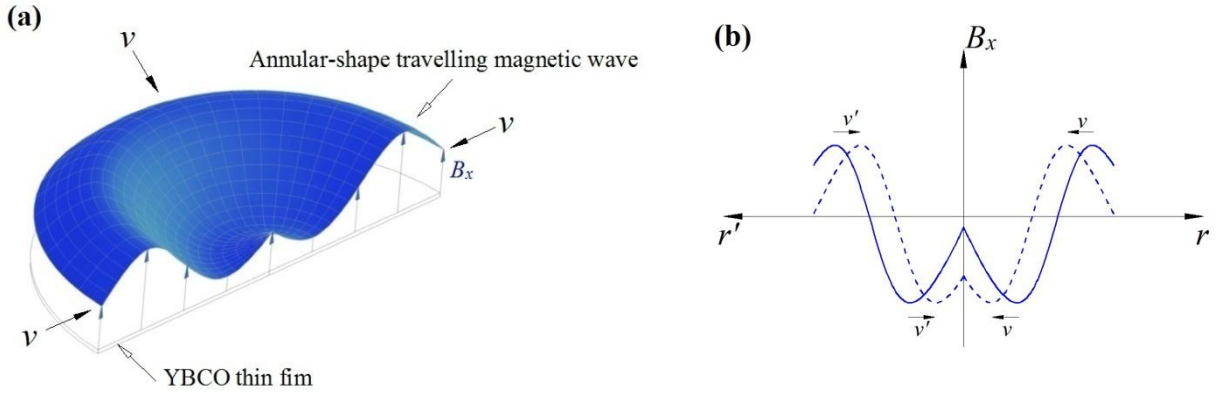

FIG. 4.2. (a) Schematic drawing of the annular-shape travelling magnetic wave generated by three-phase windings, and offset by the dc coils. (b) Demonstration of the travelling magnetic wave; the wave travels from outside of the sample to the centre. The magnetic field B_x is perpendicular to the surface (a-b plane) of the sample.

4.2 The original CTMFP magnets

4.2.1 Magnet design

As mentioned in the previous section, a single CTMFP magnet may lead to the "cross field effect" [68] or "flux shaking effect" [125, 126]. If these effects arose during the experiment, they would affect the ability to control the equipment precisely, which would compromise the validity of the experimental results. One method for avoiding the cross field effect is to overlap two identical CTMFP magnets. The two identical CTMFP magnets face each other, with a small gap between them in which the YBCO sample is fitted. Between the two CTMFP magnets, should be no magnetic component in the radial direction, and the YBCO sample inserted between the two magnets should not experience a magnetic field parallel to its surface. The CTMFP experimental system was designed and built with this concept in mind. Fig. 4.3 shows the design of the CTMFP magnets, and Fig. 4.4 shows their geometry.

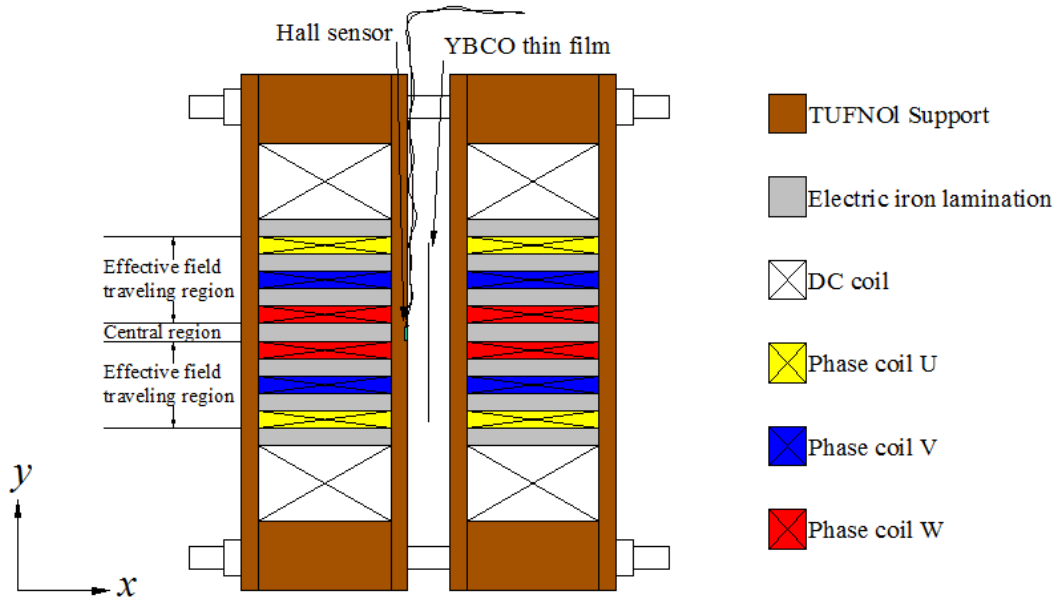

FIG. 4.3. The configuration of the CTMFP. Each coil contains three phase windings and a dc coil. A Hall sensor is placed in the centre of the device.

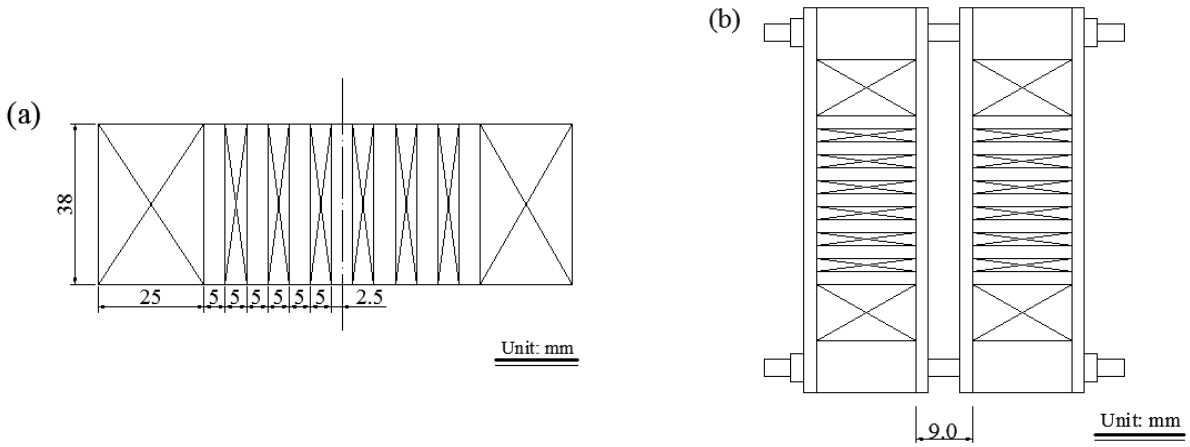

FIG. 4.4. (a) The geometry of each CTMFP magnet; (b) the size of the gap between two CTMFP magnets.

The CTMFP device comprises of two identical CTMFP magnets, as shown in Fig. 4.3. Each CTMFP magnet comprises three phase windings and a dc winding. As shown in Fig. 4.4, the width of each phase winding and the iron lamination was 5 mm and the height was 38 mm. The gap between the CTMFP magnets was 9 mm, as shown in Fig. 4.4. The region between the phase windings was defined as the "effective field travelling region", since the wave is travelling in this region. The region in the centre was defined as the "central region", in which the magnetic field oscillates but does not travel. The diameter of the phase windings was determined by the diameter of the YBCO samples. As discussed in later paragraphs, the sample uses for the study was a 2 inch diameter YBCO thin film. The diameter of the travelling region was 55 mm, which is slightly larger than the diameter of the sample (≈ 50.8 mm).

The two magnets were embedded in TUFNOL supports, which are electrically insulating and mechanically strong. Thin TUFNOL plates were installed to cover the surfaces of the magnets. The two magnets were assembled using threaded studding at the four corners of the TUFNOL support.

Originally, one Hall sensor was installed in the middle of the device as shown in Fig. 4.3. However, as will be mentioned in later paragraphs, a six Hall sensor array was also be used to measure the magnetic gradient. The YBCO sample was inserted into the central gap in the CTMFP device. The properties of the sample and the machining of the sample holder are described in later paragraphs.

4.2.2 CTMFP magnet and circuit analysis

Fig. 4.5 shows the two identical CTMFP magnets, "unfolded" from the configuration shown in Fig. 4.3. Both the magnets were wound by hand. The brown components are the enameled magnet wires. The axle at the centre of each magnet is machined from soft iron. The hole at the centre is approximately 3.0 mm deep, and threaded for the convenience of coil winding. The diameter of each hole is 2.5 mm. As illustrated in Fig. 4.3, the layers in between the wire windings are electric (silicon) iron laminations. The iron lamination is very thin (0.25 mm) and is tightly wrapped around the wire windings. The width of the lamination is 38 mm. The polished surface of the innermost electric iron layers is silver, and the unpolished surface is black. Electric iron laminations are normally used in electric machines to reduce eddy current losses in an ac magnetic field.

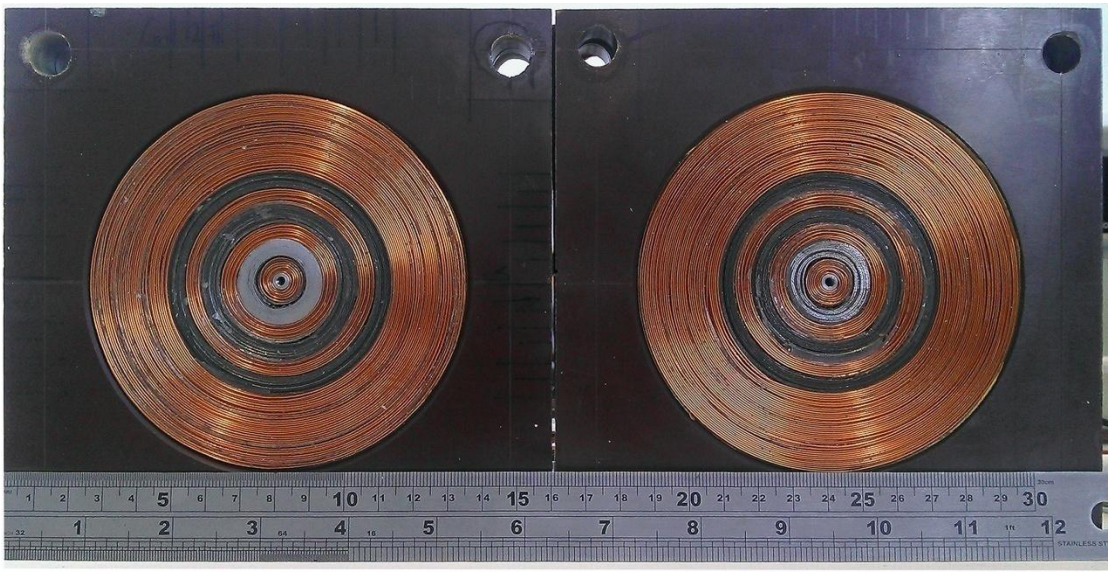

FIG. 4.5. The actual experimental CTMFP coils embedded in the TUFNOL supports. The materials between the coil windings are the electric iron lamination.

The magnet wire has a diameter of 0.5 mm. Since the height of each magnet is 38 mm, each layer of the winding has approximately 76 turns. Each phase winding has 8 layers, and each dc winding has 40 layers. The terminals of the windings lie at the back of the magnet, and are not shown in Fig. 4.5. The principle of the wire connection is that, for each phase, the two identical windings (from two magnets) work as a single solenoid. In order to achieve this, the wire connected to the backs of the magnets should reverse the direction as illustrated in Fig. 4.6. The windings of each phase are connected in series.

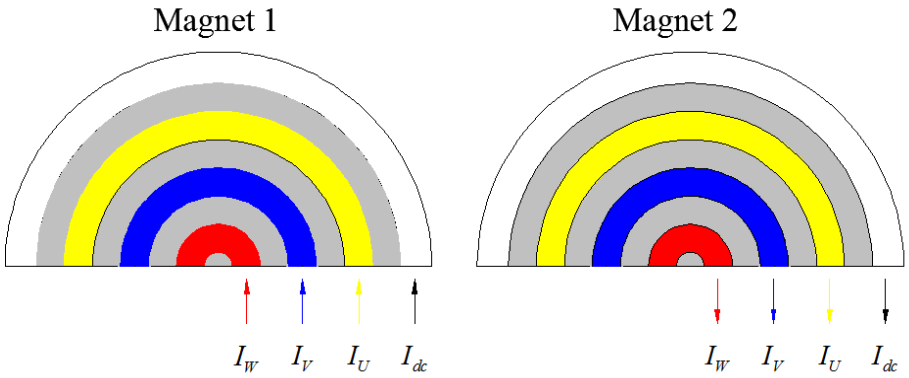

FIG. 4.6. Demonstration of the wire connections in the back of the CTMFP magnets.

After the connection is made between the CTMFP magnets, the electric resistance and the inductance of the each phase and the dc windings were measured. The measured properties are shown in Table 4.1.

TABLE 4.1
PROPERTIES OF THE CONNECTED WINDINGS

Phase	Inner-diameter (mm)	Outer-diameter (mm)	Layers of winding	Turns	Resistance 300 K (connected)	Resistance 77 K (connected)	Inductance (connected)
U	45	55	8	~1216	15.4 Ω	2.6 Ω	122.2 mH
V	25	35	8	~1216	9.2 Ω	1.6 Ω	62.2 mH
W	5	15	8	~1216	3.4 Ω	0.6 Ω	5.7 mH
DC	65	115	40	~6080			

The resistances of the three phase windings at 77 K are listed in Table 4.1, and were measured at R_U = 2.6 Ω, R_V = 1.6 Ω, and R_W = 0.6 Ω, where R_U, R_V and R_W represent the resistances for phase windings U, V and W. In order to balance the resistances, 300 Ω power resistors were connected in series with each phase coil, so that $R'_U \approx R'_V \approx R'_W \approx 300$ Ω.

The inductances of the three phase windings were measured at: L_U = 122.2 mH, L_V = 62.2 mH, and L_W = 5.7 mH. In order to avoid phase shift under ac current conditions, the real part of the impedances

was increased (by connecting 300 Ω power resistors) to minimise the phase shifting. The connections of the phase coils followed the star connection, as demonstrated in Fig. 4.7.

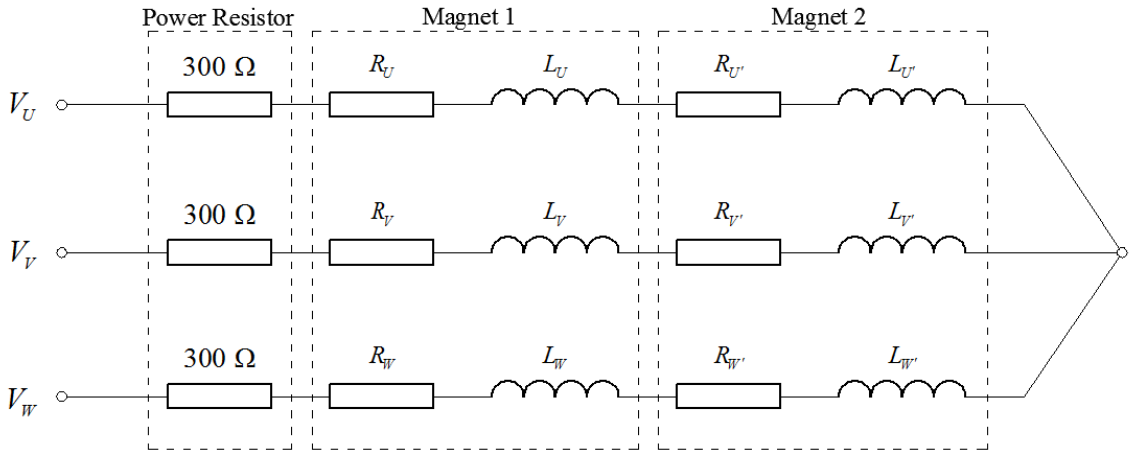

FIG. 4.7. The circuit of the CTMFP magnets.

The impedances were calculated using Equation (4.1):

$$Z_i = R_i' + j\omega L_i \tag{4.1}$$

where $\omega=2\pi f$, which is the angular speed.

The impedances were estimated at f=1.0, 10.0, 100.0, and 400.0 Hz, and the results are shown in Table 4.2. Up to f=100.0 Hz, changes to the absolute value of the impedance were negligible (a maximum change of 3%) and the phase coils were predominantly resistive (maximum phase shift 14 °). However, at f=400.0 Hz, the inductances greatly affected the impedance (a maximum 43 % impedance change and 45 ° phase shift for phase U). The inverter used for the experiments had a maximum output of 1000 Hz (in the high frequency mode). However, it was more reliable to use the "normal frequency mode" (which has a maximum output frequency of 400 Hz) since there is a sudden drop of output voltage at f=51.0 Hz in the "high frequency mode". In most of the experiments, the required output frequency was below 100 Hz. Therefore, connecting a 300 Ω power resister to each phase helped balance the loads.

TABLE 4.2
IMPEDANCE ACCORDING TO DIFFERENT FREQUENCIES

f (Hz)	Abs(Z_U, Z_V, Z_W) (Ω)	Angle(Z_U, Z_V, Z_W) (°)
1.0	300, 300, 300	0, 0, 0
10.0	300, 300, 300	1, 1, 0
100.0	310, 303, 300	14, 7, 1
400.0	429, 338, 300	45, 28, 3

4.3 An updated CTMFP magnet

In order to further study how field inhomogeneity influences the magnetisation of YBCO film, updated CTMFP magnets were designed and built. Compared to the original CTMFP magnets, the updated CTMFP magnets have s stronger field inhomogeneity. This was achieved by decreasing the wavelength of the travelling wave. The width of the phase windings in the updated CTMFP magnets is a quarter of the width of the original CTMFP magnets. There are two kinds of phase connections for the updated CTMFP magnets: one is the six phase connection, which produces a travelling wave with two pole-pairs; another is the three phase connection, which produces a travelling wave with four pole-pairs. This section introduces the design and the build of the updated CTMFP magnets.

4.3.1 Magnet design

In order to achieve a stronger field inhomogeneity, the CTMFP magnets were updated to produce with 1/2 (six phase connection) or 1/4 (three phase connection) of the wavelength compared to the original CTMFP magnets. Compared to the design in Section 4.2, the width of the phase windings and iron yoke in the updated CTMFP magnets is a quarter of the width of the original CTMFP magnets. The phase windings were increased accordingly to cover the whole area of the superconducting sample. In the six phase connection, the phases used were not only the U, V and W as indicated in Fig. 4.3 for 120 °phase shift. Three other phases –U, -V, -W were added between U, V, W, to ensure

the 60 ºphase shift between neighbouring windings. The 60 ºphase shift is illustrated in Fig. 4.8. The magnetic wave produced from the 60 ºphase shift is smoother than that from the 120 ºphase shift. The differences between the original CTMFP magnets and the updated CTMFP magnets are listed in Table 4.3.

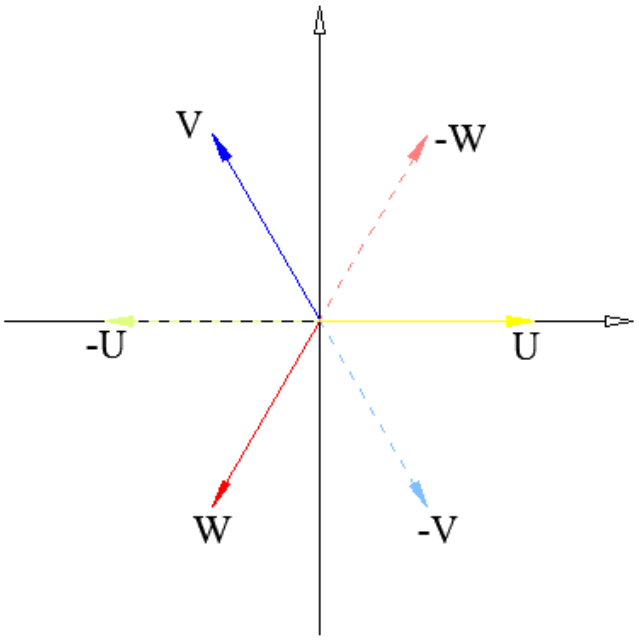

FIG. 4.8. The phase diagram for the six phases winding for the updated CTMFP magnets. The phase shift is 60 ºfor the neighbouring phases.

TABLE 4.3
THE DIFFERENCES BETWEEN THE ORIGINAL AND UPDATED CTMFP MAGNETS

	Diameter of the phase windings (mm)	Phase width (mm)	Phase number	Name of phases (in sequence)	Phase shift	Number of pole
Original	65.0	5.0	3	U, V, W	120 º	single pole
Updated (Six phase)	70.0	1.25	6	U, -W, V, -U, W, -V	60 º	2 pole-pairs
Updated (Three phase)	70.0	1.25	3	U, V, W	120 º	4 pole-pairs

Fig. 4.9 shows the design of the updated CTMFP magnets. Each of the magnets contains two parts: the phase windings and the dc coil. Like the original CTMFP magnets, the updated CTMFP magnets have two regions: the effective travelling region and the central region. The effective travelling region is the area in which the magnetic wave travels, and the central region is the area where the magnetic field oscillates but does not travel. The YBCO sample was inserted in the centre of the device during experiments, as illustrated in Fig. 4.9. The Hall sensors were installed above the surface of the YBCO sample in order to measure the magnetic field. The geometry of the updated CTMFP magnets is shown in Fig. 4.10.

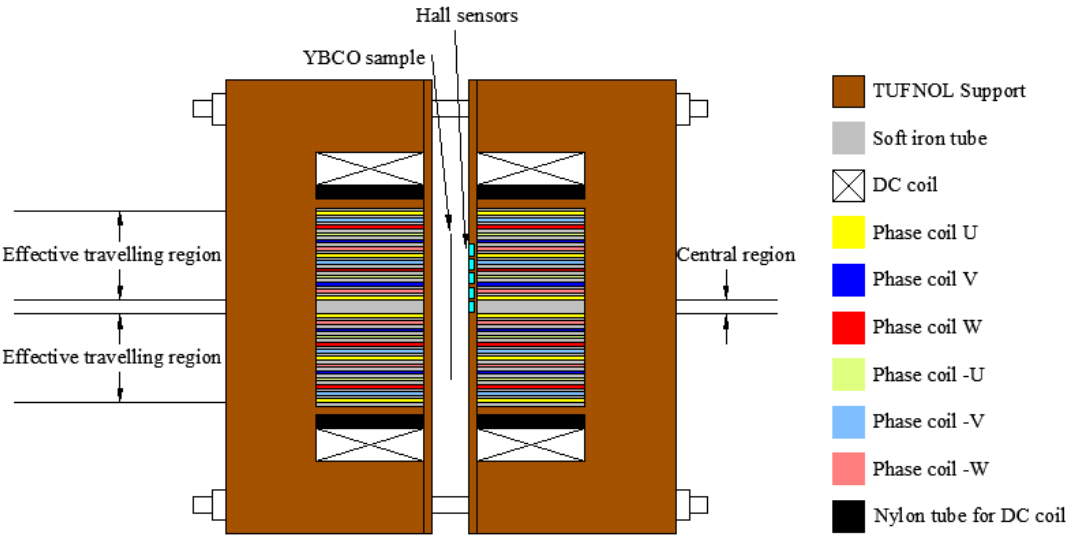

FIG. 4.9. The updated CTMFP magnets design. Each CTMFP magnet contains a phase winding and a dc coil. The two magnets are completely symmetrical, which is ensured by the TUFNOL support.

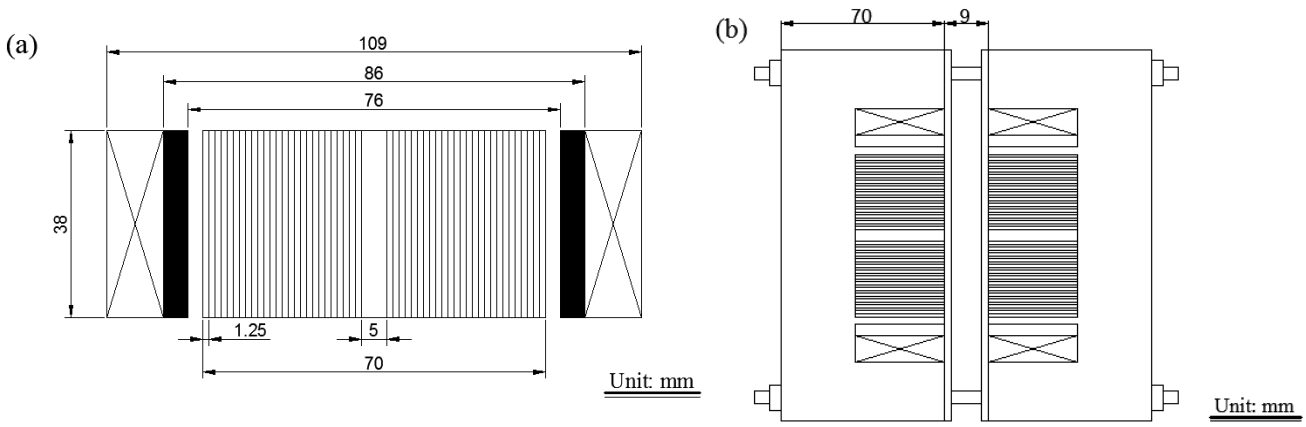

FIG. 4.10. The designed geometry for the updated CTMFP magnets.

Accuracy of the geometry was very important for the updated CTMFP magnets, since the width of the phase windings and the iron yoke is very small (1.25 mm). This problem could reasonably be ignored in the original CTMFP magnets since the width of the phase windings and the iron yoke was relatively large (5.0 mm). A misshaped phase winding or electric iron winding would not have changed the magnetic waveform in the original CTMFP magnets, however, for the updated CTMFP magnets, it was necessary to strictly control the geometry of the phase windings and the iron yoke since even a slightly misshapen geometry or asymmetry of the two magnets could lead to a change in the magnetic profile. In order to avoid this problem, the iron tubes for phase windings were machined from soft iron instead of using electric iron laminations. Soft iron cylinders were purchased, and then machined using a Lathe. Fig. 4.11 shows the machined soft iron tubes ready for coil winding. There were 14 tubes for each of the updated CTMFP magnets. The smallest is a solid cylinder with a diameter of 5.0 mm. The centre was threaded for the convenience of coil windings. The outer diameters of the other 13 tubes were 10 mm, 15 mm, 20 mm …65 mm, and 70 mm. The inner diameters were: 7.5 mm, 12.5 mm, 17.5 mm …62.5 mm, and 67.5 mm.

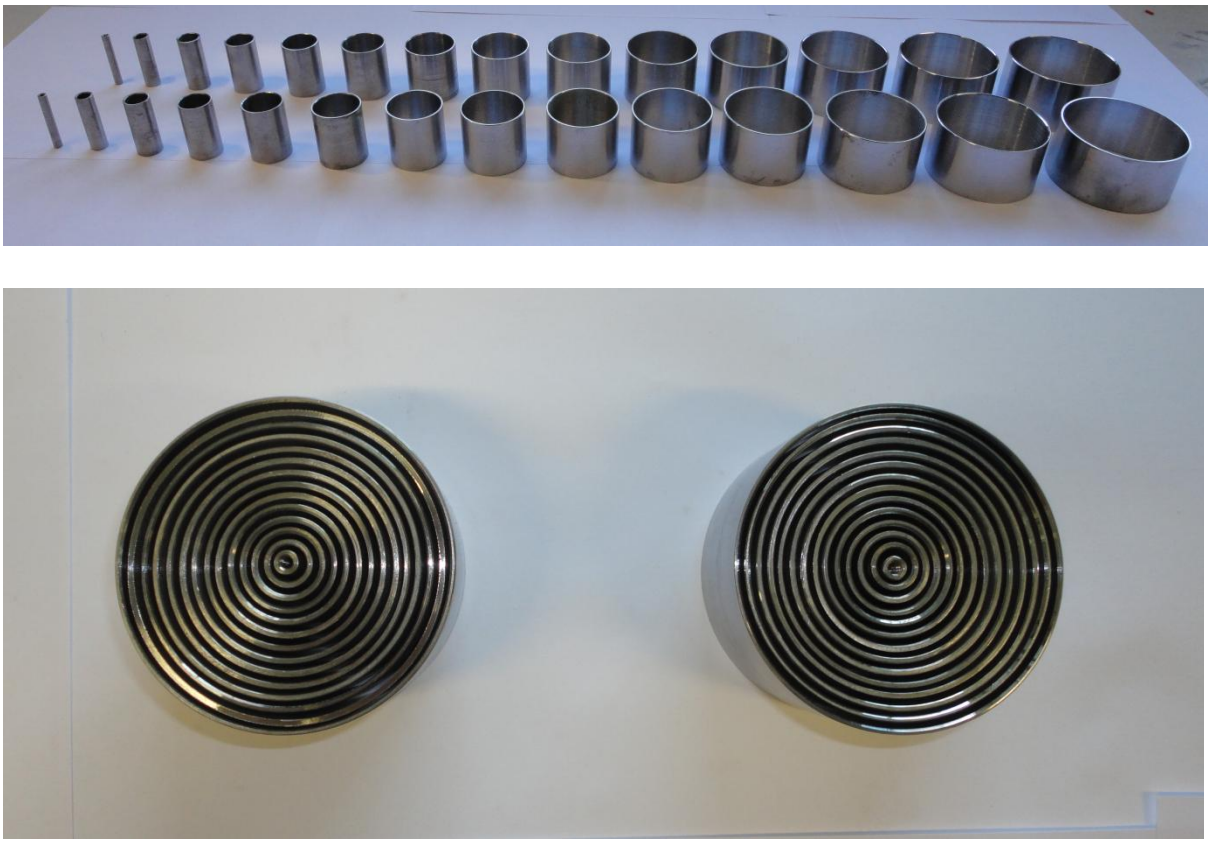

FIG. 4.11. The soft iron tubes machined from soft iron cylinders.

4.3.2 Build of the magnet

In order to ensure that the phase windings of the two magnets were perfectly aligned after installation in the TUFNOL support, the dc coils were separated from the phase winding and wound onto a nylon tube. Fig. 4.9 and Fig. 4.10 show that the inner diameter of the nylon tube was slightly larger than the phase windings. The gap between the nylon tube and the phase winding was supported by the TUFNOL. This design ensured that the phase windings of the two CTMFP magnets were aligned after installation, as shown in Fig. 4.9. Fig. 4.12 shows the updated CTMFP magnets installed on the TUFNOL support according to the design shown in Fig. 4.9 and Fig. 4.10.

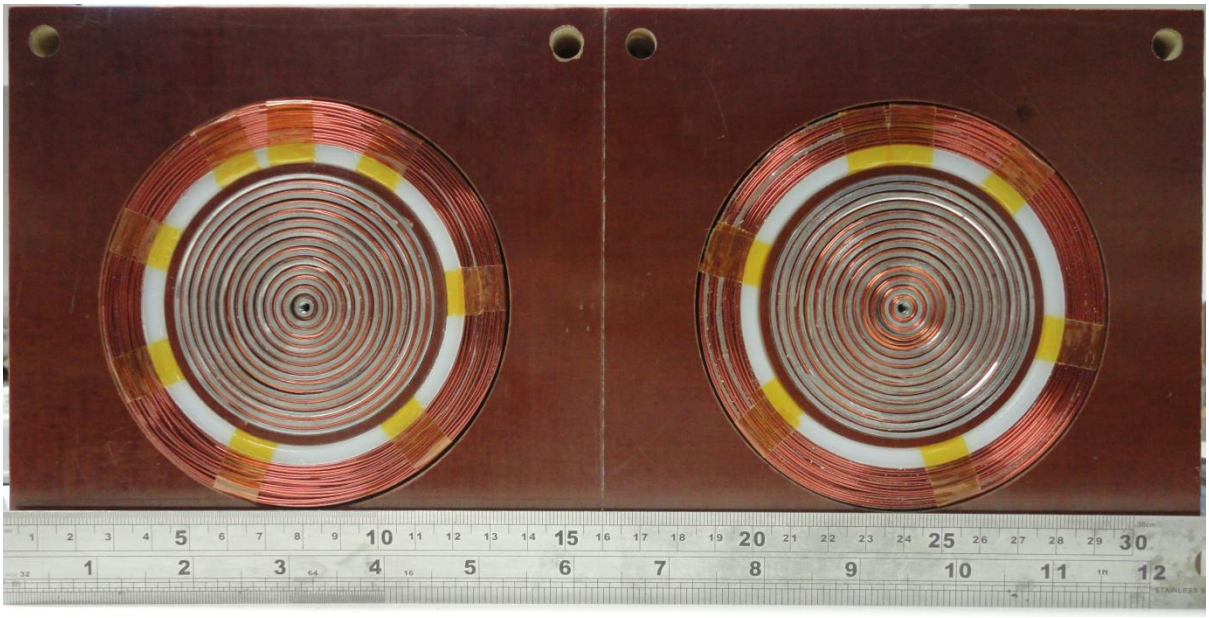

FIG. 4.12. The two updated CTMFP magnets on the TUFNOL support as designed from Fig. 4.9 and Fig. 4.10.

After the phase windings and the dc coils were connected, the resistances and inductances of the windings were measured. The results are shown in Table 4.4. Compared to the original CTMFP magnets shown in Table 4.1, the resistances and inductances of the phase windings were effectively balanced. Each phase was also connected using a 300 Ω power resistor. This helped to balance the phase current, as discussed in Section 4.2.2.

TABLE 4.4
PROPERTIES OF THE CONNECTED WINDINGS

Phase	Resistance 300 K (connected)	Resistance 77 K (connected)	Inductance (connected)
U (-U)*	13.3 Ω	2.2 Ω	19.78 mH
V (-V)	11.4 Ω	1.9 Ω	16.51 mH
W (-W)	10.0 Ω	1.8 Ω	12.05 mH
DC	45.4 Ω	5.0 Ω	

* Phase U and phase –U are connected in series.

4.4 Power supplies for wire windings.

The power supplies for the wire windings included a three phase inverter and a dc power supply. The three phase inverter was purchased from OMRON, model MX-2. The rated power was 0.75 kW. The out frequency could be varied from 0.1 Hz to 400 Hz (in normal mode) or to 1000 Hz (high frequency mode). The rated output voltage was 230 V, and the rated output current was 5.0 A. The experiment used the "Free V/F Control", which defines the voltage-frequency relationship for the convenience of the user.

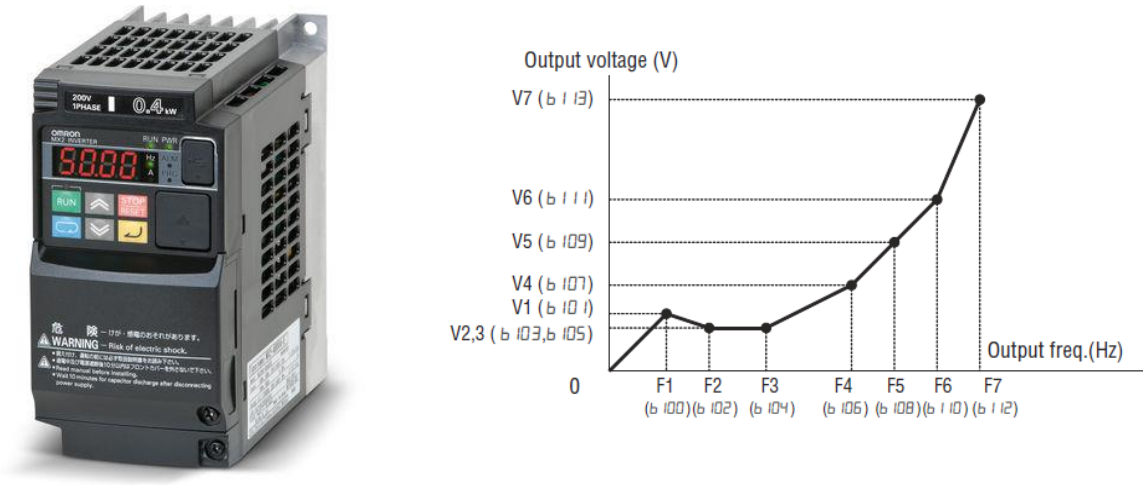

FIG. 4.13. The figure on the left shows the picture of a OMRON inverter, mode MX-2. The figure on the right shows the "Free V/F Control".

The dc power supply was a variable dc voltage source. The maximum output current was 10 A, and the maximum output voltage was 30 V.

4.5 Measurement system

4.5.1 Hall sensors

Two types of Hall sensors were used for measurement. One was the model HZ-312C and the other was HZ-116C. Both were made by Asahi Kasei Microdevices Corp. The model HZ-312C was used to measure the magnetic field for the original CTMFP system, while the model HZ-116C was used for the updated CTMFP system. Fig. 4.14 shows a photo and the geometry of the model HZ-312C. Fig.4.15 shows the photo and geometry of the model HZ-116C. For the original CTMFP system, either a single HZ-312C Hall sensor installed in the middle of the device was used, or six HZ-312C Hall sensors were used to build a Hall sensor array. The single Hall sensor was used to measure the change of magnetic field in the middle of the sample, while the six Hall sensor array was used to measure the change in magnetic gradient across the sample. Fig.4.16 shows the six Hall sensor array and its relative position above the 2 inch YBCO sample (as discussed in a later section).

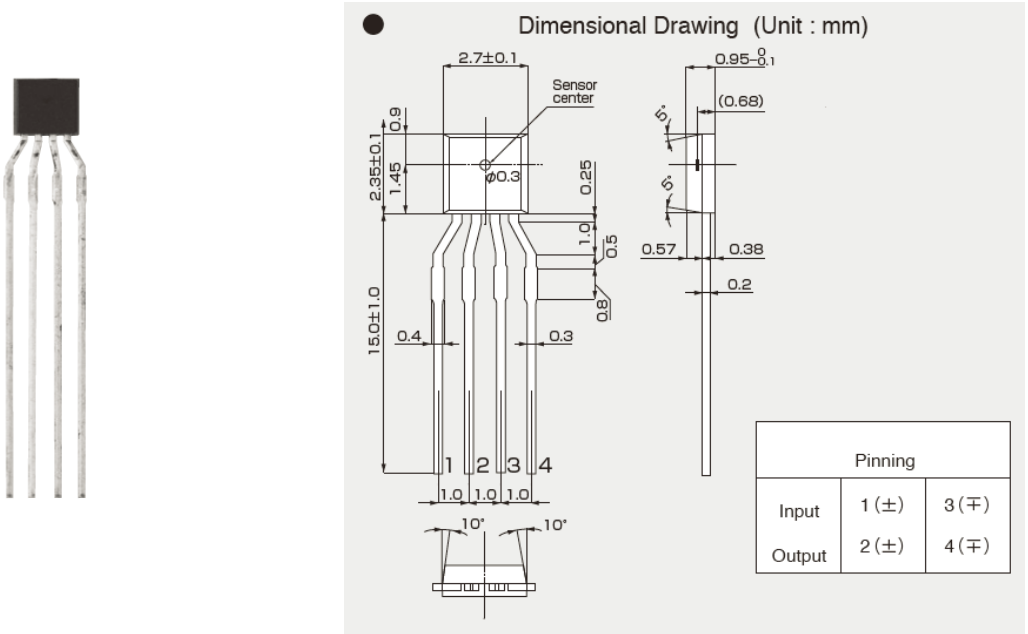

FIG. 4.14. The model HZ-312C from Asahi Kasei Microdevices which was used for measurement of the original CTMFP system [127].

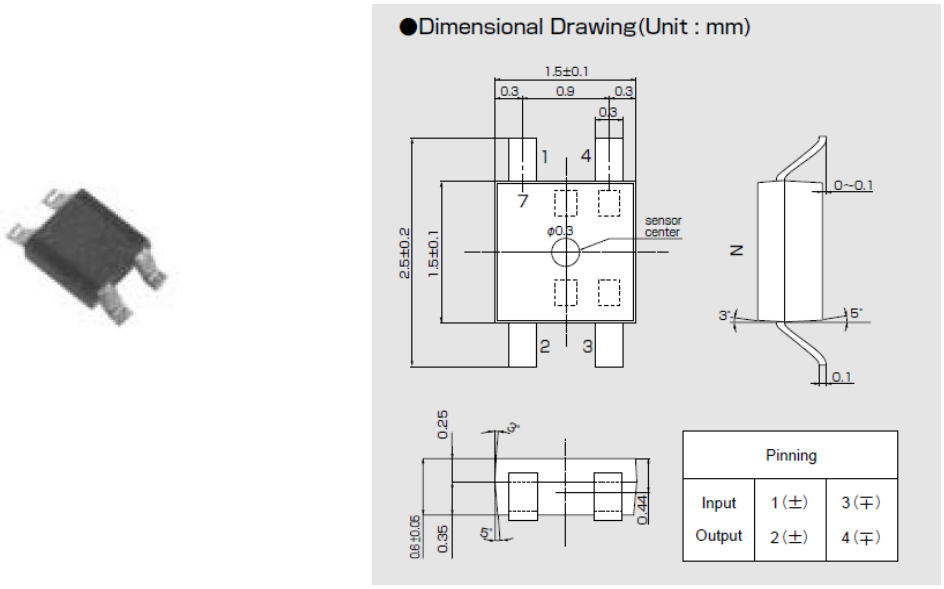

FIG. 4.15. The model HZ-116C from Asahi Kasei Microdevices which was used for measurement of the updated CTMFP system.

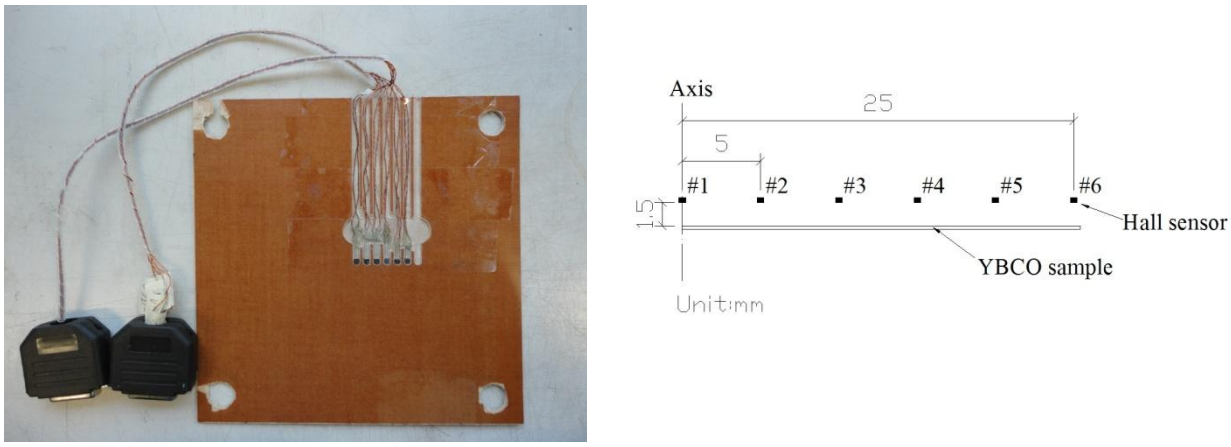

FIG. 4.16. The six Hall sensor arrays installed on the TUFNOL plate (left figure) and their relative positions above the 2 inch diameter YBCO sample (right figure). The Hall sensors were the model HZ-312C from Asahi Kasei Microdevices. This Hall sensors array was only used for the measurement of the original CTMFP system.

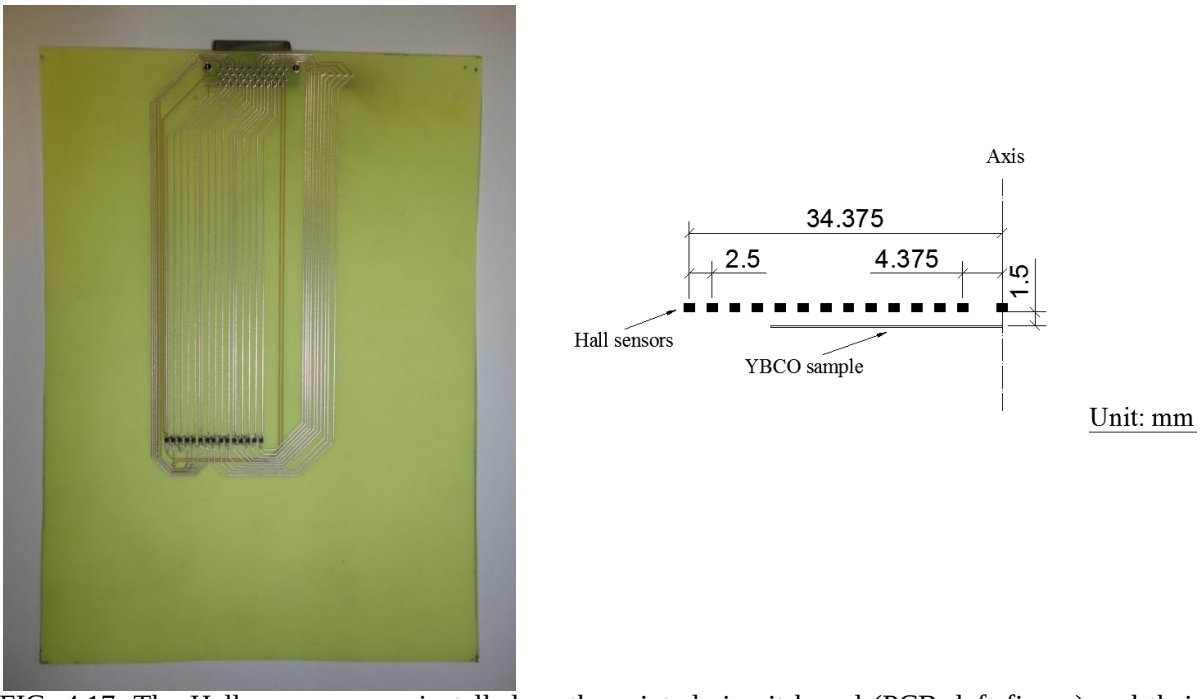

FIG. 4.17. The Hall sensors array installed on the printed circuit board (PCB, left figure) and their relative positions above the YBCO sample (right figure). The YBCO sample was either a 2 inch diameter disc or a square shaped YBCO sample, as discussed in a later section). The Hall sensors are the model HZ-116C from Asahi Kasei Microdevices. This Hall sensor array was used for measurement of the updated CTMFP system.

The Hall sensor HZ-312C was calibrated individually as demonstrated in Fig.4.18. The gaussmetre was placed on the surface at the centre of the iron rod as shown in Fig. 4.18(a). The solenoid was connected to a dc power supply. The current – magnetic flux density relationship $I_{dc} - B$ was recorded as the current I_{dc} increased from zero to a certain value. In the second step, the Hall sensor was placed at the same position as the gaussmeter. The Hall sensor was powered using a constant current supply set to 5 mA. The Hall voltage V_h was measured using a voltmeter. The carrier velocity inside the Hall sensor can be different at different temperature, therefore, in order to calibrate correctly, the Hall sensor should be cooled down to 77 K. Since the Hall sensor has a very small mass and thereby a small heat capacity, the cooling could be simplified by pouring a small amount of liquid nitrogen onto the Hall sensor during the measurement, as shown in Fig. 4.18(b). The measured Hall voltage ΔV_h increases (increase of the carrier velocity inside the Hall sensor) and stabilises in a short period of time (over several seconds), and thereafter, the stabilised Hall voltage ΔV_h was recorded as a function of I_{dc}. It is not recommended to pour too much liquid nitrogen during calibration, since it might also lower the temperature of the iron rod and the dc coil, which would increase the iron permeability and decrease the resistance of the coil.

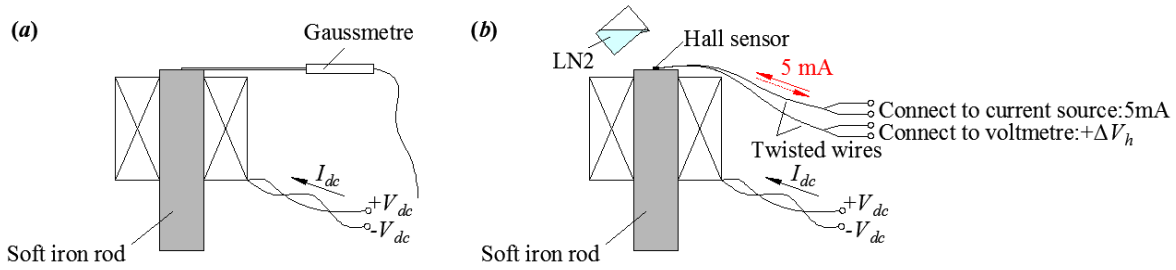

FIG. 4.18. Demonstration of the calibration of Hall sensors HZ-312C model.

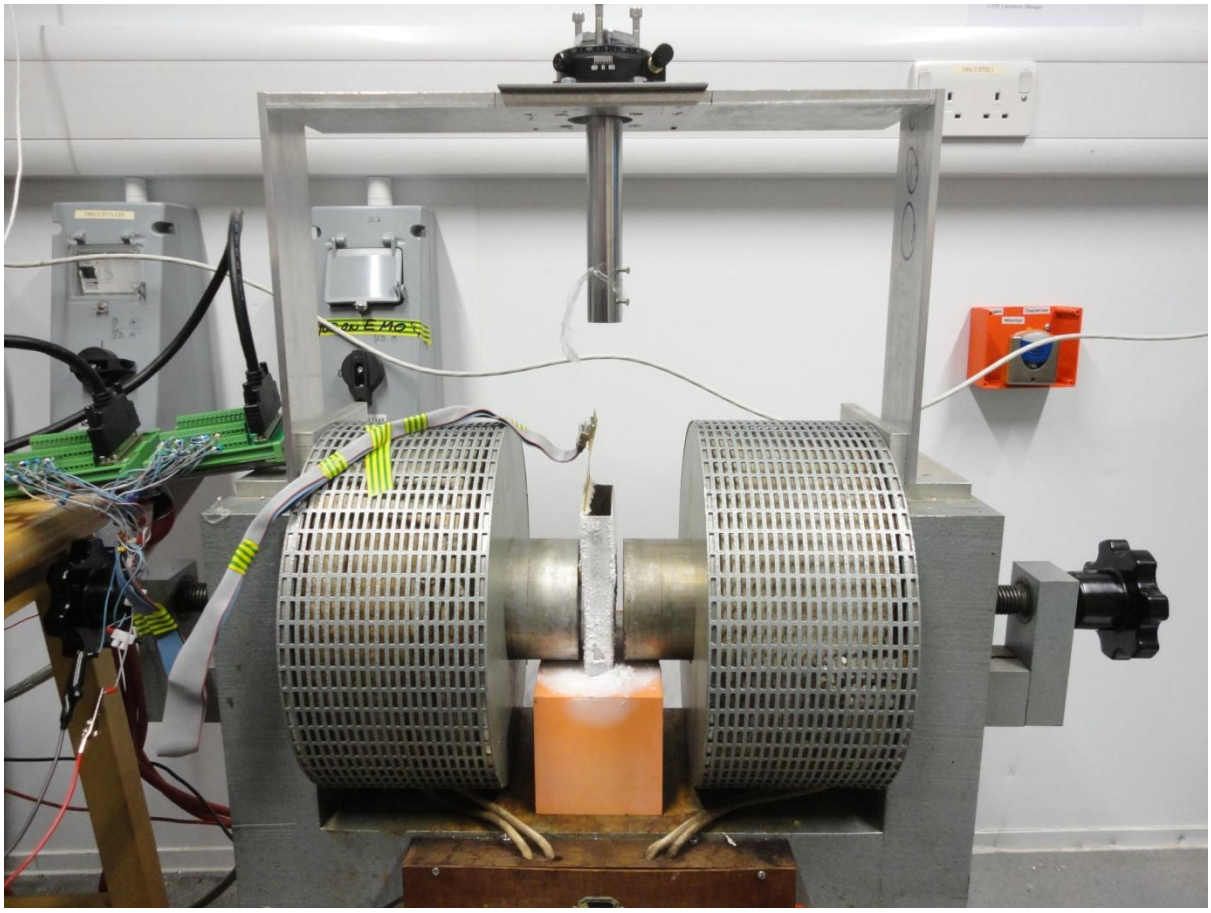

FIG. 4.19. Calibrating the Hall sensor array on the PCB, as shown in Fig.4.17. The PCB was pasted to a non-magnetic container then inserted into the gap in the dc magnet.

The Hall sensor array on the PCB was calibrated using a different method than that shown in Fig. 4.18. As shown in Fig.4.19, the PCB was pasted inside a non-magnetic container using Kapton tape, then inserted into the gap in the dc magnet. The field within the gap of the dc magnet was homogeneous. During calibration, the container was filled with liquid nitrogen.

After measurements were taken, as shown in Fig. 4.18 and Fig.4.19, the relationship between the magnetic flux density B and the Hall voltage V_h was obtained. An example of the B-V_h relationship is shown in Fig. 4.20. The Hall sensor responds differently at different calibration temperatures. For the same applied magnetic field, a lower temperature produces a higher Hall voltage. For one particular Hall sensor as shown in Fig. 4.12, the slope at 300 K was 1.816 mT/V while for 77 K the slope was 1.709 mT/V.

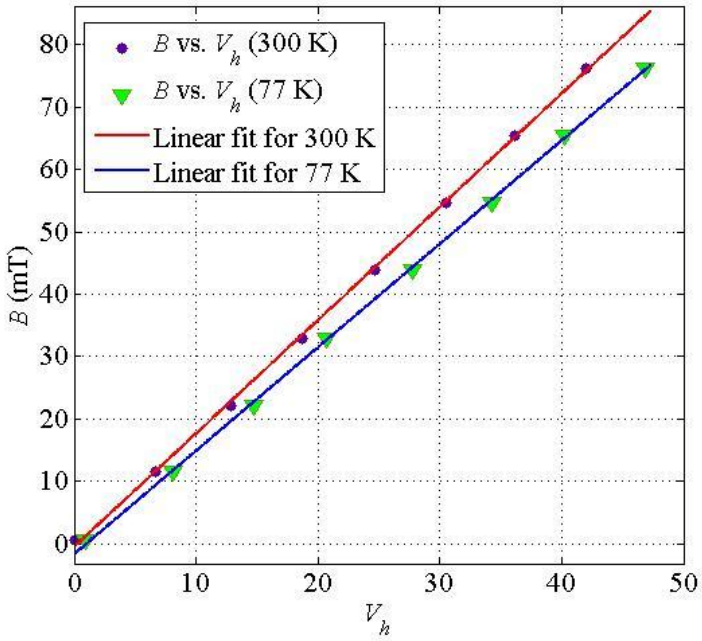

FIG. 4.20. The B-V_h relationship obtained from one of the HZ-312C Hall sensors at two different temperatures: 300 K and 77 K.

4.5.2 Data acquisition

For the original CTMFP, either a single Hall sensor or six Hall sensors (Fig. 4.16) were used. For the single Hall sensor measurement, a single channel data acquisition was needed, while for the six Hall sensor measurement, multi-channel data acquisition was required. The device used for the single channel data acquisition was an Agilent Multimeter 34401a, and the device for the multi-channel data acquisition was an Agilent U2353A. For the single channel Agilent Multimeter 34401a, the data was transferred to the computer using a GPIB-USB interface. For the multi-channel Agilent U2353A, the data was transferred to the computer using a USB2.0 cable.

FIG.4.21. The voltmeter used for measurement and data-acquisition of the Hall voltage. The figure on the left is the single channel Agilent Multimeter 34401a and the figure on the right is the multi-channel voltmeter Agilent U2353A.

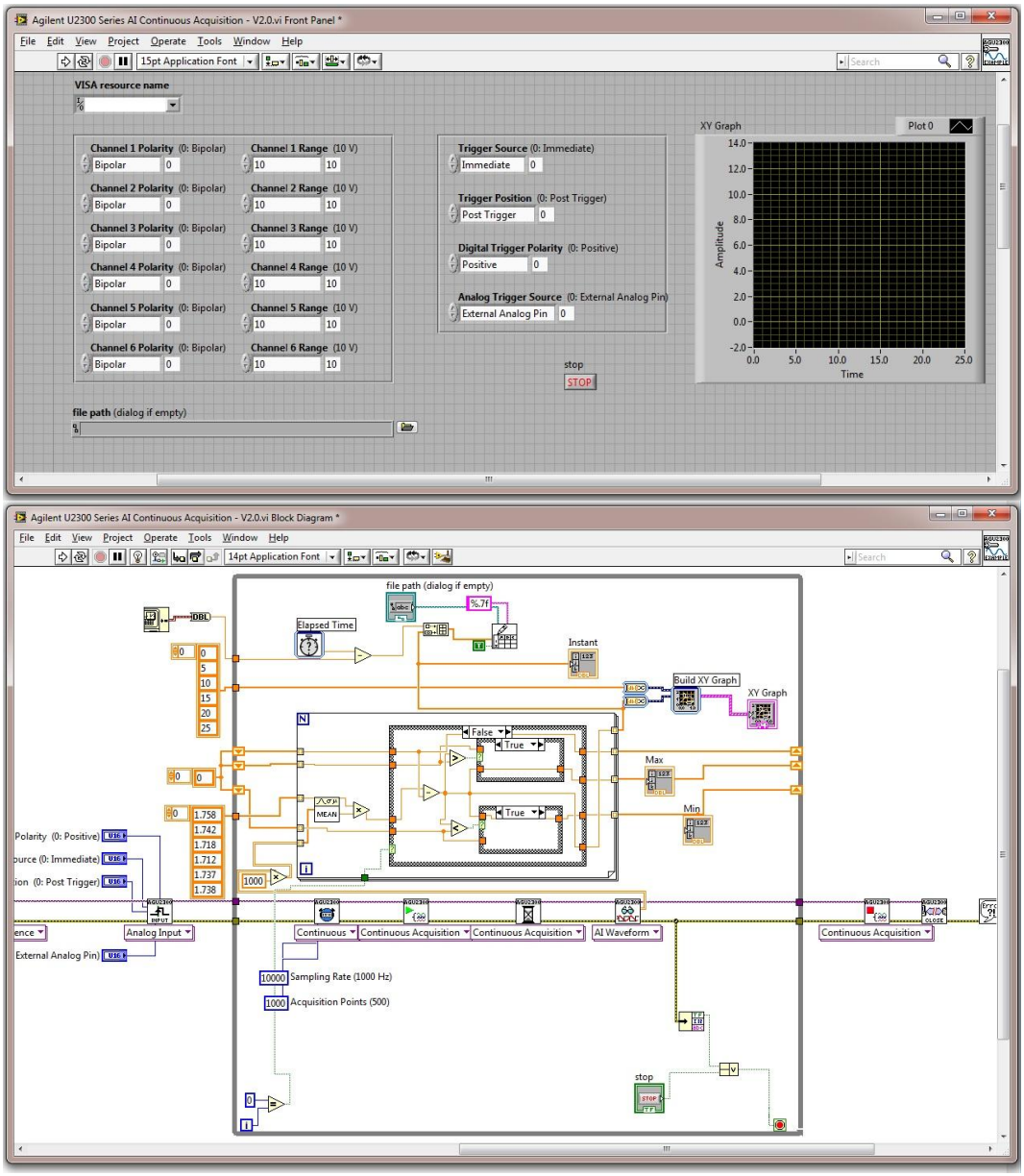

FIG. 4.22. The Labview program for the multi-channel Agilent U2353A used to measure the six Hall sensor array.

After the data transferred to the computer, it was processed using a Labview program. The Labview program calculated the strength of the magnetic field from the measured voltage, displayed the values on the screen and recorded them to the hard disk. Fig. 4.22 shows an example of the Labview program for the multi-channel Agilent U2353A used to measure the six Hall sensor array. The top figure of Fig. 4.22 is the interface of the Labview program, and the bottom figure is the program used for data processing (the only part shown).

4.6 YBCO samples

There were two types of YBCO sample used in the experiment. The first type was a 2 inch diameter round YBCO thin film provided by Ceraco Ceramic Coating GmbH, Germany. The second type was a 46 mm square YBCO tape provided by American Superconductor Corp and Francis Bitter Magnet Lab, MIT.

4.6.1 Round shape thin film

The 2 inch diameter $YBa_2Cu_3O_{7-\delta}$ thin film was provided by Ceraco Ceramic Coating GmbH, Germany. The thickness of the YBCO layer was 200 nm. The YBCO layer was deposited onto a 2 inch diameter Al_2O_3 wafer. The critical temperature T_C of the YBCO sample was 87.0 K. In order to protect the YBCO layer from humidity, a 60 nm thick Au layer was deposited on the top of the YBCO layer in a vacuum evaporator. Fig. 4.23 shows the YBCO sample before and after gold deposition. Fig. 4.24 shows the measured geometry of the YBCO sample.

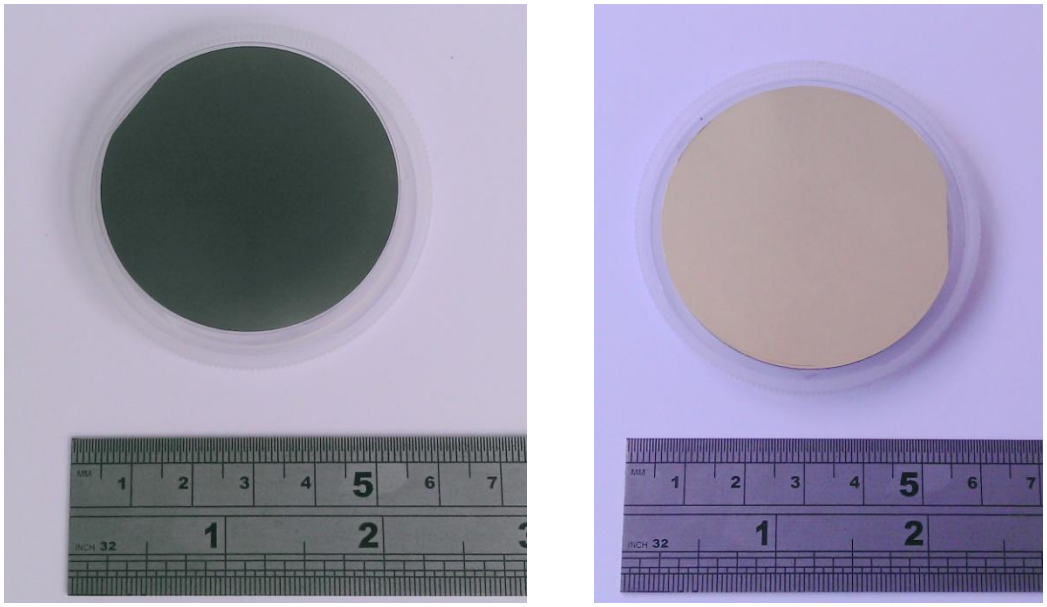

FIG. 4.23. $YBa_2Cu_3O_{7-\delta}$ thin film before (left) and after (right) gold deposition. The YBCO layer was deposited onto a 2 inch diameter Al_2O_3 wafer. The thickness of the YBCO layer was 200 nm, and the thickness of the gold layer was 60 nm. The sample was provided by Ceraco Ceramic Coating GmbH, Germany.

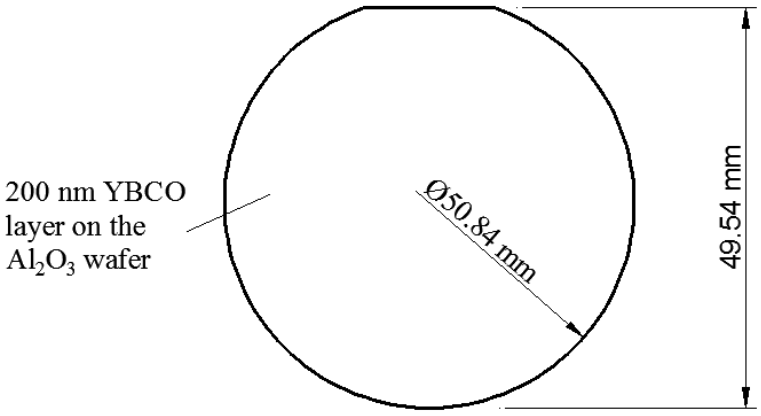

FIG. 4.24. The geometry of the 2 inch diameter YBCO sample.

In order to protect the YBCO sample from scratches during the experiment, a TUFNOL sample holder was designed and machined. Fig. 4.25 shows the design of the recess inside the 3 mm thick TUFNOL plate. The design sealed the YBCO sample inside a recess in a 3 mm thick TUFNOL plate. Fig 4.25 shows the YBCO layer facing down in the recess so that the YBCO layer does not come into direct contact with the TUFNOL plate. A very small edge was left to support the sample. This design

protected the YBCO layer during the experiment. A TUFNOL plate 1 mm thick was used to cover the top of the sample, and the surroundings were sealed using Araldite epoxy to prevent humidity from penetrating the chamber. As shown in Fig. 4.5, the distance from the centre of the CTMFP magnet to the bottom surface of the TUFNOL support was 80 mm. In order to make sure that the sample centre was aligned with the centre of the magnet, the distance from the centre of the sample to the bottom surface of the holder was also be 80 mm as illustrated in Fig. 4.26. Fig. 4.26(a) shows the geometric design of the sample holder and Fig. 4.26(b) shows the sample holder with the YBCO sample sealed inside.

After the YBCO sample was sealed inside the sample holder as shown in Fig. 4.26, the sample could be guaranteed to be free of humidity and scratches, and was ready to be slotted into the gap between the CTMFP magnets.

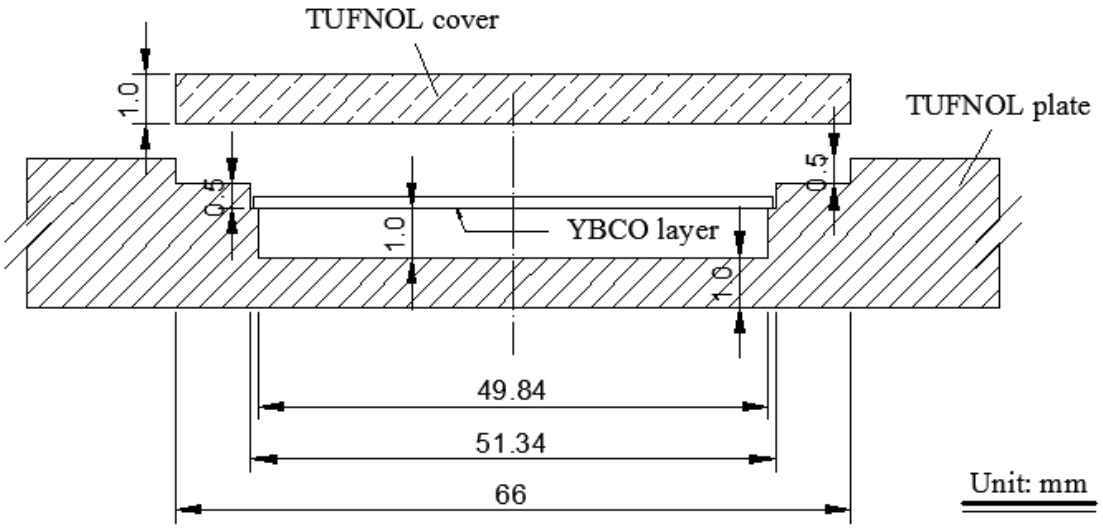

FIG. 4.25. The geometric design of the TUFNOL holder for the YBCO sample.

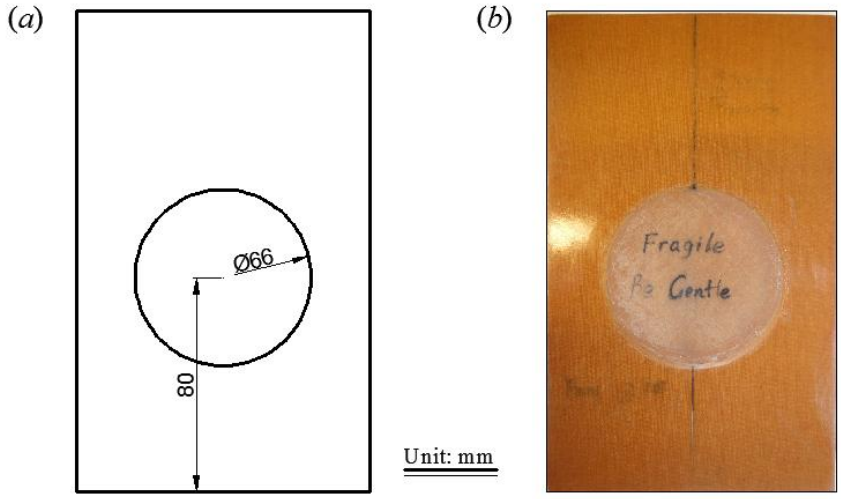

FIG. 4.26. (a) the geometric design of the 2 inch diameter YBCO sample holder; (b) the sample holder with YBCO sample sealed inside.

4.6.2 Square shaped YBCO sample

Another YBCO sample investigated in the experiment was a square shaped YBCO sample with a hole through the centre. Ten identical samples were borrowed from Francis Bitter Magnet Laboratory (FBML), MIT and American Superconductor (AMSC) Corp. Since 2009, MIT built a series of annuli NMR magnets using a stack of these YBCO plates produced by AMSC [1, 128, 129]. Two types of square shape YBCO sample were used for their annuli magnets. The first type had dimensions of 40 mm × 40 mm, and the other had dimensions of 46 mm × 46 mm. The samples were cut from standard wide tapes manufactured by AMSC using the rolling assisted Bi-axially textured substrate (RABiTS) method. Hahn et al. assembled 500 pieces of 40 mm × 40 mm YBCO thin plate to build the first annuli magnet YP500 [1]. At 77 K, a single plate can have a trap field of 22.1 mT, while the assembled YP500 can have a maximum trap field of 0.18 T [1]. The model YP750 which uses 750 pieces of 40 mm × 40 mm YBCO plates was built in 2011, with peak trapped fields of 0.42 T at 77 K [130]. The model YP2800 was built in 2012 using 850 pieces of 40 mm × 40 mm YBCO plates and 1950 pieces of 46 mm × 46 mm YBCO plates, to produce a peak centre field at 77 K of 0.64 T [131, 132].

Ten pieces of square shaped YBCO plates were borrowed from FBML and MIT. These were 46 mm × 46 mm plates with a 26 mm diameter hole through the middle. Fig. 4.27 shows a photo of the ten pieces of YBCO plate, with their dimensions drawn to the right of the figure. Table 4.5 lists the properties of the sample [1].

Since the square shapes YBCO sample is covered by the substrate and the YBCO layer is not exposed to the air, it is not necessary to seal the sample inside a sample holder, as was needed for the round shaped YBCO sample in Fig. 4.26. However, for the convenience of the experiment, we designed and machined a sample holder for the YBCO plates. The sample holder has to be able to hold the YBCO samples either singly or in multiple layers. For the multi-layer experiment, it was necessary to be able to rotate the sample by 45 ° as suggested by Kim [133], in order to reduce the field inhomogeneity. Fig. 4.28 shows the geometric design and the machined sample holder. The sample holder was made of 3 mm thick TUFNOL plate. As shown in Fig. 4.28, a recess was machined into a 3 mm thick TUFNOL plate to hold the YBCO plates either horizontally or rotated by 45 º. Another TUFNOL ring was machined with an inner diameter slightly smaller than the outer diameter of the circle on the TUFNUL plate, so that the TUFNUL ring can clamp onto the TUFNUL plate to prevent the YBCO samples falling out of the recess.

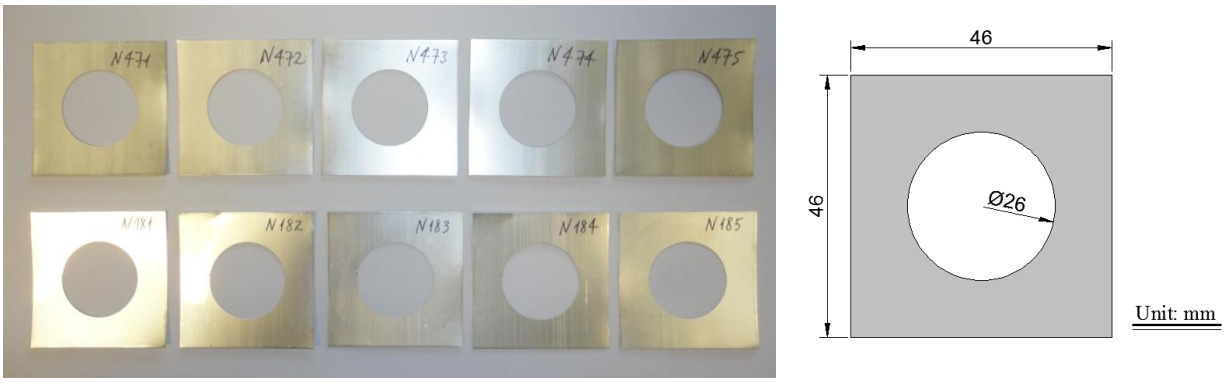

FIG. 4.27. The photo (left) of the ten pieces of YBCO plate and their dimensions (right).

TABLE 4.5
PROPERTIES OF THE SQUARE SHAPED YBCO SAMPLES [1]

Parameter	Unit	Value
Material		YBCO
Manufacturer		AMSC
Width × Length	[mm]	46 × 46
Centre hole inner diameter	[mm]	26
Overall thickness	[μm]	80
YBCO layer thickness	[μm]	0.8
Nickel substrate thickness	[μm]	75
J_C of YBCO @ 77 K, 0.2 T	[MA/cm^2]	0.2 – 0.6

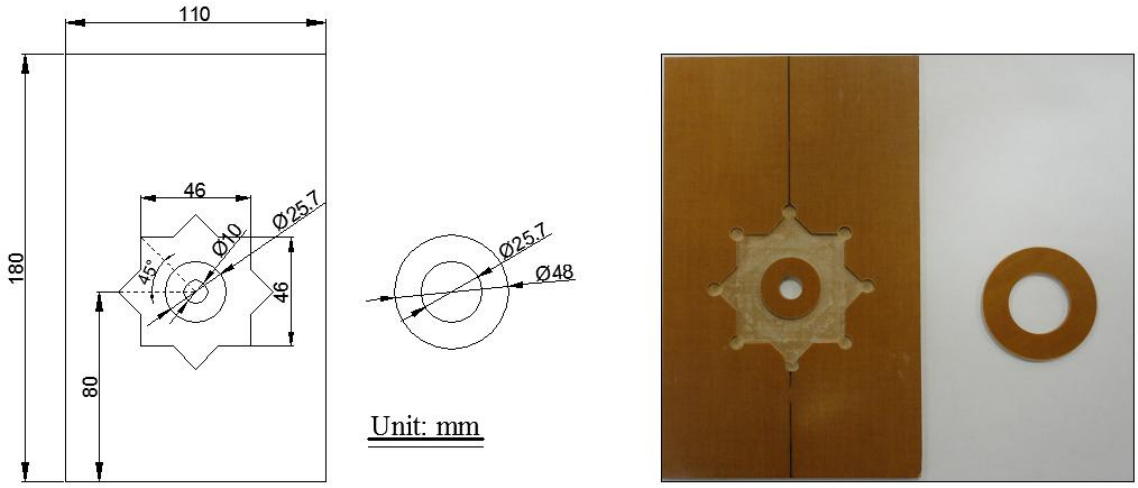

FIG. 4.28. (a) The geometric design of the sample holder for square shape YBCO samples; (b) the machined TUFNOL holder of 3 mm thick for the square shape YBCO samples.

4.7 System integration

The whole experimental system included:

1. CTMFP magnet: either the original CTMFP magnet or the updated CTMFP magnet;
2. YBCO sample: either round shape or square shape;
3. Power sources for the three phase coils, the dc coils and the Hall sensors;
4. Data acquisition for either single channel or multi-channel Hall voltages;
5. A computer installed with the Labview program to record experimental data.

Fig. 4.29 shows a schematic of the experimental system using the original CTMFP magnets and single channel data-acquisition equipment, and Fig. 4.30 is a photo of the experimental system. For the single Hall sensor measurement, the single Hall sensor installed in the middle of the CTMFP magnet was be connected to the single channel Microvoltmeter Agilent 34401 a. For multi-channel data acquisition, the Microvoltmeter Agilent 34401a shown in Fig. 4.29 was changed to a multi-channel data acquisition card Agilent U2353A. When experimenting with the updated CTMFP system, the magnets shown in Fig. 4.29 were changed to the updated CTMFP magnet. The YBCO sample shown in Fig. 4.29 was either the round shape YBCO sample or square shape YBCO sample, which were installed inside the 3 mm TUFNUL plate. The magnets and YBCO sample were submerged in liquid nitrogen at 77 K inside a Styrofoam dewar. Two versions of the Labview program were developed. The first version was for the single channel data acquisition, and the second version was for the multi-channel data acquisition.

The whole experiment system was able to perform under several conditions such as zero-field cooling, field-cooling; a travelling wave with differing amplitudes, speeds and directions. Measurements were taken of the centre field (single Hall sensor) or the magnetic gradient (six Hall sensor array). The two different kinds of CTMFP magnet provided information on how the degree of inhomogeneity influences magnetisation, since the updated CTMFP magnets possess a stronger field inhomogeneity. The two kinds of samples (round shaped YBCO and square shaped YBCO) show the difference in magnetisation due to the presence or absence of the hole in the centre. In general, the established experimental system was able to provide extensive details regarding the magnetisation of the YBCO sample under the influence of a travelling wave.

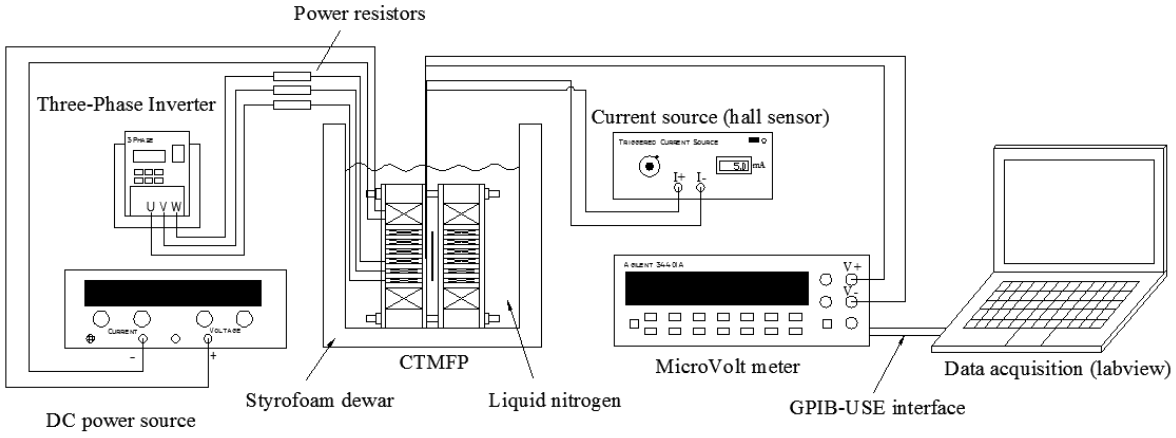

FIG. 4.29. Schematic of the experimental setup. Both the CTMFP and the YBCO thin film are immersed in liquid nitrogen (77 K). The three phase coils are wired to the output of the three phase inverter. The dc coils are connected to a dc power supply. The Hall probe (placed in the centre of the CTMFP coil) is powered by a dc current source. The Hall voltage is read using an Agilent Multimeter 34401a, and the data are calibrated and collected using a computer through a GPIB-USB interface.

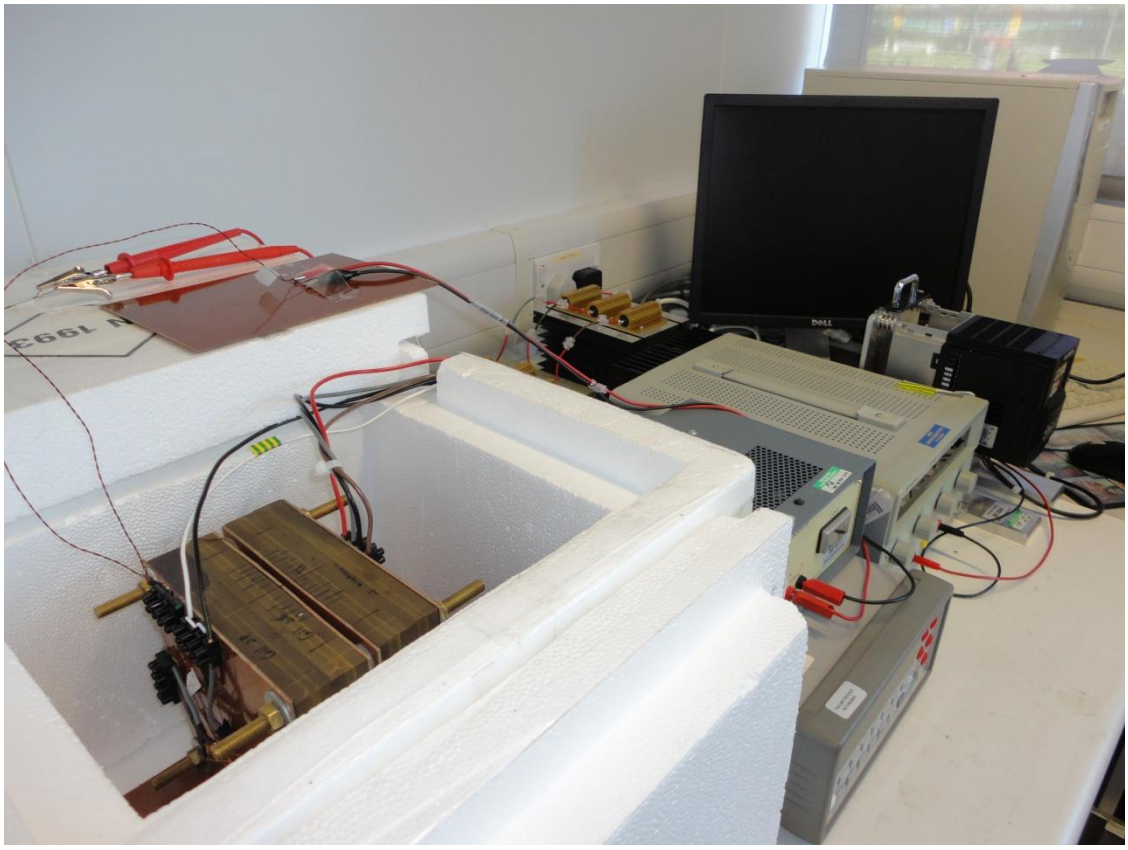

FIG. 4.30. The experimental setup of the CTMFP based on the first generation CTMFP magnet and the single data – acquisition channel.

4.8 Simulation method

The numerical simulation was based on the H-formulation, as proposed by Hong et al. [11, 134-137], to simulate a superconductor with the help of the commercial finite element (FEM) software COMSOL Multiphysics. COMSOL Multiphysics is an equation-based FEM software package which allows users to modify equations. This exempted users from laborious programming of the underlying finite element equations, which can take a long time to accomplish. The simulation to be modelled was the electromagnetic equation in the low frequency region, whilst displacement current in the Maxwell's equation is ignored. The governing equation includes Ampere's law of circulation and Faraday's Law of induction, which is written as:

$$\nabla \times \boldsymbol{H} = \boldsymbol{J} \tag{4.2}$$

$$\nabla \times \boldsymbol{E} = -\frac{\partial \boldsymbol{B}}{\partial t} \tag{4.3}$$

where $\boldsymbol{H}$ is the magnetic field, $\boldsymbol{B}$ is the magnetic flux density, $\boldsymbol{E}$ is the electric field and $\boldsymbol{J}$ is the current density. The displacement current in equation (4.2) is omitted because the experiment is operated at a low frequency.

The two CTMFP magnets are axially symmetric, which suggest that an axial symmetric FEM model is needed to simulate experimental behaviour. Fig. 4.31 shows the basic domains and boundary conditions of the simulation. The magnetic field $\boldsymbol{H}$ and the magnetic flux density $\boldsymbol{B}$ are the only components on the plane as shown in Fig. 4.31, while the current density $\boldsymbol{J}$ and electric field $\boldsymbol{E}$ only have components in or out of the plane (φ - direction). Calculating the H – formulation using the axial symmetric model solves the magnetic field $H = [H_r, H_z]$. In a cylindrical coordinate system, the curl of the magnetic field is expressed as:

$$\nabla \times \boldsymbol{H} = \frac{1}{r}\begin{bmatrix} \boldsymbol{e}_r & r\boldsymbol{e}_\varphi & \boldsymbol{e}_z \\ \dfrac{\partial}{\partial r} & \dfrac{\partial}{\partial \varphi} & \dfrac{\partial}{\partial z} \\ H_r & 0 & H_z \end{bmatrix} = \boldsymbol{e}_\varphi \left(\frac{\partial H_r}{\partial z} - \frac{\partial H_z}{\partial r} \right) \tag{4.4}$$

The relationship between current density $\boldsymbol{J}$ and electric field $\boldsymbol{E}$ is:

$$\boldsymbol{E} = \rho \boldsymbol{J} \tag{4.5}$$

where ρ is the resistivity of the material. Ideally, the resistivity for the air (dielectric) is infinite, and the resistivity for the copper and ferromagnetic materials (iron) follows the linear relationship (Ohm's law), i.e. ρ is equal to a constant. The resistivity for the superconductor follows the *E-J* power relationship which is expressed as:

$$E = E_C \left(\frac{J}{J_C} \right)^n \tag{4.6}$$

where E_C=10^{-4} V/m is the criterion used to determine the critical current density J_C in the four-point measurement. J_C is the critical current density which is a function of temperature, amplitude and angle of magnetic field, however, in the calculation J_C was assumed to be a constant, since the temperature is fixed at 77 K and the field strength only varied over a small range (below 20 mT). n is a value which determines the steepness of the *E-J* relationship. The resistivity for the superconductor is derived from Equation (4.5) as [138]:

$$\rho = \frac{E}{J} = E_C \frac{J^{n-1}}{J_C^n} \tag{4.7}$$

When Equation (4.4) and (4.5) are input into equation (4.2) one has:

$$\boldsymbol{E} = \boldsymbol{e}_{\varphi}\rho\left(\frac{\partial H_r}{\partial z} - \frac{\partial H_z}{\partial r}\right) \tag{4.8}$$

Taking the curl of equation (4.8):

$$\nabla \times \boldsymbol{E} = \frac{1}{r}\begin{vmatrix} \boldsymbol{e}_r & r\boldsymbol{e}_{\varphi} & \boldsymbol{e}_z \\ \frac{\partial}{\partial r} & \frac{\partial}{\partial \varphi} & \frac{\partial}{\partial z} \\ 0 & r\rho\left(\frac{\partial H_r}{\partial z} - \frac{\partial H_z}{\partial r}\right) & 0 \end{vmatrix} = -\boldsymbol{e}_r\rho\left(\frac{\partial^2 H_r}{\partial z^2} - \frac{\partial^2 H_z}{\partial r \partial z}\right) + \boldsymbol{e}_z \frac{1}{r}\frac{\partial}{\partial r}\left[r\rho\left(\frac{\partial H_r}{\partial z} - \frac{\partial H_z}{\partial r}\right)\right] \tag{4.9}$$

The relationship between the magnetic field $\boldsymbol{H}$ and magnetic flux density $\boldsymbol{B}$ is:

$$\boldsymbol{B} = \mu_0 \mu_r \boldsymbol{H} \tag{4.10}$$

where μ_0 is the permeability in free space, and is equal to $4\pi\times10^{-7}$ H/m, μ_r is the relative permeability which is equal to 1.0 for air, copper and the superconductor, but equal to a large value for ferromagnetic materials.

Substituting equations (4.9) and (4.10) into equation (4.3) gives:

$$\begin{pmatrix} -\frac{\partial^2 H_r}{\partial z^2} + \frac{\partial^2 H_z}{\partial r \partial z} \\ \frac{1}{r}\frac{\partial}{\partial r}\left[r\rho\left(\frac{\partial H_r}{\partial z} - \frac{\partial H_z}{\partial r}\right)\right] \end{pmatrix} = -\mu_0\mu_r \begin{pmatrix} \frac{\partial H_r}{\partial t} \\ \frac{\partial H_z}{\partial t} \end{pmatrix} \tag{4.11}$$

which is the governing equation for the H-formulation in a cylindrical coordinate system.

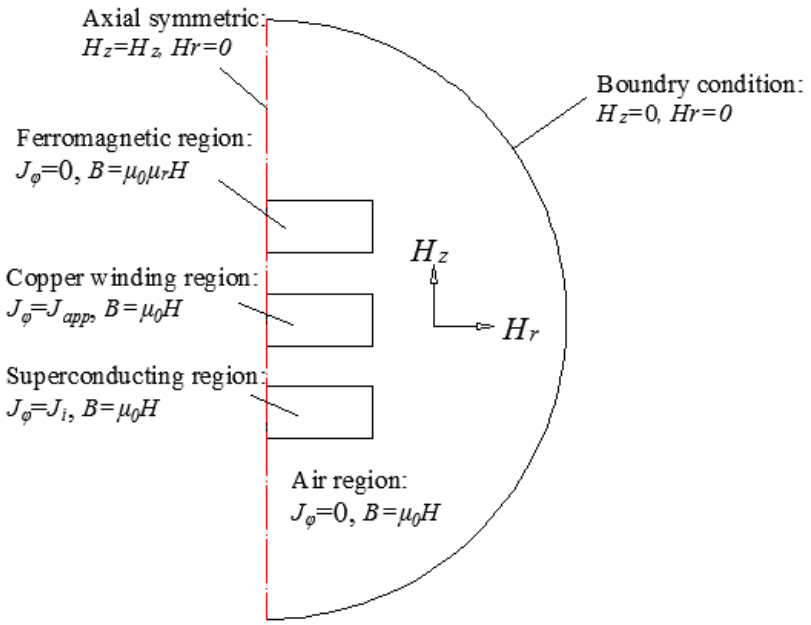

FIG. 4.31. The variables in each domain and boundary in the PDE mode cylindrical coordinate system.

In order to solve the FEM model, the boundary conditions must also be set. Since the axial symmetric model was used, there is an axial boundary as shown in Fig.4.31. In the model, the boundary condition for the axial boundary is:

$$\begin{pmatrix} H_r \\ H_z \end{pmatrix} = \begin{pmatrix} 0 \\ H_z \end{pmatrix} \tag{4.12}$$

In Equation (4.12), H_r=0 shows that the boundary condition is axially symmetric; H_z=H_z shows that the value of H_z is based on the solution of the FEM model. The boundary condition of the half circle is set to zero as shown in Fig. 4.31. The boundary conditions for all internal boundaries are set to be continuous.

In order to apply the current in the copper windings, the current within the copper region was integrated and equalised to a function. From Equation (4.4):

$$J_\varphi = \frac{\partial H_r}{\partial z} - \frac{\partial H_z}{\partial r} \tag{4.13}$$

Integrating Equation (4.13) in the copper region and setting it to a preset function for an applied current:

$$\int_S J_\varphi dS = f(t) \tag{4.14}$$

Thereby, the current is applied in the copper windings which generates the applied field in the FEM model.

4.9 Conclusion

This chapter has introduced the experimental system for the circular type magnetic flux pump, and a numerical method using the FEM software COMSOL Multiphysics. Two different CTMFP magnets have been designed and built, using the original CTMFP magnets and the updated CTMFP magnets. Both designs can produce an annular shape travelling wave, however the updated CTMFP has a stronger field inhomogeneity than the original CTMFP. The wavelength of the updated CTMFP magnets in six phase connection is half that of the original CTMFP magnets. The original CTMFP produces a single pole during the operation while the updated CTMFP produces two pole pairs for six phase connection, and four pole pairs for three phase connection.

To measure the magnetic field, either a single Hall sensor or a Hall sensor array was used during the experiment. The single Hall sensor was installed in the centre of the CTMFP magnet and was connected to the single channel Microvoltmeter Agilent 34401a. The Hall sensor array was connected to the multi-channel data acquisition device Agilent U2353A. The single Hall sensor measured the change of magnetic field at the centre of the sample, and the Hall sensor array measured the change in magnetic gradient due to the travelling wave. The values of the magnetic field were calibrated and recorded using the Labview program.

There were two different YBCO samples used in the experiment: a 2 inch diameter YBCO thin film, and a square shaped YBCO tape (46 mm×46 mm) with a hole in the centre (ϕ26 mm). The 2 inch diameter YBCO thin film was provided by the Ceraco Ceramic Coating GmbH, Germany. The YBCO layer was 200 nm thick, and a 60 nm Au layer was deposited above it. The sample was sealed inside a TUFNOL sample holder to protect it from humidity and scratches. The square shaped YBCO tapes were provided by American Superconductor Corporation and Francis Bitter Magnet Laboratory, MIT. A sample holder was also designed and built for convenience in the experiment.

The numerical modelling method was based on the H-formulation, and used the commercial FEM software COMSOL Multiphysics. The governing equations used were Ampere's law and Faraday's

law. The model is axially symmetric, and equations were deduced for the model. The *E-J* power law was used for the superconducting regions. Boundary conditions were also introduced.

CHAPTER 5

THE ORIGINAL CTMFP: EXPERIMENTAL RESULTS

This chapter discusses the experimental and simulated results using the original CTMFP magnets. The experiment will be performed on the 2 inch diameter YBCO thin film. The purpose of the study is to find out the effect of travelling wave on the YBCO sample, and comparison will be made between the homogeneous oscillating field. Attempts will be made to "pump" magnetic flux into the sample with the help of the travelling wave. This work not only improves the understanding of type-II superconducting flux pump, but may also help understanding the magnetisation and the ac loss in travelling wave condition.

In order to achieve successful "pumping" of magnetic flux into the sample, two factors should be considered: one is that the travelling wave can efficiently transport the flux in the sample; another is that the magnetic coupling should be present, or the magnetisation is dependent on the travelling direction. The first factor will be observed in the experiment as the travelling wave tends to attenuate the existing magnetic gradient, as will be discussed later. However, the second factor will not be observed in this experiment. Discussion will be provided in the end of this chapter, which leads to the development of the updated CTMFP magnet.

In this chapter, Section 5.1 introduces the characteristics of the annular shaped travelling wave produced by the original CTMFP magnet, and Section 5.2 introduces the properties of the round shape YBCO sample. Section 5.3 compares the magnetisation differences between a travelling wave and a homogeneous oscillating field following ZFC. It will show that the magnetisation based on the travelling wave can be very different from the homogeneous oscillating field: while the magnetisation based on the homogeneous oscillating field can be well predicted by the Bean model, the magnetisation based on the travelling wave cannot. It will also show that the travelling wave is very efficient in transporting the flux inside the sample, as the critical magnetic gradient will be attenuated by the travelling wave. This is ascribed to the local movement of the magnetic flux inside the sample due to the field inhomogeneity. Section 5.4 further discusses the magnetisation profiles under various conditions, such as ZFC, FC and delta-shape. This section provides evidences that the field

inhomogeneity tends to attenuate the existing magnetic gradient in general. Section 5.5 discusses how a travelling wave penetrates the YBCO sample under a null dc background field. It will show that, comparing with the homogeneous oscillating field, it is easier for the travelling wave to penetrate the sample, which supports the idea that the travelling wave is very efficient in transporting the magnetic flux. Section 5.6 discusses the influence of the travelling speed (frequency) and the travelling direction of the wave on the magnetisation in the ZFC condition. It will show that the magnetisation is dependent on the sweep speed of the travelling wave. However, in this experiment, it will show that the magnetisation is independent of the travelling direction, which suggests that the magnetic coupling is not present in the experiment. It might suggest that the field inhomogeneity from the original CTMFP magnet is not strong enough to cause magnetic coupling, which lead to the development of the updated CTMFP magnets as mentioned in the last chapter. Inspired by the unique magnetisation results from the travelling wave, Section 5.7 proposes a special topic on how ac losses are different in a travelling wave, compared to a homogeneous oscillating field. This section can be useful for a better understanding of ac magnetisation losses under travelling wave conditions, such as inside a rotating superconducting electric machine.

5.1 Characteristics of the magnetic wave

Before the original CTMFP magnet was built, the travelling wave generated by the device has been simulated to show its characteristics. The simulation is based on the AC/DC mode in COMSOL. The geometry of the simulation is based on the design shown in Fig. 4.4. Fig. 5.1 is a screen shot of the axial symmetric AC/DC mode in COMSOL for the original CTMFP magnet. The YBCO film is not included in the model. The domain names are labelled in the figure, and their properties are listed in Table. 5.1.

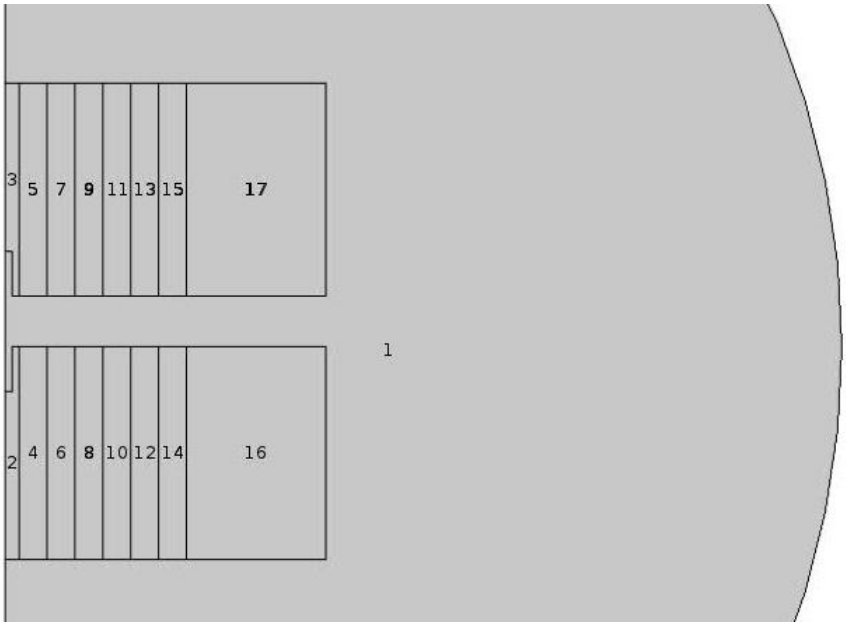

FIG. 5.1. The screen shot of the axial symmetric AC/DC mode in COMSOL for the original CTMFP magnet.

TABLE 5.1
DOMAINS AND PARAMETERS FOR FIG. 5.1

	Air	Soft iron	Silicon iron sheet	Phase U	Phase V	Phase W	DC windings
Domains	1	2, 3	6, 7, 10, 11, 14, 15	12, 13	8, 9	4, 5	16, 17
ρ (Ω·m)	1.0	1.0	1.0	1.0	1.0	1.0	1.0
μ_r	1.0	40000	40000	1.0	1.0	1.0	1.0

* ρ =1.0 Ω·m refers to a large resistivity in the model, which represents dielectric property of the air, and help preventing the non-uniform distribution of the current inside the copper regions.

In the model, three phase currents were imposed on the three phase windings U (domain 12, 13), V (domain 8, 9) and W (4, 5). The current densities J_U, J_V, J_W are set as:

$$J_U = J_a \cdot sin(\omega t) \tag{5.1}$$

$$J_V = J_a \cdot sin(\omega t - 2\pi/3) \tag{5.2}$$

$$J_W = J_a \cdot sin(\omega t - 4\pi/3) \tag{5.3}$$

where J_a is the amplitude of the phase current, $\omega = 2\pi f$ is the angular speed, and f is the frequency.

For the dc windings (domain 16, 17), a dc current density J_{dc} was assigned to the domain:

$$J_{dc} = \left(1 - e^{-\tau \cdot (t - t_0)}\right) \cdot J_0 \tag{5.4}$$

where the terms in the brackets show the "switching on" of the dc current. τ is the time constant, t_0 is the time when the dc current is switched on, and J_0 is the value of the dc current.

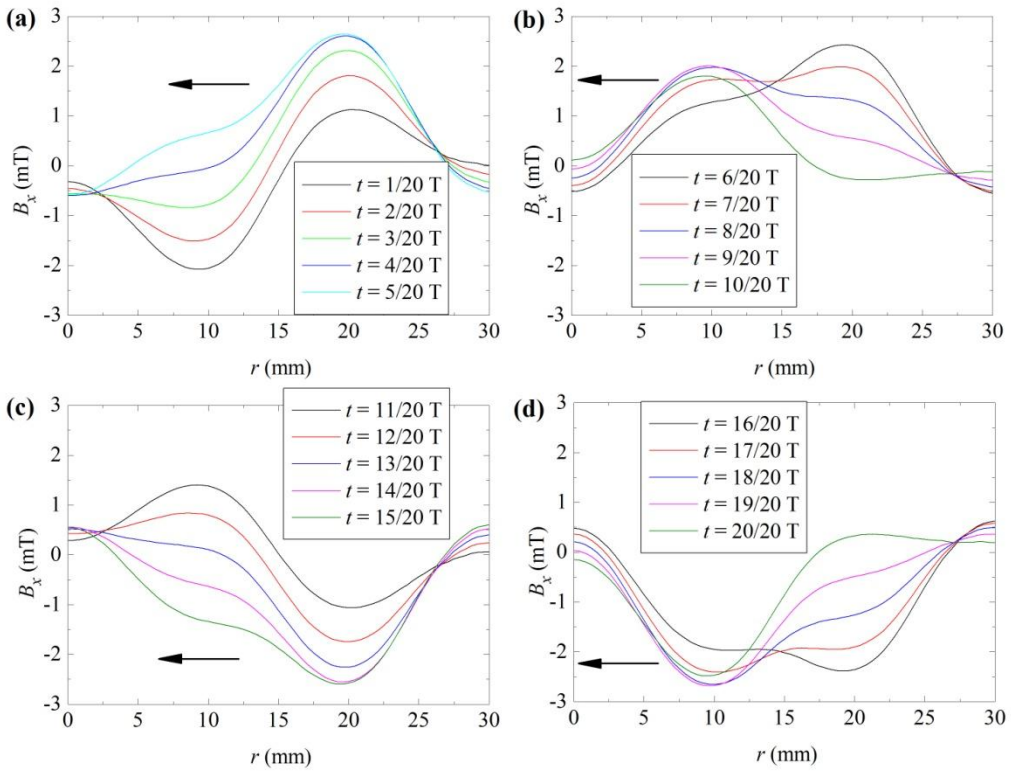

FIG. 5.2. The travelling magnetic wave simulated using the AC/DC mode in COMSOL. The time interval for each curve is 1/20 phase (T).

In the simulation, the terms in the brackets of Equation (5.4) should also be assigned to Equation (5.1) – (5.3) to avoid a sudden change in the value. Additionally, to switch off the applied current densities at a certain time, similar terms should be added in the equations to exponentially decrease the value of the applied current densities.

Fig.5.2 shows the simulated results of the travelling magnetic wave using the AC/DC mode in COMSOL. Later sections show that this simulation matches the experimental results, which suggests that the original CTMFP operates as expected.

In the experiment, it would be useful to know the maximum value (amplitude) at each point across the radius of the device. The six Hall sensor array shown in Fig. 4.16 was used to measure the amplitude of the travelling wave at r = 0 mm, 5 mm, 10 mm, 15 mm, 20 mm, and 25 mm. As discussed in Chapter 4, in order to generate the travelling wave, the phase windings were connected to a three phase inverter. The output voltage of the inverter was varied from V_{ac} = 10 V to 200 V. Section 4.2.2 shows that the resistance in different phase coils is equal to ~300 Ω, therefore the value of the phase currents in the phase coils range from ~0.033 A (V_{ac} =10 V) to ~0.667 A (V_{ac} =200 V). Fig. 5.3 shows the measured amplitude at each position with different output voltages. Fig. 5.3 shows that there are two peak regions, one at r =10 mm and the other at r =20 mm, both of which lie above the iron yokes. The centre field is relatively small compared to the field in the effective travelling region. Fig. 5.3 does not represent the waveform generated by the CTMFP magnets; it is the maximum value (amplitude) measured at each point in space.

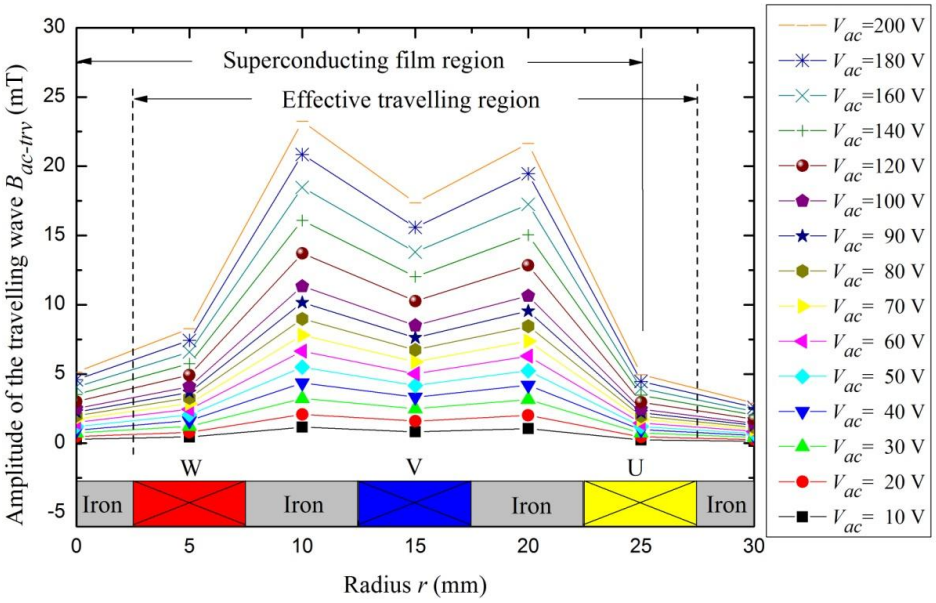

FIG. 5.3. Measured amplitudes of the travelling magnetic field B_x across the radius of CTMFP.

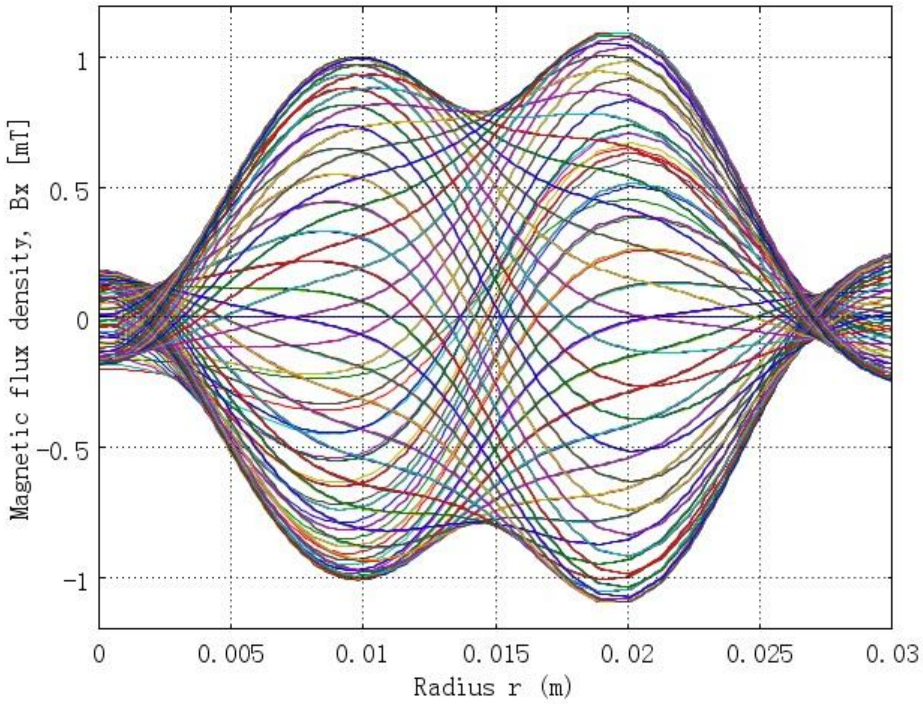

FIG. 5.4. The simulated results of the travelling magnetic wave over one period (with 0.01 period interval), to be compared with Fig. 5.3.

If all the four figures of Fig. 5.2 are combined into a single figure, and the time interval is set to 1/100 phases (T), it becomes possible to see the amplitude of the travelling wave across the area. The simulated result is shown in Fig. 5.4. Comparison of Fig.5.4 with Fig.5.3 shows that the experimental result matches the simulated result, which suggests that the magnetic wave generated by the original CTMFP magnet matches the design.

5.2 The properties of the round shape YBCO sample

As discussed in Section 2.3.2 and Section 4.8, the *E-J* power law is the most widely accepted constitutive relation for the simulation of HTS materials. There are two methods for obtaining the critical current J_C and the n value for the *E-J* power law: the transport current measurement and the induction measurement. The transport current measurement requires the four-point probe method [65], where the four probes are normally soldered to the HTS sample. Another method is to determine J_C and n using the induction measurement [96]. This method is non-destructive, however measurement is not as accurate as the transport current method. For a round shaped YBCO film

sample, the conventional method is to measure the properties of the type-II superconducting sample using the induction method. The induction measurement measures the trapped field at the centre of the HTS sample after field cooling (FC). In this calculation, it is assumed that the current density is uniform across the YBCO sample. Thereby, it is possible to derive a relationahip between the current density in the sample and the field measured at the centre using the Biot-Savart Law. By measuring the decay of the trapped field in the centre, it is possible to obtain the *n* value through the magnetic relaxation theories of the type-II superconducting materials [139].

A single Hall sensor placed in the centre of the original CTMFP magnet was used to take measurements, as shown in Fig.4.3. The dc magnetic field was switched on and the round shape YBCO sample was cooled according to FC. The magnetic relaxation measured in the centre of the sample (1.5 mm above the surface) is shown in Fig. 5.5.

The relationship between the current density in the 2 inch diameter 200 nm thick YBCO thin film (fully magnetised) and the magnetic field 1.5 mm above the centre of the sample was derived by fitting the results to a simple FEM model. The relationship is linear according to the Biot-Savart law.

$$B_{1.5mm} = 3.172 \times J \tag{5.5}$$

Equation (5.5) gives the value of the current density inside the round shape YBCO sample after measuring the field at the centre. From this, a decay curve for *J* can be derived, as shown in Fig. 5.5. From the theories of magnetic relaxation in type-II superconducting materials [139], it is possible to determine the critical current J_C and the *n* value in the YBCO sample by fitting the curve obtained from Fig.5.5 to Equation (5.6):

$$J = J_{C0}\left[1 - \frac{kT}{U_0}\ln\left(\frac{t}{t_0}\right)\right] \tag{5.6}$$

where J_{C0}=2.467 MA/cm^2, which is the critical current density without thermal activation. $n=U_0/kT$=43.54 where U_0 is the activation energy barrier, k is the Boltzmann constant, T is the absolute temperature in liquid nitrogen (77 K), and t_0=6.166 s which is the time constant.

The value U_0/kT=43.54 is equal to the value *n* in the E-J power law. This value is relatively large compared to the conventional value for YBCO (n=21). This is due to the fact that the field dependency of the critical current $J_{C0}(B)$ was not considered in Equation (5.5). If the field dependency is considered, the method described in [68] can be used to determine the value of *n*:

$$J_C = J^*\left(|B| / B^*\right)^{-\gamma} \tag{5.7}$$

$$-\frac{U_0}{kT} = \frac{1}{1-n(1+\gamma)} \tag{5.8}$$

where γ is the exponent determined by fitting J_c(B) [68]. When $\gamma \approx 0.8$, n=24.74.

During simulation of the YBCO sample, the field dependence of J_C on the magnetic field B is ignored. This is due to the fact that, in most cases, the travelling wave applied to the YBCO sample varies over a very small range (2.0 mT), and for which is not necessary to consider the field dependence for J_C.

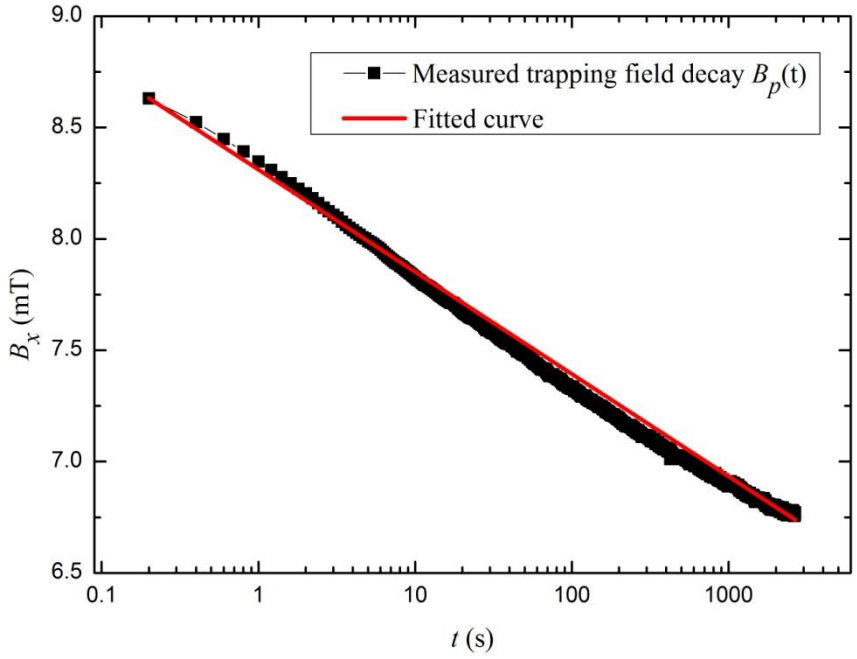

FIG. 5.5. Logarithmic decay of the trapping field B_p measured 1.5 mm above the centre of the YBCO sample in 77 K after field cooling.

As previously mentioned, the induction measurement method is not as accurate as the transport measurement method. There are many factors that might cause errors, such as the exact position of the Hall sensor, the exact starting time, etc. During the simulations, it was aimed at best fitting the experimental results. It was found that when J_C=1.865 MA/cm^2 and n=30, the simulated results were mostly equivalent to our experimental observations. Thereby, for the simulation, J_C=1.865 MA/cm^2 and n=30 were chosen for this 2 inch diameter YBCO sample at 77 K.

5.3 Travelling wave and homogeneous oscillating field: a comparison

Homogeneous oscillating field and travelling waves are the two conventional wave conditions in space. By definition, a homogeneous oscillating field is uniform over space, and can be normally found in the middle of a long solenoid or Helmholtz coil [140]. In the case of a travelling magnetic wave, the field is inhomogeneous over space, and a crest region and a trough region will be present.

To date, most theories developed to understand macroscopic electromagnetic phenomena are based on homogeneous oscillating field. For instance, the Bean model described in Section 2.3.1 assumes a homogeneous oscillating field. Much research has been done to calculate the magnetisation and ac losses for a homogeneous oscillating field [50], but very little attention has been paid to the magnetisation problem in the case of a travelling magnetic wave, even though ac losses in travelling waves are common conditions, such as inside a superconducting electric machine [141-143]. Although there have been limited studies into magnetisation caused by travelling waves, explanations for these are nevertheless based on a homogeneous oscillating field [144, 145].

This section compares the magnetisation of the 2 inch diameter YBCO sample under a travelling wave and a homogeneous oscillating field after ZFC. This experiment was intended to show the differences caused by a travelling wave, compared to a homogeneous oscillating field. After the sample has been cooled down, a dc background field was applied to magnetise the YBCO sample. Then either a travelling wave or a homogeneous oscillating field of the same amplitude was applied to the magnetised sample. The magnetisation differences caused by the homogeneous oscillating field and the travelling wave were compared. This method identified a novel magnetisation phenomenon caused by the travelling magnetic wave. The phenomenon was further studied by measuring the change in magnetic gradient above the YBCO sample with the help of a six Hall sensor array (as shown in Fig.4.16). The experimental results suggested that the travelling wave tends to attenuate the existing magnetic gradient, which is unconventional according to the Bean model. A simulation based on FEM software was also performed to reveal the current density distribution inside the YBCO sample. The simulation showed that the constant current density assumption incorporated in the Bean model does not apply to a travelling wave.

5.3.1 Single Hall sensor measurement[3]

For the single Hall sensor measurement, a single Hall sensor was placed 1.5 mm above the centre of the YBCO sample as shown in Fig.4.3. The experiment was performed under zero-field cooling (ZFC) conditions, is which the YBCO sample was cooled in a zero background field at 77 K, before the magnetic field was applied.

Under a travelling wave, the dc background field was provided by the dc windings, and the travelling wave was provided by the three phase windings. The dc current for the dc windings came from a dc power source, and the three phase currents came from the inverter as discussed in Section 4.4. The output voltage was preset as V_{ac}=6.0 V, which produced a maximum field of 1.0 mT at r = 10 mm. The amplitudes of the travelling wave across the radius of the CTMFP magnet was measured for V_{ac}=6.0 V, and the results are shown in Fig.5.6. The frequency of the inverter was set at 1.0 Hz.

Under a homogeneous oscillating field, the dc windings provided both the dc background field and the ac homogeneous oscillating field. This was achieved by offsetting a one phase ac signal from a function generator (FG). However, due to the limitations of the FG, it was only possible to switch on and off both the dc offset and the ac signal simultaneously. The ac voltage was set so that the amplitude of the homogeneous oscillating field measured in the device centre was equal to 1.0 mT. The frequency was also set at 1.0 Hz.

The dc background field for both the travelling wave and the homogeneous oscillating field remained constant so that the results could be compared. This was achieved by carefully adjusting the dc current from the dc power supply and the offset from the FG.

Under the travelling wave, the sequence of the experiment was: start data acquisition (DAC) (t=0 s); dc power on (t=10 s); inverter on (t=20 s); inverter off (t=40 s); dc power off (t=50 s); DAC off (t=60 s). The experiment was repeated with different dc background field conditions. The results for B_{dc} = 5.0 mT, 7.0 mT and 11.5 mT are shown in Fig.5.7.

As shown in Fig.5.7, after dc background field was switched on (between t=10 s and 20 s), there was clear field-shielding behaviour. Note that when B_p≈6.9 mT, the shielding behaviour roughly followed the Bean model. The flux creep phenomenon was also clear between t=10 s and 20 s. The flux densities measured at t=19 s were denoted as B_1.

[3] Published in J. Appl. Phys. **113**, 213906 (2013)

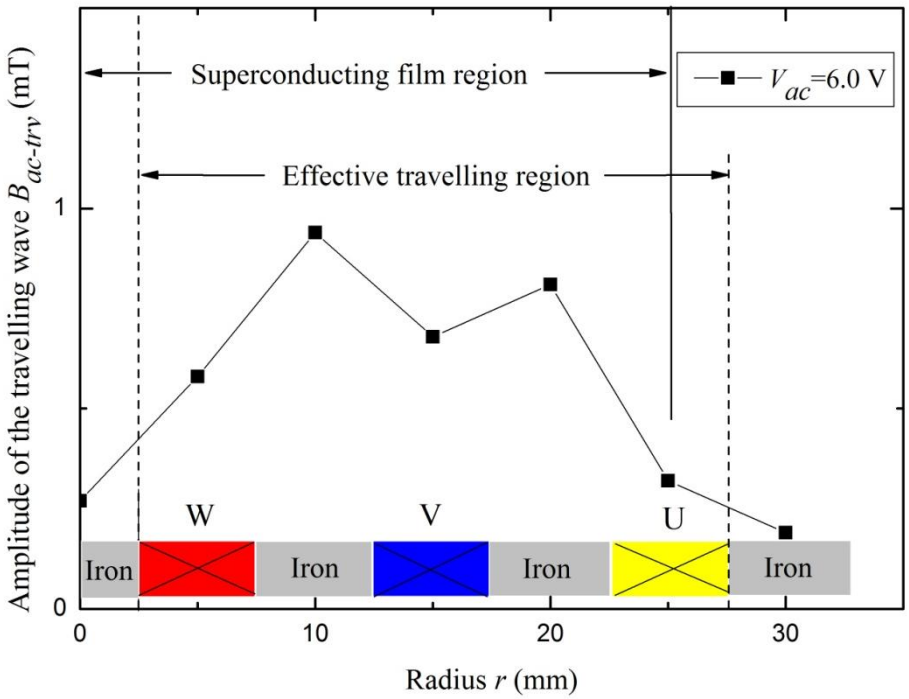

FIG. 5.6. Measured amplitudes of the annular shape travelling magnetic field across the radius of the CTMFP.

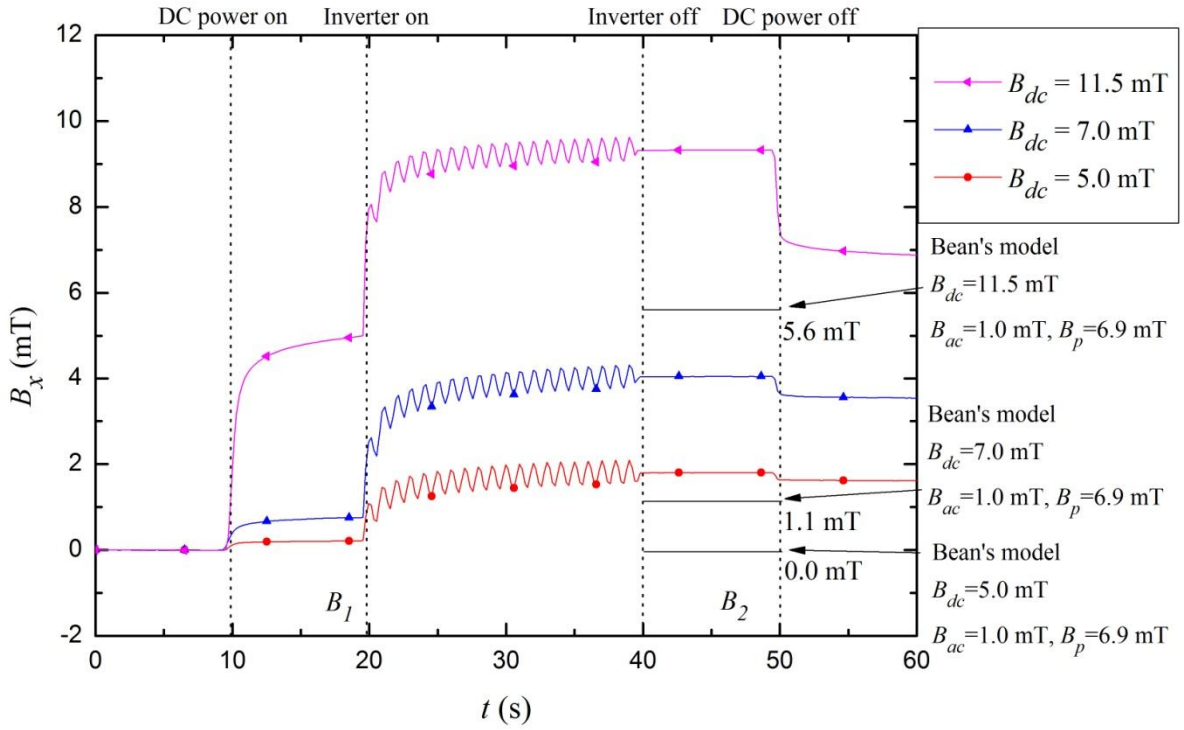

FIG. 5.7. Measured magnetic flux density B_x under different background fields B_{dc} after ZFC in a travelling wave. The sequence of each measurement (curve) is: start data acquisition (t=0 s), dc power

on (t=10 s), inverter on (t=20 s), inverter off (t=40 s), dc power off (t=50 s) and data acquisition off (t=60 s)

An interesting phenomenon occurred after the travelling wave was switched on at t=20 s. As shown in Fig. 5.7, the field in the centre increased drastically. Most of the increase occurred within the first three periods. Especially in the first period, immediately after the travelling wave was applied, there was a sudden increase of flux density at the centre. For the fully penetrated sample ($B_{dc} \geq 6.9$ mT), the increase of field at the centre was much greater than the amplitude of the travelling wave itself (1.0 mT). It is likely that the existence of the magnetic wave triggered a massive migration of flux into the centre of the sample. When the travelling wave was switched off, the field remained quite stable between t=40 s and 50 s. The flux creep phenomenon was not as clear as usual between t=10 s and 20s. The flux density between t=40 s and 50 s is denoted as B_2. It was measured that B_2=1.8 mT, 4.1 mT and 9.3 mT for three different dc background field conditions.

Three straight lines have been drawn between t=40 s and 50 s in Fig.5.7 to indicate the theoretical predictions based on the Bean model for the different background fields B_{dc} combined with B_{ac}=1.0 mT and the maximum trapping field B_p=6.9 mT. There are great discrepancies between the Bean model predictions and the experimental results. The travelling wave helps more flux migrate into the sample centre compared to predictions based on the Bean model. As discussed in Section 2.3.1, the Bean model normally describes a homogeneous oscillating field, which is homogeneous over space provided the superconductor has a regular shape (either a long rod or slab). Although the sample used had a large demagnetisation factor (≈1.0), the magnetisation of this sample could still be precisely predicted using the Bean model when it was subjected to a homogeneous oscillating field. The experiment with the travelling wave suggested that the magnetic stress variation over space (high in the crest region and low in the trough region) from the travelling wave may help vortices to move more effectively compared to a homogeneous oscillating field.

In Fig. 5.8(a), B_{dc}-B_1 and B_{dc}-B_2 are plotted as a function of B_{dc}. B_{dc}-B_1 shows the flux density shielded in the centre before application of the travelling wave. B_{dc}-B_2 shows the flux density shielded after application of the travelling wave. In the curve B_{dc}-B_1, the shielded flux density increased with the applied dc field then slowly decreased, which is normally explained by the field-dependence of the critical current density (the Kim model) [146]. However, in the curves B_{dc}-B_2 for V_{ac}=6.0 V, after applying the travelling magnetic wave, a drastic decrease in the field-shielding was observed, which suggests that the travelling wave greatly compromised the field shielding of the YBCO sample.

In Fig. 5.8(b), the values B_2 - B_1 for V_{ac}=6.0 V are taken as a function of B_{dc} which shows that the flux density increased in the centre after the travelling waves were applied for 20 s. A maximum

increment of 4.35 mT was observed. Even for a very weak dc field, i.e., B_{dc}=2.5 mT, an increment of 0.4 mT was observed in the centre when the applied peak field was less than 3.5 mT, which is half of B_p (~6.9 mT).

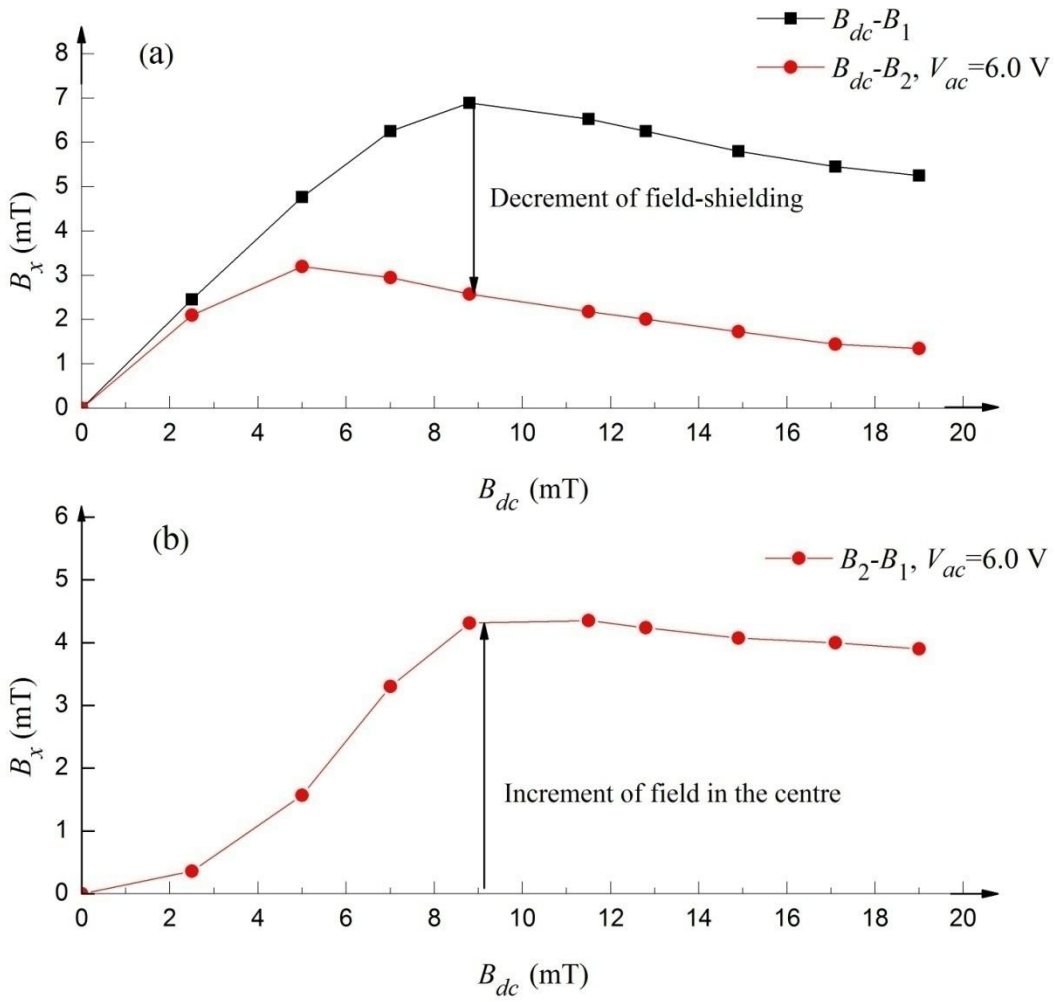

FIG. 5.8. Experimental data from Fig.5.7. (a) B_{dc}-B_1 and B_{dc}-B_2 as functions of B_{dc}, which shows the field shielded by the sample in the centre before and after applied the travelling wave; (b) B_2-B_1 as a function of B_{dc} which shows the increment of field in the centre after applied the travelling magnetic wave.

The experiment results provide evidence that a travelling wave of very small amplitude helps vortices to migrate into the centre of the sample under zero-field cooling conditions. The increase of flux density in the centre is much greater than predictions from the Bean model would suggest using conventional ac wave (homogeneous oscillating field). The following paragraphs will demonstrate the

validity of the Bean model for the homogeneous oscillating field when it is applied to the sample in this experiment. The difference will reveal that magnetisation based on a travelling wave is very different from magnetisation based on a homogeneous oscillating field.

A homogeneous oscillating field with the same amplitude as the travelling wave was applied, and oscillating homogeneously in the superconducting region, which is conventional outcome. The dc coils were connected to a function generator (FG) to provide both the homogeneous oscillating field and the dc background field. The three phase coils were disconnected from the inverter. The homogeneous oscillating field was controlled using the ac voltage output of the FG. The frequency was set as f=1.0 Hz, which was the same as frequency of the travelling wave. The ac signal was offset by a dc voltage from the FG, which produced a dc background field B_{dc}. The sample was cooled under ZFC conditions. The amplitude of the ac homogeneous oscillating field was measured as $B_{ac\text{-}std}$=1.0 mT at the centre of the device, which was equal to the maximum amplitude of the travelling wave as shown in Fig. 5.6. Three different dc field cases were studied, at B_{dc}=5.0 mT, 7.0 mT, and 11.5 mT. These were the same in the travelling wave study.

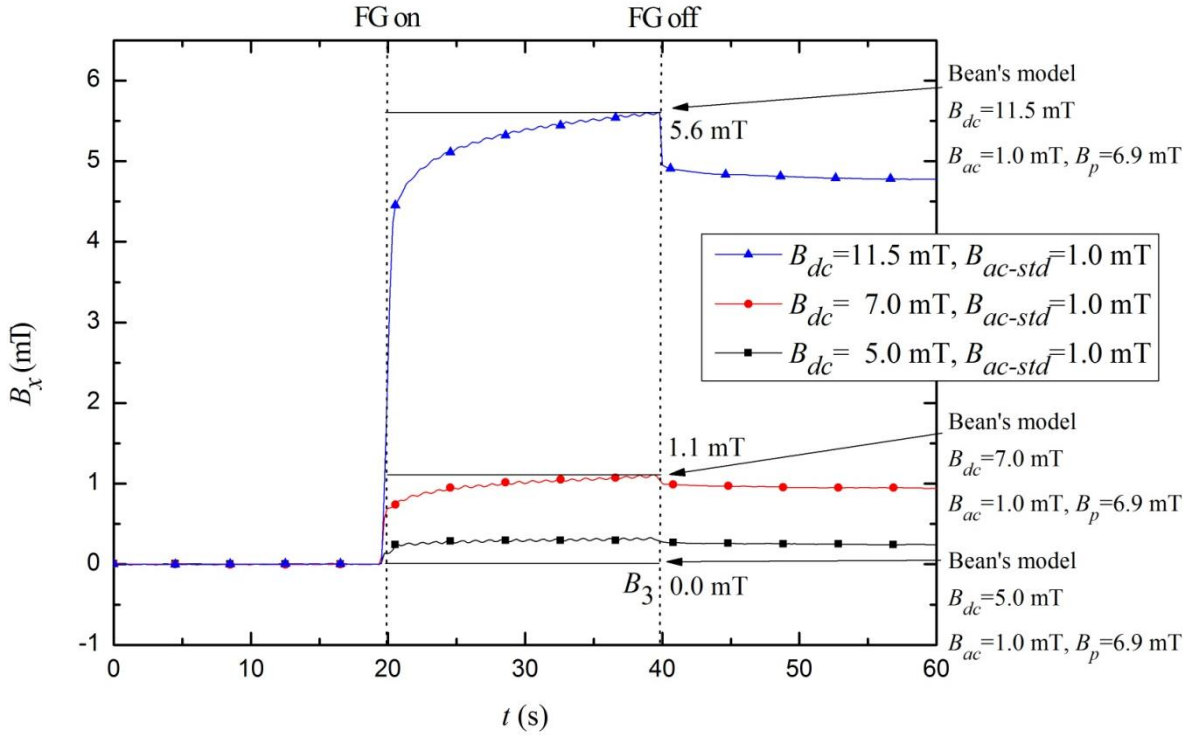

FIG. 5.9. Experimental results using the dc coils connected to a FG, while the three phase-coils were disconnected from the power source. The magnetic field was measured at the centre of the device, the same in Fig. 4.3. B_{dc} stands for the background dc field measured at the centre of the rig, and $B_{ac\text{-}std}$ stands for the amplitude of the ac field measured at the centre. The sequence of each experiment was: DAC on (t=0 s); FG on (t=20 s); FG off (t=40 s); DAC off (t=60 s).

The experimental results are shown in Fig. 5.9. The timeline is marked on the top of the diagram. The sequence of each experiment was: DAC on (t=0 s); FG on (t=20 s); FG off (t=40 s); DAC off (t=60 s). As mentioned before, the ac field and dc offset were switched on at the same time due to the limitations of the FG. We denote the flux density at t=39 s (before the FG was switched off) as B_3. It was measured that B_3=0.3 mT, 1.1 mT and 5.6 mT for three different dc background cases. Three straight lines were drawn between t=20 s and 40 s, to indicate the prediction based on the Bean model ($B_3 \approx 0$ for $B_{dc}+B_{ac\text{-}std}<B_p$ and $B_{dc}+B_{ac\text{-}std}-B_p \approx B_3$ for $B_{dc}+B_{ac\text{-}std} \geq B_p$). It can see that, although the $YBa_2Cu_3O_{7-\delta}$ film had a large demagnetisation factor (≈1.0), the experimental results agreed closely with the Bean model prediction.

In the above experiments, either the travelling wave or the homogeneous oscillating field with the same amplitude (1.0 mT) was applied to the same YBCO sample, and found very different results. This showed that magnetisation by a homogeneous oscillating field can be easily predicted using the Bean model, however, a travelling wave cause a much greater degree of vortex migration into the sample centre compared to a homogeneous oscillating field.

The difference between the travelling wave and homogeneous oscillating field is that a travelling wave involves magnetic stress variations over space, and an ideal homogeneous oscillating field inside a solenoid does not. Basic vortex dynamics were discussed in Section 2.2.4 and the "dc transformer" in Section 3.3. The movement of a single vortex is the balance between the Lorentz force and the pinning force. From the perspective of energy, the distribution of the FLL is based on minimising the potential energies inside the type-II superconductors. This principle of energy minimisation also applies to the macroscopic magnetic behaviours of type-II superconductors [147]. For a homogeneous oscillating field, the magnetic stress is homogeneous over space. In the presence of a type-II superconductor, the change of the homogeneous oscillating field results in changing the depth and direction of the circulating current. Only if the change of magnetic field is greater than the maximum trapping field B_p, can the change of flux be observed at the centre of the sample. However, for a travelling wave, the distribution of magnetic stress over space becomes complicated, because the magnetic stress increases locally in the crest region while decreasing locally in the neighbouring trough region. This causes local movement of vortices inside a type-II superconductor. The non-uniform distribution of magnetic stress may help the vortices to migrate within the superconductor.

This vortex migration phenomenon is different from the observed crossed magnetic field effect and the flux shaking effect, as discussed in Section 2.3.4. These effects involve a dc field perpendicular to the sample surface and a small ac field perpendicular to both the dc field and the sample surface. However, in our experiment, both the dc field and the ac field were perpendicular to the sample surface. There is no cross field parallel to the sample surface. This was ensured by the magnetic structure in the centre of a solenoid and can be verified using our numerical model.

The next section further studies this phenomenon with the help of the six Hall sensor array. A simulation based on the H-formulation is also performed to understand the current distribution inside the YBCO thin film.

5.3.2 Six Hall sensors array measurement[4]

In order to understand the phenomenon described in the previous section, the six Hall sensor array were placed above the YBCO sample to measure the change in the magnetic gradient. Information regarding the six Hall sensor array can be found in Section 4.5.1. The six Hall sensors were connected to a multi-channel data acquisition card Agilent U2353a as discussed in Section 4.5.2. The real-time Hall voltages were collected and calibrated using Labview. In order to determine the phase of the travelling wave, another Hall sensor was attached to the back of the CTMFP coil as shown in Fig.5.10(a). The relative positions between the Hall sensors and the YBCO sample are shown in Fig.5.10(b).

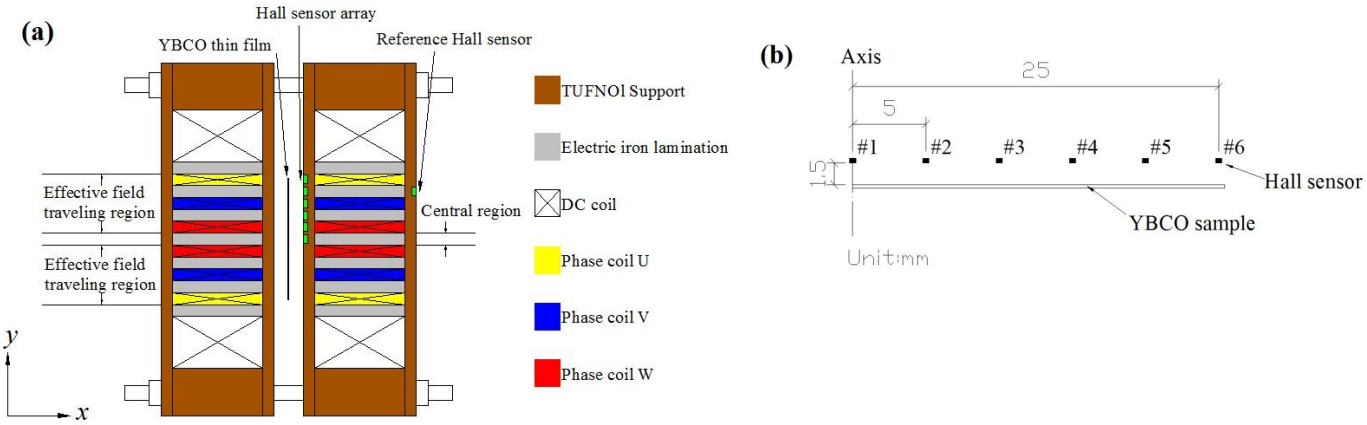

FIG. 5.10. The circular-type magnetic flux pump device. (a) the CTMFP; (b) the six Hall sensor array.

A numerical simulation was also performed to simulate the behaviour of the YBCO sample under the influence of a travelling wave. The simulation method was based on the H-formulation, as described in Section 4.8. The problem is axially symmetrical and the governing equation is a combination of Faraday's law and Ampere's law, which is solved using finite element (FEM) software. The governing equation is rearranged as [138]:

[4] Published in *Appl. Phys. Lett.* **104**, 032602 (2014)

$$\mu_r \mu_0 \frac{\partial \boldsymbol{H}}{\partial t} + \nabla \times \left(\rho \nabla \times \boldsymbol{H} \right) = 0 \tag{5.9}$$

In the axial symmetric model, two components of the magnetic field were solved: $\boldsymbol{H} = [H_r, H_z]^{\mathrm{T}}$. For the YBCO sample, ρ was derived using the *E-J* power law, which is expressed as: $\rho = J^{n-1} E_C / J_C^n$. We used J_C =1.865 MA/cm^2, n=30, E_C =10^{-4} V/m in our calculation. The values of J_C and n were chosen by best fitting the experimental results. The anisotropy and the field dependency of the critical current were not considered in the calculation, since the applied field is always normal to the sample surface and the applied traveling wave only varies over a small range (~2.0 mT).

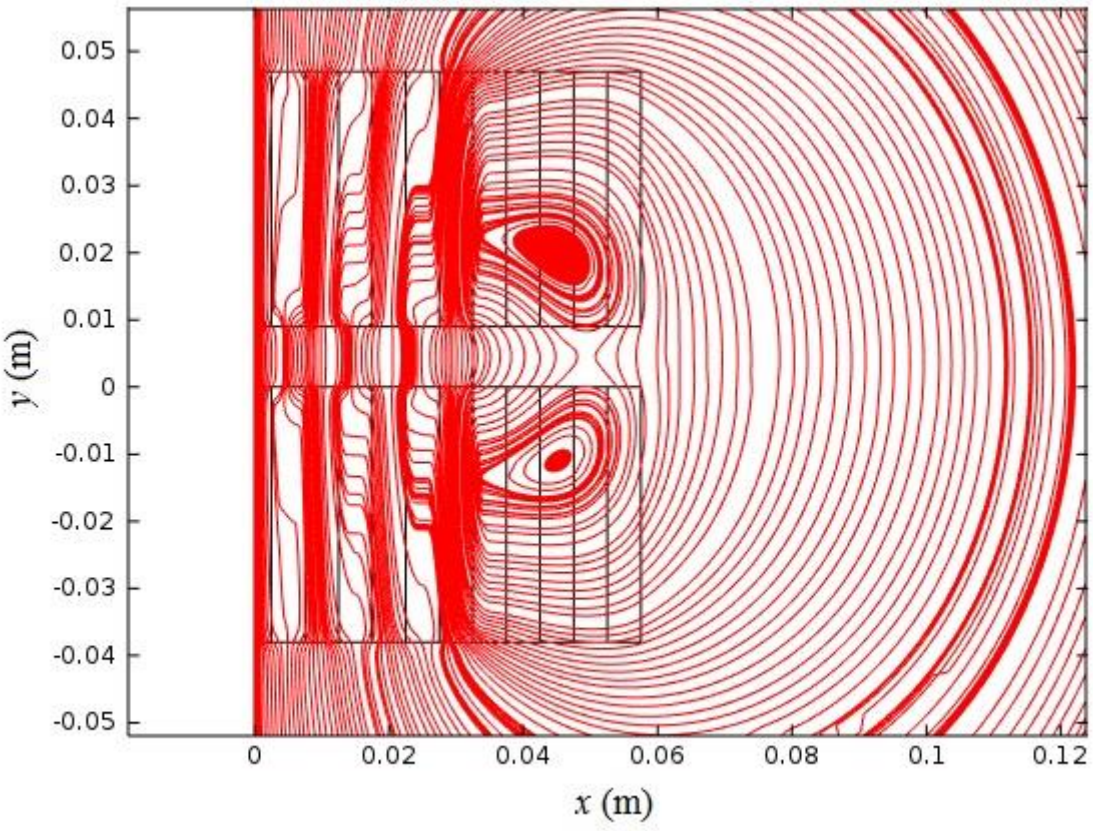

FIG. 5.11. The calculated dc magnetic field distribution of the original CTMFP magnets.

Fig. 5.11 shows the calculated dc magnetic field distribution of the original CTMFP magnets. The dc magnetic field was provided by the dc current of the dc coils. It is clear that, due to the presence of the iron yokes, the magnetic field distribution is slightly non-uniform across the centre of the device (y=0.0045 m): the iron yokes concentrate the flux so that increase the field in the regions between the corresponding iron yokes of the two magnets. However, this field inhomogeneity is tolerable in the experiment as will be show in Fig. 5.12.

In this section, the ZFC experiment was performed again using the six Hall sensor array. The output voltage of the inverter was increased to 10 V and the amplitude of the travelling wave was about 2 mT. The frequency was set at 0.1 Hz. It is interesting to learn why the field in the centre of the sample increases drastically and how the current inside the superconductor changes due to the travelling wave. Fig. 5.12 shows the process as the field in the centre rises as the wave travels. The simulation results are also shown in these figures to show the validity of the model. The calculated current density distributions are plotted in the figures as well to help understand the magnetisation process.

The left column in Fig. 5.12 shows the applied field without a superconductor, i.e., the dc background field in Fig.5.12(a) and the travelling magnetic wave in Fig. 5.12(c), (e), (g), (i), where the dc background field (Fig. 5.12(a)) was present throughout the whole experimental process. The right column in Fig. 5.12 shows the measured field in the presence of the YBCO sample at the corresponding time: Fig. 5.12(b) shows the magnetic shielding profile after applying the dc background field; Fig. 5.12(d), (f), (h), (j) show the resultant field at the corresponding phase of the applied travelling wave, as shown in the left column. The calculated current density profiles were plotted for each time step. Since the sample is very thin (200 nm), the current density does not change across the thickness, as can be verified using the simulated model. Therefore, the current density was measured across the centre of the sample, then normalised it using its critical current J_C.

In Fig. 5.12(b), as the dc background field is applied to the sample there is clearly a magnetic shielding profile. The simulation shows that the current remains constant across the radius and is about 80% of J_C. This is a typical magnetisation profile after applying a homogeneous field, as suggested by the Bean model [149]. In Fig. 5.12(c) and 5.12(d), as the crest region of the travelling wave arrives at r = 20 mm, the current density near the edge of the sample increases to about 95% of J_C while the current density in the inner area drops to 45% of J_C. As the crest region travels further at r = 10 mm, it is the sample is re-magnetised to 80% of J_C. However, the current density on the edge decreases to zero. As the trough region travels at r = 20 mm as in Fig. 5.12(g), the current density at the edge reverses direction to about 80% of J_C as shown in Fig. 5.12(h). Meanwhile, there is a clear increase in flux density at the centre of the sample. As the wave travels further into the sample, shown in Fig. 5.12(i) and 5.12(j), that the current density between r = 10 mm and 20 mm decreases while the flux density in the centre increases further to 5.2 mT. Comparing the current density profiles in Fig. 5.12(h) and 5.12(j) with Fig. 5.12(d) and 5.12(f), it is clear that as the trough region travels into the superconductor, the magnetic flux in the centre region gradually increases.

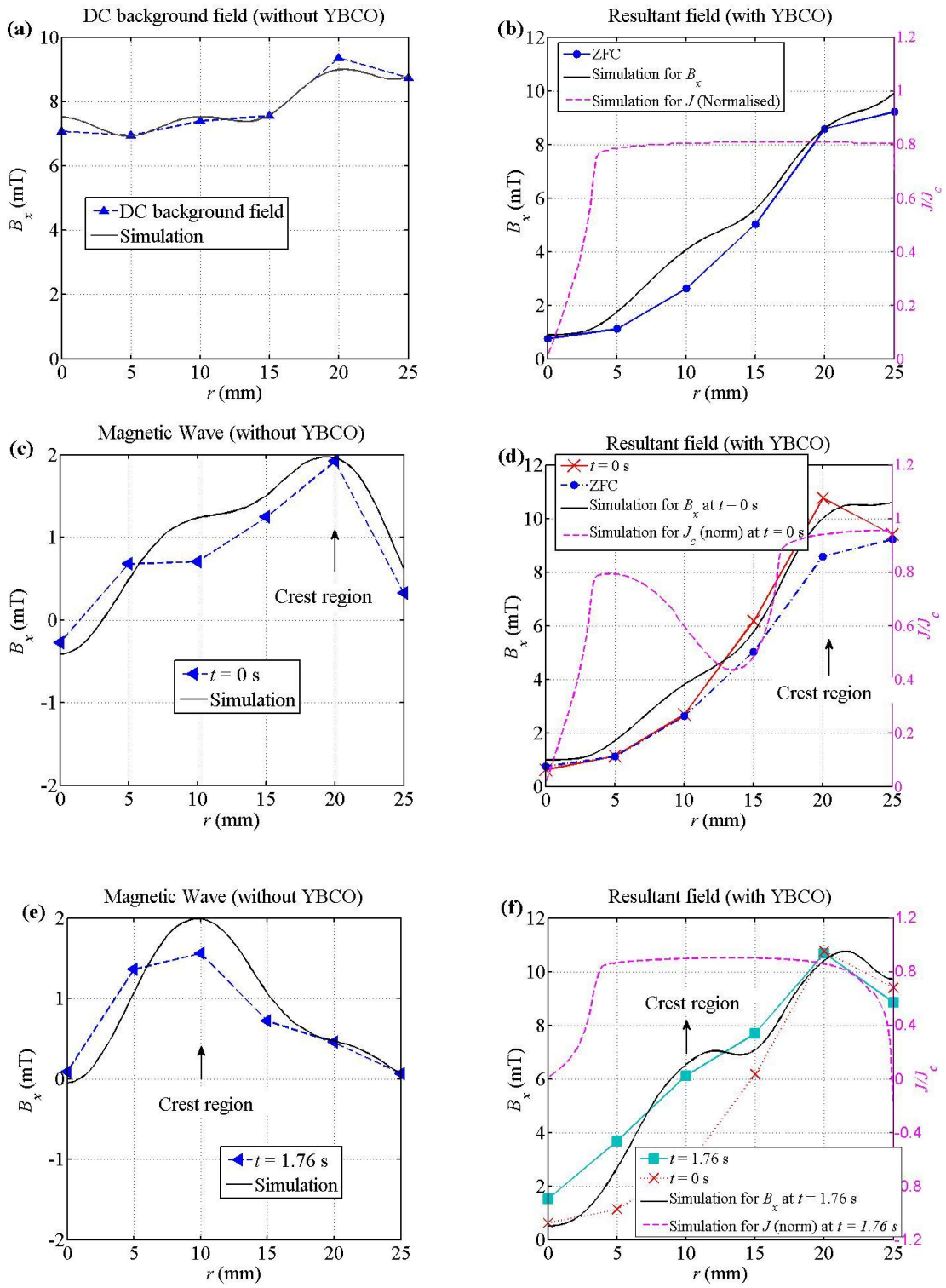
(a)
DC background field (without YBCO)
DC background field
Simulation
B_x (mT)
r (mm)
(b)
Resultant field (with YBCO)
ZFC
Simulation for B_x
Simulation for J (Normalised)
B_x (mT)
J/J_c
r (mm)
(c)
Magnetic Wave (without YBCO)
Crest region
t = 0 s
Simulation
B_x (mT)
r (mm)
(d)
Resultant field (with YBCO)
t = 0 s
ZFC
Simulation for B_x at t = 0 s
Simulation for J_c (norm) at t = 0 s
Crest region
B_x (mT)
J/J_c
r (mm)
(e)
Magnetic Wave (without YBCO)
Crest region
t = 1.76 s
Simulation
B_x (mT)
r (mm)
(f)
Resultant field (with YBCO)
Crest region
t = 1.76 s
t = 0 s
Simulation for B_x at t = 1.76 s
Simulation for J (norm) at t = 1.76 s
B_x (mT)
J/J_c
r (mm)

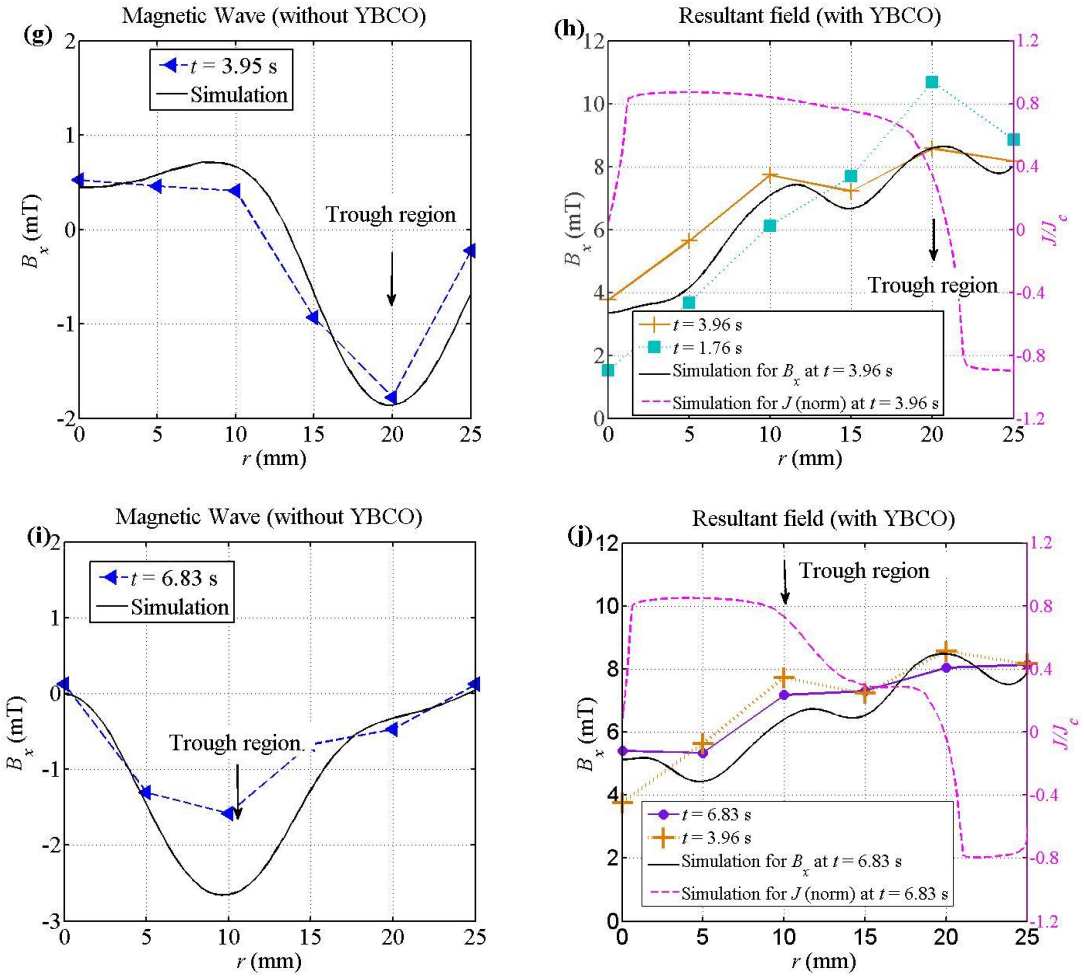

FIG. 5.12. The measured evolution of the magnetic gradient and calculated current density distributions (normalised by J_C) after application of the travelling magnetic wave. The left column shows the measured field (dc background field and travelling wave) without the YBCO sample, while the right column shows the resultant field with the YBCO sample. The iron yokes are in the regions: $r \leq 2.5$ mm, 7.5 mm $\leq r \leq$ 12.5 mm, 17.5 mm $\leq r \leq$ 22.5 mm.

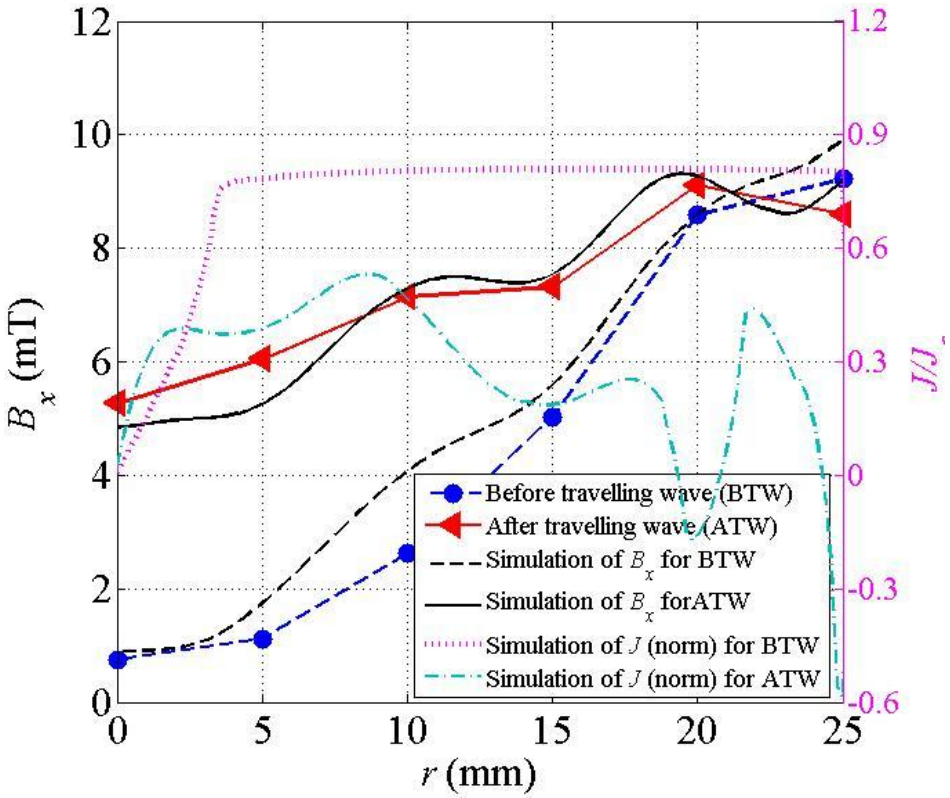

FIG. 5.13. The magnetic gradient measured 1.5 mm above the sample and the calculated current density distribution before and after applying the travelling wave.

Fig. 5.12 only shows the first 6.83 s during the first cycle of the travelling wave. As shown in the previous section, the increased flux density at the centre of the sample occurs mostly during the first three cycles (and predominantly in the first period). Following cycles do not significantly change the magnetisation. Fig. 5.13 shows the final field profile after applying the travelling wave (over 12 periods). This result can be compared to the field profile before the travelling wave was applied. The calculated current densities are also plotted in the figure. After applying the travelling wave, the magnetic gradient decreases drastically. Moreover, the simulation results show that the current density is almost uniform across the sample (about 80% of J_C) before the travelling wave was applied. However, after applying the travelling wave for 12 cycles, the current density distribution inside the sample becomes very complicated. In general, the value of the current density becomes much smaller than its critical current.

Now come back again to the argument that the decrease in current density might been caused by the cross field effect [68] or the flux shaking effect[150]. Our FEM model tested the field at the centre of the gap where the superconducting sample is placed. The results show that there is absolutely no

cross field, i.e., the field parallel to the sample surface is zero. The applied field is always normal to the sample surface, so therefore this behaviour cannot be caused by the cross field effect.

This experiment has shown that the magnetisation caused by the travelling wave is much more complicated than that caused by a homogeneous oscillating field, and it does not follow the constant current density assumption as suggested by the Bean model. The field inhomogeneity in space can lead to local variations of current density inside the type-II superconducting thin film, which our experiment suggests is more likely to compromise the existing magnetic gradient. This effect should be considered in ac loss calculations, especially for superconducting motors.

Also, it was shown that the travelling wave is more efficient in transporting the flux inside the YBCO sample. This interesting vortex dynamics phenomenon might suggest that the travelling wave can be used to magnetise type-II superconducting coils: in the case of a superconducting loop, such as superconducting coils, the travelling wave may help the vortices migrate from outside into the loop, which could gradually magnetise the superconducting coils as shown in Hoffman's [116] and Bai's [89] works as introduced in Chapter 3. The mechanism of this flux pump shows complete distinction from the conventional type-I superconducting flux pump, in which the flux migrates with the help of normal spots [87].

5.4 Magnetisation under various conditions: ZFC, FC and delta shaped trapped field

The previous section studied the magnetisation caused by a travelling wave after ZFC. It was found that an existing magnetic gradient becomes compromised by the application of a travelling wave of small amplitude. This section extends the study to different conditions, such as ZFC, FC and a delta shaped trapped field. These three conditions are commonly found in the magnetisation of a type–II superconducting materials. Studying these conditions can increase understanding of how a travelling wave influences the magnetisation profile of a type-II superconducting film.

In this section, it will show that, the travelling wave tends to attenuate the existing critical magnetic gradient in all three cases. It was suggested that, the field inhomogeneity can help the

vortices to move locally, so that the critical magnetic gradient has been flattened out. It is very unique compare with the magnetisation based on the homogeneous oscillating field, which follows the constant current density assumption (Bean model). However, as will be shown in this section, the magnetisation based on the travelling wave can be well predicted by the FEM software using E-J power law. This is very interesting phenomenon since the E-J power law is very close to the constitutive relation of the Bean model. This section provides a general idea of how the travelling wave may influence the magnetisation of the YBCO thin film.

5.4.1 ZFC condition

Fig. 5.14 shows the experimental and simulated results of the YBCO sample under a varied dc background field (B_{dc}=2.5 mT, 5.0 mT, 7.0 mT, 10.0 mT) and a constant amplitude travelling wave (V_{ac}=10 V, corresponding to ~2.0 mT peak amplitude at r =10 mm) after ZFC. Fig. 5.14(a) shows the experimental and simulated results of the magnetic gradient across the surface of the sample (1.5 mm above) after application of a dc field to the zero-field cooled sample. Fig. 5.14(b) shows the simulated results of the current density distribution inside the YBCO sample (normalised by J_C). From Fig. 5.14(a) and (b) it is clear that the constant current assumption of the Bean model does apply to the homogeneous oscillating field condition, so that an increasing dc background field gradually penetrates the sample centre and induces current inside the sample equal to 80% of J_C. This is typical magnetisation profile frequently appears in text books about the magnetisation of type-II superconductors.

Fig. 5.14(c) and (d), show the experimental and simulated results after 12 cycles of a travelling wave applied to the YBCO sample. By comparison of Fig. 5.14(a) and (c), it is clear that the travelling wave tends to attenuate the existing magnetic gradient. This behaviour is effectively simulated using FEM software and the *E-J* power law. Fig. 5.14(d) shows the corresponding current distribution after application of the travelling wave for 12 cycles. Comparison of Fig. 5.14(b) and (d), it is clear that the constant current density distribution becomes disturbed by the travelling wave, and the average current density is much lower than the critical current density. In Fig. 5.14(d), for the fully penetrated sample (B_{dc}=7.0, 10.0 mT), the calculated current distribution is the same as for B_{dc}=5.0 mT, and only small discrepancies are observed in the central region. For B_{dc}=2.5 mT the central region is different, however, in the region r>8 mm, the calculated current distribution overlaps with the other three cases.

The final current distribution is dependent on the final phase of the travelling wave being switched off in the numerical model. If the final phase changes, the final current distribution changes correspondingly. However, this does not change the fact that the overall magnetic gradient becomes attenuated by the travelling wave as shown in Fig. 5.14(c). The simulated results shown in Fig. 5.14(d) are due to the fact that the travelling wave was switched off at the same phase in the FEM model.

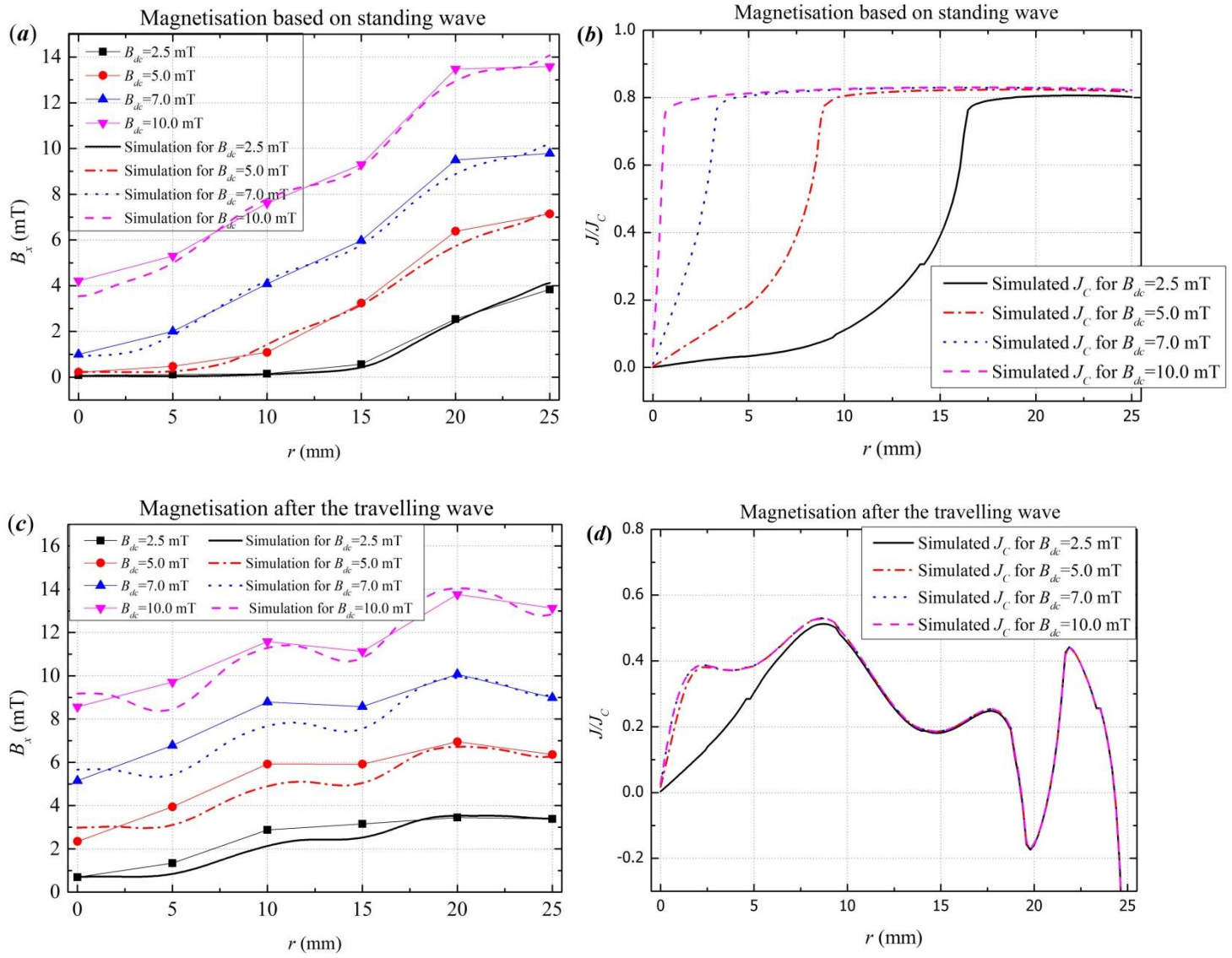

FIG. 5.14. The experimental and simulated results of the magnetic gradient in various dc background fields (a) before and (c) after application of a travelling wave (V_{ac}=10 V). The calculated current density distributions are shown in (b) and (d) for each condition.

The next study increases the amplitude of the travelling wave to show how the amplitude influences the magnetisation of the sample. The single Hall sensor was placed in the centre of the CTMFP magnet. The experiment follows the ZFC process. After application of the dc field and travelling wave, the travelling wave was switched off at a random time and records the trapped field at the centre of the sample. If the field measured in the centre before the travelling wave is defined as as B_1 and the field measured after the travelling wave as B_2 (as in Fig. 5.7), then B_2-B_1 shows an increase of magnetic flux in the centre of the sample.

B_{dc}=7.0 mT and 2.5 mT were chosen for the study as they indicate two different cases: a fully penetrated sample and a sample not fully penetrated by the dc background field. The output voltage of the inverter V_{ac} was changed from 10 V to 200 V. B_2-B_1 is plotted as a function of V_{ac}. The results for B_{dc}=7.0 mT and 2.5 mT are shown in Fig. 5.15. Each point shown in Fig. 5.15 is derived from the experimental process shown in Fig. 5.7.

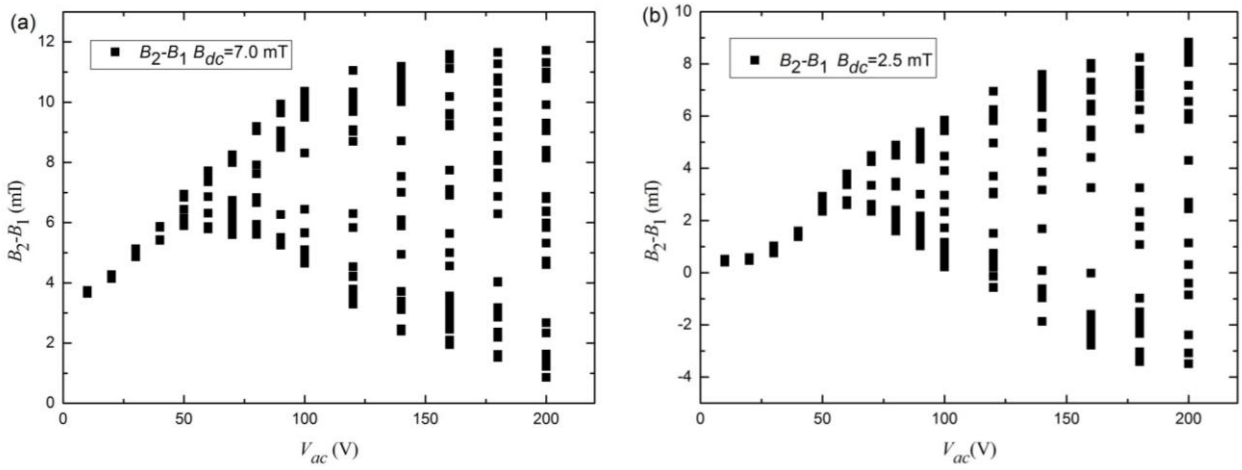

FIG. 5.15. Plot of B_2-B_1 for B_{dc}=7.0 mT and 2.5 mT as a function of different output voltage of the inverter.

Both Fig. 5.15(a) and (b) show an increase in the field at the centre at V_{ac}<40 V, but an oscillation of the field at V_{ac}≥40 V. As will be discussed in Section 5.5, after V_{ac}≥40 V, the travelling wave starts to penetrate the sample centre, causing the field to oscillate at the centre. Therefore, the resultant field in the centre is highly dependent on the final phase of the travelling wave. For V_{ac}<40 V when the travelling wave hadn't penetrated into the centre, the increase in the field was simply due to the decrease in the magnetic gradient. Also, as the amplitude of the travelling wave increased, the

resultant field increased correspondingly, which suggest that a further decrease of the magnetic gradient as V_{ac} increases.

The above experiments support the idea that, the travelling wave attenuates the existing magnetic gradient, and the attenuation is dependent on the degree of the field inhomogeneity (amplitude of the wave).

5.4.2 FC condition

In the ZFC condition, the existing critical magnetic gradient is positive (as shown in Fig. 5.14) and the direction of the travelling wave is inwardly. However, it would be interesting to know the influence of the travelling wave on the negative critical magnetic gradient, while the travelling direction is still inwardly. The negative critical magnetic gradient is achieved in the FC condition. In the FC condition, three different cases of a dc background field were studied: B_{dc}=10.0 mT, 5.0 mT and 2.5 mT. Since the maximum trapping field of the sample was 7.0 mT, for the case B_{dc}=10.0 mT, after switching off the dc background field, it was expected to obtain a conical magnetic profile based on the Bean model. For the cases B_{dc}=5.0 mT and 2.5 mT, it was expected to obtain a truncated conical magnetic profile. Fig. 5.16 shows the measured magnetic flux density above the centre of the YBCO sample for three different dc conditions. The output of the inverter was set at V_{ac}=10.0 V, and f=0.1 Hz. The timeline is marked at the top of the diagram. The sequence of the experiments was: DAC on (t=0 s); dc off (t=30 s); inverter on (t=90 s); inverter off (t=210 s); DAC off (t=270 s).

As shown in Fig. 5.16, after the inverter was switched, a drastic decay was observed for B_{dc}=10.0 mT , and minor decays for B_{dc}=5.0 mT and 2.5 mT. It was known that, for V_{ac}=10.0 V, the maximum flux density is ~2.0 mT which is located at r=10 mm. If consider the Bean model with an oscillating field of amplitude 2.0 mT, it was expected to obtain 5.0 mT for B_{dc}=10.0 mT and 5.0 mT, and 2.5 mT for B_{dc}=2.5 mT as indicated in Fig. 5.16. However, the final field was much lower than predicted using the Bean model for B_{dc}=10.0 mT and 5.0 mT. For B_{dc}=2.5 mT, the oscillating field shouldn't have had any influence at the centre of the sample, however a slight decay was observed at the sample centre.

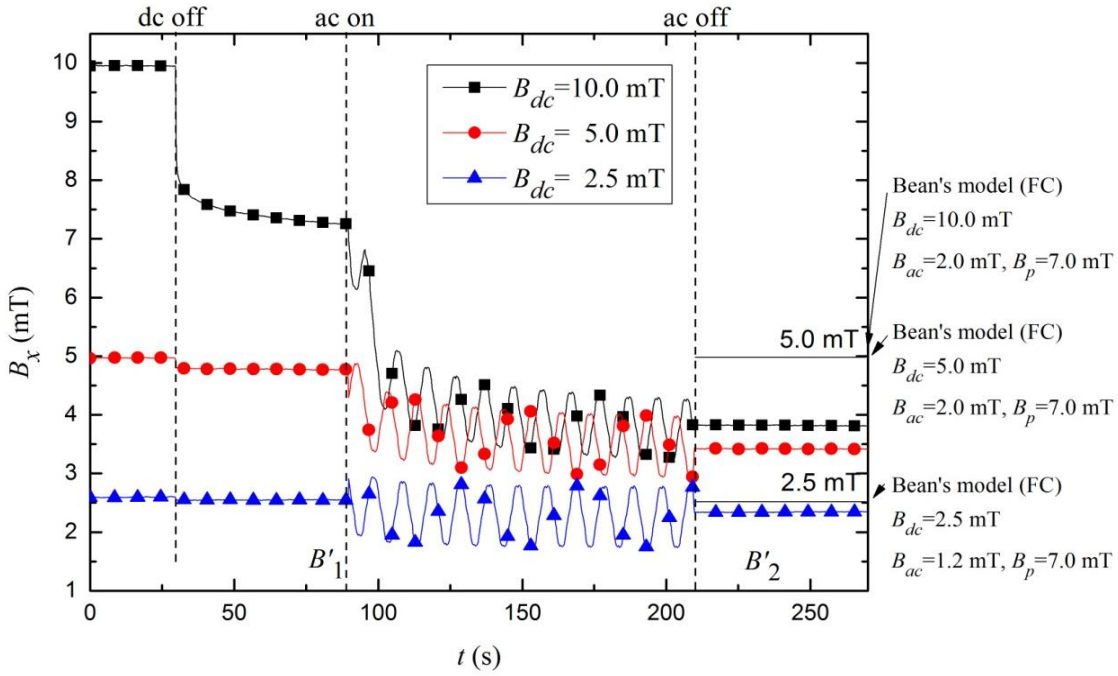

FIG. 5.16. Measured magnetic flux density above the centre of the YBCO sample for three different cases of field cooling (B_{dc}=10.0, 5.0 and 2.5 mT). The output of the inverter was set as: V_{ac}=10.0 V, f=0.1 Hz. The timeline is marked at the top of the diagram.

In order to clarify this phenomenon, the six Hall sensor array was used to directly measure the change in the magnetic gradient. Fig. 5.17(a) shows the measured and calculated magnetic gradient under different dc background conditions before switching on the inverter. Fig. 5.17(b) shows the normalised current density inside the YBCO sample based on the simulation. The magnetic field profile follows the Bean model prediction. For B_{dc}=10.0 mT, a conical trapped field was obtained, and for B_{dc}=5.0 mT and 2.5 mT truncated conical trapped fields were obtained. The calculated current densities show more accurately that the constant current assumption from the Bean model does apply to these cases.

Fig. 5.17(c) shows the field profile after application of the travelling wave, and Fig. 5.17(d) shows the calculated normalised current density. Comparison of Fig. 5.17(c) with (a) shows, that after the application of the travelling wave, the magnetic gradients become much smaller than previously. Fig. 5.17(d) shows more directly that the current densities are much lower than Fig. 5.17(b), and the constant current density assumption does not apply in this case.

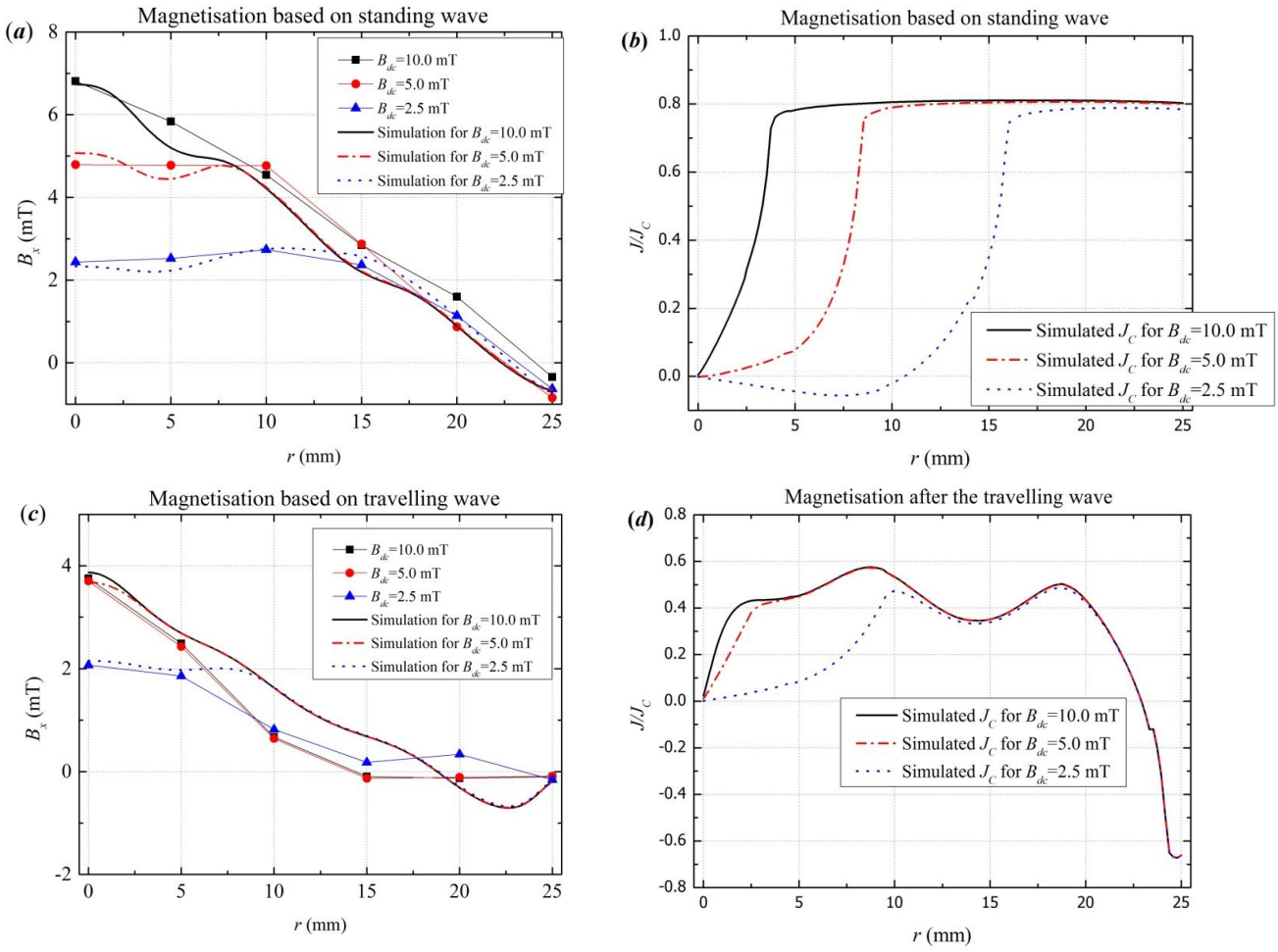

FIG. 5.17. The experimental and the simulated results of the magnetic gradient in various FC conditions before (a) and after (c) application of the travelling wave (V_{ac}=10 V). The calculated current density distributions are shown in (c) and (d) for each condition.

The experiment in this part indicates that, the travelling wave tends to attenuate the critical magnetic gradient in general, which does not necessarily depend on the direction of the gradient (positive or negative). In other words, as long as the field inhomogeneity is strong enough in space, the vortices will be rebalanced to minimize the potential energy, which attenuates the existing critical magnetic gradient. This electromagnetic behaviour can also be well simulated by the same FEM model. To further investigate this behaviour, the delta shaped trapped field will be studied next.

5.4.3 Delta shape

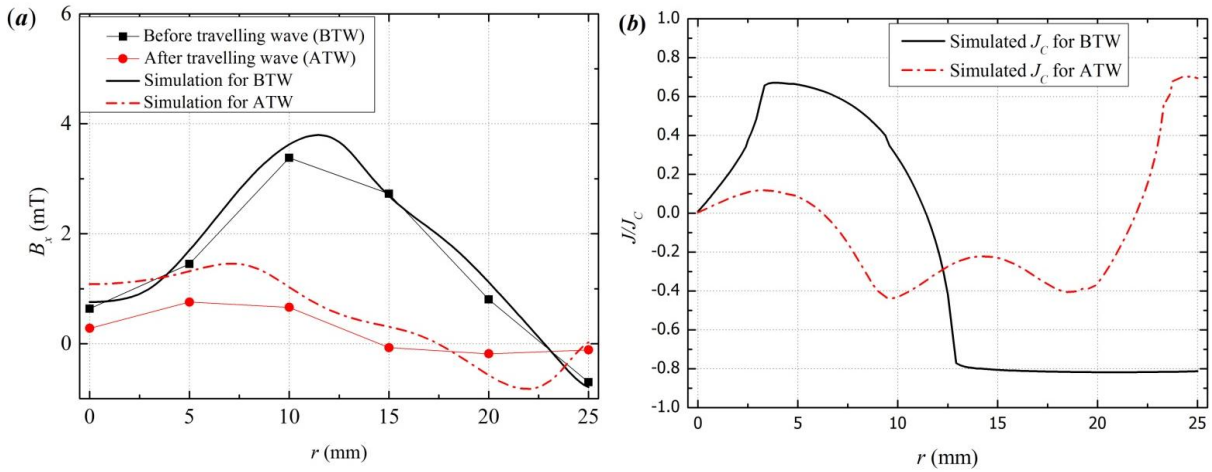

FIG. 5.18. (a) the experimental and simulated magnetic profile before and after application of the travelling wave to the delta shape trapped field; (b) the simulated current density distributions before and after applied the travelling wave.

If the dc background field was switched on until it has just fully penetrated the YBCO sample, and then switched off, a delta shape magnetisation profile is obtained using the Bean model. Both positive and negative magnetic gradient will be present in the sample. In this case, it is interesting to know how the flux moves inside the YBCO sample under the influence of the travelling wave. Fig. 5.18 shows the experimental and simulated results for this case. The dc background field was set at 7.0 mT, and the output voltage of the inverter was set at V_{ac}=10 V (~2.0 mT). The frequency of the inverter was 0.1 Hz while the travelling wave was directed inward.

As shown in Fig. 5.18(a), a delta shaped magnetic profile was obtained after switching off the dc background field. After applying the travelling wave, the existing magnetic gradient became almost flat, as shown in Fig. 5.18(a). The flattening of the existing magnetic gradient occurs with both the positive and negative magnetic gradients. As shown in Fig. 5.18(b), before application of the travelling wave, the current density distribution more or less follows the Bean model prediction. However, after applying the travelling wave, the current density is much lower than the critical current density. In general, the application of a travelling magnetic wave tends to compromise the existing critical magnetic gradient in the round shaped YBCO sample.

In conclusion, the above experiments have shown that, the travelling wave tends to attenuate the existing critical magnetic gradients in the YBCO thin film. This is a very interesting phenomenon, since the E-J power law is highly non-linear, which is a relation very close to the Bean model. However, the simulation gives rise to a magnetic profile that is not suitable for the Bean model prediction (the constant current assumption), and it fits the results obtained from the experimental measurements in all cases. Although the E-J power relationship is a fitted equation from the direct four-point measurement, it does represent the two basic vortex behaviours in the type-II superconductor: flux creep ($J < J_C$) and flux flow($J \geq J_C$). The flux flow is caused by the rebalance of magnetic stress inside the superconductor, i.e. as the magnetic stress (or the density of vortices) increases on one side, the magnetic force (or Lorentz force) pushes the vortex to a lower density position. This force is balanced by the pinning force from the defects of Lattice of the material (pinning centres), which give rise to critical magnetic gradient in macroscopic scale. Therefore, the unbalance of the magnetic stress inside the type-II superconductor is the main dragging force which helps flux flow moving inside the material.

In the homogeneous oscillating field conditions, as the magnetic field increases, the magnetic energy increase uniformly in space. For a single vortex placed on the existing critical magnetic gradient in the type-II superconductor, the uniform change of magnetic energy surround it does not alter the net force acting on it. Therefore, the vortex is till balance and not moved by the change of the background field, and the critical magnetic gradient keeps stable, which is the ideal condition of the Bean model. However, for the travelling wave condition, the problem can be different, since the magnetic energy is inhomogeneous in space: the crest region and the trough region coexist. Suppose a single vortex is again place on an existing critical magnetic gradient, then the magnetic energy is increased on one side (crest region) but decreased on other side (trough region), then the net force acting on the vortex will be altered, which leads to the locally movement of the vortex to a new position, which ends up with a lower magnetic gradient as suggested in the experiments and simulations.

The change of the existing critical magnetic gradient caused by the travelling wave can be very clear to identify, since the magnetic gradient was in a “critical state”, and can be easily altered by the unbalanced magnetic energy (field inhomogeneity such as travelling wave). There are other ways to show the effect of travelling wave as experiment on the penetration of the sample with the travelling wave which will be introduced in the next section. Both of these studies suggest that, the travelling wave can be very efficient in transporting the flux inside the YBCO sample comparing with the homogeneous oscillating field.

The geometry of the sample can be also very important to identify this phenomenon. If the sample has a small demagnetization factor (or a thick sample), there is enough superconducting region to

shield the applied field, and the current distribution is not uniform across the thickness of the sample, which made it hard to identify the change of the magnetic gradient. However, for a superconducting sample with large demagnetization factor (as the YBCO sample used in our experiment), the current distribution is almost uniform across the thickness (can be verified from our FEM model), and the change of magnetic gradient can be directly measured. Also, the sample should be sufficiently large, otherwise the crest region and the trough will not be coexist in the sample region to provide enough field inhomogeneity.

5.5 Study into the penetration of a round shape YBCO sample with the travelling magnetic wave [5]

There are many factors which might affect the migration of flux caused by a travelling wave, such as the pinning force in the film, the geometry of the film, inhomogeneity such as wavelength and the amplitude of the travelling wave, etc. In order to "pump" flux into the superconducting loop, the flux must be able to travel across the superconducting film. In this experiment, a travelling wave at different amplitudes (output voltage of the inverter) is applied to the round shaped YBCO sample to study how the YBCO sample is penetrated by the travelling wave. The experiment began with a single Hall sensor measurement, and a detailed study followed using a six Hall sensor array.

Unlike the experiments shown in the last sections, the round shape YBCO sample is not pre-magnetised to give a critical magnetic gradient. The purpose of the study is to show that the travelling wave is efficient in transporting flux inside the sample. The results from this experiment can be useful in better understanding of the HTS flux pump, as it shows how the flux migrates through the YBCO thin film.

5.5.1 Single Hall Sensor Measurement

The experiment was performed in a zero dc background field. During the experiment, only the travelling wave was applied to the YBCO sample. The flux density B_x was measured 1.5 mm above the centre of the sample. The output voltages of the inverter were selected as: V_{ac}=10.0 V, 20.0 V,

[5] Published in *IEEE Transactions on Applied Superconductivity* **24** (3), 4600304 (2014)

100.0 V, and the output frequency was preset at f=0.1 Hz. The travelling wave was set in the inward direction. The experimental results for V_{ac}=10.0 V are shown in Fig. 5.19. The measured amplitude of the travelling wave without a sample is denoted as B_{field}, and the measured amplitude in the presence of the YBCO sample is denoted as B_{YBCO}, It was found that, in the presence of the YBCO sample, the measured amplitude of the magnetic wave at the centre was higher than the applied travelling wave. The ratio of $B_{\mathrm{YBCO}}/B_{\mathrm{field}}$ is plotted in Fig. 5.20. For r = 0 mm (at the centre of the sample), after inserting the YBCO sample, the field measured at the centre was roughly twice that of the applied field.

Superconductors are better known for shielding an applied field rather than amplifying the field. Although amplification of an applied magnetic field can be achieved using magnetic lenses [151-154], this is also based on the fact that the superconductors expel the flux from their central regions. In order to clarify this phenomenon, the single Hall sensor was placed at r = 10 mm. The amplitude of the travelling wave at r = 10 mm was much bigger than at r = 0 mm, as shown in Fig. 5.3. The ratio of $B_{\mathrm{YBCO}}/B_{\mathrm{field}}$ is also plotted in Fig. 5.20. At r = 10 mm, the amplitude of the wave was reduced in the presence of the sample ($B_{\mathrm{YBCO}}/B_{\mathrm{field}}$ <1.0).

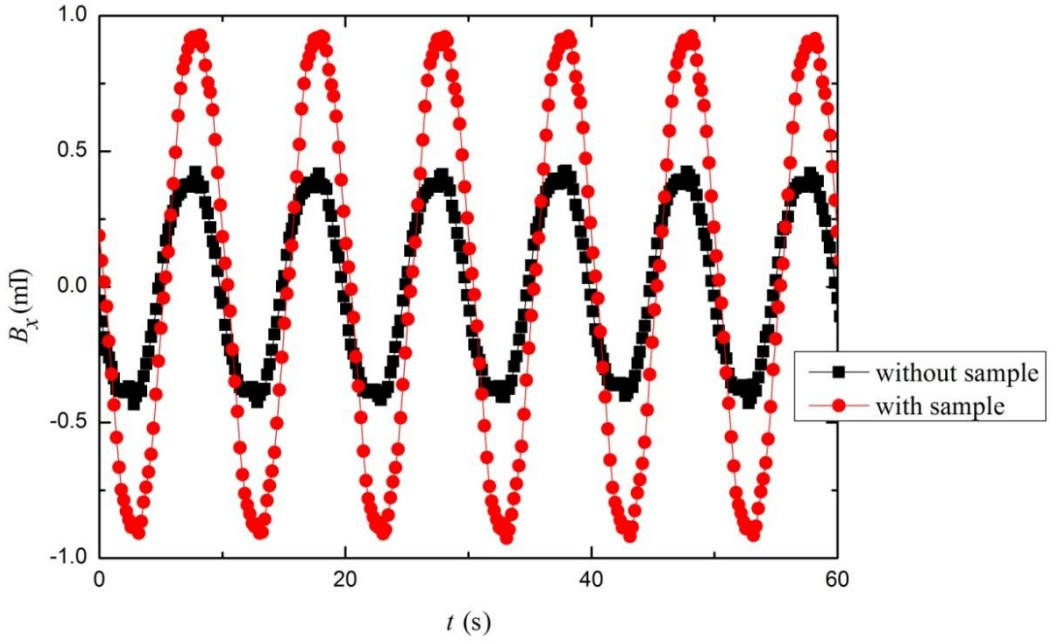

FIG. 5.19. Amplification of the flux density in the presence of a YBCO sample in the centre of the rig. The output voltage of the inverter was set as V_{ac} =10.0 V (~2.0 mT), frequency f=0.1 Hz.

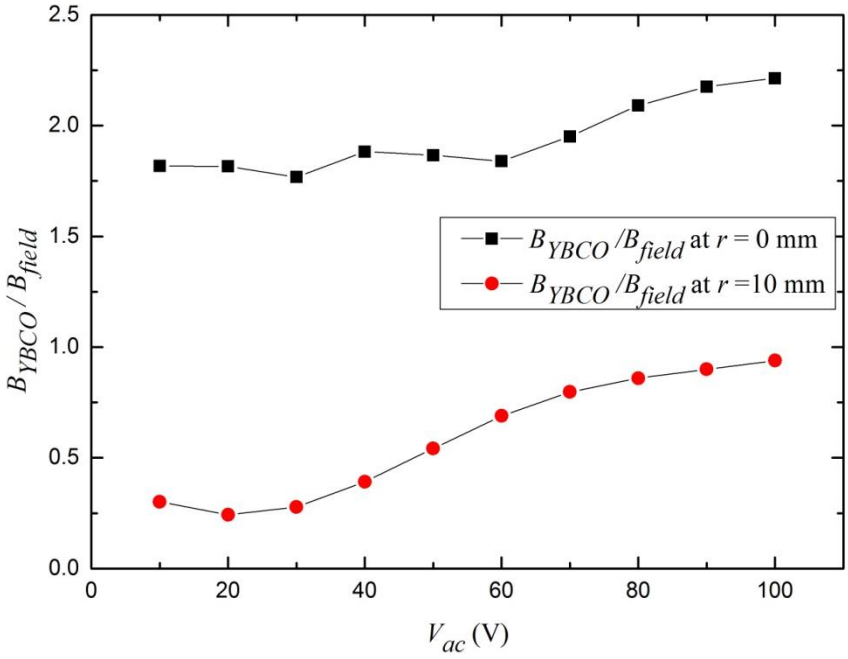

FIG. 5.20. Coefficient of amplification B_{YBCO}/B_{field} measured at r =0 mm and r =10 mm inside the rig.

There are two possible explanation for the phenomenon described above:

1. The high magnetic strength at r = 10 mm helped the flux to move from r = 10 mm to r = 0 mm inside the YBCO sample, which could explain the increase of the measured field at r = 0 mm and the decrease of the field at r= 10 mm.
2. The round shaped YBCO sample acts as a magnetic lens and the magnetic flux is bent above the YBCO sample. Since the single Hall sensor does not directly touch the surface of the sample, it measures the bent flux instead of the actual flux in the YBCO sample.

The first explanation suggests that the flux actually migrates into the sample centre with the help of the travelling wave, while the second explanation suggests that the flux is not necessarily "pushed" into the sample centre. In order to clarify this phenomenon, the six Hall sensor array was used to measure the trapped field inside the YBCO sample.

5.5.2 Six hall Sensor Array Measurement

In order to clarify the phenomenon described in the previous section and to observe the penetration process of the travelling wave into the YBCO sample, the six Hall sensor array was used to measure the trapped field along a radius. The experiment was performed in a zero dc field. After ZFC, the travelling wave was switched on and off at random times. During the time that the travelling wave was switched off, the trapped magnetic flux across the radius of the sample was recorded by the six Hall sensors. This gives the value of flux trapped inside the YBCO sample at each location. The output voltage of the inverter was selected as: V_{ac} = 10 V, 20 V, and 40 V. The output frequency was preset as: f=1.0 Hz. The travelling wave was set to move in an inward direction. For each output voltage, the travelling wave was switched on and off 20 times to obtain a profile of the trapped field.

Fig. 5.21 shows the experimental results at V_{ac} = 10 V. The maximum amplitude was measured as 1.17 mT at r =10 mm, as shown in Fig. 5.3. There was no trapped field measured at $r \leq 10$ mm, which indicates that there was no net magnetisation in the central region, i.e. the travelling wave did not penetrate into the central region of the sample.

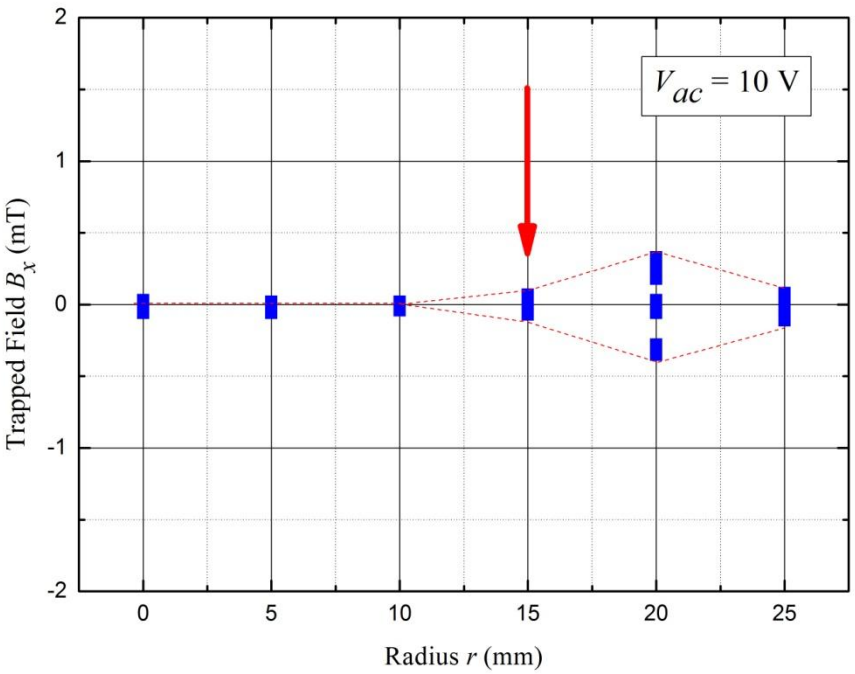

FIG. 5.21. Measured trapped field after application of a travelling wave at V_{ac}=10 V. Each position was measured 20 times. The oscillation was observed at r =15 mm as marked by the red arrow.

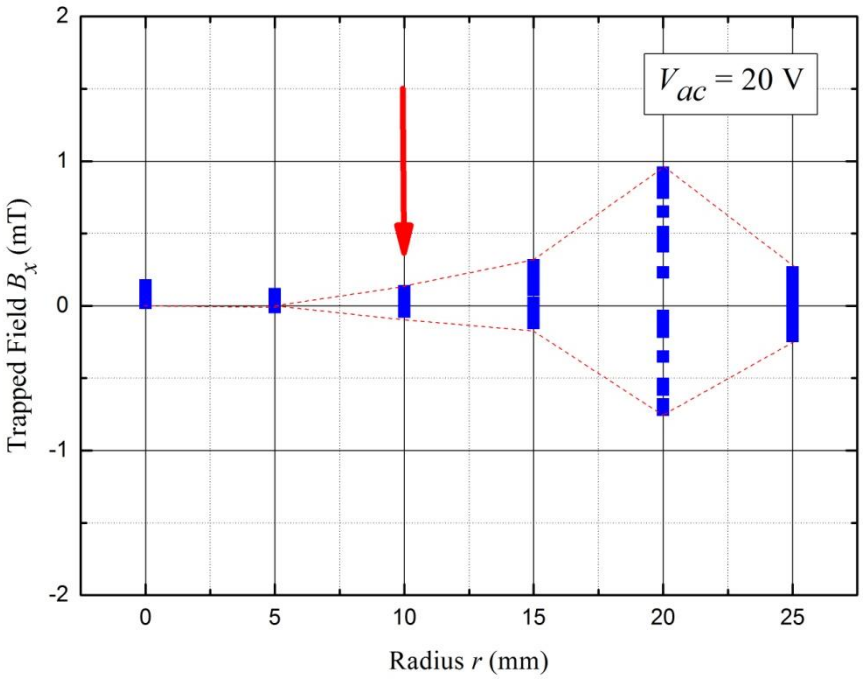

FIG. 5.22. Measured trapped field after application of a travelling wave at V_{ac}=20 V. Each position was measured 20 times. The oscillation was observed at r =10 mm as marked by the red arrow.

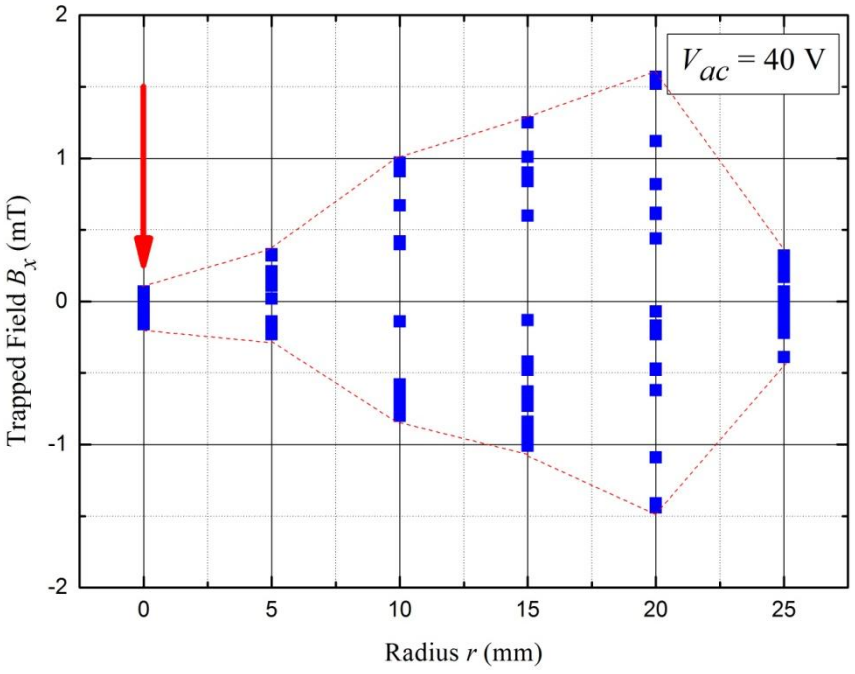

FIG. 5.23. Measured trapped field after application of a travelling wave at V_{ac}=40 V. Each position was measured 20 times. The oscillation was observed at r =0 mm as marked by the red arrow.

Fig. 5.22 shows the experimental result at V_{ac} = 20 V. The maximum amplitude was measured as 2.08 mT at r =10 mm, as shown in Fig. 5.3. The oscillation of the field was observed at r = 10 mm, which indicates that the travelling wave had penetrated to r =10 mm. In the second curve (B_{YBCO} /B_{field} at r=10 mm) in Fig. 5.20, the point at V_{ac}= 20 V is at the minimum value. It seems that after V_{ac}≥20 V, the flux began to penetrate into the region $r \leq 20$ mm, which resulted in the rising of the curve B_{YBCO} /B_{field} at r=10 mm in Fig. 5.20.

Fig. 5.23 shows the experimental result at V_{ac} = 40 V. The maximum amplitude was measured as 4.36 mT at r =10 mm, as shown in Fig. 5.3. Fig. 5.23 shows that the travelling wave has fully penetrated the YBCO sample. Oscillation of the trapped field was observed at the centre of the sample. As discussed earlier in this chapter, for a conventional homogeneous oscillating field to fully penetrate this YBCO sample requires an amplitude of 7.0 mT. However, in Fig. 5.23, the sample was fully penetrated at a maximum amplitude of 4.36 mT. Compared to a homogeneous oscillating field, a travelling wave is more efficient in penetrating the YBCO sample. Additionally, it is clear that as the width of the YBCO film increases, it becomes harder for the travelling wave to help the flux to move across the sample. However, this obstacle can be overcome by increasing the field inhomogeneity such as increase the amplitude of the travelling wave.

Now come back to the two possibilities proposed in Section 5.5.1. As can be seen from Fig.5.21 to Fig.5.23, the magnetic flux was gradually penetrated into the YBCO sample as the output voltage of the inverter increases. The sample was fully penetrated only at V_{ac}≥40 V, thereby, the amplification of the wave measured in Fig. 5.19 is rather caused by the bending of magnetic flux above the sample.

This experiment suggests that, comparing with the homogeneous oscillating field, the travelling wave is more efficient in transporting the magnetic flux inside the YBCO sample. Moreover, it suggests that, in order to transport the flux across a wide sample, the amplitude of the applied travelling wave should increase accordingly. Therefore, in order to build an efficient HTS flux pump for HTS coil, to carefully choose the width of the sample and the amplitude of the travelling wave is crucially important.

5.6 The influence of the travelling speed and travelling direction on the magnetisation of the round shape YBCO sample

In the previous experiments, the output frequency was preset at f=0.1 or 1.0 Hz. The travelling wave was set to move in the inward direction. However, it is uncertain whether the travelling speed

and the travelling direction influence the magnetisation of the round shaped YBCO sample. This section increases the output frequency 10.0 Hz, 100.0 Hz, and 400.0 Hz. The magnetisation results were compared to the case f=0.1 and 1.0 Hz. In the latter part of this section, the travelling wave is reversed to move in the outward direction, and the magnetisation results are compared with the inward case.

The purpose of changing the output frequency of the inverter is to show that the magnetisation is dependent on the sweeping speed of the travelling wave: as the sweeping speed increases, the amount of change decreases.

To reverse the travelling direction, it was aimed at finding a possible magnetic coupling phenomenon in the YBCO sample: if the magnetic coupling is present in the experiment, the magnetisation should be dependent on the travelling direction. However, in this experiment, the final magnetisation profile is independent on the direction, which suggests that the magnetic coupling is not present in current experiment. This might due to the fact that the field inhomogeneity from this device is not strong enough to cause magnetic coupling, which is one of the reason of developing the updated CTMFP magnet with shorter wavelength.

5.6.1 The influence of the travelling speed

The experiment was performed under ZFC conditions. The sequence of the experiment was: cool the sample under ZFC conditions; the DAC on (t = 0 s); dc field on (B_{dc} = 7.0 mT, t=30 s); travelling wave on (V_{ac} =10 V, t = 90 s); travelling wave off (t = 210 s); dc field off (t = 240 s); DAC off (t = 300 s). The output frequency of the inverter was selected as: f = 0.1 Hz, 1.0 Hz, 10.0 Hz, 100.0 Hz, and 400.0 Hz. As shown in Table 4.2, up to f=100.0 Hz, the change in impedance was quite small for the three phase windings. Only in the case f=400.0 Hz were the changes to the impedance of phases U and V reasonably large.

Fig. 5.24 shows the experimental results before and after application of the travelling wave at different output frequencies of the inverter. The attenuation of the existing magnetic gradient was dependent on the travelling speed of the wave. As the speed of the wave increases, the demagnetisation is reduced so that there is a smaller increase in the magnetic gradient.

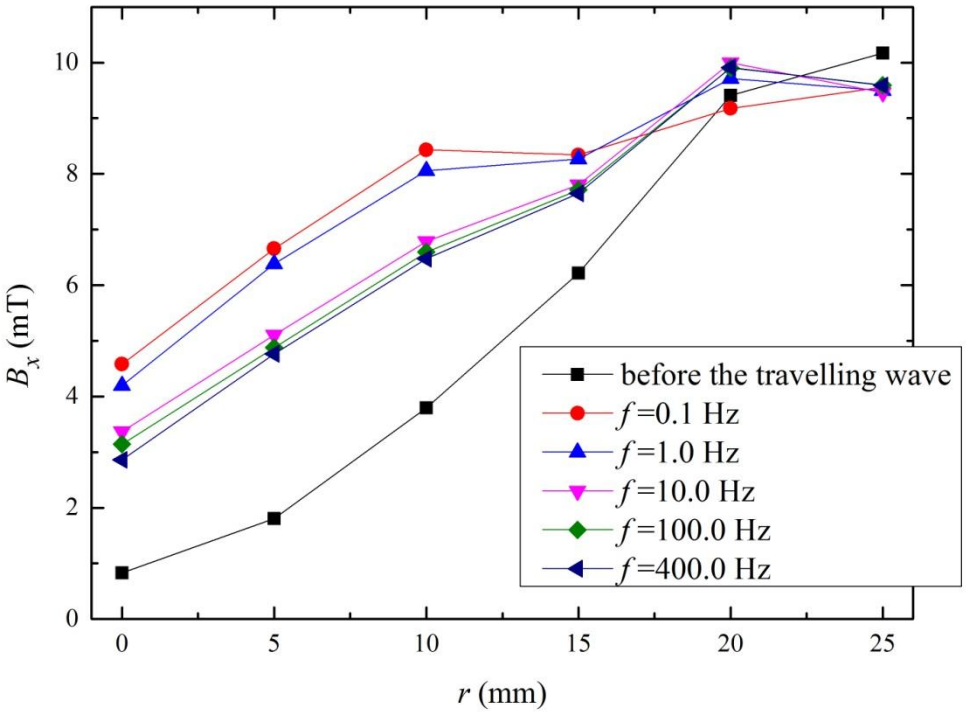

FIG. 5.24. The measured magnetic gradient before and after application of the travelling wave with different output frequencies of the inverter.

5.6.2 The influence of the travelling direction

In all the experiments mentioned above, the travelling direction of the magnetic wave was preset to the inward direction, i.e. travelling toward the sample centre, as indicated in Fig. 4.2. The sequences of the phase windings are indicated in Fig. 4.1. However, it is unknown whether the travelling direction of the wave affects the final magnetic profile. In other words, if the magnetisation is dependent on the travelling direction, a macroscopic magnetic coupling phenomenon (as suggested by the "dc transformer" in Section 3.3) might be identified in the experiment. In this part of experiment, the travelling direction was reversed to move in the outward direction, i.e. travelling from the sample centre to the edge of the sample.

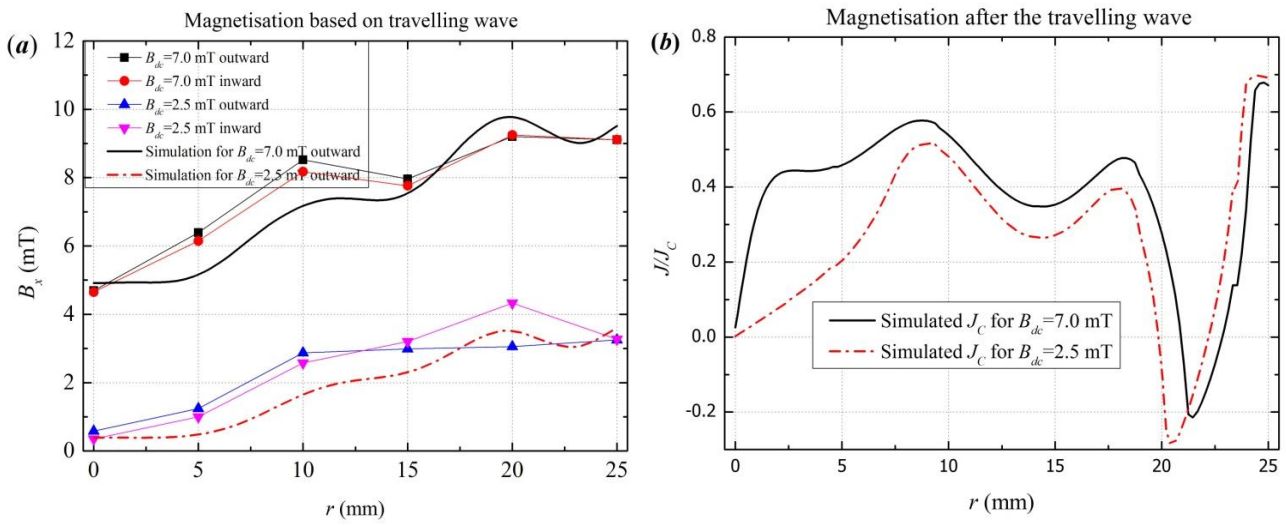

FIG. 5.25. (a) the experimental and simulated magnetic gradient after applying a travelling magnetic wave which travels outwardly, a comparison is made with the condition that the wave travel inwardly; (b) the simulated current density distribution for different dc background conditions.

The experiment follows the same ZFC process as described in Section 5.6.1. The output voltage of the inverter was set at V_{ac}=10.0 V, and the output frequency of the inverter was preset at f=0.1 Hz. Two different dc conditions were selected: B_{dc}=7.0 mT and 2.5 mT. The experiment and simulated results are shown in Fig. 5.25. In Fig. 5.25(a), it is clear that, after application of the travelling wave to the existing magnetic gradient, the resultant magnetisation gradients are almost the same in both directions. These results suggest that **there was no magnetic coupling phenomenon observed in this experiment**. The results could also be reliably predicted using the FEM model. The decrease in existing current density was also observed in the simulation, as shown in Fig.5.25(b).

The absent of magnetic coupling in the experiment might suggest that, the field inhomogeneity is not strong enough to cause the vortices to travel with the wave. In other words, if the field inhomogeneity is strong enough, some regions of the travelling wave might work like a potential well, which traps the vortices inside and helps it moving with the wave. The methods to increase the field inhomogeneity include: increase the amplitude of the travelling wave, the other way is to shorten the wavelength. The first method can be easily achieved by increasing the output voltage of the inverter. However, as suggested in Section 5.4.1, as the amplitude of the wave increases, the trapped field starts

to oscillate inside the sample, while the monotonic increase of the field in the centre was not clear in the experiment, which suggests that the "magnetic coupling" was not clearly observed. This is probably due to the fact that, comparing with the width of the YBCO thin film, the wavelength of the CTMFP magnets was too long (comparable to the radius of the sample). Suppose one wavelength presents one potential well, if the dimension of the potential well is slightly larger than the sample dimension (as in our experiment), then it does not necessarily lead to the coupling phenomenon since the whole superconducting region is inside the potential well. Therefore, the best way to make a clear observation is to shorten the wavelength. For an established CTMFP magnet with three phase connection, the wavelength is determined by the width of the phase windings and iron yokes, and cannot be altered. To shorten the wavelength, the CTMFP magnet should be redesigned with a smaller width of the phase windings and iron yokes. For this reason, the updated CTMFP magnet was developed to shorten the wavelength to increase the field inhomogeneity, while keeping the amplitude constant. The experimental results will be discussed in the next chapter.

5.7 Special topic on ac losses

In this section, a special topic is proposed on ac losses caused by a travelling magnetic wave. Under an ac magnetic field, the movement of magnetic flux inside type-II superconductor will produce heat (as discussed in Chapter 2). AC loss estimation is very important to the design of superconducting electric motors and cooling systems. Studies on ac losses from superconducting coils are also important since they help understanding of how ac losses are generated inside the coil, and how they might be minimised. To date, there are numerous publications regarding the estimation of ac losses in HTS coils [155-157].

Inside a superconducting electric machine, ac loss can be classified into two categories: transport current loss [158] and magnetisation loss [159]. The transport current loss is induced by the current flow through the superconducting coil, and the magnetisation loss is induced by the external ac magnetic field. Inside a superconducting electric machine, the magnetisation loss is caused by the travelling magnetic wave from the three phase windings and the field of the rotor. The magnetisation due to the travelling wave can be very different from that due to a homogeneous oscillating field, as suggested in the previous sections. Therefore, a discussion is proposed as to whether the travelling wave can be treated the same as a homogeneous oscillating field in ac magnetisation loss calculations.

This section studies the ac loss based on the round shaped YBCO sample with the help the FEM

model validated in the early part of this chapter. This study intends to seek insight into how the ac loss differs between a travelling wave and a homogeneous oscillating field in this particular sample.

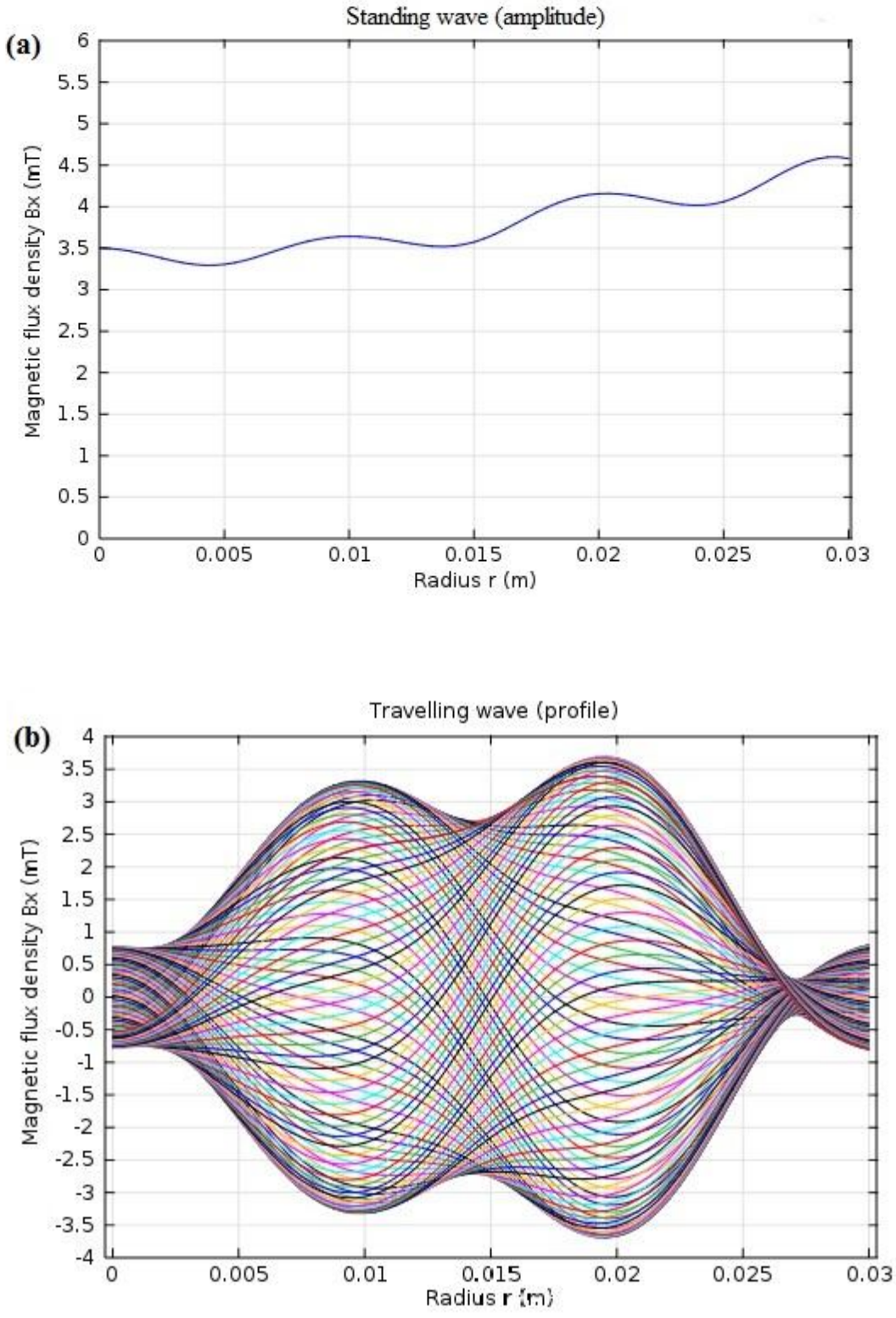

FIG. 5.26. The applied magnetic wave at 3.5 mT. (a) the amplitude of the homogeneous oscillating field; (b) the travelling wave profile over one period.

In the simulation, the amplitude of the waves (both travelling wave and homogeneous oscillating field) was selected as 3.5 mT or 7.0 mT. In the case of 3.5 mT, the YBCO sample is not fully penetrated by both waves; in the case of 7.0 mT, the YBCO sample is fully penetrated by both waves. The travelling wave profile and the amplitude of the homogeneous oscillating field for B_{ac}=3.5 mT are shown in Fig. 5.26.

The heat power at a specific point inside the YBCO film can be calculated by the scalar multiplication of the electric field and current density:

$$P = \boldsymbol{E} \cdot \boldsymbol{J} \tag{5.10}$$

Since the electric field always lies parallel to the current density in an HTS film, the heat power in Equation (5.10) is always positive. The ac loss per cycle can be calculated using the integration of the heat power over the superconducting region over one period:

$$Q = \int_0^T dt \int_V \boldsymbol{E} \cdot \boldsymbol{J} dV \tag{5.11}$$

For this specific 2 inch diameter YBCO sample, the heat power is uniform across the thickness, which can be verified in the model. Therefore Equation (5.11) is extended to:

$$Q = 2\pi D \int_0^T dt \int_0^R \left(\boldsymbol{E} \cdot \boldsymbol{J} \right) r dr \tag{5.12}$$

where D =200 nm is the thickness of the YBCO layer, R=25.4 mm is the radius of the sample, and T=10 s is the period of the wave.

The calculated results of the travelling wave and homogeneous oscillating field at B_{ac}=3.5 mT are shown in Fig. 5.27. Although the amplitudes of the travelling wave and homogeneous oscillating field are the same, the ac loss caused by the travelling wave is about 1/3 as much as the ac loss caused by the homogeneous oscillating field. For the homogeneous oscillating field, the highest value of ac loss occurs at the edge of the YBCO sample, as shown in Fig. 5.27(a), and then linearly decreases into the sample and stops at $r \approx 21$ mm. This ac loss profile is very common based on the Bean model estimation, since the sample edge experiences the greatest flux flow and the inner area experience progressively less flux flow as the radius decreases. However, for the travelling wave condition as shown in Fig. 5.27(b), there are two separate regions which produce heat: $12\ \text{mm} \lesssim r \lesssim 19\ \text{mm}$ and $r \gtrsim 22.5\ \text{mm}$. There is no heat generated between the regions, which suggests that the current density induced in this region is lower than the critical current density.

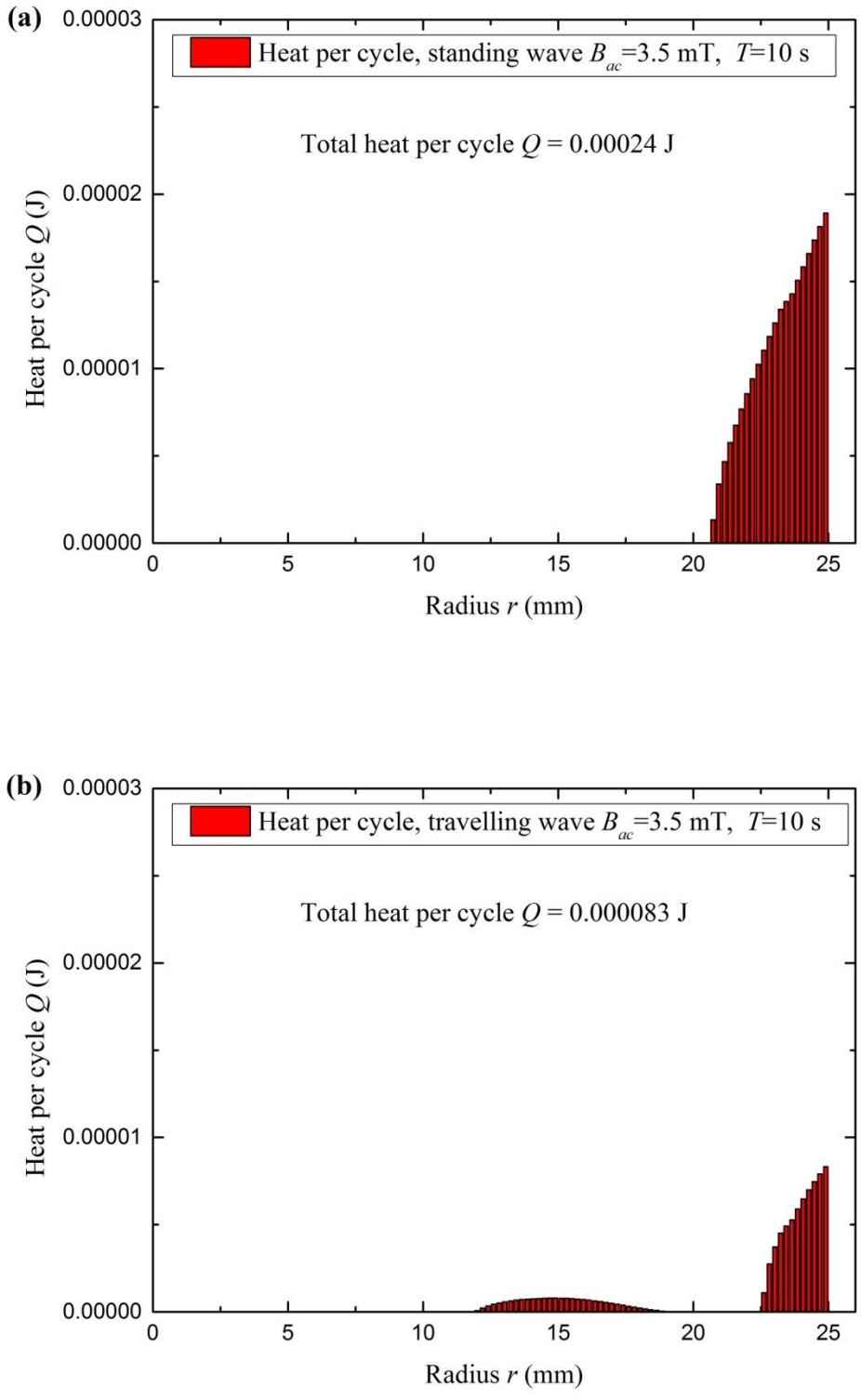

FIG. 5.27. The heat per cycle for the (a) homogeneous oscillating field condition, (b) travelling wave condition, both with B_{ac}=3.5 mT, f=0.1 Hz.

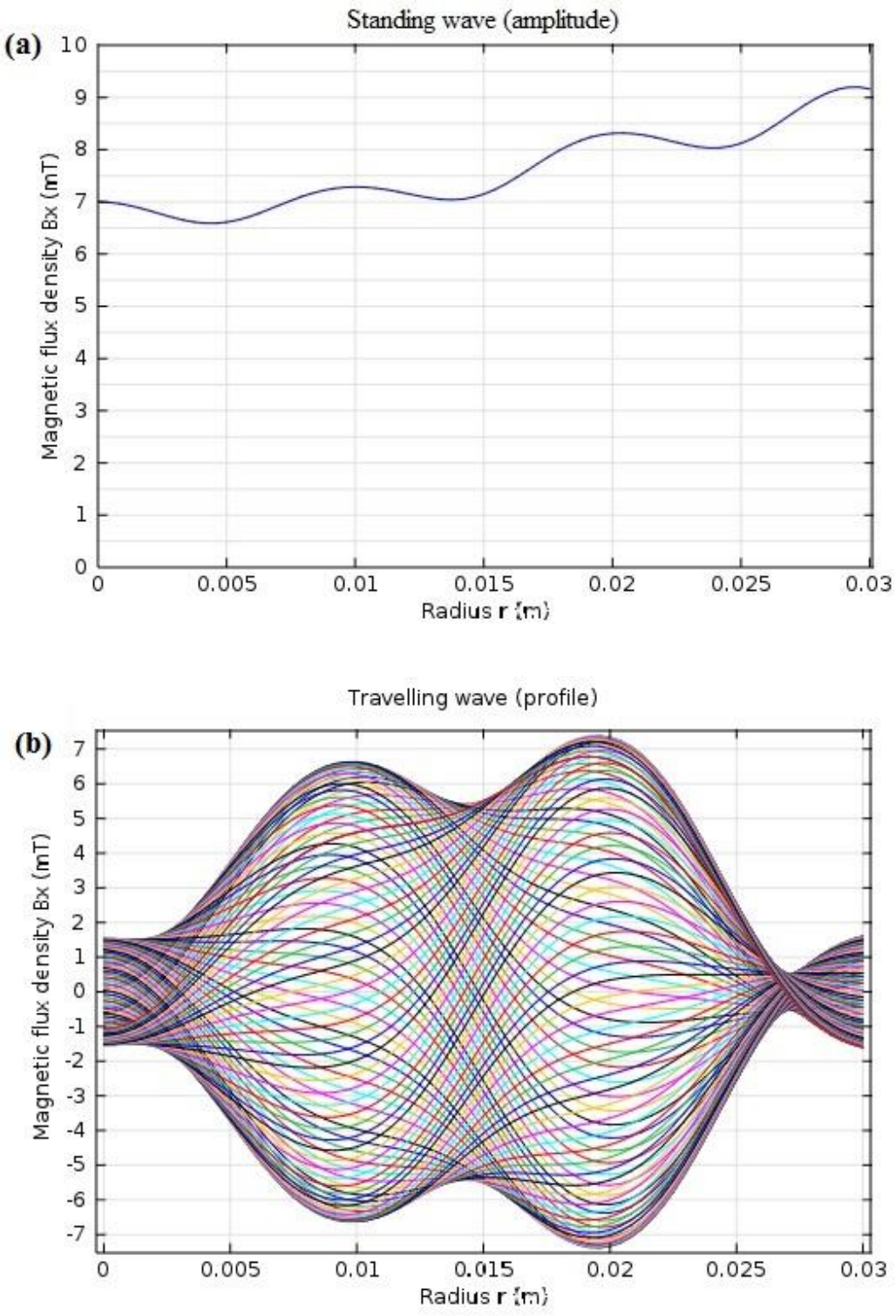

FIG. 5.28. The applied magnetic wave at 7.0 mT. (a) the amplitude of the homogeneous oscillating field; (b) the travelling wave profile over one period.

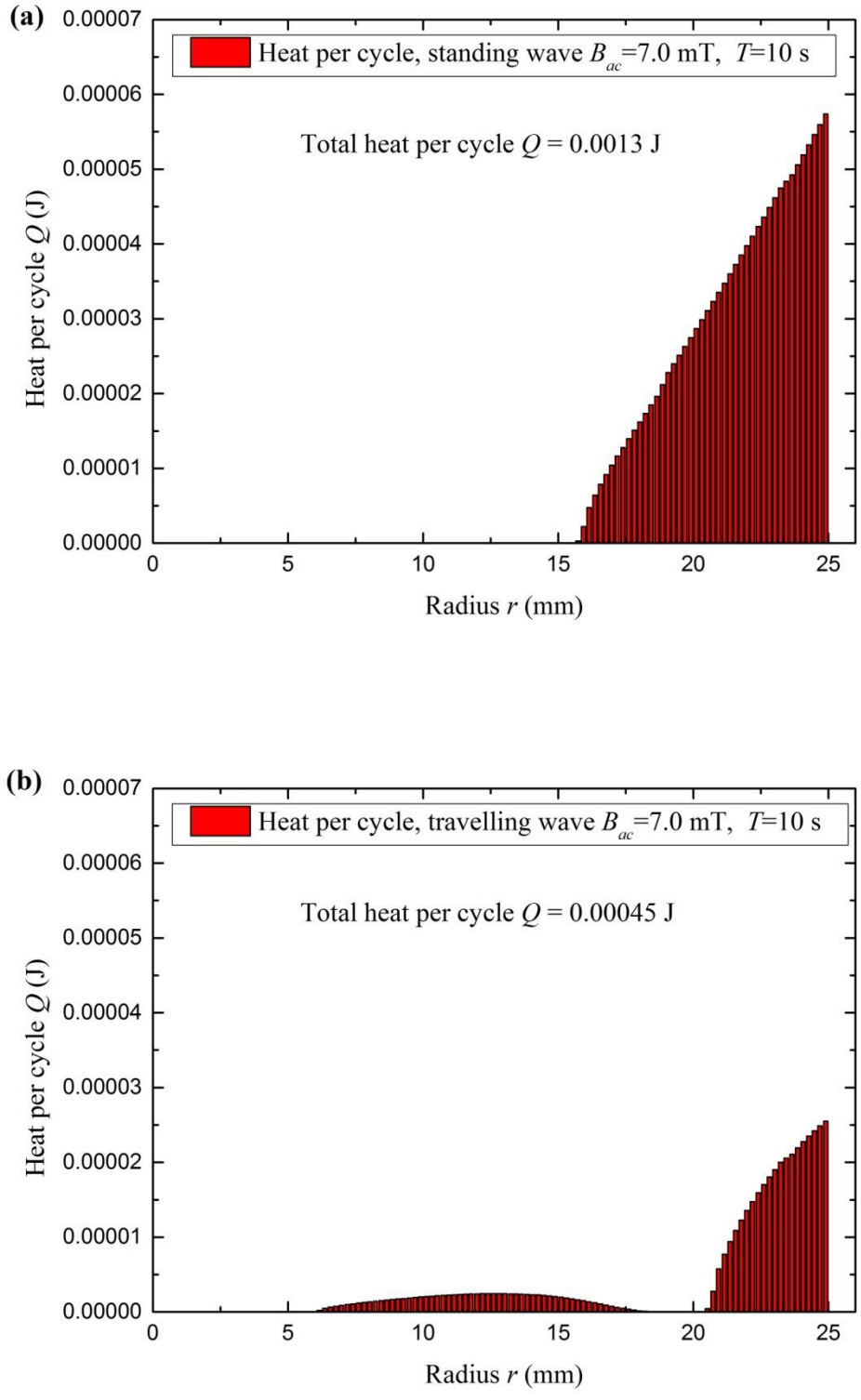

FIG. 5.29. The heat per cycle for the (a) homogeneous oscillating field condition, (b) travelling wave condition, both with B_{ac}=7.0 mT, f=0.1 Hz.

The travelling wave profile and the amplitude of the homogeneous oscillating field for B_{ac}=7.0 mT are shown in Fig. 5.28. The calculated results of the ac losses are shown in Fig. 5.29 for the homogeneous oscillating field and the travelling wave, respectively. The ac loss per cycle of the travelling wave is about 1/3 of the ac loss per cycle of the homogeneous oscillating field. In a homogeneous oscillating field, the greatest ac loss is at the edge, and then decreases linearly as the radius decreases. However, for the travelling wave condition, the greatest ac loss occurs within the regions $6\ \text{mm} \lesssim r \lesssim 17\ \text{mm}$ and $r \gtrsim 21\ \text{mm}$. These results are similar to the conditions at B_{ac}=3.5 mT as shown in Fig. 5.27. Under a homogeneous oscillating field, although the magnetic field penetrates much further into the YBCO film, heat is only generated in the restricted regions near the edge. This is due to the fact that the induced currents in the central regions are slightly lower than the critical current density J_C, and thus no heat is generated based on the *E*- *J* power relation (negligible *E* value). Additionally, Fig.5.27 and Fig.5.29 show that even though the magnetic field penetrated much further into the sample, heat is only generated in restricted regions. This indicates that the induced current density is higher than J_C only in these regions.

For both conditions, the homogeneous oscillating field and the travelling wave have the same amplitude (B_{ac}=3.5 mT and 7.0 mT). However, for the single layer round shaped YBCO sample, the ac loss caused by the travelling wave is about 1/3 of that caused by the homogeneous oscillating field. The distribution of the ac loss inside the sample is also different between the homogeneous oscillating field and the travelling wave. This provides a clue that, the ac magnetisation losses caused by a travelling wave can be very different from those caused by a homogeneous oscillating field, although the amplitude is the same. These simulation results are understandable from the viewpoint which has been mentioned in previous sections. In the homogeneous oscillating field condition, the change of magnetic energy is homogeneous in space, the flux flow in the penetrated regions keeps the magnetic gradient equals to the critical gradient. Therefore, the change of flux density $-dB/dt$ is almost uniform in the region which experiences the flux flow. The value $-dB/dt$ gives rise to the induced electric field *E* as from the Faraday's law, which suggest *E* is uniform in the flux flow region. Since the magnetic gradient keeps stable ($\pm J_C$), based on Equation (5.10), the heat power is uniform in the flux flow regions. In the homogeneous oscillating field, the edge of the sample experiences the flux flow at all time, which gives rise to the most of the heat generated based Equation (5.12). However, as the radius decrease, the time of the inner region experiencing the flux flow decreases based on the Bean model, which leads to the decrease of heat generated into the inner region as shown in Fig.5.27(a) and Fig.5.29(a). However, in the experiment, for the travelling wave condition, the non-uniform distribution of background magnetic energy helps some regions to have local flux flow (internally) rather than the uniform flux flow as in the homogeneous oscillating field condition. This gives rise to the inner region which produces heat as shown in Fig. 5.27(b) and Fig. 5.29(b). This

inner region is not connected to the outer region, which suggests that the flux flow is rather locally, and these flux does not necessarily have to flow in and out from the sample edge. The heat produced by the travelling wave is 1/3 of the homogeneous oscillating field is due to the fact that, the current density in the travelling wave condition is much smaller than J_C in many regions of the superconducting film. Based on the non-linear *E-J* power law, this leads to negligible *E* which leads to negligible heat generated.

This part of work only provides the calculated ac magnetisation loss in this specific single layer round shape YBCO sample. However, for HTS coil working in travelling wave conditions, it should be studied more deeply, since it has more complicated geometries and structures. Nevertheless, this study provides a clue that, the ac magnetic loss caused by the travelling wave might need to be clarified from the one caused by the homogeneous oscillating field.

5.8 Conclusion

In this chapter, the 2 inch diameter round shape YBCO sample was studied with the help of the original CTMFP magnet. It was found that the magnetisation based on a travelling wave is very different from a homogeneous oscillating field. While the magnetisation based on the homogeneous oscillating field can be accurately predicted using the Bean model, magnetisation based on a travelling wave does not follow the Bean model prediction. The six Hall sensor array was used to measure the change in magnetic gradient under the influence of a travelling wave, and the results showed that the existing critical magnetic gradient is compromised by a travelling wave. The simulation based on the FEM software shows that the current density is attenuated across the sample. This suggests that the constant current density assumption used in the Bean model does not apply to a travelling wave. It was also found that a travelling wave is more likely to penetrate into the YBCO sample than a homogeneous oscillating field. Moreover, the decrease in the existing magnetic gradient is related to the sweeping speed of the travelling wave, but not related to the travelling direction. In other words, there was no macroscopic magnetic coupling phenomenon found in this experiment.

These results suggest that:

1. In the magnetisation and ac loss calculations, a travelling wave cannot be equated to a homogeneous oscillating field. The validity of simplify a travelling wave as a homogeneous oscillating field in such cases should be investigated.

2. A travelling wave is more likely to cause the flux to move inside the YBCO thin film, which suggests that it is possible to apply a travelling wave in order to transport flux into a superconducting loop.

In this experiment, the device used for the study is the original CTMFP magnet, which has a fixed wavelength. In order to have a clue of how the field inhomogeneity influence the magnetisation, the updated CTMFP magnet was proposed, which has a shorter wavelength comparing with the original CTMFP. Moreover, in this experiment, the magnetic coupling is not observed, which might suggest that the field inhomogeneity is not strong enough in the present device. For these reasons, the updated CTMFP magnet was developed and the experimental results with the round shape YBCO sample will be presented in the next chapter.

CHAPTER 6

THE UPDATED CTMFP: EXPERIMENTAL RESULTS

This chapter presents the experimental results for the updated CTMFP magnet and the round shaped YBCO sample. As discussed in Chapter 4, the magnetic wave produced by the updated CTMFP magnet has a greater field inhomogeneity compared to the magnetic wave produced by the original CTMFP magnet. The original CTMFP magnet can only produce a travelling wave with a single pole-pair, whereas the updated CTMFP magnet can produce two pole pairs (with six phase connections) or four pole pairs (with three phase connections). The purpose of designing the updated CTMFP magnet was to show how the degree of field inhomogeneity influences the magnetisation of a YBCO sample.

In this chapter, the experiments will focus on indentifying the effect of field inhomogeneity on the magnetisation of the YBCO sample. Moreover, the experiment will also intend to find the possible magnetic coupling phenomenon as the wavelength decreases.

Section 6.1 studies the travelling magnetic waves produced by the updated CTMFP magnet. The magnetic waves are compared between the original CTMFP magnet, the updated CTMFP magnet with a six phase connection, and the updated CTMFP magnet with a three phase connection. Section 6.2 presents and discusses the experimental results with the six phase connection on the round shape YBCO sample. Section 6.3 discusses the experimental results with the three phase connection on the round shape YBCO sample. In comparison with the experimental results of the six phase connection and the three phase connection, it was found that, as the degree of the field inhomogeneity increases, more flux have been transported into the YBCO sample, even though the amplitudes of the travelling waves are the same. It supports the idea that the field inhomogeneity is the key factor that causes the flux migration. Moreover, in Section 6.3, a possible magnetic coupling phenomenon has been observed. However, this phenomenon requires further investigation in the future.

6.1 Characteristics of the travelling wave

In this section, the characteristics of the travelling waves from the original CTMFP magnet, the updated CTMFP magnet with six phase connection, and the updated CTMFP magnet with three phase connection will be compared and studied. As discussed in Section 4.3, there are two methods for connecting the phase windings to the updated CTMFP magnet. One method is to connect the phase windings with a 60 ºphase shift. The phase sequence in this instance is: U, -W, V, -U, W, -V. Another method is to connect the phase windings with a 120 ºphase shift, as was done for the original CTMFP magnet. The phase sequence in this instance is: U, V, W. For the original CTMFP, the width of the phase windings and the iron yoke was 5.0 mm. The original CTMFP magnet can produce a travelling wave of single pole-pair as discussed in Section 5.1. However, the width of the phase windings and the iron yoke is 1.25 mm for the updated CTMFP magnet, which is 1/4 of the width of the original CTMFP magnet (5.0 mm). For the six phase connection with 60 ºphase shift, the wavelength of the updated CTMFP magnet is 1/2 of the wavelength compared to the original CTMFP magnet. For the three phase connection with 120 ºphase shift, the wavelength of the updated CTMFP magnet is 1/4 of the wavelength compared to the original CTMFP magnet. A simulation was performed with the help of the AC/DC mode in COMSOL to visualise the waveform. The domains in the model are shown in Fig. 6.1 and their properties are shown in Table 6.1 for the six phase connection and in Table 6.2 for three phase connection.

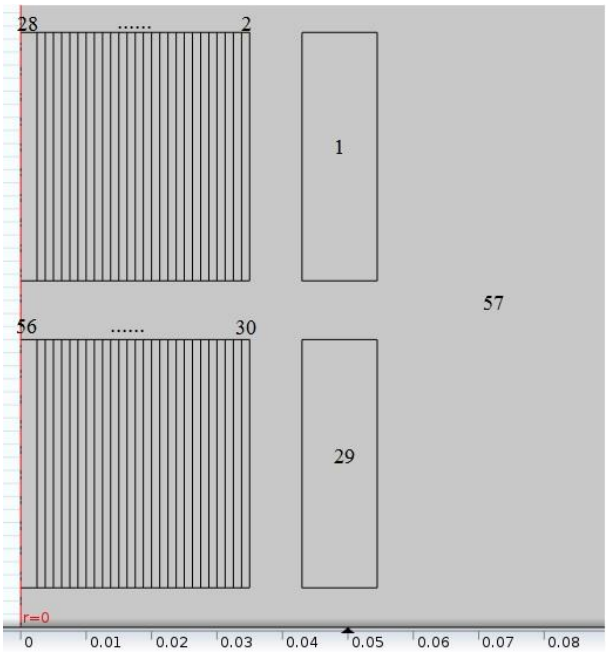

FIG. 6.1. The COMSOL AC/DC model for the updated CTMFP magnet and the geometry labels.

TABLE 6.1

DOMAINS AND PARAMETERS FOR FIG. 6.1 (SIX PHASE CONNECTION)

	Air	Soft iron	Phase U	Phase -W	Phase V	Phase -U	Phase W	Phase -V	DC windings
Domain	57	2, 4, 6,…28; 30, 32, 34, …56	3, 15, 27; 31, 43, 55	5, 17; 33, 45	7, 19; 35, 47	9, 21; 37, 49	11, 23; 39,51	13, 25; 41, 53	1, 29
ρ (Ω/m)	1.0	1.0	1.0	1.0	1.0	1.0	1.0	1.0	1.0
μ_r	1.0	40000	1.0	1.0	1.0	1.0	1.0	1.0	1.0

* ρ =1.0 Ω·m refers to a large resistivity in the model, which represents dielectric property of the air, and help preventing the non-uniform distribution of the current inside the copper regions.

TABLE 6.2

DOMAINS AND PARAMETERS FOR FIG. 6.1 (THREE PHASE CONNECTION)

	Air	Soft iron	Phase U	Phase V	Phase W	DC windings
Domain	57	2, 4, 6,…28; 30, 32, 34, …56	3, 9, 15, 21, 27; 31,37,43,49, 55	5, 11, 17, 23; 33,39,45,51	7,13,19,25; 35,41,47,53	1, 29
ρ (Ω/m)	1.0	1.0	1.0	1.0	1.0	1.0
μ_r	1.0	40000	1.0	1.0	1.0	1.0

* ρ =1.0 Ω·m refers to a large resistivity in the model, which represents dielectric property of the air, and help preventing the non-uniform distribution of the current inside the copper regions.

In Fig. 6.2, the travelling waves produced by the original CTMFP magnet, the updated CTMFP magnet with six phase connection and the updated CTMFP magnet with three phase connection are compared. The waveforms were simulated using the AC/DC model in COMSOL. The travelling magnetic wave produced by the original CTMFP magnet has a single pole-pair, whereas the travelling wave produced by the updated CTMFP magnet with the six phase connection has two pole pairs, and the travelling wave from the updated CTMFP magnet with the three phase connection has four pole-pairs. For travelling waves of equal amplitude, the wave produced by the original CTMFP magnet has the smallest inhomogeneity, and the wave produced by the updated CTMFP magnet with the three phase connection has the greatest inhomogeneity.

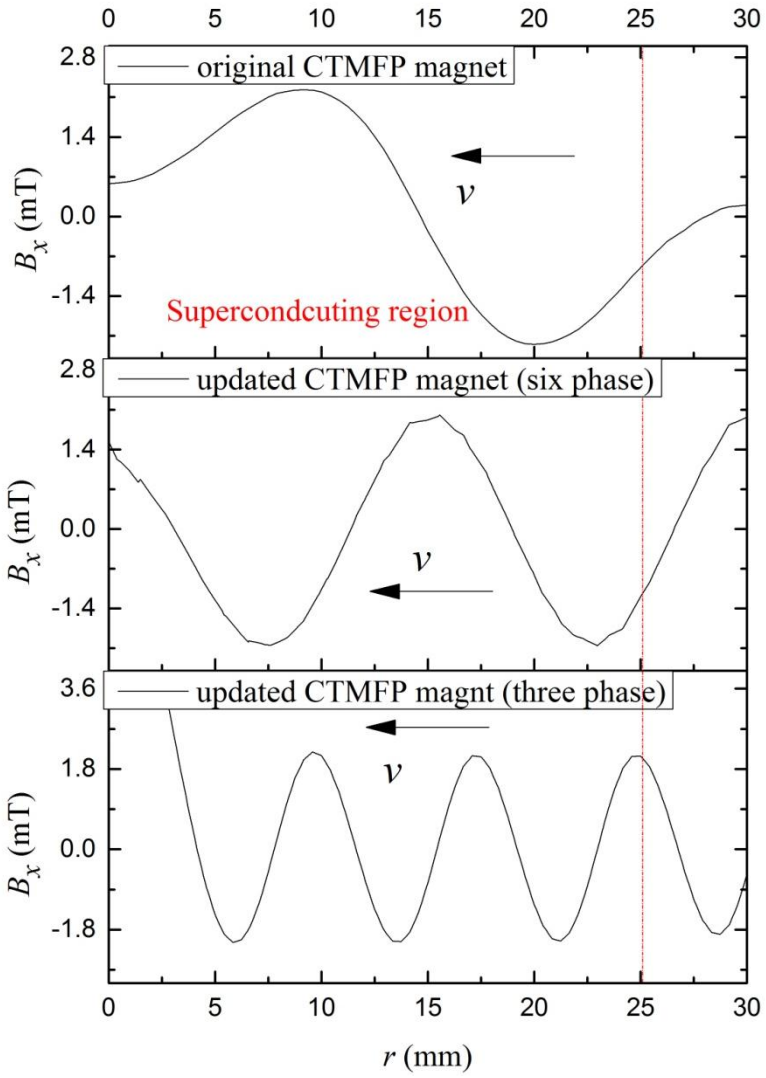

FIG. 6.2. The simulated results for a travelling magnetic wave generated by the original CMTFP magnet, the updated CTMFP magnet with a six phase connection, and the updated CTMFP magnet with a three phase connection.

The following sections discuss the results of the travelling wave produced by the CTMFP magnet with either a six phase connection or a three phase connection.

6.1.1 The travelling wave produced by a six phase connection

This section analyses the travelling wave produced by the updated CTMFP magnet with a six phase connection. The connection of the phase windings followed the consequence as shown in Fig. 4.9 and Table 6.1. The phase shift between the neighbouring windings was 60 º.

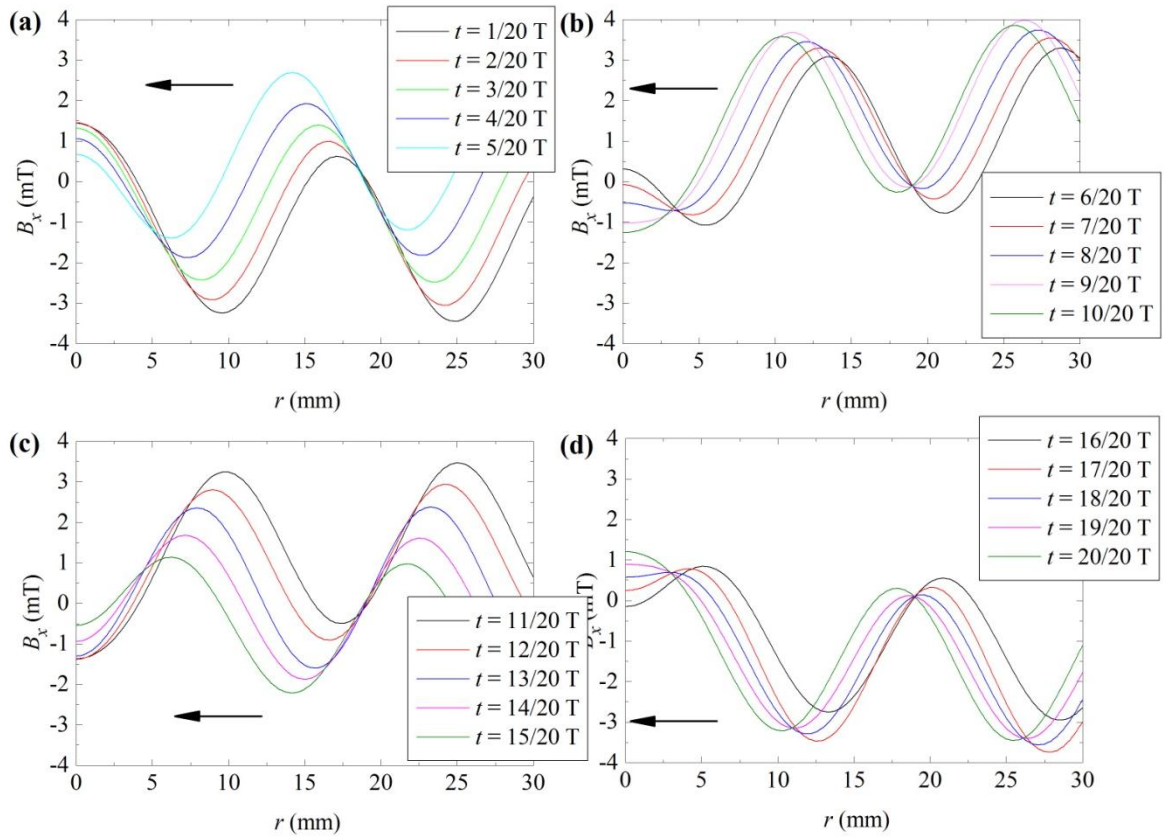

FIG. 6.3. The travelling magnetic wave simulated using the AC/DC mode in COMSOL for the updated CTMFP magnet with six phase connection. The time interval for each curve is 1/20 phase (T).

The travelling wave was simulated using the AC/DC mode in COMSOL. The results of the simulation are shown in Fig. 6.3. The time interval between the neighbouring curves is 1/20 period. The magnetic wave not only travels, but the centre line of the wave also oscillates. This was not conducive to the experiment. However, as long as the wave travels and the crest regions and trough regions coexist, there was no harm done to our ability to determine the effects of the travelling wave on the YBCO sample.

In Fig.6.4, 100 curves within one period (1/00 period interval) are plotted together to show the magnetic profile of the travelling wave. There are two peaks located at $r \approx 12$ mm and $r \approx 27$ mm. The field at $r \approx 18$ mm is almost equal to zero throughout the whole period. The fifteen Hall sensor array shown in Fig. 4.17 was installed to measure the maximum values of the field at each location. The results are plotted in Fig. 6.5. Comparing Fig.6.5 with Fig.6.4, shows that the updated CTMFP magnet

is operational and in good condition, and its magnetic behaviour can be accurately predicted using the FEM software.

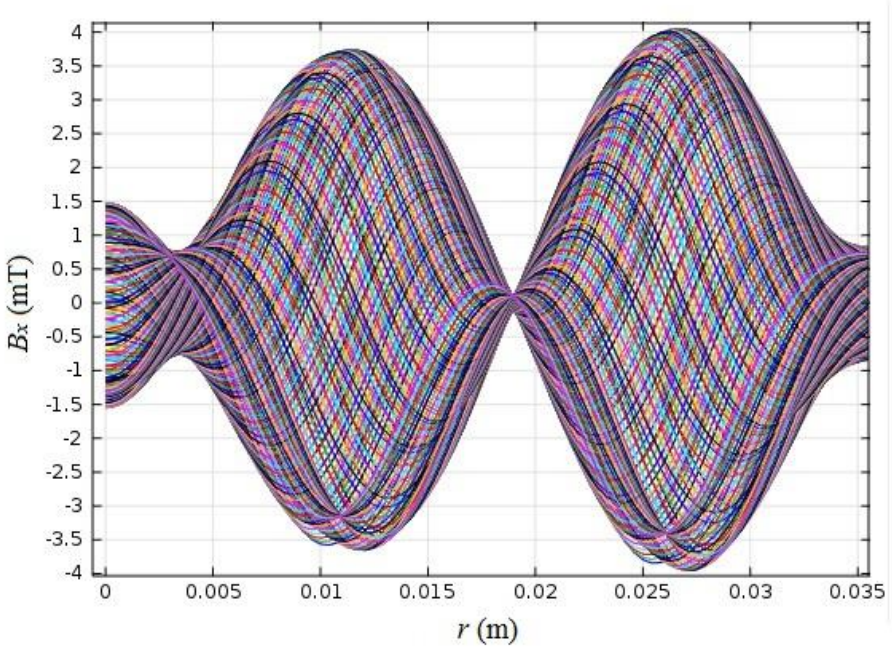

FIG. 6.4. The simulated result of the travelling wave over one period produced by the updated CTMFP magnet with a six phase connection. The time interval for neighbouring curves is 1/100 period.

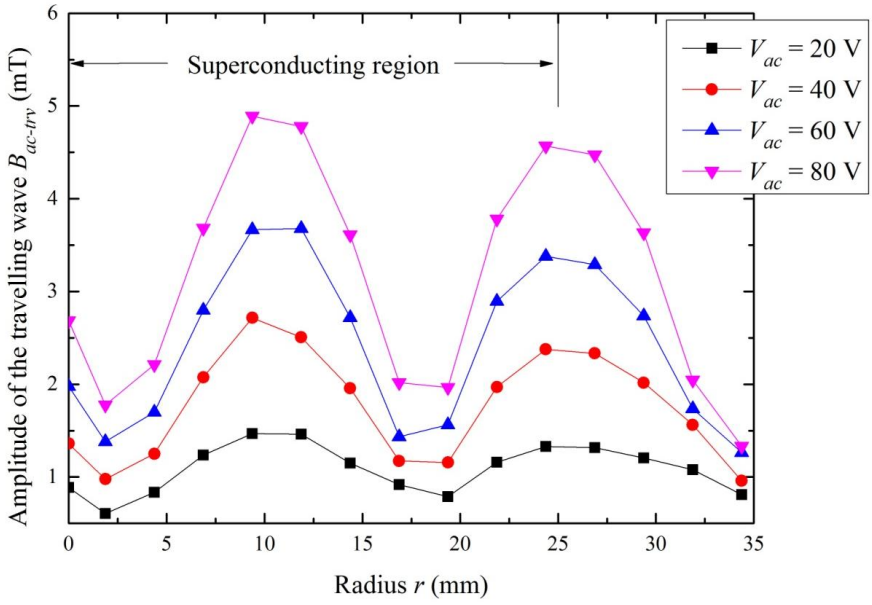

FIG. 6.5. The measured maximum values of the travelling wave across the radius of the updated CTMFP magnet with a six phase connection.

Comparison of Fig.6.3 and Fig.6.4 shows that the magnetic profile shown in Fig.6.4 does not necessarily present the actual amplitude of the travelling wave, since the centre line of the wave is oscillating as the wave travels. From the model, it was estimated that the actual amplitude of the travelling wave is about 53% of the maximum value at $r \approx 12$ mm in Fig. 6.4. Therefore, for the four cases shown in Fig. 6.5, the actual amplitudes of the wave are: ~0.78 mT (V_{ac}=20 V), ~1.44 mT (V_{ac}=40 V), ~1.94 mT (V_{ac}=60 V), and ~2.59 mT (V_{ac}=80 V).

6.1.2 The travelling wave produced by a three phase connection

In the three phase connection, the phase windings follow the sequence U, V, W. The arrangement of the phases is listed in Table 6.2. With this connection method, the phase difference between neighbouring windings is 120 º. The wave length is 1/4 of the original CTMFP magnet, and 1/2 of the updated CTMFP with six phase connection.

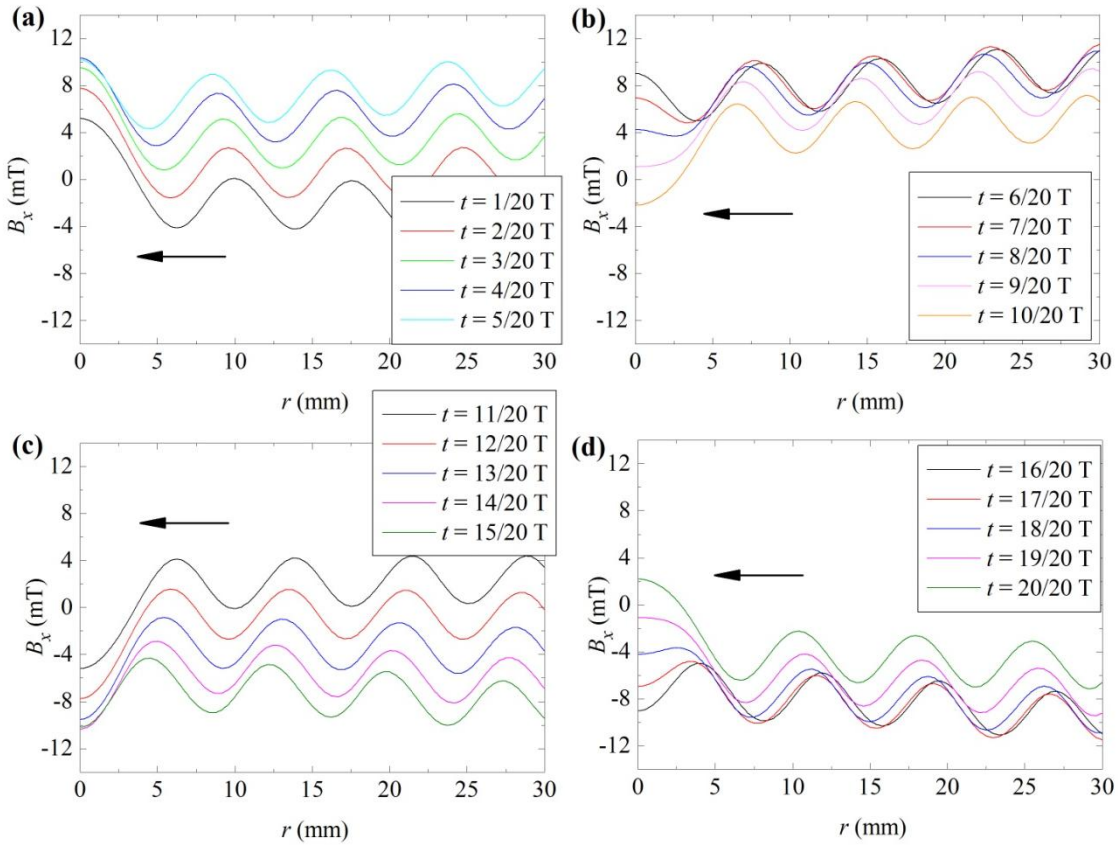

FIG. 6.6. The travelling magnetic wave simulated using the AC/DC mode in COMSOL for the updated CTMFP magnet with a three phase connection. The time interval for each curve is 1/20 phase.

The travelling wave for the updated CTMFP magnet with a three phase connection was simulated using the AC/DC mode in COMSOL, and the results are shown in Fig. 6.6. The time interval is 1/20 period between the neighbouring curves. Compared towith Fig. 6.3, the wavelength from the three phase connection is about half that of the six phase connection. Fig. 6.3 shows that the waves produced are similar to the waves produced by the six phase connection. The centre line of the waves produced by the six phase connection also oscillates.

In Fig.6.7 shows 100 curves within one period (1/00 period interval) plotted to show the maximum value of the travelling wave at each location. There are five peaks in the diagram. The fifteen hall sensor array shown in Fig. 4.17 was installed to measure the maximum value of the field at each location. The results are plotted in Fig. 6.8. Comparison Fig.6.8 to Fig.6.7 shows that the magnetic wave produced by the updated CTMFP magnet with three phase connection can be accurately predicted by using FEM software.

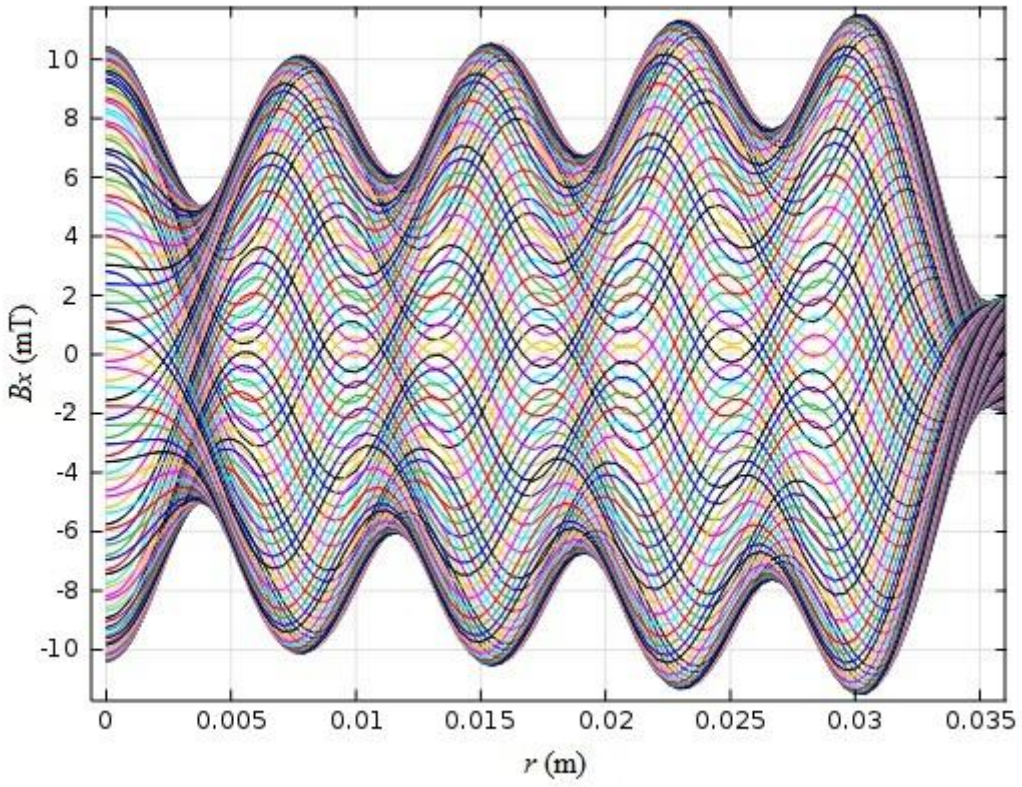

FIG. 6.7. The simulated result of the travelling wave over one period produced by the updated CTMFP magnet with a three phase connection. The time interval for neighbouring curve is 1/100 period.

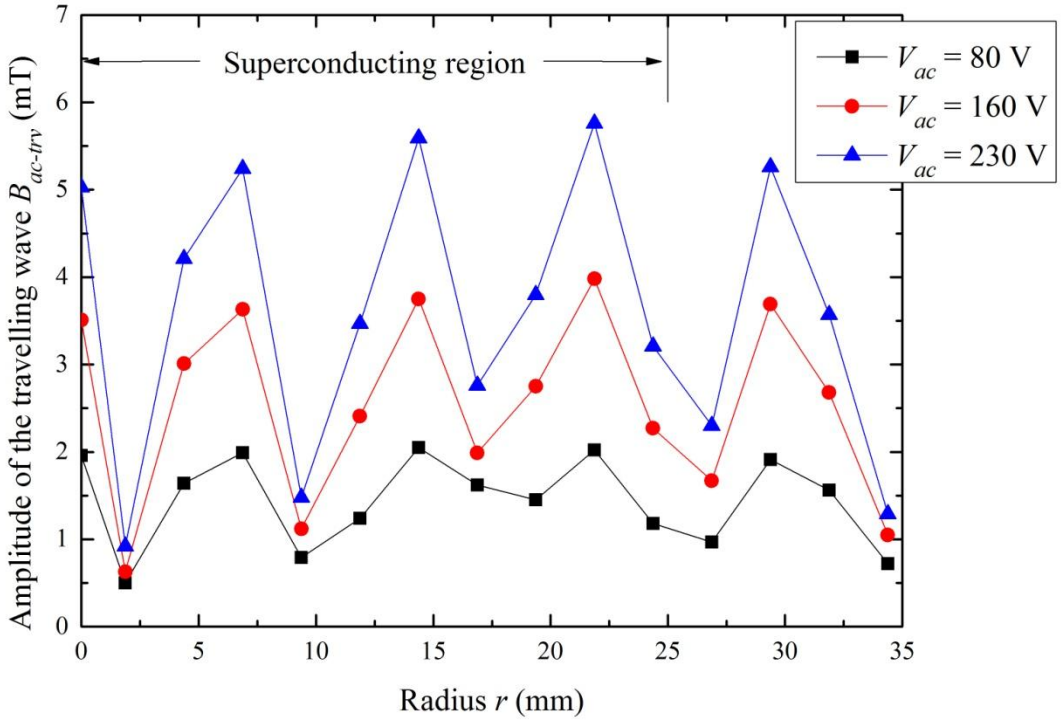

FIG. 6.8. The measured maximum values of the travelling wave across the radius of the updated CTMFP magnet with a three phase connection.

Comparison of Fig. 6.6 and Fig. 6.7 shows that the magnetic waves shown in Fig.6.7 do not necessarily represent the actual amplitude of the travelling wave, since the centre line of the wave oscillates as the wave travels. From the model, it can be estimated that the actual amplitude of the travelling wave shown is about 23% of the maximum value at r ≈7.5 mm shown in Fig. 6.7. Therefore, for the three cases shown in Fig. 6.8, the actual amplitudes of the wave are: ~0.47 mT (V_{ac}=80 V), ~0.86 mT (V_{ac}=160 V), and ~1.29 mT (V_{ac}=230 V).

In this section, it can be seen that, the travelling waves produced by the updated CTMFP magnet fit the simulation results, which suggests that the updated CTMFP magnet is well established and its magnetic behaviour can be well predicted.

In the following sections, experiments will be performed on the round shape YBCO sample with the updated CTMFP magnets.

6.2 Experiment on the updated CTMFP magnet with a six phase connection

This section studies the magnetisation of the 2 inch diameter YBCO thin film using the updated CTMFP magnet with a six phase connection. As shown in Fig.6.2, the six phase connection produces a travelling wave with two pole-pairs, whose wavelength is half of the original CTMFP magnet. The YBCO sample was studied under different conditions such as ZFC, FC, different sweeping speeds and different travelling directions. The study aims to discover whether halving the wavelength of the travelling wave will produce a different magnetisation result for the same YBCO sample.

6.2.1 ZFC condition

Under the ZFC condition, the YBCO sample was cooled in a zero background field, and then a dc field was applied to the sample. The values of the dc background field were chosen as (measured at the centre of the device): B_{dc}=2.5 mT and 7.0 mT, where B_{dc}=2.5 mT stands for the case in which the sample is not fully penetrated and B_{dc}=7.0 mT stands for the case in which the sample is fully penetrated. The output voltages of the inverter were chosen as V_{ac} = 20 V, 40 V, 60 V, and 80 V. The sequence of the experiment was: DAC on (t=0 s); dc field on (t=10 s); travelling wave on (t=20 s); travelling wave off (t=40 s); dc field off (t=50 s); DAC off (t=60 s).

The experimental results for the case B_{dc}=2.5 mT are shown in Fig. 6.9. The first curve in Fig.6.9 is the measured magnetic gradient after application of the dc field but before applying the travelling wave (at t≈19 s). The four other curves are the magnetic gradients after applying the travelling wave but before switching off the dc field (at t≈49 s).

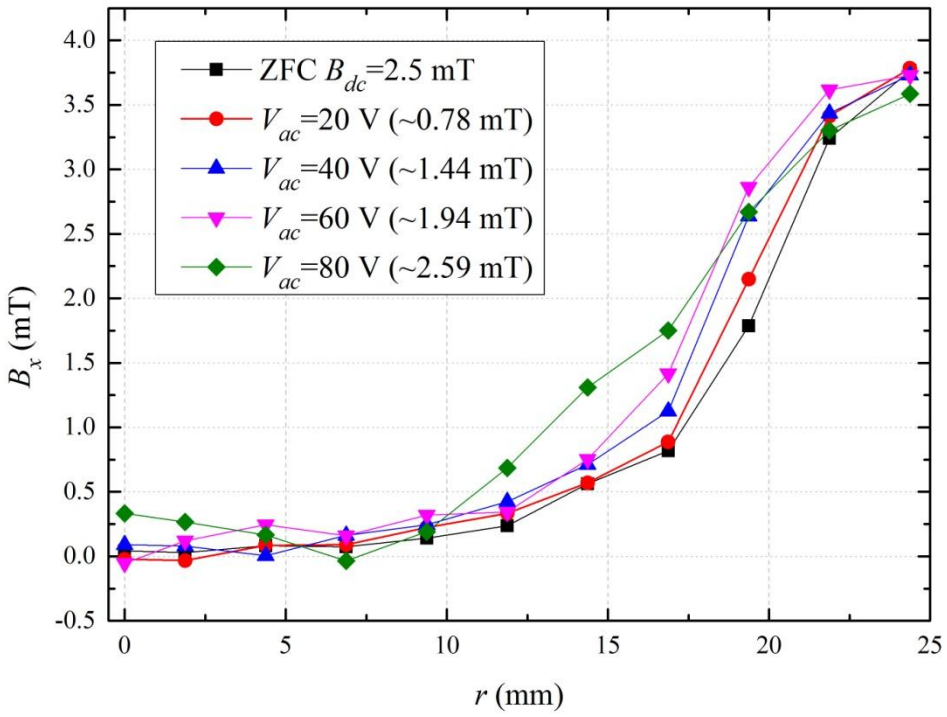

FIG. 6.9. The measured magnetic gradient for the round shaped YBCO sample when B_{dc}=2.5 mT before and after applying the travelling wave with a six phase connection.

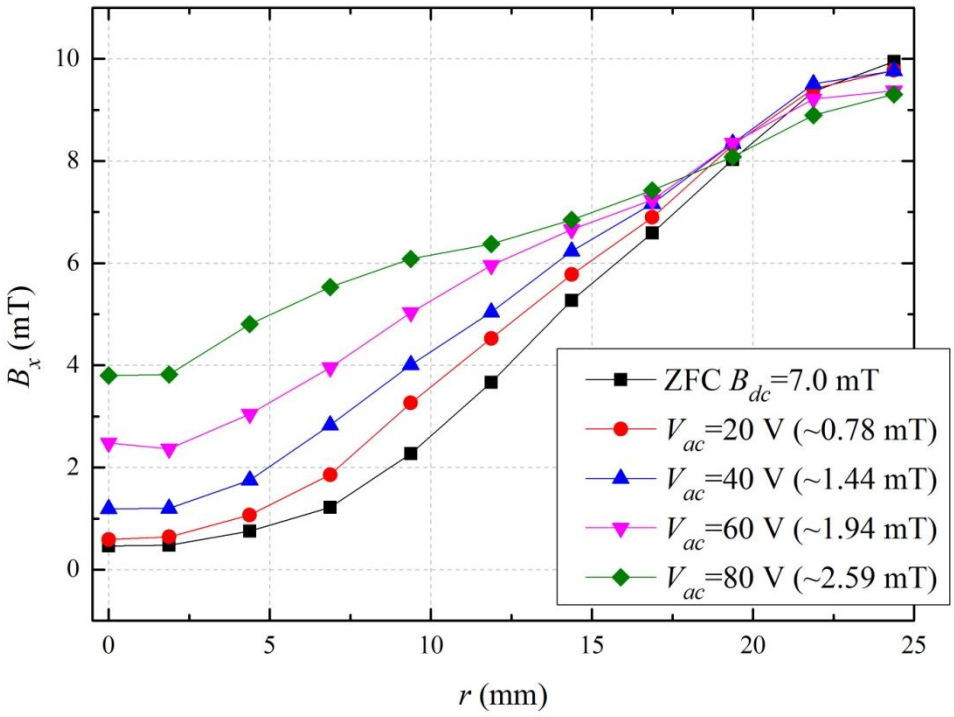

FIG. 6.10. The measured magnetic gradient for the round shaped YBCO sample when B_{dc}=7.0 mT before and after applying the travelling wave with a six phase connection.

In Fig. 6.9, after having switched on the travelling wave in the cases V_{ac}=20 V, 40 V, and 60 V, there were no clear changes to the magnetic gradient. Only in the case V_{ac}=80 V was a clear change of the magnetic gradient observed in comparison to the first curve. As discussed in Section 6.1.1, the actual amplitudes of the wave are: ~0.78 mT (V_{ac}=20 V), ~1.44 mT (V_{ac}=40 V), ~1.94 mT (V_{ac}=60 V), and ~2.59 mT (V_{ac}=80 V). The results shown in Fig. 6.9 are unexpected when compared to the same dc background field condition for the original CTMFP magnet shown in Fig. 5.14. In Fig. 5.14, a travelling wave of amplitude 2.0 mT was applied to the sample, which was pre-magnetised using a dc field B_{dc}=2.5 mT, and a clear decrease in the magnetic gradient was observed. However, in Fig. 6.9, for the curve V_{ac} =60 V (~1.94 mT), although the wavelength is half that of the original CTMFP magnet, the change in magnetic gradient was only observed near the edge of the sample.

The experimental results for the case B_{dc}=7.0 mT are shown in Fig. 6.10. In this figure, after applying the travelling wave, a decrease in the existing magnetic gradient was observed, such that the larger the amplitude of the wave, the greater the decrease of the magnetic gradient. These results coincide with the experimental results shown in Chapter 5. However, the change of the magnetic gradient is smaller when compared to the results in Fig. 5.13. With the travelling wave of 2.0 mT in Fig.5.13, the magnetic flux density in the centre of the sample increased to 5.0 mT, whereas in Fig.6.10 for the curve V_{ac} =60 V (~1.94 mT), after applying the travelling wave, the flux density at the centre only increased to 2.5 mT.

These results appear to contradict our previous speculations that, by increasing the degree of field inhomogeneity, more flux ought to migrate into the centre of the sample. The reason for these results is not yet clearly understood. However, it might have something to do with the different waveforms between the original CTMFP magnet and the updated CTMFP magnet. More study is needed in this area.

6.2.2 FC condition

Under FC conditions, the sample was cooled under a dc background field of either 5.0 mT or 10.0 mT. In the case of B_{dc}=5.0 mT, the sample was partially magnetised and a truncated conical trapped field was expected. In the case of B_{dc}=10.0 mT, the sample was fully magnetised and a conical trapped field was expected. The output voltage of the inverter was preset at V_{ac} =40 V (~1.44 mT). The wave was set to travel in the inward direction. The sequence of the experiment was: DAC on (t=0 s); dc field off (t=10 s); travelling wave on (t=20 s); travelling wave off (t=40 s); DAC off (t=50 s). The measured magnetic gradients before (at t=19 s) and after (at t=50 s) applying the travelling wave are shown in Fig. 6.11.

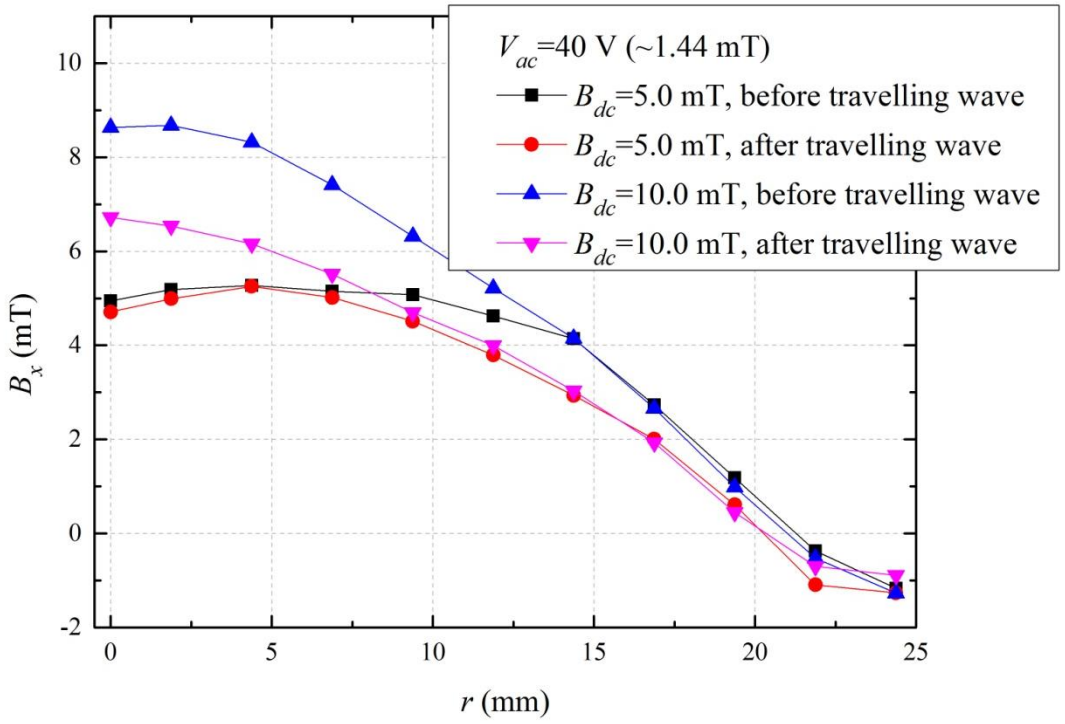

FIG. 6.11. The measured magnetic gradients in the FC condition before (at t=19 s) and after (at t=50 s) applying the travelling wave with a six phase connection.

In Fig. 6.11, for the case B_{dc}=5.0 mT, after applying the travelling wave, there was no clear change in flux density in the centre of the sample, however, there was a decrease in magnetic gradient at the edge of the sample (r >7.0 mm). For the case B_{dc}=10.0 mT, after applying the travelling wave, there was a clear decrease in flux density at the centre. Section 6.3.2 will compare these results with the experimental results for the updated CTMFP magnet with a three phase connection.

6.2.3 Travelling speed and direction

An experiment was carried out to investigate the effect of altering the sweeping speed (frequency) and travelling direction (inwardly or outwardly) to the magnetic gradient for a travelling wave produced by the updated CTMFP magnet with a six phase connection. As discussed in Section 5.6, the output frequency of the inverter could be increased to increase the sweeping speed of the wave, and the travelling direction could be reversed by changing the "rotate direction" in the inverter. In this experiment, the sample was be fully penetrated by a dc field of 7.0 mT. The output voltage was set at

V_{ac}=80 V (~2.59 mT). By changing the sweeping speed, the output frequency was chosen at: f=0.1 Hz, 1.0 Hz, 10.0 Hz, 100.0 Hz, and 400.0 Hz. The sequence of the experiment was: DAC on (t=0 s); dc field on (t=30 s); travelling wave on (t=90 s); travelling wave off (t=210 s); dc field off (t=240 s); DAC off (t=270 s). The travelling wave was set in the inward direction. By reversing the sweeping direction, the sequence of the experiment remained the same except that the travelling wave was reversed to the outward direction. The frequency was chosen to be f=1.0 Hz.

The experimental results are shown in Fig. 6.12. The magnetic gradients before (at t=89 s) and after (at t=239 s) applying the travelling wave are shown in Fig.6.12. The change in magnetic gradient is frequency dependent. As the frequency increases, the magnetic gradient becomes more unlikely to be altered by a change in direction of the travelling wave. These results are similar to the experimental results found in Section 5.6 (Fig. 5.24) for the original CTMFP magnet.

In Fig. 6.12, by reversing the travelling direction from "inward" to "outward" at f=1.0 Hz, the resulting magnetic gradients are almost the same, which suggests that the travelling direction has no influence on the change in magnetic gradient. There is no "magnetic coupling" observed in this instance. This result is the same as the experimental result obtained using the original CTMFP magnet (Section 5.6.2).

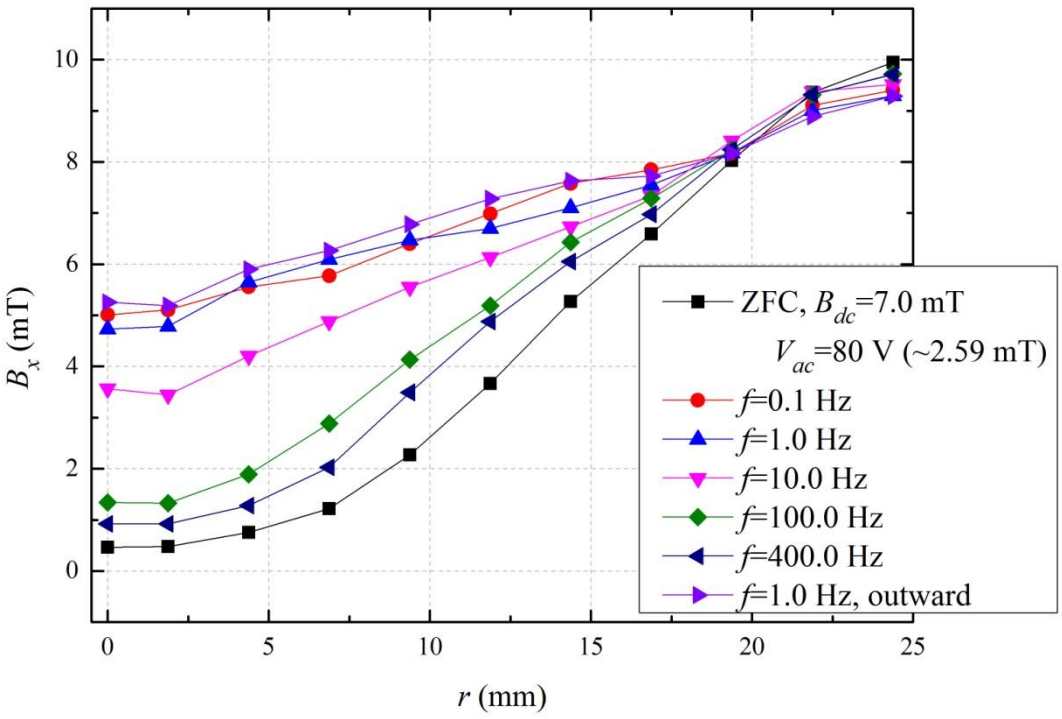

FIG. 6.12. The measured magnetic field of the round shaped YBCO sample in the case B_{dc}=7.0 mT before (at t=89 s) and after (at t=239 s) applying the travelling wave with different sweeping speeds (frequency) and directions (inward or outward).

In this section, experimental results have been provided for the updated CTMFP magnet with six phase connection. The results are slightly different from the previous speculation that, by halving the wavelength comparing with the original CTMFP magnet, more flux should have been transported into the YBCO sample. However, this might have been caused by the special waveform of the updated CTMFP magnet with six phase connection. At this stage, it is not well understood which requires further investigation in the future.

In the later part of the section, it was shown that the magnetic coupling phenomenon was not observed up to date. Therefore, it would be helpful to further decrease the wavelength by changing the six phase connection to three phase connection, to judge the effect of field inhomogeneity and find possible magnetic coupling phenomenon.

6.3 Experiment on the updated CTMFP magnet with a three phase connection

In this section, the wavelength is further decreased by connecting the phase windings with a three phase connection. As shown in Fig. 6.2, this connection can produce a travelling wave with four pole pairs. The experiment was also performed on the round shaped YBCO sample. Different magnetisation conditions such as ZFC, FC, frequency and reverse direction were studied for comparison with the experimental results in Chapter 5 and Section 6.2.

6.3.1 ZFC condition

In the ZFC condition, the values of the dc background field were chosen to be: B_{dc}=2.5 mT and 7.0 mT, where B_{dc}=2.5 mT stands for the case in which the sample is not fully penetrated and B_{dc}=7.0 mT stands for the case in which the sample is fully penetrated. The output voltages of the inverter were chosen to be V_{ac} = 80 V, 160 V, and 230 V. The output frequency was selected to be f=1.0 Hz. The sequence of the experiment was: DAC on (t=0 s); dc field on (t=10 s); travelling wave on (t=20 s); travelling wave off (t=40 s); dc field off (t=50 s); DAC off (t=60 s).

Section 6.1.2 established that the actual amplitudes of the wave were: ~0.47 mT (V_{ac}=80 V), ~0.86 mT (V_{ac}=160 V), and ~1.29 mT (V_{ac}=230 V). For each experiment, the magnetic gradients before (at

t=19 s) and after (at *t*=49 s) applying the travelling wave were selected. The results are shown in Fig. 6.13 and Fig. 6.14.

The experimental results for the case B_{dc}=2.5 mT are shown in Fig. 6.13. The first curve in Fig. 6.13 is the measured magnetic gradient after applying the dc field but before applying the travelling wave (t≈19 s). The three other curves are the measured magnetic gradients after applying the travelling wave but before switching off the dc field (t≈49 s). Fig. 6.13 can be compared to Fig.6.9. In Fig.6.9, in the case V_{ac}=40 V (~1.44 mT), the change in magnetic gradient is not readily apparent; however, in Fig. 6.13, in the case V_{ac}=230 V (~1.29 mT), there is a clear change in magnetic gradient. These results might suggest that the degree of inhomogeneity of the travelling wave influences the magnetisation. With a stronger inhomogeneity, the change in magnetic gradient becomes clearer.

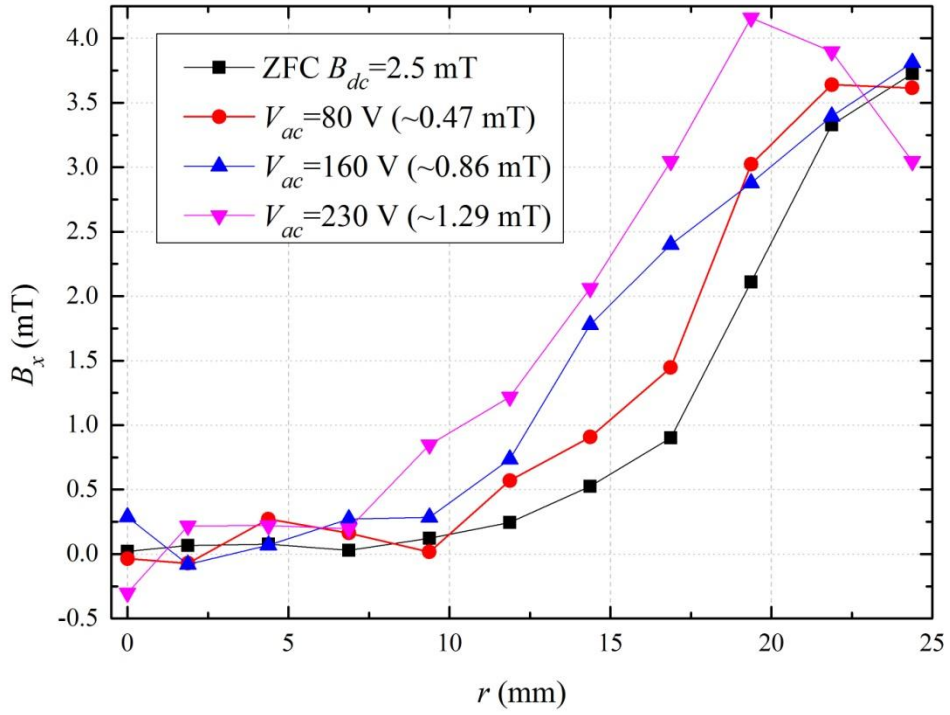

FIG. 6.13. The measured magnetic field for the round shaped YBCO sample in the case that B_{dc}=2.5 mT before (at t=19 s) and after (at t=49 s) applying the travelling wave for the updated CTMFP magnet with a three phase connection.

The experimental results for the case B_{dc}=7.0 mT are shown in Fig. 6.14. In the figure, after applying the travelling wave, clear decreases in the magnetic gradient were observed. The greater the increase in amplitude of the travelling wave, the greater the decrease in the magnetic gradient. Fig.

6.14 can be compared to Fig. 6.10. In Fig.6.10, for the case V_{ac}=40 V (~1.44 mT), the change in magnetic gradient is very small and the flux density at the centre increased to 1.2 mT. However, in Fig. 6.14, for the case V_{ac}=230 V (~1.29 mT), the change in magnetic gradient is much clearer than Fig. 6.10, and the flux density at the centre increased to 3.1 mT. These results also suggest that **by shortening the wavelength (strengthening the field inhomogeneity), the magnetic gradient becomes more likely to be changed**.

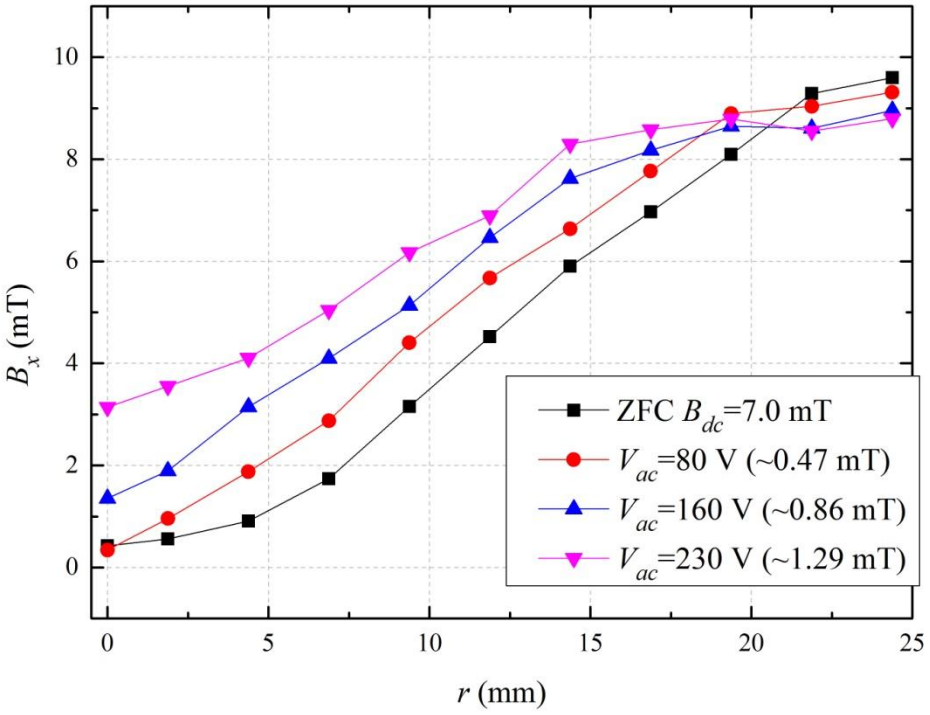

FIG. 6.14. The measured magnetic field for the round shaped YBCO sample in the case that B_{dc}=7.0 mT before (at t=19 s) and after (at t=49 s) applying the travelling wave for the updated CTMFP magnet with a three phase connection.

6.3.2 FC condition

Under FC conditions, the experiment was performed at two different dc background field strengths: B_{ac}=5.0 mT and 10.0 mT, as the same as in Section 6.2.2. The output voltage of the inverter was preset at V_{ac}=230 V (~1.29 mT). The sequence of the experiment was: DAC on (t=0 s); dc field off (t=10 s); travelling wave on (t=20 s); travelling wave off (t=40 s); DAC off (t=50 s).

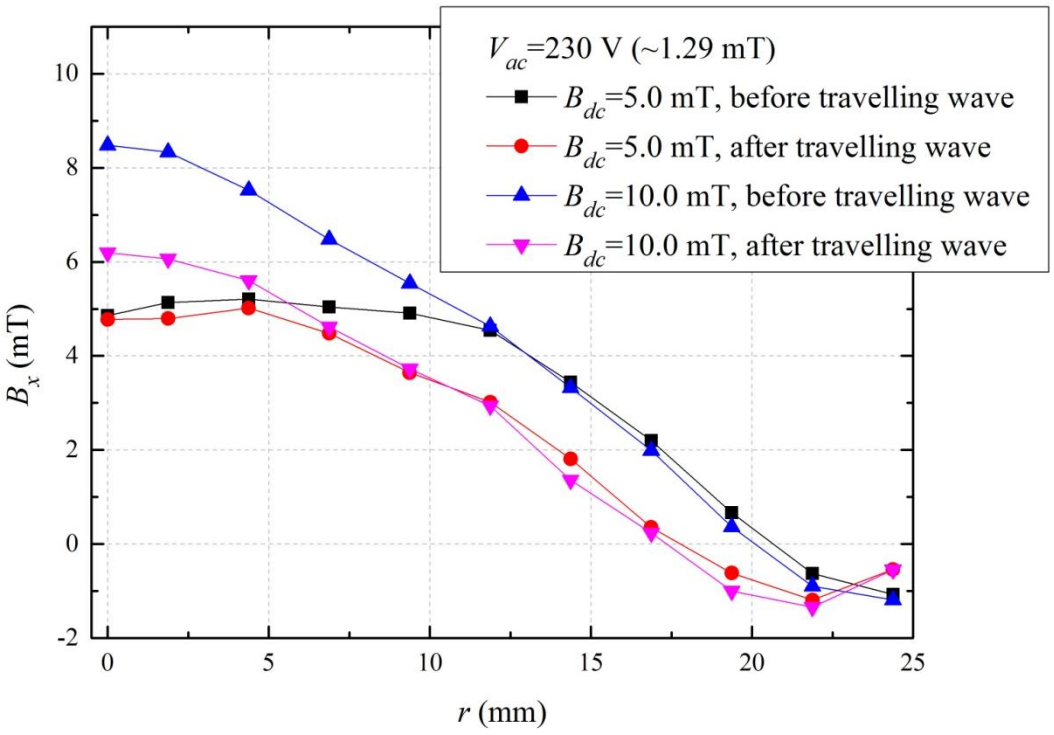

FIG. 6.15. The measured magnetic field in the FC condition before (at t=19 s) and after (at t=50 s) applying the travelling wave with the three phase connection.

Fig. 6.15 shows the measured magnetic gradient before (at t=19 s) and after (at t=50 s) applying the travelling wave. The experimental results can be compared to the results shown in Fig. 6.11 with the six phase connection. In Fig. 6.11, the amplitude of the travelling wave was ~1.44 mT, whereas in Fig. 6.15, the amplitude of the travelling wave was ~1.29 mT. In the case B_{dc}=5.0 mT, after applying the travelling wave, the decrease in the existing magnetic gradient is clearer in Fig. 6.15 than in Fig. 6.11. In Fig.6.11, the change of flux density reached r = 6.875 mm (the fourth Hall sensor), however, in Fig. 6.15, the change of flux density reached r = 4.375 mm (the third Hall sensor).

In the case B_{dc}=7.0 mT, after applying the travelling wave, in Fig. 6.11, the flux density decreased to 6.7 mT, however, in Fig. 6.15, the flux density decreased to 6.2 mT. The amplitude of the travelling wave in Fig. 6.15 is slightly lower than the amplitude of the wave in Fig. 6.11. However, the change caused by the travelling wave is larger in Fig. 6.15. This suggests that the degree of field inhomogeneity has an influence on the final magnetisation, and the stronger the field inhomogeneity, the stronger the change in the magnetic gradient.

6.2.3 Travelling speed and direction

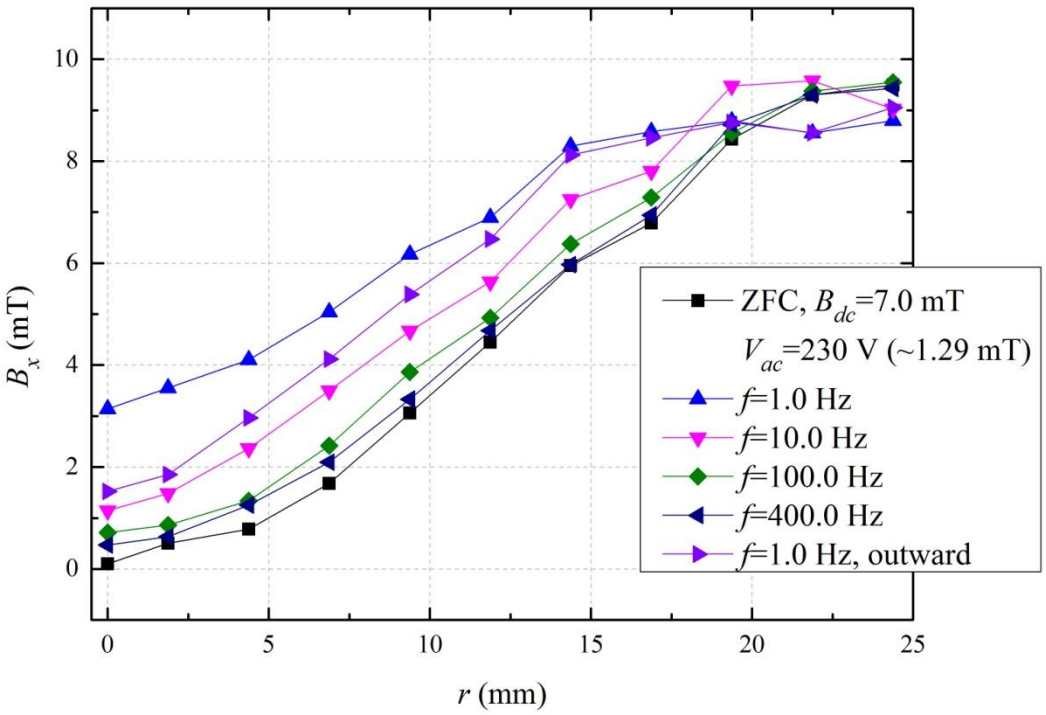

FIG. 6.16. The measured magnetic field of the round shaped YBCO sample in the case B_{dc}=7.0 mT before (at t=89 s) and after (at t=239 s) applying the travelling wave at different sweeping speeds (frequencies) and directions (inward or outward).

In order to understand how the travelling speed of the travelling wave influences magnetisation, the output frequency of the inverter was increased from a low frequency to a high frequency, as in Section 6.2.3. The experiment was performed under ZFC conditions with B_{dc}=7.0 mT. The output voltage of the inverter was chosen to be V_{ac}=230 V (~1.29 mT). The following output frequencies were considered in the experiment: f=1.0 Hz, 10.0 Hz, 100.0 Hz, and 400.0 Hz. The sequence of the experiment was: DAC on (t=0 s); dc field on (t=30 s); travelling wave on (t=90 s); travelling wave off (t=210 s); dc field off (t=240 s); DAC off (t=270 s). The travelling direction was chosen to move in the inward direction.

The experimental results are shown in Fig. 6.16. Similar to the results shown in Fig. 6.12, the magnetisation is dependent on the sweeping speed. As the output frequency increases, the magnetic gradient is less likely to be altered by the travelling wave.

In Fig. 6.16, as the travelling direction was reversed from "inward" to "outward" at f=1.0 Hz, the magnetic gradient for the "outward" direction was steeper than for the "inward" direction. This phenomenon was not found in Fig. 6.12 or Fig. 5.24. The results shown in Fig. 6.16 may suggest that the magnetisation becomes dependent on the travelling direction as the wavelength decreases to 1/4 of the original CTMFP magnet. In other words, **a "magnetic coupling phenomenon" may have been observed in this case**. However, this phenomenon is not yet confirmed, and further study is needed.

6.4 Conclusion

This chapter investigated the magnetisation of the round shaped YBCO sample with the updated CTMFP magnet. Travelling magnetic waves with either a six phase connection or a three phase connection were studied numerically and experimentally. For the six phase connection, the wavelength was about half that of the original CTMFP magnet. For the three phase connection, the wavelength was about one quarter of the original CTMFP magnet.

The experiments were performed under ZFC conditions, FC conditions, different sweeping speeds and travelling directions. By comparing the ZFC condition and the FC condition for the six phase connection and the three phase connection, it was confirmed that the degree of field inhomogeneity influence the final magnetisation profile. For a travelling wave of constant amplitude, the stronger the field inhomogeneity (shorter wavelength), the greater the change in the existing critical magnetic gradient. By increasing the sweeping speed of the travelling wave, it was found that the magnetic gradient is less likely to be changed, which suggests that the magnetisation is dependent on the sweeping speed. This phenomenon requires further study in the future.

By reversing the travelling direction from "inward" to "outward" with the six phase connection there was no clear change of the magnetic gradient. However, with the three phase connection there was a clear change of magnetic gradient. The increase in magnetic flux at the centre was larger when the travelling wave travelled inward compared to when the wave travelled outward. This phenomenon suggests that a possible magnetic coupling phenomenon was observed. However, this phenomenon is not confirmed at this stage, and further study is required.

CHAPTER 7

EXPERIMENTS USING THE SQUARE SHAPED YBCO SAMPLES

This chapter discusses experiments performed using the square shaped YBCO samples with the help of the original CTMFP magnet, the updated CTMFP magnet with a six phase connection and the updated CTMFP magnet with a three phase connection.

As discussed in Section 3.3, inducing a persistent current in a type-II superconducting loop requires that the vortices must be created at the outer edge and transported across the superconducting tape to be annihilated at the inner edge. In Chapter 5 and Chapter 6, the experiments were performed on a round shaped YBCO sample. The final step (annihilation of vortices) cannot be fulfilled in a round shaped sample. Therefore, the square shaped YBCO samples shown in Fig. 4.27 were used for the investigations in this chapter. The width of the square shaped YBCO sample is 46 mm and the diameter of the hole in the centre is 26 mm. These samples were provided by AMSC and FBML, MIT.

In Chapter 5 and Chapter 6, the experimental results showed that the travelling wave tends to attenuate the existing magnetic gradient, which indicates that a travelling wave is more efficient at transporting the magnetic flux within the YBCO film compared to a homogeneous oscillating field. However, at this stage it is still uncertain whether a magnetic coupling phenomenon (the dc transformer in Section 3.3) can be found at the macroscopic scale with the help of a travelling wave (the phenomenon found in Fig.6.16 requires further authentification). However, the "magnetic coupling" can be crucial to the magnetisation of a superconducting loop since it helps the flux to migrate in a determined direction. In this chapter, a tentatively study is performed to show whether the magnetic flux can be transported into a type-II superconducting loop with the help of travelling waves of three different wavelengths.

The experiments were performed under FC conditions, i.e. the sample was cooled under a smaller dc background field (3.0 mT). The dc background field was present throughout the experiment. The purpose of the dc background field was to provide an offset to the travelling magnetic wave. The

reason for a dc offset is that, if the magnetic coupling is present in the experiment, by slightly offsetting the travelling wave, the positive and negative magnetic flux transported into the superconducting sample are not balanced, which leads to a net magnetic flux accumulated inside the type-II superconducting loop.

The travelling wave was preset to the inward direction and the output frequency of the inverter was preset to f=1.0 Hz. The experiment began by testing the sample using the original CTMFP magnet, and then the same sample was tested using the updated CTMFP magnet with a six phase connection. Finally the sample was tested using the updated CTMFP magnet with a three phase connection. The sequence of each experiment was: switching the dc background field on (B_{dc}=3.0 mT) before the experiment, FC the sample, DAC on (t=0 s), ac on (t=10 s), ac off (t=40 s), DAC off (t=50 s).

7.1 The maximum trapped field of the square shaped YBCO sample

Before commencing the experiment, the trapped fields of five square shaped YBCO samples were tested. The maximum trapped fields are shown in Fig. 7.1. The five samples were labelled as N181, N182, N183, N184 and N185, as shown in Fig. 4.27. The maximum trapped fields of the five samples were apprximately 16.0 mT at the centre. The superconducting region lies between 13 mm $\leq r \leq$ 23 mm as marked in the Fig. 7.1 (also in Fig. 4.27).

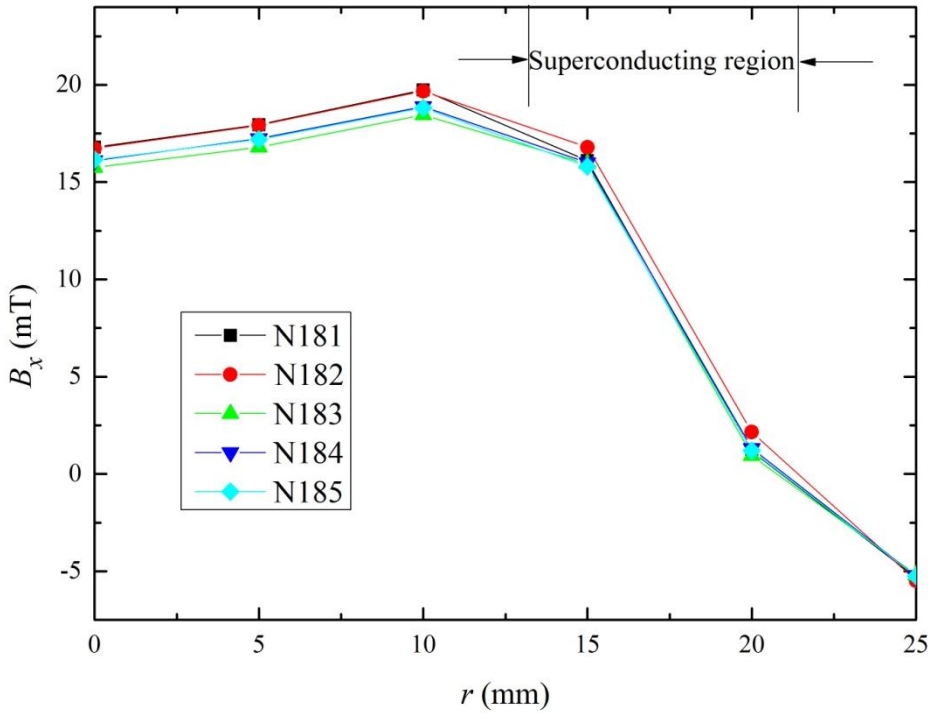

FIG. 7.1. The maximum trapped field of the five square shaped YBCO samples.

7.2 Experiment using the original CTMFP magnet

In this section, the square shaped YBCO sample was tested using the original CTMFP magnet. The purpose of the research was to show whether the travelling wave from the original CTMFP magnet could help the magnetic flux to move across the superconducting loop. The travelling wave produced by the CTMFP magnet is shown in Fig. 7.2 (the same as shown in Fig. 5.2) and the superconducting region is indicated in the diagram. In order to transport the flux across the superconducting region, the field inhomogeneity must be strong enough in the superconducting region, otherwise the travelling wave would behave similarly to a homogeneous oscillating field.

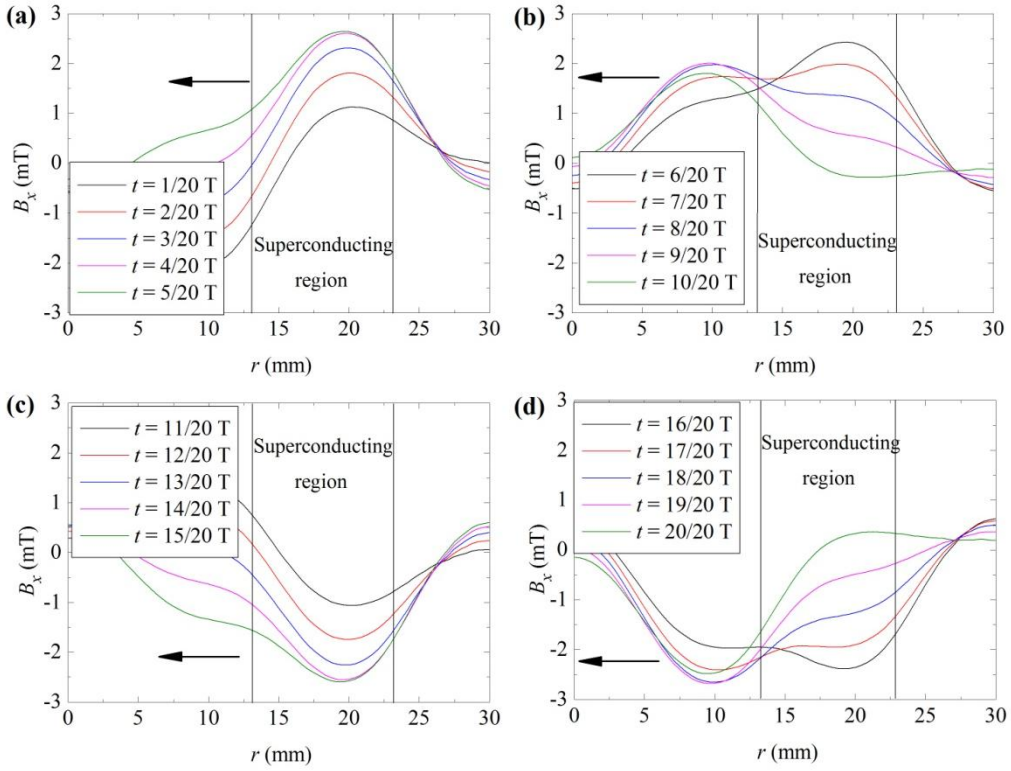

FIG. 7.2. The travelling wave produced by the original CTMFP magnet (the same as Fig. 5.2) with the superconducting region indicated (square shaped YBCO)

The output voltages of the inverter were set at V_{ac} = 50 V, 100 V, 150 V, and 200 V. Fig. 7.3 shows the experimental results before and after applying the travelling magnetic wave under FC conditions. Up to the output voltage of 200 V (corresponding to a maximum amplitude of 23.2 mT, as

shown in Fig. 5.3), there was no clear change to the magnetic flux at the centre of the sample after applying the travelling wave. However, this amplitude (at r = 10 mm) is already greater than the maximum trapped field of the sample. It suggests that using the travelling wave of the original CTMFP magnet to magnetise the square shaped YBCO sample was unsuccessful. The field inhomogeneity in the superconducting region might not be strong enough to transport the magnetic flux across the superconducting tape.

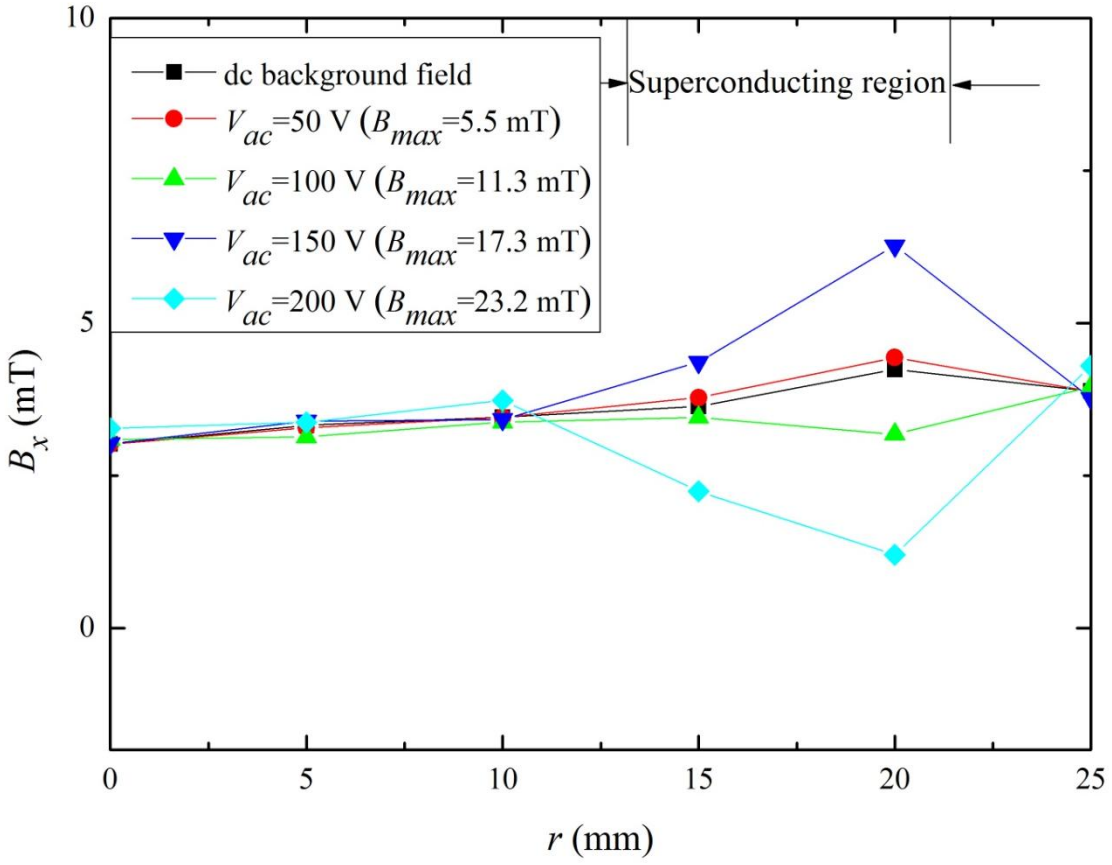

FIG. 7.3. The magnetic field measured across the square shape YBCO using the original CTMFP magnet before and after applying the travelling wave under FC conditions (B_{dc}=3.0 mT). The square shaped YBCO sample used for the experiment was labelled as N185.

7.3 Experiment using the updated CTMFP magnet with a six phase connection

In this section, the square shaped YBCO sample labelled N185 was tested using the updated CTMFP magnet with a six phase connection. The travelling magnetic waves produced by the updated CTMFP magnet with a six phase connection are shown in Fig. 7.4 (the same as in Fig. 6.3). The superconducting region for the square shaped YBCO sample is indicated in the figure. It is clear that the superconducting region is slightly longer than half of the wavelength. It therefore has a stronger field inhomogeneity compared to the original CTMFP (Fig.7.2) with a travelling wave of the same amplitude.

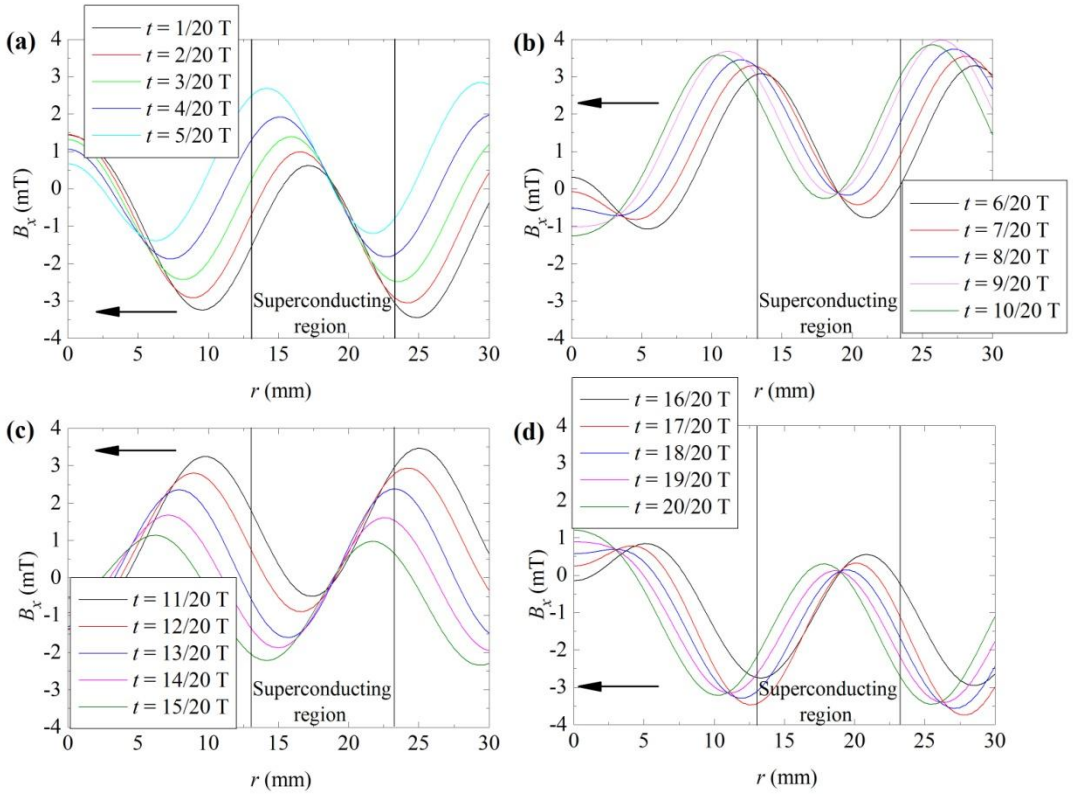

FIG. 7.4. The travelling wave produced by the updated CTMFP magnet with six phase windings (the same as Fig. 6.3) with superconducting region indicated (square shaped YBCO).

The experimental procedure was the same as described in the previous section. Since the maximum output voltage of the inverter is 230 V, in order to achieve a higher amplitude for the travelling wave, power resistors of 100 Ω were connected to each phase instead of 300 Ω. The output voltage of the inverter was selected to be: V_{ac} = 50 V, 100 V, 150 V, and 200 V. The amplitude of the travelling wave for each output voltage was measured. It was known from Section 6.1 that, for the

updated CTMFP magnet with a six phase connection, the actual amplitude of the travelling wave is approximately 53% of the measured maximum value.

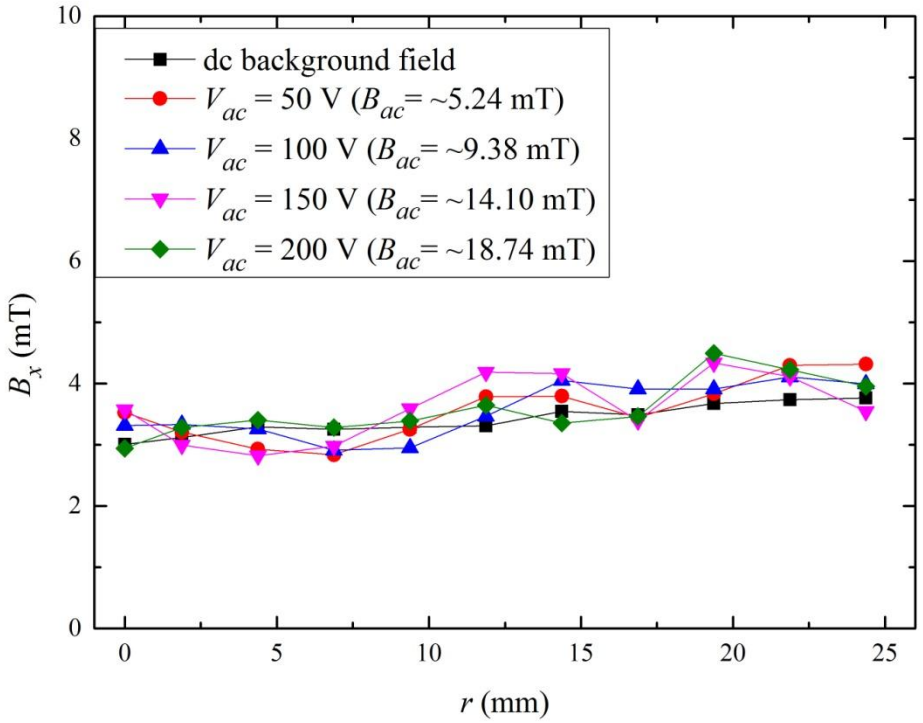

FIG. 7.5. The magnetic field measured across the square shaped YBCO using the updated CTMFP magnet with a six phase connection before and after applying the travelling wave under FC conditions (B_{dc}=3.0 mT). The square shaped YBCO sample used for the experiment was labelled as N185.

The experimental results are shown in Fig. 7.5. Up to the amplitude of 18.74 mT, there were no observed changes in magnetic flux at the centre of the sample. The curves do not precisely overlap each other due to residual magnetisation in the iron yoke. The amplitude of the wave at V_{ac}=200 V has already exceeded the maximum trapped field of the square shaped sample. However, there was no clear increase in flux density observed in the experiment.

7.4 Experiment using the updated CTMFP magnet with a three phase connection

In this section, the square shaped YBCO sample labelled N185 was tested using the updated CTMFP magnet with a three phase connection. The travelling magnetic wave produced by the

updated CTMFP magnet with three phase windings produces the shortest wavelength and the strongest field inhomogeneity. Fig. 7.6 shows the travelling wave produced by the updated CTMFP with a three phase connection (the same as Fig. 6.6), and the superconducting region of the square shaped YBCO sample is indicated in the figure. The superconducting region is slightly longer than one wavelength. The field inhomogeneity is the strongest compared to the other two kinds of travelling wave.

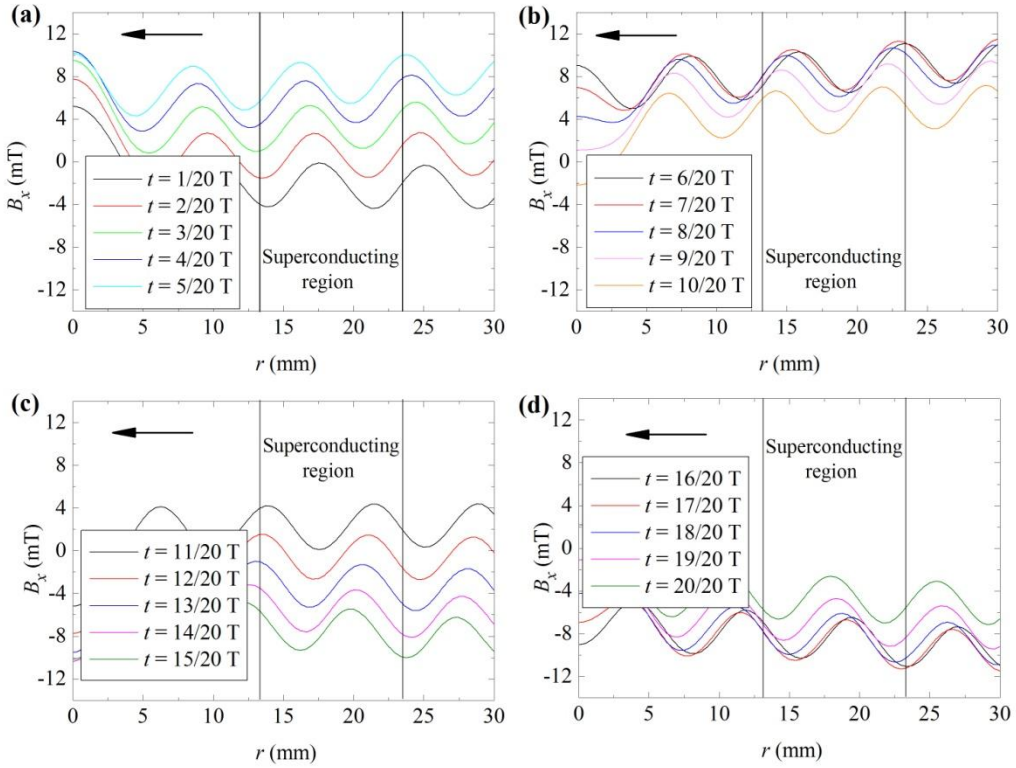

FIG. 7.6. The travelling wave produced by the updated CTMFP magnet with three phase windings (the same as Fig. 6.6) with superconducting region indicated (square shaped YBCO).

The power resistors connected to the phase windings were reduced to 100 Ω in order to increase the amplitude of the travelling wave. The output voltage of the inverter was selected to be : V_{ac}=50 V, 100 V, 150 V, and 200 V. As mentioned in Section 6.1, for the travelling wave produced by the updated CTMFP magnet with three phase windings, the amplitude of the travelling wave was about 23% of the measured amplitude. In this experiment, the maximum amplitude was about 3.67 mT (V_{ac}=200 V).

The experimental results are shown in Fig. 7.7. After applying the travelling magnetic wave up to the maximum amplitude of 3.67 mT, there was no observable change to the magnetic flux inside the

superconducting loop. The discrepancies between the curves are most likely due to residual magnetisation inside the iron yoke.

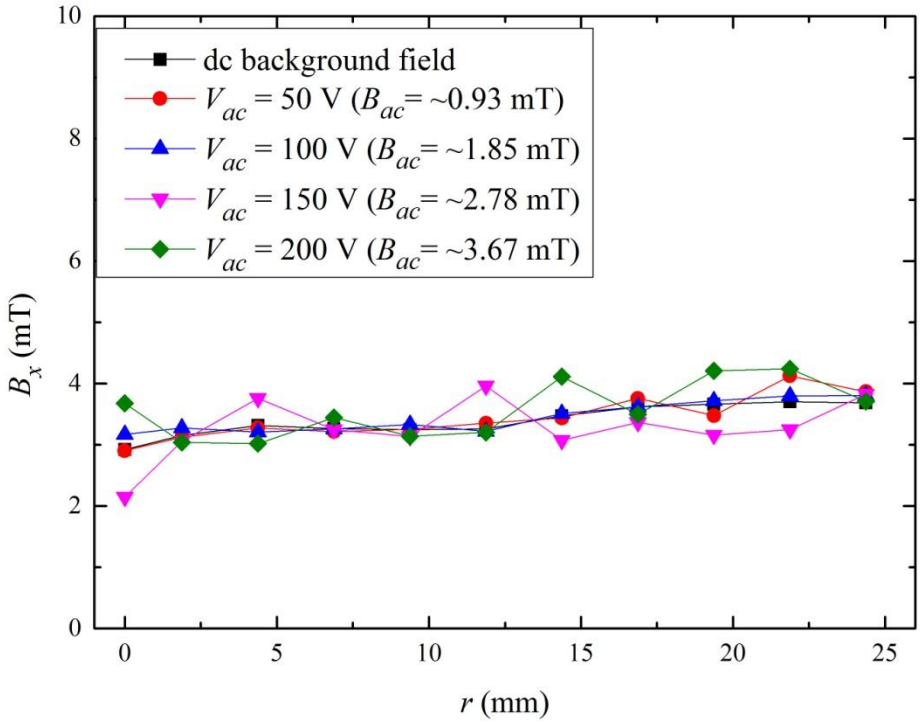

FIG. 7.7. The magnetic field measured across the square shaped YBCO in the updated CTMFP magnet with a six phase connection before and after applying the travelling wave under FC conditions (B_{dc}=3.0 mT). The square shaped YBCO sample used for the experiment was labelled as N185.

7.5 Conclusion

In this chapter, a single layer square shaped YBCO sample was tested using travelling waves of three different wavelengths. These were produced by the original CTMFP magnet, the updated CTMFP magnet with a six phase connection, and the updated CTMFP magnet with a three phase connection. The experiments tried to "pump" the flux into the superconducting loop with the help of the travelling wave. Up to this point, no observable "flux pumping" phenomenon was observed in the experiments. The reason for these results is not well understood at this stage. Since the superconducting layer of the square shape YBCO sample is 1.0 μm, which is five times larger than the round shape YBCO sample, it might increase the difficulty of transporting the magnetic flux inside the sample. However, it should have been overcome by increasing the amplitude of the

travelling wave. Another problem is that, the magnetic coupling should be present in the experiment to successfully transport the flux into the superconducting loop. However, the width of the superconducting region is relatively small, which leads to the fact that, the field inhomogeneity might not be strong enough in the superconducting region. Since the magnetic coupling might have been observed in Fig.6.16 in the three phase connection, it might be helpful to perform the experiment again with the three phase connection with larger amplitude. The experimental results presented at this stage are preliminary studies, and further investigations are required.

CHAPTER 8

CONCLUSION AND FUTURE WORK

This thesis has studied the emerging flux pumping technologies for HTS coils. The key technology of this HTS flux pump is to use the travelling magnetic wave, to transport the magnetic flux across an HTS film, into the superconducting loop. Therefore, in order to understand the HTS flux pump, the priority of the study is to understand how the magnetic flux can be transported by the travelling wave. To date, the magnetisation of a type-II superconducting sample has been studied thoroughly, however, most of the studies are limited to the homogeneous oscillating field condition, little knowledge was contributed to the magnetisation based on the travelling wave.

The definition of the travelling wave is that, the travelling wave may have crest region and trough region in space, i.e. the field is inhomogeneous over space. This kind of field can be generated by a moving magnet or three phase windings. Contrary to the travelling wave, the homogeneous oscillating field refers to the field which is homogeneous over space. This kind of field can be found inside a single phase coil.

In the early studies of the "dc transformer", it was found that the field inhomogeneity can help the vortices migrate inside the type-II superconducting film. This phenomenon is known as "magnetic coupling" and the coupling force comes from the field inhomogeneity. In the "dc transformer", the field inhomogeneity comes from the vortices which are in microscopic scale. The misalignment of the vortices between two layers of superconducting film increases the potential energy which helps moving the vortices in the secondary film. This argument is inspiring in that, by providing the field inhomogeneity, there might be dragging force acting on the vortices in the HTS film, which helps them moving with the travelling wave accordingly.

In this thesis, the author aims at developing a novel device, which could be able to show the unique magnetisation profile of the travelling wave on the HTS film. This novel device is named as the circular-type magnetic flux pump device, which can generate an annular shape travelling magnetic wave. The purpose of the study is to show that:

1. Comparing with the homogeneous oscillating field, the travelling wave is more efficient in transporting the magnetic flux inside the YBCO sample;
2. The "magnetic coupling" phenomenon might be possible in macroscopic scale giving that the field inhomogeneity is strong enough.

According to the requirements of the studies, there are two types of CTMFP were designed and built: the original CTMFP magnet and the updated CTMFP magnet. The original CTMFP travelling wave can produce a travelling wave with a single pole-pair and have the longest wavelength; the updated CTMFP with six phase connection produces two pole-pairs which halves the wavelength; the updated CTMFP with three phase connection produces four pole-pairs which quarters the wavelength (the strongest field inhomogeneity). In the experiment, two types of YBCO samples were studied: the 2 inch diameter round shaped YBCO thin film and the 46 mm×46 mm square shaped YBCO tape with a hole of Φ26 mm in the centre.

In the thesis, a great deal of work focused on the study of the round shaped YBCO thin film. It was discovered that a travelling wave is more likely to migrate the magnetic flux inside the round shaped YBCO sample compared to a homogeneous oscillating field. It was identified that a travelling wave tends to compromise the existing magnetic gradient (the critical gradient based on the Bean model). This phenomenon applies to ZFC, FC, and delta shape trapped field conditions, and can be accurately predicted using FEM software with Maxwell's equations and the *E-J* power law. The simulation revealed that the magnetisation based on the travelling wave does not follow the constant critical current density assumption from the Bean model: after applying the travelling wave, the magnetisation current inside the YBCO sample was much lower than the critical current density. This phenomenon was explained as the effect of the field inhomogeneity: in the presence of the travelling wave, the non-uniform distribution of the magnetic energy in space unbalances the distribution of vortices in the YBCO sample, which helps the vortices to move locally, which ends up with the decrease of existing critical magnetic gradient. There are two methods of increasing the field inhomogeneity: one is to increase the amplitude of the travelling wave; another is to decrease the wavelength of the travelling wave. It was verified that, in both methods, by increasing the field inhomogeneity, more magnetic flux has been migrated into the YBCO sample. It supports that idea that, the field inhomogeneity is the main "dragging force" which moves the vortices inside the YBCO sample. This novel magnetic phenomenon can be very useful in understanding both the HTS coil flux pump and the ac magnetisation loss in travelling wave conditions such as inside a superconducting electric machine, etc.

In the search of the macroscopic "magnetic coupling" phenomenon, the travelling direction of the wave has been reversed to show whether the magnetisation is dependent on the travelling direction: if the resultant magnetic profiles are dependent on the travelling direction, then it suggests that part of

the vortices are coupled with the travelling wave. This can be understood from the "dc transformer" experiment: if the field inhomogeneity is strong enough, then the travelling wave can provide enough "dragging force" to migrate the vortices in corresponding direction. However, this should be distinguished from the merely change of magnetic gradient: change of magnetic gradient can be present if there is field inhomogeneity; however, to achieve the magnetic coupling, the field inhomogeneity must be strong enough to provide a potential trap, which traps the vortices and transports in a certain direction. In the thesis, for the original CTMFP magnet and updated CTMFP magnet with six phase connection (1/2 wavelength), as the travelling direction reverses, there is no clear change of the resultant magnetisation; however, for the updated CTMFP magnet with three phase connection (1/4 wavelength), a clear difference of resultant magnetisation has been observed, which suggests that, as the wavelength drops to one quarter of the original CTMFP magnet, a possible magnetic coupling phenomenon has been observed. However, this finding requires further confirmation and investigation in the future.

To the author's understanding, the transportation of the magnetic flux and the "magnetic coupling" are the two key factors which enable the successful "pumping" of magnetic flux into the HTS coil. The experiments in this thesis show that, it is possible to achieve both functions with the help of a travelling magnetic wave of enough field inhomogeneity. However, future studies still needs to be carried out, especially on a practical flux pumping device for the HTS coils.

Apart from the experimental findings mentioned above, it was also shown that, the travelling wave is more likely to fully penetrate the round shape YBCO sample comparing with the homogeneous oscillating field of the same amplitude. This also supports the idea that the travelling wave is more efficient in transporting the flux inside the YBCO sample. It was also shown that, the magnetisation is dependent on the sweeping speed of the travelling wave: as the sweeping speed decreases, more magnetic flux has been transported into the round shape YBCO sample. This might have been related to the relaxation time of the sample: as the sweeping speed decreases, which gives more time for the flux line lattice to relax (flux creep), which ends up with more magnetic flux enters the YBCO sample.

Based on the FEM model which has been successfully built to predict the magnetisation of the round shape YBCO sample with the original CTMFP magnet, a special topic has been proposed to discuss the differences of ac magnetisation losses between travelling wave and homogeneous oscillating field. It was found that, for the single layer round shape YBCO sample used in the experiment, the ac magnetisation loss caused by the travelling wave is about 1/3 of the homogeneous oscillating field, giving that the amplitudes of the two waves are the same. Moreover, the regions which lead to ac magnetisation loss can also be different from the two waves. This work suggests that, in the ac magnetisation loss calculations in the travelling wave conditions such as inside the

superconducting motor, the travelling wave might not be able to be equalised as a homogeneous oscillating field. However, this work requires more extensive studies in the future.

A preliminary study using the single layer square shaped YBCO sample was performed in the final chapter. The difference between the square shape sample and the the round shape sample is that, the square shape sample is hollowed in the centre (Φ26 mm), and the thickness of the YBCO layer is 1.0 μm. The experiments try to "pump" magnetic flux into the superconducting loop with the help of the travelling wave. The sample was cooled in FC condition with a dc background field B_{dc}=3.0 mT. The dc field is to unbalance the magnetic flux that might be "pumped" into the superconducting loop. Three types of travelling waves were tried in the experiment: the wave from the original CTMFP magnet; the wave from the updated CTMFP magnet with six phase connection (1/2 wavelength); the wave from the updated CTMFP magnet with three phase connection (1/4 wavelength). In three cases, after applied the travelling wave, there were no clear change of magnetic flux observed in the sample centre. This might be attributed to the fact that, the field inhomogeneity is not strong enough to cause flux migration in the experiments, and the YBCO layer is relatively thicker which increases the difficulties. Moreover, the width of the superconducting region is relatively small (10 mm), in order to help magnetic flux migrate into the superconducting loop, the field inhomogeneity must be strong enough in the superconducting region, which increases the technical difficulties. However, this might be able to be accomplished by increase the amplitude of the travelling waves. Some experiments will be carried out in the future.

To conclude, for the future work, three directions of studies involving the CTMFP magnets can therefore be suggested:

1. Further study is needed to identify the possible macroscopic magnetic coupling phenomenon which was suggested in the experiment using the updated CTMFP magnet with three phase windings and the round shape YBCO sample;
2. Further study should be carried out regarding magnetising the square shaped YBCO sample with the help of a travelling wave of larger amplitude;
3. Further study should be carried out on the magnetisation dependence of the sweeping speed.

Based on the research in this thesis, two major studies can be suggested for future investigation on the HTS coil flux pump and the ac magnetisation loss studies:

1. Further study is suggested into HTS flux pump technologies for HTS coils, based on a deep understanding of the effects of travelling waves on HTS films. More experiments should be performed to learn how a travelling wave transports flux into the HTS coils.

2. Further study is recommended to investigate ac losses generated by a travelling wave, as compared to a homogeneous oscillating field. This work would be widely beneficial for the general understanding of basic magnetisation phenomenon in HTS tapes. This work would also be very important in identifying ac loss inside an HTS motor using HTS coils;

In conclusion, this thesis describes two novel CTMFP magnet devices and their effects on two different kinds of YBCO film sample. Several new electromagnetic phenomena were identified with the help of the CTMFP magnet devices, which will be useful for a better understanding of how travelling waves influence the magnetisation of HTS films. Additionally, these new phenomena can help to deepen knowledge of the HTS flux pumps and ac magnetisation loss for HTS coils. Further studies are also recommended in this area.

REFERENCES

[1] H. Seungyong, K. Seok-Beom, A. Min Cheol, J. Voccio, J. Bascunan, and Y. Iwasa, "Trapped Field Characteristics of Stacked YBCO Thin Plates for Compact NMR Magnets: Spatial Field Distribution and Temporal Stability," *IEEE Transactions on Applied Superconductivity,* vol. 20, pp. 1037-1040, 2010.

[2] J. G. Bednorz and K. A. Müller, "Possible highT c superconductivity in the Ba−La−Cu−O system," *Zeitschrift für Physik B Condensed Matter*, vol. 64, pp. 189-193, 1986.

[3] M. K. Wu, J. R. Ashburn, C. J. Torng, P. H. Hor, R. L. Meng, L. Gao, *et al.*, "Superconductivity at 93 K in a new mixed-phase YBaCuO compound system at ambient pressure," *Physical Review Letters,* vol. 58, pp. 908-910, 1987.

[4] J. Nagamatsu, N. Nakagawa, T. Muranaka, Y. Zenitani, and J. Akimitsu, "Superconductivity at 39 K in magnesium diboride," *Nature,* vol. 410, pp. 63-64, Mar 2001.

[5] "http://en.wikipedia.org/wiki/Superconductivity."

[6] F. N. Werfel, U. Floegel-Delor, R. Rothfeld, B. Goebel, D. Wippich, and T. Riedel, "Modelling and construction of a compact 500 kg HTS magnetic bearing," *Superconductor Science and Technology,* vol. 18, p. S19, 2005.

[7] J. R. Hull, "Superconducting bearings," *Superconductor Science and Technology,* vol. 13, p. R1, 2000.

[8] T. A. Coombs, A. Cansiz, and A. M. Campbell, "A superconducting thrust-bearing system for an energy storage flywheel," *Superconductor Science and Technology,* vol. 15, p. 831, 2002.

[9] J. Wang, S. Wang, Y. Zeng, H. Huang, F. Luo, Z. Xu, *et al.*, "The first man-loading high temperature superconducting Maglev test vehicle in the world," *Physica C: Superconductivity*, vol. 378–381, Part 1, pp. 809-814, 2002.

[10] D. Zhou, M. Izumi, M. Miki, B. Felder, T. Ida, and M. Kitano, "An overview of rotating machine systems with high-temperature bulk superconductors," *Superconductor Science and Technology*, vol. 25, p. 103001, 2012.

[11] Y. Jiang, R. Pei, W. Xian, Z. Hong, and T. A. Coombs, "The design, magnetization and control of a superconducting permanent magnet synchronous motor," *Superconductor Science and Technology*, vol. 21, p. 065011, 2008.

[12] T. Oka, H. Kanayama, S. Fukui, J. Ogawa, T. Sato, M. Ooizumi, *et al.*, "Application of HTS bulk magnet system to the magnetic separation techniques for water purification," *Physica C: Superconductivity*, vol. 468, pp. 2128-2132, 2008.

[13] M. Tsuda, T. Kojima, T. Yagai, and T. Hamajima, "Vibration Characteristics in Magnetic Levitation Type Seismic Isolation Device Composed of Multiple HTS Bulks and Permanent Magnets," *IEEE Transactions on Applied Superconductivity*, vol. 17, pp. 2059-2062, 2007.

[14] D. W. Hazelton, V. Selvamanickam, J. M. Duval, D. C. Larbalestier, W. D. Markiewicz, H. W. Weijers, *et al.*, "Recent Developments in 2G HTS Coil Technology," *IEEE Transactions on Applied Superconductivity*, vol. 19, pp. 2218-2222, 2009.

[15] S. Honghai, P. Brownsey, Z. Yifei, J. Waterman, T. Fukushima, and D. Hazelton, "2G HTS Coil Technology Development at SuperPower," *IEEE Transactions on Applied Superconductivity*, vol. 23, pp. 4600806-4600806, 2013.

[16] X. Ying, G. Weizhi, N. Xiaoye, C. Zhengjian, Z. Jingyin, T. Bo, *et al.*, "Development of Saturated Iron Core HTS Fault Current Limiters," *IEEE Transactions on Applied Superconductivity*, vol. 17, pp. 1760-1763, 2007.

[17] M. Noe and M. Steurer, "High-temperature superconductor fault current limiters: concepts, applications, and development status," *Superconductor Science and Technology*, vol. 20, p. R15, 2007.

[18] C. S. Weber, C. T. Reis, A. Dada, T. Masuda, and J. Moscovic, "Overview of the underground 34.5 kV HTS power cable program in albany, NY," *IEEE Transactions on Applied Superconductivity*, vol. 15, pp. 1793-1797, 2005.

[19] L. Masur, D. Parker, M. Tanner, E. Podtburg, D. Buczek, J. Scudiere, *et al.*, "Long length manufacturing of high performance BSCCO-2223 tape for the Detroit Edison Power Cable Project," *IEEE Transactions on Applied Superconductivity*, vol. 11, pp. 3256-3260, 2001.

[20] M. W. Rupich, U. Schoop, D. T. Verebelyi, C. L. H. Thieme, D. Buczek, X. Li, *et al.*, "The Development of Second Generation HTS Wire at American Superconductor," *IEEE Transactions on Applied Superconductivity*, vol. 17, pp. 3379-3382, 2007.

[21] M. W. Rupich, X. Li, C. Thieme, S. Sathyamurthy, S. Fleshler, D. Tucker, *et al.*, "Advances in second generation high temperature superconducting wire manufacturing and R&D at American Superconductor Corporation," *Superconductor Science and Technology*, vol. 23, p. 014015, 2010.

[22] W. Meissner and R. Ochsenfeld, "Ein neuer Effekt bei Eintritt der Supraleitfähigkeit," *Naturwissenschaften*, vol. 21, pp. 787-788, 1933.

[23] B. L. D. Haas-Lorentz, *Physica*, vol. 5, p. 384, 1925.

[24] F. London and H. London, "The Electromagnetic Equations of the Supraconductor," *Proceedings of the Royal Society of London. Series A - Mathematical and Physical Sciences*, vol. 149, pp. 71-88, 1935.

[25] K. Fossheim and A. Sudbø, "Superconductivity : physics and applications," ed. Chichester: Wiley, 2004.

[26] E. J. Rothwell and M. J. Cloud, "Electromagnetics," in *Electrical engineering textbook series ; 2* vol. 2, ed. Boca Raton, Fla. ;London: CRC Press, 2001.

[27] C. P. Poole, "Superconductivity," 2nd / Charles P. Poole, Jr. ... [et al.]. ed. Amsterdam ;London: Academic Press, 2007.

[28] W. Wang, M. Zhang, Z. Huang, Y. Zhai, Z. Zhong, F. Spaven, *et al.*, "Study of the Penetration of a 2 Inches Diameter YBCO Thin Film With the Travelling Magnetic Wave," *IEEE Transactions on Applied Superconductivity*, vol. 24, pp. 4600304, 2014.

[29] L. D. Landau, E. M. Lifshi͡ts, and L. P. Pitaevskiĭ, "Statistical physics. Part 2, Theory of the condensed state," in *Pergamon international library of science, technology, engineering, and social studies.* vol. v. 9, [3rd]. / by E. M. Lifshitz and L. P. Pitaevskiĭ ; translated from the Russian by J. B. Sykes and M. J. Kearsley. ed. Oxford: Pergamon, 1980.

[30] L. D. Landau and D. t. Haar, "Collected papers of L.D.Landau," 1st ed. Oxford: Pergamon, 1965.

[31] C. P. Poole, "Handbook of superconductivity," ed. San Diego, Calif. ;London: Academic Press, 2000.

[32] C. P. Poole, H. A. Farach, and R. J. Creswick, "Superconductivity," ed. San Diego ;London: Academic Press, 1995.

[33] H. Van Beelen, J. P. Van Braam Houckgeest, R. De Bruyn Ouboter, and K. W. Taconis, "The motion of vortices in a type II superconductor under the influence of a transport current," *Physica,* vol. 36, pp. 225-240, 1967.

[34] H. F. Hess, R. B. Robinson, R. C. Dynes, J. M. Valles, and J. V. Waszczak, "Scanning-Tunneling-Microscope Observation of the Abrikosov Flux Lattice and the Density of States near and inside a Fluxoid," *Physical Review Letters,* vol. 62, pp. 214-216, 1989.

[35] K. Harada, T. Matsuda, J. Bonevich, M. Igarashi, S. Kondo, G. Pozzi, *et al.,* "REAL-TIME OBSERVATION OF VORTEX LATTICES IN A SUPERCONDUCTOR BY ELECTRON-MICROSCOPY," *Nature,* vol. 360, pp. 51-53, Nov 1992.

[36] E. H. Brandt, "The flux-line lattice in superconductors," *Reports on Progress in Physics,* vol. 58, p. 1465, 1995.

[37] H. W. Weber, J. Schelten, and G. Lippmann, "Microscopic Magnetic Field Distribution in Superconducting Niobium Single Crystals in the “Dirty Limit”," *physica status solidi (b),* vol. 57, pp. 515-522, 1973.

[38] J. W. Lynn, N. Rosov, T. E. Grigereit, H. Zhang, and T. W. Clinton, "Vortex dynamics and melting in niobium," *Physical Review Letters,* vol. 72, pp. 3413-3416, 1994.

[39] P. L. Gammel, D. J. Bishop, J. P. Rice, and D. M. Ginsberg, "Images of the vortex chain state in untwinned YBaCuO crystals," *Physical Review Letters,* vol. 68, pp. 3343-3346, 1992.

[40] L. Y. Vinnikov, L. A. Gurevich, G. A. Yemelchenko, and Y. A. Ossipyan, "Direct observation of the lattice of Abrikosov vortices in high-Tc superconductor YBa2Cu3Ox single crystals," *Solid State Communications,* vol. 67, pp. 421-423, 1988.

[41] C. Duran, J. Yazyi, F. de la Cruz, D. J. Bishop, D. B. Mitzi, and A. Kapitulnik, "Flux-lattice melting, anisotropy, and the role of interlayer coupling in BiSrCaCuO single crystals," *Physical Review B,* vol. 44, pp. 7737-7740, 1991.

[42] H. F. Hess, C. A. Murray, and J. V. Waszczak, "Flux lattice and vortex structure in 2H-NbSe2 in inclined fields," *Physical Review B,* vol. 50, pp. 16528-16540, 1994.

[43] C. Renner, A. D. Kent, P. Niedermann, Ø. Fischer, and F. Lévy, "Scanning tunneling spectroscopy of a vortex core from the clean to the dirty limit," *Physical Review Letters,* vol. 67, pp. 1650-1652, 1991.

[44] S. Behler, P. Jess, A. Baratoff, and H. J. Güntherodt, "Visualization of vortex pinning in NbSe2 by scanning tunneling microscopy," *Physica C: Superconductivity*, vol. 235–240, Part 4, pp. 2703-2704, 1994.

[45] A. Tonomura, H. Kasai, O. Kamimura, T. Matsuda, K. Harada, J. Shimoyama, *et al.*, "Motion of vortices in superconductors," *Nature*, vol. 397, pp. 308-309, Jan 1999.

[46] S. R. Foltyn, L. Civale, J. L. Macmanus-Driscoll, Q. X. Jia, B. Maiorov, H. Wang, *et al.*, "Materials science challenges for high-temperature superconducting wire," *Nature Materials*, vol. 6, pp. 631-642, Sep 2007.

[47] C. P. Bean, "Magnetization of High-Field Superconductors," *Reviews of Modern Physics*, vol. 36, pp. 31-39, 1964.

[48] M. Tomita and M. Murakami, "High-temperature superconductor bulk magnets that can trap magnetic fields of over 17 tesla at 29 K," *Nature*, vol. 421, pp. 517-520, Jan 2003.

[49] U. Mizutani, T. Oka, Y. Itoh, Y. Yanagi, M. Yoshikawa, and H. Ikuta, "Pulsed-field magnetization applied to high-Tc superconductors," *Applied Superconductivity*, vol. 6, pp. 235-246, 1998.

[50] W. J. Carr, "AC loss and macroscopic theory of superconductors," 2nd ed. London: Taylor & Francis, 2001.

[51] Y. B. Kim, C. F. Hempstead, and A. R. Strnad, "Magnetization and Critical Supercurrents," *Physical Review*, vol. 129, pp. 528-535, 1963.

[52] D. X. Chen and R. B. Goldfarb, "Kim model for magnetization of type-II superconductors," *Journal of Applied Physics*, vol. 66, pp. 2489-2500, 1989.

[53] Y. B. Kim, C. F. Hempstead, and A. R. Strnad, "Critical Persistent Currents in Hard Superconductors," *Physical Review Letters*, vol. 9, pp. 306-309, 1962.

[54] P. W. Anderson and Y. B. Kim, "Hard Superconductivity: Theory of the Motion of Abrikosov Flux Lines," *Reviews of Modern Physics*, vol. 36, pp. 39-43, 1964.

[55] A. P. Malozemoff, "Flux creep in high temperature superconductors," *Physica C: Superconductivity*, vol. 185–189, Part 1, pp. 264-269, 1991.

[56] W. G. V. Rosser, "An introduction to the theory of relativity," ed. London: Butterworths, 1964.

[57] J. Bardeen and M. J. Stephen, "Theory of the Motion of Vortices in Superconductors," *Physical Review,* vol. 140, pp. A1197-A1207, 1965.

[58] A. T. Dorsey, "Vortex motion and the Hall effect in type-II superconductors: A time-dependent Ginzburg-Landau theory approach," *Physical Review B,* vol. 46, pp. 8376-8392, 1992.

[59] N. B. Kopnin and A. V. Lopatin, "Flux-flow Hall effect in clean type-II superconductors," *Physical Review B,* vol. 51, pp. 15291-15303, 1995.

[60] N. B. Kopnin, "Vortex dynamics and mutual friction in superconductors and Fermi superfluids," *Reports on Progress in Physics,* vol. 65, p. 1633, 2002.

[61] P. W. Anderson, "Theory of Flux Creep in Hard Superconductors," *Physical Review Letters,* vol. 9, pp. 309-311, 1962.

[62] M. R. Beasley, R. Labusch, and W. W. Webb, "Flux Creep in Type-II Superconductors," *Physical Review,* vol. 181, pp. 682-700, 1969.

[63] Y. Luo, T. Takagi, and K. Miya, "Reduction of levitation decay in high Tc superconducting magnetic bearings," *Cryogenics,* vol. 39, pp. 331-338, 1999.

[64] Y. Yoshida, M. Uesaka, and K. Miya, "Magnetic field and force analysis of high Tc superconductor with flux flow and creep," *IEEE Transactions on Magnetics,* vol. 30, pp. 3503-3506, 1994.

[65] "http://www.imagesco.com/articles/superconductors/four-point-electrical-probe.html."

[66] A. Gladun, G. Fuchs, K. Fischer, D. Busch, R. Eujen, and J. Huedepohl, "Critical current densities and activation energy of BiPbSrCaCuO tapes," *IEEE Transactions on Applied Superconductivity,* vol. 3, pp. 1390-1393, 1993.

[67] L. Civale, B. Maiorov, A. Serquis, J. O. Willis, J. Y. Coulter, H. Wang, *et al.*, "Angular-dependent vortex pinning mechanisms in YBa2Cu3O7 coated conductors and thin films," *Applied Physics Letters,* vol. 84, pp. 2121-2123, 2004.

[68] P. Vanderbemden, Z. Hong, T. A. Coombs, S. Denis, M. Ausloos, J. Schwartz, *et al.*, "Behavior of bulk high-temperature superconductors of finite thickness subjected to crossed magnetic fields: Experiment and model," *Physical Review B,* vol. 75, p. 174515, 2007.

[69] E. H. Brandt and G. P. Mikitik, "Why an ac Magnetic Field Shifts the Irreversibility Line in Type-II Superconductors," *Physical Review Letters,* vol. 89, p. 027002, 2002.

[70] H. Wada, M. Sekino, H. Ohsaki, T. Hisatsune, H. Ikehira, and T. Kiyoshi, "Prospect of High-Field MRI," *IEEE Transactions on Applied Superconductivity,* vol. 20, pp. 115-122, 2010.

[71] L. Siyuan, J. Xiaohua, C. Guolin, and C. Jiangbo, "Superconducting Joint and Persistent Current Switch for a 7-T Animal MRI Magnet," *IEEE Transactions on Applied Superconductivity,* vol. 23, pp. 4400504-4400504, 2013.

[72] M. J. Leupold and Y. Iwasa, "Superconducting joint between multifilamentary wires 1. Joint-making and joint results," *Cryogenics,* vol. 16, pp. 215-216, 1976.

[73] C. A. Swenson and W. D. Markiewicz, "Persistent joint development for high field NMR," *IEEE Transactions on Applied Superconductivity,* vol. 9, pp. 185-188, 1999.

[74] J. E. C. Williams, S. Pourrahimi, Y. Iwasa, L. J. Neuringer, and L. Motowidlo, "600 MHz spectrometer magnet," *IEEE Transactions on Magnetics,* vol. 25, pp. 1767-1770, 1989.

[75] R. Thorton, "Superconducting joint for superconducting wires and coils and method of forming," *U.S. Patent 4,* 1998.

[76] K. Nemoto, S. Saito, Y. Sanada, K. Sasaki, S. Miyake, and H. Hashiguchi, "Niobium-tin persistent-current switch for the superconducting magnet of Maglev," *IEEE Transactions on Applied Superconductivity,* vol. 9, pp. 181-184, 1999.

[77] T. K. Ko, Y. S. Oh, and S. J. Lee, "Optimal design of the superconducting persistent current switch with respect to the heater currents and the operating currents," *IEEE Transactions on Applied Superconductivity,* vol. 5, pp. 262-265, 1995.

[78] K. Rock-Kil, B. Joon-Han, S. Ki-Deok, L. Eon-Young, K. Hae-Jong, K. Young-Kil, *et al.*, "Performance test of a persistent current switch insulated with cotton tape," *IEEE Transactions on Applied Superconductivity,* vol. 11, pp. 2425-2428, 2001.

[79] B. J. Parkinson, R. Slade, M. J. D. Mallett, and V. Chamritski, "Development of a Cryogen Free 1.5 T YBCO HTS Magnet for MRI," *IEEE Transactions on Applied Superconductivity,* vol. 23, pp. 4400405-4400405, 2013.

[80] R. Gupta, M. Anerella, A. Ghosh, H. Kirk, P. Joshi, S. Lalitha, *et al.*, "High Field HTS Solenoid for a Muon Collider - Demonstrations, Challenges and Strategies," *IEEE Transactions on Applied Superconductivity,* vol. 24, pp. 4301705, 2013.

[81] Y. Iwasa, "HTS magnets: stability; protection; cryogenics; economics; current stability/protection activities at FBML," *Cryogenics,* vol. 43, pp. 303-316, 2003.

[82] G. Fuchs, K. H. Müller, A. Handstein, K. Nenkov, V. N. Narozhnyi, D. Eckert, *et al.*, "Upper critical field and irreversibility line in superconducting MgB2," *Solid State Communications*, vol. 118, pp. 497-501, 2001.

[83] Y. Wolfus, Y. Fleger, A. Friedman, F. Kopansky, B. Kalisky, Y. Yeshurun, *et al.*, "Estimation of the critical current of BSCCO coils based on the field dependent I–V curves of BSCCO tapes," *Physica C: Superconductivity*, vol. 401, pp. 222-226, 2004.

[84] V. Lombardo, E. Barzi, D. Turrioni, and A. V. Zlobin, "Critical Currents of YBaCuO Tapes and BSCCO Wires at Different Temperatures and Magnetic Fields," *IEEE Transactions on Applied Superconductivity*, vol. 21, pp. 3247-3250, 2011.

[85] V. Moshchalkov, M. Menghini, T. Nishio, Q. H. Chen, A. V. Silhanek, V. H. Dao, *et al.*, "Type-1.5 Superconductivity," *Physical Review Letters*, vol. 102, p. 117001, 2009.

[86] Y. Yeshurun and A. P. Malozemoff, "Giant Flux Creep and Irreversibility in an YBaCuO Crystal: An Alternative to the Superconducting-Glass Model," *Physical Review Letters*, vol. 60, pp. 2202-2205, 1988.

[87] L. J. M. van de Klundert and H. H. J. ten Kate, "Fully superconducting rectifiers and fluxpumps Part 1: Realized methods for pumping flux," *Cryogenics*, vol. 21, pp. 195-206, 1981.

[88] V. L. Newhouse, "On minimizing flux pump heat dissipation," *IEEE Transactions on Magnetics*, vol. 4, pp. 482-485, 1968.

[89] Z. Bai, G. Yan, C. Wu, S. Ding, and C. Chen, "A novel high temperature superconducting magnetic flux pump for MRI magnets," *Cryogenics*, vol. 50, pp. 688-692, 2010.

[90] C. Yoon Do, K. Hyoung Ku, Y. Yong-Soo, and K. Tae-Kuk, "Theoretical Analysis and Design Consideration of Advanced Linear Type Magnetic Flux Pump," *IEEE Transactions on Applied Superconductivity*, vol. 21, pp. 1097-1100, 2011.

[91] D. L. Atherton, "METHOD AND MEANS FOK OBTAINING HIGH MAGNETIC FIELDS," ed: Google Patents, 1967.

[92] T. G. Berlincourt, "Method and apparatus for magnetic flux accumulation and current generation," ed: Google Patents, 1966.

[93] C. Yoondo, T. Hoshino, and T. Nakamura, "Current Pumping Performance of Linear-Type Magnetic Flux Pump With Use of Feedback Control Circuit System," *IEEE Transactions on Applied Superconductivity*, vol. 16, pp. 1638-1641, 2006.

[94] Y. D. Chung, I. Muta, T. Hoshino, T. Nakamura, and M. H. Shon, "Design and performance of compensator for decremental persistent current in HTS magnets using linear type magnetic flux pump," *Cryogenics*, vol. 44, pp. 839-844, 2004.

[95] C. Yoondo, M. Itsuya, T. Hoshino, and T. Nakamura, "Performances of a linear type magnetic flux pump for compensating a little decremented persistent current of HTS magnets," *IEEE Transactions on Applied Superconductivity*, vol. 14, pp. 1723-1726, 2004.

[96] P. N. Mikheenko and Y. E. Kuzovlev, "Inductance measurements of HTSC films with high critical currents," *Physica C: Superconductivity*, vol. 204, pp. 229-236, 1993.

[97] J. F. Marchand and J. Volger, "Radiation-induced transport of magnetic flux along a superconducting sheet," *Physics Letters*, vol. 2, pp. 118-119, 1962.

[98] H. Van Beelen, M. A. J. P. T. Arnold, H. A. Sypkens, J. P. Van Braam Houckgeest, R. De Bruyn Ouboter, J. J. M. Beenakker, *et al.*, "Flux pumps and superconducting solenoids," *Physica*, vol. 31, pp. 413-443, 1965.

[99] I. Giaever, "Magnetic Coupling Between Two Adjacent Type-II Superconductors," *Physical Review Letters*, vol. 15, pp. 825-827, 1965.

[100] J. R. Clem, "Theory of the coupling force in magnetically coupled type-II superconducting films," *Physical Review B*, vol. 12, pp. 1742-1752, 1975.

[101] R. Deltour and M. Tinkham, "Coupled Motion of Vortices in Superposed Superconducting Films," *Physical Review*, vol. 174, pp. 478-481, 1968.

[102] I. Giaever, "Flux Pinning and Flux-Flow Resistivity in Magnetically Coupled Superconducting Films," *Physical Review Letters*, vol. 16, pp. 460-462, 1966.

[103] P. E. Cladis, R. D. Parks, and J. M. Daniels, "Phase Incoherence in the dc Superconducting Transformer," *Physical Review Letters*, vol. 21, pp. 1521-1524, 1968.

[104] S. Berger, K. Bouzehouane, D. Crété, and J.-P. Contour, "Realization of a flux-flow DC-transformer using high temperature superconductors," *The European Physical Journal - Applied Physics*, vol. 6, pp. 111-113, 1999.

[105] M. D. Sherrill and W. A. Lindstrom, "Superconducting dc transformer coupling," *Physical Review B*, vol. 11, pp. 1125-1130, 1975.

[106] J. W. Ekin and J. R. Clem, "Magnetic coupling force of the superconducting dc transformer," *Physical Review B*, vol. 12, pp. 1753-1765, 1975.

[107] J. R. Clem, "Theory of magnetically coupled type-II superconducting films," *Physical Review B*, vol. 9, pp. 898-911, 1974.

[108] P. R. Solomon, "Flux Motion in Type-I Superconductors," *Physical Review*, vol. 179, pp. 475-484, 1969.

[109] T. Coombs, Z. Hong, and X. Zhu, "A thermally actuated superconducting flux pump," *Physica C: Superconductivity*, vol. 468, pp. 153-159, 2008.

[110] Y. Yu, L. Quan, and T. A. Coombs, "Thermally actuated magnetization flux pump in single-grain YBCO bulk," *Superconductor Science and Technology*, vol. 22, p. 105011, 2009.

[111] T. A. Coombs, Z. Hong, Y. Yan, and C. D. Rawlings, "The Next Generation of Superconducting Permanent Magnets: The Flux Pumping Method," *IEEE Transactions on Applied Superconductivity*, vol. 19, pp. 2169-2173, 2009.

[112] T. A. Coombs, Z. Hong, X. Zhu, and G. Krabbes, "A novel heat engine for magnetizing superconductors," *Superconductor Science and Technology*, vol. 21, p. 034001, 2008.

[113] Y. Yu, H. Chiahao, H. Zhiyong, X. Wei, W. Yuan, and T. A. Coombs, "A Novel Design of Thermally Actuated Magnetization Flux Pump for High Temperature Superconducting Bulks," *IEEE Transactions on Applied Superconductivity*, vol. 21, pp. 1568-1571, 2011.

[114] T. A. Coombs, O. Hadeler, M. Zhang, and K. Matsuda, "Flux pumping, fluctuations and climbing fields," *Superconductor Science and Technology*, vol. 25, p. 104007, 2012.

[115] T. A. Coombs, "A Finite Element Model of Magnetization of Superconducting Bulks Using a Solid-State Flux Pump," *IEEE Transactions on Applied Superconductivity*, vol. 21, pp. 3581-3586, 2011.

[116] C. Hoffmann, D. Pooke, and A. D. Caplin, "Flux Pump for HTS Magnets," *IEEE Transactions on Applied Superconductivity*, vol. 21, pp. 1628-1631, 2011.

[117] R. M. Walsh, R. Slade, D. Pooke, and C. Hoffmann, "Characterization of Current Stability in an HTS NMR System Energized by an HTS Flux Pump," *IEEE Transactions on Applied Superconductivity*, vol. 24, pp. 1-5, 2014.

[118] Z. Bai, C. Chen, Y. Wu, and Z. Zhen, "Effect of various pulse wave forms for pulse-type magnetic flux pump," *Cryogenics*, vol. 51, pp. 530-533, 2011.

[119] C. Yoon Do, M. Itsuya, T. Hoshino, and T. Nakamura, "Characteristics of a persistent current compensator for Superconducting NMR magnets using linear type magnetic flux pump," *IEEE Transactions on Applied Superconductivity*, vol. 15, pp. 1338-1341, 2005.

[120] Y. Yan, Q. Li, and T. A. Coombs, "Thermally actuated magnetization flux pump in single-grain YBCO bulk," *Superconductor Science and Technology*, vol. 22, p. 105011, 2009.

[121] Y. Yu, H. Zhiyong, L. Quan, X. Wei, W. Yuan, and T. A. Coombs, "Thermally Actuated Magnetization Method in High Temperature Superconductor Bulks," *IEEE Transactions on Applied Superconductivity*, vol. 20, pp. 1823-1826, 2010.

[122] Q. Li, Y. Yan, C. Rawlings, and T. Coombs, "Magnetization of Bulk Superconductors Using Thermally Actuated Magnetic Waves," *IEEE Transactions on Applied Superconductivity*, vol. 20, pp. 2243-2247, 2010.

[123] L. Quan, Y. Yu, R. Colin, and C. Tim, "Numerical analysis of thermally actuated magnets for magnetization of superconductors," *Journal of Physics: Conference Series*, vol. 234, p. 032035, 2010.

[124] W. Wang, M. Zhang, C. Hsu, and T. Coombs, "Design Consideration of a Circular Type Magnetic Flux Pump Device," *IEEE Transactions on Applied Superconductivity*, vol. 22, pp. 5201304-5201304, 2012.

[125] E. H. Brandt and G. P. Mikitik, "Why an ac magnetic field shifts the irreversibility line in type-II superconductors," *Physical Review Letters*, vol. 89, Jul 2002.

[126] E. H. Brandt and G. P. Mikitik, "Vortex shaking in superconducting platelets in an inclined magnetic field," *Superconductor Science & Technology*, vol. 20, pp. S111-S116, Sep 2007.

[127] "http://www.akm.com/akm/en/file/datasheet/HZ-312C.pdf."

[128] Y. Iwasa, J. Bascunan, H. Seungyong, M. Tomita, and Y. Weijun, "High-Temperature Superconducting Magnets for NMR and MRI: R&D Activities at the MIT Francis Bitter Magnet Laboratory," *IEEE Transactions on Applied Superconductivity*, vol. 20, pp. 718-721, 2010.

[129] Y. Iwasa, H. Seung-yong, M. Tomita, L. Haigun, and J. Bascunan, "A "persistent-mode" magnet comprised of YBCO annuli," *IEEE Transactions on Applied Superconductivity*, vol. 15, pp. 2352-2355, 2005.

[130] H. Seungyong, J. Voccio, S. Bermond, P. Dong-Keun, J. Bascunan, K. Seok-Beom, *et al.*, "Field Performance of an Optimized Stack of YBCO Square "Annuli" for a Compact NMR Magnet," *IEEE Transactions on Applied Superconductivity*, vol. 21, pp. 1632-1635, 2011.

[131] H. Seungyong, J. Voccio, P. Dong Keun, K. Kwang-Min, M. Tomita, J. Bascunan, *et al.*, "A Stack of YBCO Annuli, Thin Plate and Bulk, for Micro-NMR Spectroscopy," *IEEE Transactions on Applied Superconductivity*, vol. 22, pp. 4302204-4302204, 2012.

[132] H. Seungyong, K. Youngjae, J. Voccio, P. Dong Keun, B. Gagnon, J. Bascunan, *et al.*, "Bulk and Plate Annulus Stacks for Compact NMR Magnets: Trapped Field Characteristics and Active Shimming Performance," *IEEE Transactions on Applied Superconductivity*, vol. 23, pp. 4300504-4300504, 2013.

[133] S. B. Kim, T. Kimoto, S. Hahn, Y. Iwasa, J. Voccio, and M. Tomita, "Study on optimization of YBCO thin film stack for compact NMR magnets," *Physica C: Superconductivity*, vol. 484, pp. 295-299, 2013.

[134] Z. Hong, A. M. Campbell, and T. A. Coombs, "Numerical solution of critical state in superconductivity by finite element software," *Superconductor Science and Technology*, vol. 19, p. 1246, 2006.

[135] Z. Hong and T. A. Coombs, "Numerical Modelling of AC Loss in Coated Conductors by Finite Element Software Using H Formulation," *Journal of Superconductivity and Novel Magnetism*, vol. 23, pp. 1551-1562, 2010.

[136] Z. Hong, A. M. Campbell, and T. A. Coombs, "Computer Modeling of Magnetisation in High Temperature Bulk Superconductors," *IEEE Transactions on Applied Superconductivity*, vol. 17, pp. 3761-3764, 2007.

[137] Z. Hong, Q. Jiang, R. Pei, A. M. Campbell, and T. A. Coombs, "A numerical method to estimate AC loss in superconducting coated conductors by finite element modelling," *Superconductor Science and Technology*, vol. 20, p. 331, 2007.

[138] M. Zhang, J. Kvitkovic, J.-H. Kim, C. H. Kim, S. V. Pamidi, and T. A. Coombs, "Alternating current loss of second-generation high-temperature superconducting coils with magnetic and non-magnetic substrate," *Applied Physics Letters*, vol. 101, pp. 102602, 2012.

[139] Y. Yeshurun, A. P. Malozemoff, and A. Shaulov, "Magnetic relaxation in high-temperature superconductors," *Reviews of Modern Physics*, vol. 68, pp. 911-949, 1996.

[140] "http://en.wikipedia.org/wiki/Helmholtz_coil."

[141] J. Yudong, R. Pei, W. Xian, Z. Hong, W. Yuan, R. Marchant, *et al.*, "Magnetization Process of an HTS Motor and the Torque Ripple Suppression," *IEEE Transactions on Applied Superconductivity,* vol. 19, pp. 1644-1647, 2009.

[142] M. D. Ainslie, Y. Jiang, W. Xian, Z. Hong, W. Yuan, R. Pei, *et al.*, "Numerical analysis and finite element modelling of an HTS synchronous motor," *Physica C: Superconductivity,* vol. 470, pp. 1752-1755, 2010.

[143] H. Zhen, X. Wei, Z. Min, M. Chudy, Y. Chen, Z. Zhaoyang, *et al.*, "Control and Operation of a High Temperature Superconducting Synchronous Motor," *IEEE Transactions on Applied Superconductivity,* vol. 23, pp. 5200204-5200204, 2013.

[144] C. H. Chiang, Y. H. Li, W. C. Chan, L. M. Wang, and J. G. Lin, "Induced Voltage Measurements on a YBa2Cu3O7−δ Superconducting Thin Film Due to a Pair of Rotating Magnets," *Journal of Superconductivity and Novel Magnetism,* vol. 20, pp. 369-371, 2007.

[145] W. C. Chan, C. B. Lin, H. Chao, and C. H. Chiang, "Measuring voltage in a YBaCuO superconductor induced by a moving magnet," *Physical Review B,* vol. 72, p. 172510, 2005.

[146] D.-X. Chen and R. B. Goldfarb, "Kim model for magnetization of type-II superconductors," *Journal of Applied Physics,* vol. 66, pp. 2489-2500, 1989.

[147] A. Sanchez and C. Navau, "Magnetic properties of finite superconducting cylinders. I. Uniform applied field," *Physical Review B,* vol. 64, p. 214506, 2001.

[148] M. Zhang, J. Kvitkovic, J.-H. Kim, C. H. Kim, S. V. Pamidi, and T. A. Coombs, "Alternating current loss of second-generation high-temperature superconducting coils with magnetic and non-magnetic substrate," *Applied Physics Letters,* vol. 101, p. 102602, 2012.

[149] C. P. Bean, "MAGNETIZATION OF HIGH-FIELD SUPERCONDUCTORS," *Reviews of Modern Physics,* vol. 36, pp. 31, 1964.

[150] M. Willemin, C. Rossel, J. Hofer, H. Keller, A. Erb, and E. Walker, "Strong shift of the irreversibility line in high-Tc superconductors upon vortex shaking with an oscillating magnetic field," *Physical Review B,* vol. 58, pp. R5940-R5943, 1998.

[151] Z. Y. Zhang, S. Matsumoto, R. Teranishi, and T. Kiyoshi, "Magnetic field, temperature and mechanical crack performance of a GdBCO magnetic lens," *Superconductor Science and Technology,* vol. 25, p. 115012, 2012.

[152] Z. Y. Zhang, S. Matsumoto, R. Teranishi, and T. Kiyoshi, "Improving the properties of GdBCO magnetic lenses by adopting a new design and resin impregnation," *Superconductor Science and Technology,* vol. 26, p. 045001, 2013.

[153] I. Hlasnik and L. Cesnak, "Magnetic flux concentration in bulk hollow superconducting cylinders," *Cryogenics,* vol. 9, pp. 95-99, 1969.

[154] T. Asano, K. Itoh, S. Matsumoto, T. Kiyoshi, H. Wada, and G. Kido, "Enhanced concentration of the magnetic flux in a superconducting cylinder," *IEEE Transactions on Applied Superconductivity,* vol. 15, pp. 3157-3160, 2005.

[155] P. A. Stephen and G. Francesco, "A strategy for the reduction of ac losses in YBCO coated conductors," *Superconductor Science and Technology,* vol. 19, p. 227, 2006.

[156] W. Yuan, M. D. Ainslie, W. Xian, Z. Hong, Y. Chen, Y. Yan, *et al.*, "Theoretical and Experimental Studies on and AC Losses of 2G HTS Coils," *IEEE Transactions on Applied Superconductivity,* vol. 21, pp. 2441-2444, 2011.

[157] J. Šouc, E. Pardo, M. Vojenčiak, and F. Gömöry, "Theoretical and experimental study of AC loss in high temperature superconductor single pancake coils," *Superconductor Science and Technology,* vol. 22, p. 015006, 2009.

[158] D. Miyagi, O. Tsukamoto, and M. Ciszek, "Study of frequency dependence of AC transport current losses in HTS conductors subject to DC background field," *IEEE Transactions on Applied Superconductivity,* vol. 11, pp. 2449-2452, 2001.

[159] K. Miyamoto, N. Amemiya, N. Banno, M. Torii, E. Hatasa, E. Mizushima, *et al.*, "Measurement and FEM analysis of magnetization loss in HTS tapes," *IEEE Transactions on Applied Superconductivity,* vol. 9, pp. 770-773, 1999.